Study on Heterogeneity of Oxide Films Formed on Polycrystalline Iron

多結晶鉄上に形成する酸化物皮膜の
不均一性に関する研究

Yu Takabatake

Graduate School of Chemical Sciences and Engineering
Hokkaido University

March 2017

Table of contents

Chapter 1 Introduction

Chapter 2 Experimental techniques and setups

Chapter 3 Grain-dependent oxidation behavior in sulfuric acid measured by micro-capillary cell

Chapter 4 Heterogeneity of thermally grown oxide film observed by two-dimensional ellipsometry

Chapter 1
Introduction

1.1. Corrosion of metals

1.1.1. Significance of corrosion study

Metals and alloys are used in a wide range of industrial fields as structural materials for purposes such as infrastructures, transportation equipment, and buildings ranging in scale from skyscrapers to individual houses. It is not too much to say that our productive activities and even our very lives are supported by metallic materials. Metallic materials with different properties (e.g., mechanical strength, flexibility, workability, corrosion resistance) have been used for particular purposes. Whenever metals and alloys are used in practice, corrosion occurs on their surfaces; it is caused by chemical reactions that develop at material-environment interfaces. Corrosion is a naturally occurring phenomenon, occurring on metallic materials and progressing through thermodynamically stable reactions by forming oxides and/or dissolving into the environment in ionic states, since Gibbs formation energies of oxides and ions are usually lower than those of metallic states [1]. Although it is not a realistic goal to stop the progress of corrosion reactions completely, it is possible to reduce corrosion rates by applying appropriate conservation measures to metallic materials. The progress of corrosion causes a functional decline and breakdown in devices and facilities; occasionally, it can cause serious accidents such as the explosion of plant equipment. The Committee on Cost of Corrosion in Japan [2] reported that corrosion costs in Japan at 1997, including economic losses and corrosion expenditures, to be 3.9 trillion JPY and 5.3 trillion JPY, as estimated by the Uhlig method and the Hoar method respectively; these figures were equivalent to 0.77% and 1.02% to Japan's gross national product (GNP). Figure 1.1 shows the breakdown of corrosion costs as estimated by the Uhlig method. Total costs, including direct and indirect costs, were estimated at 9.7 trillion JPY in 1997 (1.88% of Japanese GNP) by the Input/Output analysis. From the viewpoint of reducing economic losses and saving energy and resources, it is necessary to use metallic materials as long as possible, from several decades to even hundreds of years. Longer service time in metallic materials is realized by prevention strategies that minimize the progression of corrosion. A knowledge of corrosion science and theories is necessary to develop appropriate strategies and aid in achieving a sustainable society. Traditionally, the progress of corrosion has been estimated from the macroscopic perspective by using the theories of uniform corrosion. In practice, non-uniform

corrosion occurs on the surface of practical metallic materials, depending on the heterogeneous characteristics of the surface (e.g., surface inclusions, metallographic texture, and crystallographic orientation). Such heterogeneous corrosion leads to undesired breakdown in materials initiated by localized corrosion that is difficult to predict with traditional theories of uniform corrosion. In order to predict the progress of localized corrosion that occurs on practical materials, it is necessary to elucidate the precise mechanisms of heterogeneous corrosion reactions from a microscopic view.

1.1.2. Anisotropic corrosion

Metals and alloys demonstrate anisotropy for their characteristics because they have a well-ordered crystal structure at the atomic level unless they are amorphous. Anisotropy affects the properties of metallic materials and is used in several applications. For example, electrical steel [3], which is a magnetic material used as the iron core of motors and electric transformers, takes advantage of magnetic anisotropy. The iron core requires high magnetic flux density (i.e., high permeability) to maintain its magnetic energy. Since the magnetization easy axis of body-centered cubic (bcc) iron is in the <0 0 1> direction, the orientation of crystal grains of the electrical steel is controlled to face the <0 0 1> direction to the substrate normal direction (ND) by rolling and annealing processes (Fig. 1.2), so that the steel achieves high magnetic flux density.

The activity of chemical reaction that occurs on the surface of metals and alloys is also affected by anisotropy. The surface crystallographic orientation of metals and alloys affects their corrosion reaction. Orientation-dependent corrosion behavior is reported using single crystals of iron [4–6], copper [7], niobium [8], titanium [9], and zinc [10]. The oxide formation rates in both air and aqueous solution depend on the surface crystallographic orientation.

Most metallic materials used in a wide range of industrial fields are polycrystalline, unless there are specific reasons to use their monocrystalline forms, as with silicon chips for electronic devices [11] and Ni-based alloys for gas turbine blades [12]. Since a polycrystalline material is composed of numerous crystal grains, the surface of the material exposes many crystal planes, each of which is characterized by individual crystallographic orientations, which means that the surface activity of the polycrystalline material is not homogeneous. Grain-dependent corrosion of polycrystalline metals has been reported for aluminum [13], copper [14–16], iron [17–20], magnesium [21,22], titanium [23–27], zinc [28], and zirconium and tantalum [29]. Grain-dependent electrochemical activity for the redox reaction of Fe(II)/Fe(III) couples has also been reported for polycrystalline platinum electrodes [30]. Through these studies, the broad trends of grain-dependent corrosion on polycrystalline metals have been revealed; orientation-dependent parameters such as surface energy and surface atomic density affect the dissolution and oxide formation rates of substrate metals. However, the precise corrosion mechanism that depends on the crystallographic orientation of the polycrystalline surface remains unclear. The progress of anisotropic corrosion may initiate localized corrosion on polycrystalline materials. When the

degradation rate of an oxide film and/or the dissolution rate of a substrate metal differ depending on the surface orientation of the substrate, corrosion progresses preferentially at a local site where corrosion resistivity is the lowest. The local site becomes a local anode, with the anodic dissolution of the metal at that site accelerating due to the high anodic current density caused by an extremely high ratio of local cathode/anode areas. This is the initiation of pitting corrosion, which is a type of localized corrosion. In order to predict the initiation of localized corrosion, it is necessary to elucidate the mechanism of grain-dependent corrosion that progresses on polycrystalline materials.

1.2. Iron

Iron is the most commonly used metal in the world; it is employed in many industries as a base element of steels. Figure 1.3 shows the total production of crude steel in the world from 1967 to 2015 [31]. Although Japanese steel production has not varied a great deal since the 1970s, production in other countries has increased slightly, with China's increasing dramatically since the early decade of the 21st century. The drop in production in 2009 was due to the 2008 financial crisis. According to a report by the Research Institute of Innovative Technology for the Earth (RITE) in Japan [32], steel production will continue to increase in the coming decades due to growing demand in developing countries. Thus, studying the corrosion behavior of iron will become ever more important in supporting steel-based societies of the future.

High-purity iron is not used as a structural material since it is easily oxidized to rust by oxygen in humid air and shows low toughness against external stress. However, knowing the electrochemical behavior of pure iron is of great importance to understanding the essentials of corrosion reactions on iron-based materials and steels.

1.2.1. General characteristics

Iron is in the transition metal family of elements (atomic number: 26, atomic weight: 55.85). Its Clarke number, which indicates the ratio of elements that exist on the earth by weight percent concentration, is 4.70 [33]. This is the second largest number among metal elements, trailing only aluminum. The crystallographic properties of iron [34] are summarized in Table 1.1. Alpha-Fe shows ferromagnetism at low temperature and paramagnetism at temperatures above the Curie or A_2 transformation point at 1044 K, with melting and boiling points of 1811 and 3003 K respectively. When α-Fe showed paramagnetic properties, it was once called β-Fe. The electronic properties of iron surfaces with low Miller indices have been studied with quantum chemistry calculations. The calculated surface atom density ρ_{surf}, the reported values of surface energy γ, and the work function Φ_w, as calculated for the α-Fe {0 0 1}, {1 0 1}, and {1 1 1} planes, are presented in Table 1.2. Although the authors report that γ shows some scattering, the average

Table 1.1. Crystallographic properties of iron.

Phase	Crystal lattice	Lattice constant (Å)	Transformation point (K)
α-Fe	body-centered cubic	2.8665	1185 (α → γ)
γ-Fe	face-centered cubic	3.6467	
δ-Fe	body-centered cubic	2.9315	1667 (γ → δ)

Table 1.2. Surface characteristics of α-Fe; ρ_{surf}, surface atom denity [18]; γ, surface energy; Φ_w, work function.

Surface	ρ_{surf} (cm^{-2})	γ ($J\ m^{-2}$)	Φ_w (eV)
{0 0 1}	1.22×10^{15}	2.661842 [a]	
		2.43 [b]	3.95 [b]
		2.47 [c]	3.91 [c]
{1 0 1}	1.73×10^{15}	2.054162 [a]	
		2.06 [b]	4.84 [b]
		2.58 [c]	4.76 [c]
{1 1 1}	1.88×10^{15}	2.512740 [a]	
		2.31 [b]	3.97 [b]
		2.37 [c]	3.95 [c]

[a] The dangling bond analysis method based on the empirical electron theory [35]

[b] Density functional theory (DFT) using the pseudopotentials plane-wave method [36]

[c] DFT total energy calculations [37]

value of γ becomes greater in the order of the {0 0 1} > {1 1 1} > {1 0 1} planes. The coordination numbers of a surface atom on α-Fe {0 0 1}, {1 1 1}, and {1 0 1} surfaces are 4, 4 and 6, and 6 respectively. Dangling bond electron density and the spatial distribution of covalent bonds have been reported to have a great influence on γ and Φ_w [35,36].

1.2.2. Corrosion behavior

The corrosion of metals and alloys progresses as a result of electrochemical reactions with chemical species in the surrounding environment; these occur at the surface. Consider the electron transfer reaction between metal M and its ion M^{z+}, a simple electrode process:

$$M \rightleftharpoons M^{z+} + ze^{-}, \tag{1.1}$$

where z is the valence. The forward and reverse processes of Eq. 1.1 are called anodic and cathodic reactions, with the rates of these electrochemical reactions expressed as the anodic current density j_a and the cathodic current density j_c respectively. Figure 1.4 illustrates a polarization curve for the electrode process in Eq. 1.1. When $j_a = j_c$, the electrode potential E

shows the equilibrium potential E_{eq} and the exchange current density j_0 (= j_a = j_c) flows. When the overpotential η (= $E - E_{eq}$) is applied to the electrode, the current j that flows through an electronic circuit is given by the Butler-Volmer equation [38]:

$$j = j_0 \left[\exp\left\{ \frac{azF\eta}{RT} \right\} - \exp\left\{ - \frac{(1-a)zF\eta}{RT} \right\} \right], \tag{1.2}$$

where a is the symmetry factor, F is the Faraday constant, R is the gas constant, and T is the absolute temperature. The left and right terms on the right-hand side of Eq. 1.2 correspond to the anodic and cathodic currents, respectively. For large values of η (either negative or positive), one of the bracketed terms in Eq. 1.2 becomes negligible. For example, at large negative overpotentials ($\eta >> RT/azF$), Eq. 1.2 becomes

$$j = j_0 \exp\left(\frac{azF\eta}{RT} \right). \tag{1.3}$$

The transformation of Eq. 1.3 into common logarithmic terms gives

$$\eta = -\left(\frac{2.303RT}{azF} \right) \log j_0 + \left(\frac{2.303RT}{azF} \right) \log j. \tag{1.4}$$

If one puts

$$A = -\frac{2.303RT}{azF} \log j_0 \tag{1.5}$$

and

$$B = -\frac{2.303RT}{azF}, \tag{1.6}$$

Eq. 1.4 is transformed into

$$\eta = A + B \log j\ . \tag{1.7}$$

Any successful model of electrode kinetics must explain the frequent validity of Eq. 1.7, which is known as the Tafel equation. The constant B is called the Tafel slope, while a plot of log j vs. η is known as a Tafel plot; it is a useful device for evaluating the kinetic parameters of electrode reactions.

When a metal electrode is exposed to an aqueous environment, equilibrium is achieved between the Fermi level of the metal and the mixed potential of the redox system in the environment. Here, a simple corrosion reaction that progresses on iron is used as an example. An iron electrode immersed in acid solution dissolves into the solution with hydrogen gas evolution. At the iron/solution interface, the following redox reactions proceed simultaneously:

$$Fe \rightleftharpoons Fe^{2+} + 2e^-, \tag{1.8}$$

$$2H^+ + 2e^- \rightleftharpoons H_2. \tag{1.9}$$

The dissolution of iron is an anodic reaction, while the evolution of hydrogen gas is a cathodic reaction. According to the local cell theory proposed by Evans [39], an iron surface is composed of numerous small cells called local cells that connect local anodes and cathodes via the electronic current J_e and the ionic current J_i through the iron substrate and aqueous solution respectively (Fig. 1.5).

Figure 1.6 presents the Tafel plots for the reactions in Eqs. 1.8 and 1.9. When the anodic and cathodic reactions are at equilibrium, external currents do not flow and the electrode shows the corrosion potential E_{corr}. Extrapolation of both linear segments to an intercept at E_{corr} gives us the corrosion current density j_{corr}. This method is called a Tafel extrapolation and enables the calculation of j_{corr}, which cannot be measured directly from polarization measurements. Bockris et al. [40] reported that the Tafel slope b_a of the iron dissolution reaction (IDR) became 40 mV decade^{-1} and that the IDR progressed according to the following mechanisms:

$$Fe + OH^- \rightleftharpoons Fe(OH)_{ads} + e^- \quad (1.10)$$

$$Fe(OH)_{ads} \rightarrow FeOH^+ + e^- \quad \text{(rate-determining step: rds)} \quad (1.11)$$

$$FeOH^+ + H^+ \rightleftharpoons Fe^{2+} + H_2O, \quad (1.12)$$

where $Fe(OH)_{ads}$ is an intermediate absorber and relates directly to the IDR. This mechanism is generally called the Bockris mechanism. Heusler [41], meanwhile, proposes the following mechanism, based on the experimental results of b_a = 30 mV decade^{-1}:

$$Fe + OH^- \rightleftharpoons Fe(OH)_{ads} + e^- \quad (1.13)$$

$$Fe + Fe(OH)_{ads} + OH^- \rightarrow FeOH^+ + Fe(OH)_{ads} + e^- \quad \text{(rds)} \quad (1.14)$$

$$FeOH^+ + H^+ \rightleftharpoons Fe^{2+} + H_2O. \quad (1.15)$$

An intermediate $Fe(OH)_{ads}$ in Eq. 1.14 works as a catalyst and does not directly relate to the IDR. The value of b_a for the IDR deviates from 30 to 60 mV decade^{-1} according to reports; it has not been fixed. It has been suggested that the surface condition of iron is changed by both preparation method and time, that the Bockris mechanism explains the IDR of low defective annealed iron electrodes well, and that the Heusler mechanism fits with the IDR of cold-worked iron electrodes that have highly concentrated surface defects, such as kinks [42–44].

Either electrons or protons or both relate to electrochemical reactions in a metal-aqueous solution system. Thus, the stable state of a metal depends on the electrode potential and/or the solution pH. Pourbaix [45] proposed constructing a potential-pH diagram, known as a Proubaix diagram, that maps out the equilibrium among metal, metal ions, and oxides with respect to their electrode potential and the pH of an aqueous solution. Figure 1.7 shows a Pourbaix diagram for the system iron-water at 298 K, with the solution pH plotted against the standard hydrogen electrode (SHE) potential. The following reactions indicate the redox reactions at the numbered lines that separate the different domains in Fig. 1.7; here, only Fe, Fe_2O_3, and Fe_3O_4 are

considered to be solid substances:

a. $H_2 \rightleftharpoons 2H^+ + 2e^-$ (1.16)

b. $4H_2O \rightleftharpoons O_2 + 4H^+ + 4e^-$ (1.17)

1. $\mathbf{Fe} \rightleftharpoons Fe^{2+} + 2e^-$ (1.18)

2. $3\mathbf{Fe} + 4H_2O \rightleftharpoons \mathbf{Fe_3O_4} + 8H^+ + 8e^-$ (1.19)

3. $\mathbf{Fe} + 2H_2O \rightleftharpoons HFeO^{2-} + 3H^+ + 2e^-$ (1.20)

4. $3HFeO^{2-} + H^+ \rightleftharpoons \mathbf{Fe_3O_4} + 2H_2O + 2e^-$ (1.21)

5. $2\mathbf{Fe_3O_4} + H_2O \rightleftharpoons 3\mathbf{Fe_2O_3} + 2H^+ + 2e^-$ (1.22)

6. $2Fe^{2+} + 3H_2O \rightleftharpoons \mathbf{Fe_2O_3} + 6H^+ + 2e^-$ (1.23)

7. $2Fe^{3+} + 3H_2O \rightleftharpoons \mathbf{Fe_2O_3} + 6H^+$. (1.24)

The Pourbaix diagram indicates the stable phase of a metal in a given environment and is useful for predicting whether or not a metal corrodes in that usage environment.

1.2.3. Passive film

A metal surface is covered by a passive oxide layer when the metal is in equilibrium in the region in which its oxide state is stable in a Pourbaix diagram. A passive film, a protective oxide layer that forms on a metal surface, plays an important role in preventing corrosion in metallic materials. Several theories for the passivation mechanism of metals have been proposed [46–49]. Two models for this passivation, the high field model and the point defect model, are presented here, after which previous studies regarding passive films formed on iron are described.

High field model—According to the Mott-Cabrera model [46] of oxide film growth, the growth of a thin film due to cation migration is given by

$$\frac{dX}{dt} = u \exp\left(\frac{X_1}{X}\right), \tag{1.25}$$

where X is the oxide thickness at time t, u is the velocity of drift of ions depending on temperature, and X_1 is the characteristic distance that depends on the interfacial potential difference and temperature. Since cation migration is assisted by the high electric field across the oxide, Eq. 1.25 is called a high field equation; it is valid for $X << X_1$. A rearrangement of Eq. 1.25 gives

$$t = \frac{1}{u}\int_0^x \exp\left(\frac{-X_1}{X}\right) \mathrm{d}X. \tag{1.26}$$

The integration of Eq. 1.26 by parts, neglecting higher terms in X/X_1, gives

$$ut = \left(\frac{X^2}{X_1}\right)\exp\left(\frac{-X_1}{X}\right). \tag{1.27}$$

For the constant V, the potential drop across a thin oxide film X meets a certain limiting thickness, even at low temperatures where u is negligibly small and the growth of the film stops. The limiting thickness X_L is defined as the thickness at which one layer of atoms is added in 10^5 s such that $dX/dt = 10^{-13}$ cm s^{-1}. Substituting $X = X_L$ into Eq. 1.27 gives

$$\frac{-X_1}{X} = \ln\left(\frac{X_1 ut}{{X_L}^2}\right), \tag{1.28}$$

which is of inverse logarithmic form. The insertion of Eq. 1.28 into Eq. 1.25 gives

$$-\ln\left(\frac{dX}{dt}\right) + \ln u = \ln\left(\frac{X_1 ut}{{X_L}^2}\right), \tag{1.29}$$

from which

$$\frac{dX}{dt} = \frac{{X_L}^2}{X_1 t}. \tag{1.30}$$

Assuming that the charge density q that entered the oxide film for time t is consumed only for oxide growth without an alternating charge-consuming process such as anodic dissolution of the metal or formation of a non-barrier oxide film, the film thickness X can be converted through Faraday's law as

$$X = \frac{Mq}{zF\rho_{OX}}, \tag{1.31}$$

where M is the molecular weight of the oxide per metal atom and ρ_{ox} is the density of the oxide. The conversion of Eq. 1.30 using Eq. 1.31 gives the following current-time relationship:

$$\ln j = \ln\left(\frac{zF{X_L}^2}{MX_1}\right) - \ln t. \tag{1.32}$$

This equation shows that the slope ($-d \log j/d \log t$) of a double logarithmic plot of j vs. t becomes unity.

Burstein and Davenport [47] present a further interpretation of current-time transients associated with Eq. 1.33 below, which describes anodic oxide film growth on metals. Substituting the current density $j = dq/dt$ driven by V and Eq. 1.31 into Eq. 1.25 gives

$$j = \bar{A}\exp\left(\frac{B'V}{q}\right), \tag{1.33}$$

where

$$\bar{A} = \frac{zFu\rho_{OX}}{M} \tag{1.34}$$

and

$$B'V = \frac{zF\rho_{OX}X_1}{M}. \tag{1.35}$$

Substituting Eqs. 1.31, 1.33, and 1.34 into the logarithmic form of Eq. 1.27 gives

$$\frac{B'V}{q} = -\ln\left(\frac{B'V\overline{A}t}{q^2}\right), \tag{1.36}$$

from which insertion into the logarithmic form of Eq. 1.33 gives

$$\ln\left(\frac{j}{\overline{A}}\right) = -\ln\left[\frac{\overline{A}t\{\ln(j/\overline{A})\}^2}{B'V}\right]. \tag{1.37}$$

After rearrangement, Eq. 1.37 becomes

$$j = \frac{B'V}{t\{\ln(j/\overline{A})\}^2}. \tag{1.38}$$

Equation 1.38 provides an expression that describes high field growth kinetics in terms of current and time. Rearranging Eq. 1.38 and taking common logarithms gives

$$\log j = \log\overline{A} + \frac{(B'V)^{1/2}}{2.303}(jt)^{-1/2}. \tag{1.39}$$

Thus, a plot of log j vs. $(jt)^{-1/2}$ shows a straight line with gradient $(B'V)^{1/2}/2.303$ and intercept $\log\overline{A}$. The current decays according to direct logarithmic kinetics in Eq. 1.32, in which $(-\mathrm{d}\log j/\mathrm{d}\log t) = 1$ requires the product of j and t to be a constant. Thus, the current-time relation observed with direct logarithmic kinetics appears as a vertical line parallel to the log j axis on a plot of log j vs. $(jt)^{-1/2}$. This model, when considered with the ohmic potential drop between the working electrode and the reference electrode, shows good agreement with current-time transients describing passivating oxide film growth on iron and titanium alloys.

Point defect model—The point defect model was first proposed by Chao, Lin, and Macdonald [48] to account for the growth kinetics of a passive film on a metal surface; it has been refined considerably by Macdonald [49]. The model is based on the following assumptions: (i) whenever the external potential E_{ext} is nobler than the Flade potential, where a metal electrode transits from the passive state to the active state, a continuous passive film will form on the surface of the metal; (ii) the passive film has a high concentration of defects: point defect species ($V_{Mx'}$ the metal vacancy, $V_O^{\cdot\cdot}$ the oxygen vacancy, e' the electrons, and $h^{\bullet}$ the holes) are expected in the passive film, and the Kröger-Vink notation is adopted to designate the point defect species; (iii) the field strength is a function of the film's chemical and electrical characteristics and is thus independent of film thickness, even for potentiostatic conditions; (iv) the electrons e' and holes $h^{\bullet}$ in the film matrix are in their equilibrium states, and the electrochemical reactions involving e' (or $h^{\bullet}$) are rate-controlled at either the metal/film (m/f) or the film/solution (f/s) interface, while the

rate-controlling step for those processes that involve $V_{Mx'}$ and $V_O^{\bullet\bullet}$ (i.e., film growth) is assumed to be the transport of the vacancies across the film.

Figure 1.8 shows the potential-position relationship between working and reference electrodes, with the following relation obtained:

$$E_{ext} + \Delta\phi_R = \Delta\phi_{m/f} + \Delta\phi_f + \Delta\phi_{f/s}, \tag{1.40}$$

where $\Delta\phi_{m/f}$, $\Delta\phi_{f/s}$, and $\Delta\phi_R$ are potential drops at the m/f, f/s, and solution/reference electrode interfaces and $\Delta\phi_f$ is the potential drop across the film. The following two reactions occur at the m/f interface:

$$m \rightleftarrows M_M + \frac{x}{2}V_O^{\bullet\bullet} + xe' \tag{1.41}$$

$$m + V_{Mx'} \rightleftarrows M_M + xe', \tag{1.42}$$

where m represents the metal atom in the metal and M_M is the metal cation in the film. When the m/f interface is at equilibrium

$$\mu_m = \mu_{M_M} + \frac{x}{2}\mu_{V_O^{\bullet\bullet}} + xF\phi_f' + x\mu_{e'} - xF\phi_m, \tag{1.43}$$

where ϕ_f' and ϕ_m are the flat band potentials for the film and metal at the m/f interface, respectively, and μ_i is the chemical potential of species i. The standard Gibbs energy ΔG_{41}^o of the reaction of Eq. 1.41 is defined as

$$\Delta G_{41}^o = \mu_{M_M}^o + \frac{x}{2}\mu_{V_O^{\bullet\bullet}}^o + x\mu_{e'}^o - \mu_m^o \tag{1.44}$$

by selecting appropriate the standard states

$$\mu_m = \mu_m^o, \tag{1.45a}$$

$$\mu_{M_M} = \mu_{M_M}^o, \tag{1.45b}$$

$$\mu_{e'} = \mu_{e'}^o, \tag{1.45c}$$

$$\phi_m - \Delta\phi_f = \Delta\phi_{m/f}, \tag{1.45d}$$

and

$$\mu_{V_O^{\bullet\bullet}} = \mu_{V_O^{\bullet\bullet}}^o + RT\ln a_{V_O^{\bullet\bullet}(m/f)}, \tag{1.46}$$

where $a_{V_O^{\bullet\bullet}(m/f)}$ is the activity of $V_O^{\bullet\bullet}$ at the m/f interface. Substituting Eqs. 1.44–46 into Eq. 1.43 yields

$$a_{V_O^{\bullet\bullet}(m/f)} = \exp\left\{\frac{2F\Delta\phi_{m/f} - (2/x)\Delta G_{41}^o}{RT}\right\}. \tag{1.47}$$

A similar treatment of Eq. 1.42 gives

$$a_{V_{Mx'}(m/f)} = \exp\left(\frac{\Delta G_{42}^{o} - xF\Delta\phi_{m/f}}{RT}\right), \tag{1.48}$$

where ΔG_{42}^{o} is the standard Gibbs energy of the reaction in Eq. 1.42. Assuming that the interaction between point defects is negligible—i.e., the point defects behave as an ideal solution—the activity coefficient is unity and the concentrations $C_{V_O^{\cdot\cdot}(m/f)}$ and $C_{V_{Mx'}(m/f)}$ of $V_O^{\cdot\cdot}$ and $V_{Mx'}$ at the m/f interface are estimated as

$$C_{V_O^{\cdot\cdot}(m/f)} = \frac{N_A}{\Omega}\exp\left\{\frac{2F\Delta\phi_{m/f} - (2/x)\Delta G_{41}^{o}}{RT}\right\} \tag{1.49}$$

and

$$C_{V_{Mx'}(m/f)} = \frac{N_A}{\Omega}\exp\left(\frac{\Delta G_{42}^{o} - xF\Delta\phi_{m/f}}{RT}\right), \tag{1.50}$$

where N_A is the Avogadro number and Ω is the molecular volume of oxide.

At the f/s interface, two other reactions occur:

$$V_O^{\cdot\cdot} + H_2O \rightleftarrows 2H^{+}(aq) + O_O \tag{1.51}$$

and

$$M_M \rightleftarrows V_{Mx'} + M^{x+}(aq), \tag{1.52}$$

where $M^{x+}(aq)$ is the hydrated metal cation in electrolyte solution. The concentration $C_{V_O^{\cdot\cdot}(f/s)}$ of $V_O^{\cdot\cdot}$ at the f/s interface is obtained in the same manner as the calculation of Eq. 1.49 with ΔG_{51}^{o}, the standard Gibbs energy of the reaction of Eq. 1.51:

$$C_{V_O^{\cdot\cdot}(f/s)} = \frac{N_A}{\Omega}\exp\left[\left(\frac{\Delta G_{51}^{o} - xF\Delta\phi_{m/f}}{RT}\right) - 4.606\ \mathrm{pH}\right]. \tag{1.53}$$

From the Schottky pair reaction,

$$\text{Null} \rightleftarrows V_{Mx'} + \frac{x}{2}V_O^{\bullet\bullet}. \tag{1.54}$$

Therefore,

$$C_{V_{Mx'}} \cdot \left[C_{V_O^{\cdot\cdot}}\right]^{x/2} = \left[\frac{N_A}{\Omega}\right]^{1+(x/2)}\exp\left(-\frac{\Delta G_S^{o}}{RT}\right), \tag{1.55}$$

where ΔG_S^{o} is the Gibbs standard energy change for the Schottky pair reaction and the multiplier on the right-hand side arises due to the use of concentrations rather than activities. From Eqs. 1.53 and 1.54, $C_{V_O^{\cdot\cdot}(f/s)}$ is obtained as

$$C_{V_O^{\cdot\cdot}(f/s)} = \frac{N_A}{\Omega}\exp\left\{\frac{xF\Delta\phi_{m/f} - \Delta G_S^{o} - (x/2)\Delta G_{51}^{o}}{RT} + 2.303\,x\ \mathrm{pH}\right\}. \tag{1.56}$$

Since it is clear from Eqs. 1.41, 1.42, 1.51, and 1.52 that the diffusion of $V_O^{\cdot\cdot}$ (or equivalently, oxygen anion) results in film growth, the diffusion rate of $V_O^{\cdot\cdot}$ is equivalent to film growth kinetics. Thus,

$$\frac{dX}{dt} = \frac{\Omega}{N_A} J_{V_O^{\cdot\cdot}}, \tag{1.57}$$

where Ω is the molar volume per cation and $J_{V_O^{\cdot\cdot}}$ is the flux of $V_O^{\cdot\cdot}$ per unit area per unit time. From the generalized Fick's first law, $J_{V_O^{\cdot\cdot}}$ can be calculated as

$$J_{V_O^{\cdot\cdot}} = 2KD^*_{V_O^{\cdot\cdot}} \frac{C_{V_O^{\cdot\cdot}(m/f)} \exp(2KX) - C_{V_O^{\cdot\cdot}(f/s)}}{\exp(2KX) - 1}, \tag{1.58}$$

where $D^*_{V_O^{\cdot\cdot}}$ is the electrochemical diffusivity of $V_O^{\cdot\cdot}$ and K is equal to $F\varepsilon_F/RT$ (ε_F is the field strength, $\varepsilon_F = \Delta\phi_f/X$). Assuming that $\Delta\phi_{f/s}$ is a function of applied potential and solution pH but is independent of film thickness, $\Delta\phi_{f/s}$ is described as

$$\Delta\phi_{f/s} = \alpha E_{ext} + \beta\,\mathrm{pH} + \phi_{f/s}^{\circ}, \tag{1.59}$$

where α and β are coefficients and $\Delta\phi_{f/s}^{\circ}$ is the value of $\Delta\phi_{f/s}$ when $E_{ext} = 0$ and pH = 0. From Eqs. 1.40 and 1.59, an expression for $\Delta\phi_{m/f}$ is derived as

$$\Delta\phi_{m/f} = (1-\alpha)E_{ext} - \beta\,\mathrm{pH} - \Delta\phi_{f/s}^{\circ} + \Delta\phi_R - \varepsilon_F X, \tag{1.60}$$

where $\Delta\phi_R$ is treated as a constant because the reference electrode is not polarized. Substituting Eqs. 1.49, 1.56, 1.58, 1.59, and 1.60 into Eq. 1.57 gives

$$\frac{dX}{dt} = \frac{A(B-1)}{\exp(2KX) - 1}, \tag{1.61}$$

where

$$A = 2KD^*_{V_O^{\cdot\cdot}} \exp\left\{-\frac{2F}{RT}\left(\alpha E_{ext} + \beta\,\mathrm{pH} + \Delta\phi_{f/s}^{\circ}\right) + \frac{\Delta G_{51}^{\circ}}{RT} - 4.606\,\mathrm{pH}\right\} \tag{1.62}$$

and

$$B = \exp\left\{\frac{2F}{RT}\left(E_{ext} + \Delta\phi_R\right) - \frac{2\Delta G_{41}^{\circ}}{xRT} - \frac{\Delta G_{51}^{\circ}}{RT} + 4.606\,\mathrm{pH}\right\}. \tag{1.63}$$

Under potentiostatic polarization, E_{ext} is equal to the applied potential E_{app} and independent of the film thickness X. Eq. 1.61 can be integrated directly, since

$$\int_0^X [\exp(2KX) - 1]\, d(2KX) = \int_0^t 2KA(B-1)dt, \tag{1.64}$$

which therefore yields

$$\exp(2KX) - 2KX - 1 = 2KA\,(B-1)\,t. \tag{1.65}$$

Equation 1.65 is the integrated rate law for film growth.

The field strength ε_F for most anodic films is of the order of 10^6 V cm^{-1} at room

temperature. Thus, $2KX = 2F\varepsilon_F/RT \sim 0.76\,X$. This means that whenever $X \geq 0.5$ nm, $\exp(2KX) >> 2KX >> 1$ and Eq. 1.65 can be simplified to

$$\exp(2KX) = 2KA\,(B-1)\,t \tag{1.66}$$

or

$$X = \frac{1}{2K}[\ln\{2KA(B-1)\} + \ln t]. \tag{1.67}$$

Equation 1.67 has the form of the logarithmic growth raw. Furthermore, when the current j is consumed only for oxide growth, it is written as

$$j = 2F\,\frac{N_A}{\Omega}\frac{dX}{dt}. \tag{1.68}$$

Substituting Eq. 1.68 into Eq. 1.67 gives

$$j = \frac{FN_A}{K\Omega}t^{-1}. \tag{1.69}$$

Equation 1.69 indicates that a current transient varies inversely with time.

On the other hand, for very small values of X, Eq. 1.65 can be reduced to

$$X = \left\{\frac{A(B-1)}{K}t\right\}^{1/2}. \tag{1.70}$$

This gives a relation of

$$j \propto \frac{dX}{dt} = \frac{1}{2}\left\{\frac{A(B-1)}{K}\right\}^{1/2} t^{-1/2}. \tag{1.71}$$

Equation 1.71 indicates that a current transient varies with the square root of time.

Due to their importance in industry, the passivation mechanism and kinetics of iron have been intensively investigated for more than half a century. In many cases, the passivation behavior and the property of the passive film on iron were studied in neutral aqueous solution, where the dissolution of the film and the substrate iron through the film into electrolyte solution was negligible and the change in the film property during measurements was minimal.

The structure of a passive film formed on iron in neutral borate buffer solution has been studied using several investigative techniques. An electron diffraction study [50] demonstrated that the film had a bi-layered spinel structure of inner Fe_3O_4 and outer γ-Fe_2O_3. A further electron diffraction study [51] showed that it was not possible to make a definitive distinction between Fe_3O_4 and γ-Fe_2O_3, but the film had a fine-grained crystalline spinel structure consisting of a varying iron concentration from the metal/oxide interface to the oxide/solution interface. On the other hand, cathodic reduction combined with ellipsometry and chemical analysis [52] led to another film structure with a barrier Fe(III) oxide layer in contact with the metal and a deposit

hydrated Fe(III) oxide or oxyhydroxide layer on the barrier layer. A bi-layer film with inner anhydrous and outer hydrated layers was also found by electron spectroscopy for chemical analysis (ESCA) and secondary ion mass spectroscopy (SIMS) [53]. Nowadays, ESCA is known as X-ray photoelectron spectroscopy (XPS). By contrast, the results of surface-enhanced Raman spectroscopy (SERS) indicated that the passive film was hydrated spinel-based oxide [54,55] or a bi-layer of inner Fe_3O_4 or defected γ-Fe_2O_3 and outer unknown ferric oxide or hydroxide [56]. More recently, high resolution *in situ* X-ray absorption near edge structure (XANES) demonstrated that the obtained absorption edge peak was consistent with the proposed Fe_3O_4/γ-Fe_2O_3 structure or a disordered structure with distorted coordination polyhedral [57–59]. A study using *in situ* synchrotron X-ray diffraction (XRD) [6] suggested that the passive film was neither Fe_3O_4 nor γ-Fe_2O_3, but was instead a new phase—the LAMM phase—that had a spinel structure with a different defect structure. The crystalline nature of the passive film was confirmed by *in situ* scanning tunneling microscopy (STM) [60]. Later STM work [61] suggested the presence of nanoscale oxide grains in the LAMM phase, but did not reveal the complete structure of the film. As noted above, while several structures of passive films on iron have been proposed, there are presently no definitive studies of the nature of the passive films, with most recent studies suggesting a structure related to Fe_3O_4 and γ-Fe_2O_3.

Due to the ultra-thin nature—in the range of a few nanometers—of passive films, direct observation of the film structure has rarely been demonstrated. Recently, a focused ion beam (FIB) technique made the preparation of a thin sample film for observation with transmission electron microscopy (TEM) easier than previously possible. A cross section of a few nanometer thick passive film on 316L stainless steel was observed by means of FIB-TEM [62,63]. However, the question remained whether or not that *ex situ* observation in vacuum examined the film structure as it exists *in situ*, so *in situ* ellipsometry under polarization measurements have been intensively demonstrated to evaluate the thickness of the passive film on iron in neutral borate buffer solution. The thickness of the passive film evaluated by ellipsometry ranged from ca. 2–7 nm depending on the formation potential, electrolyte pH, and anion species and concentration in electrolyte solution [64–67].

The electric property of the passive film has been evaluated by means of electrochemical impedance spectroscopy (EIS). The charge transfer resistance R_{ct} for ionic and electronic conductions through the film is usually obtained from curve fitting of impedance spectra obtained from EIS measurements. Values of R_{ct} = 0.2–1.5 MΩ cm^2 were reported for the passive film formed on iron in borate solution [68,69]. Mott-Schottky (MS) analysis based on EIS evaluated an n-type semiconductive property of the passive film from the positive slope in the so-called MS plot, which draws the variation of inverse squares of space-charge capacitance as a function of evaluation potential. The passive film showed a flat band potential E_{fb} of 0.3–0.5 V versus reversible hydrogen electrode (RHE) potential and a donor density N_D of 2–30 × 10^{20} cm^{-3} [69–73]. The slight scattering observed in these parameters is due to differences in formation potential

and time. The value of E_{fb} was almost constant at potentials less than 1.5 V (RHE) [70], at which the oxygen evolution reaction occurred. On the contrary, N_D decreased with increasing formation potential or oxidation time due to the reduction of defect sites [70]. A study of MS analysis and photocurrent measurements [72] concluded that the doping species of the passive film was Fe(II) ion and the further oxidation of Fe(II) into Fe(III) in the film decreased N_D in the high potential region.

Recent developments in the field of computer science have enabled the use of computational calculation for the investigation of the growth mechanism and electronic property of the passive film. Density functional theory (DFT) calculations suggested that the proposed LAMM phase was metastable with respect to the iron substrate [74] and that cation transport during oxide growth was dominated by grain boundary diffusion [75]. A numerical simulation based on a finite element method showed that Fe(III) interstitials and oxygen vacancies were the species responsible for the transport of mass in the oxide film [76].

1.3. Analytical techniques

In this section, typical techniques used to analyze the structure, composition, and property of oxide films formed on iron are introduced, along with practical examples.

1.3.1. Vacuum analysis

X-ray photoelectron spectroscopy is a highly sensitive surface analysis technique that examines the composition, chemical state, and electronic state of the elements that exist on a sample surface. Photoelectron spectra are obtained by simultaneously measuring the kinetic energy E_k and the number of electrons that escape from the top ca. 10 nm of the sample by X-ray irradiation. Generally, photoelectron intensity is shown as a function of the binding energy E_b between an electron and an atomic nucleus, according to the following relation:

$$E_b = h\nu - E_k - \Phi_w, \tag{1.72}$$

where $h\nu$ is the photon energy of an incident X-ray (h is the Plank constant and ν is the frequency) and Φ_w is the work function dependent on both the spectrometer and the sample [77]. Figure 1.9 illustrates the emission of a photoelectron caused by the incident X-ray. Taking advantage of its surface sensitivity, XPS has used to investigate the composition and structure of ultra-thin passive films [78–80]. A passive film formed on pure iron in neutral solution was studied *ex situ* after being transferred from electrolyte solution to the vacuum chamber of a spectrometer; a bi-layer film structure with an inner iron oxide containing both Fe(II) and Fe(III) and outer hydrated oxides was reported [81]. Angle-resolved XPS found that a passive film formed in phosphate buffer solution contained a significant amount of phosphate in the outer part of the film, whereas boron species were not significantly incorporated into the film formed in borate buffer solution

[66]. The standard peaks of Fe $2p_{3/2}$ and O 1s electrons that are necessary to examine chemical shifts of the passive film on iron are summarized in Table 1.3. The reported E_b shows some deviations, according to the authors; these deviations are believed to be caused by the different environments of cations in different compositions of oxides, such as Fe_2O_3, $Fe(OH)_2$, and FeOOH, and by small differences of measurement conditions, since XPS is a notably sensitive measurement technique. Although XPS shows ultra-high surface sensitivity, XPS is not suitable for analyzing micro-regions since it is difficult to focus the beam of X-rays.

Table 1.3. Binding energies of Fe $2p_{3/2}$ and O 1s electrons.

Element and orbital	Chemical state	E_b (eV)
Fe $2p_{3/2}$	Fe^{3+}	710.97 [a], 710.5 [b], 710.5 [c], 711.2 [d]
	Fe^{2+}	709.0 [a], 709.6 [b], 709.5 [d],
	Fe^0	706.82 [a], 706.7 [b], 707.2 [c], 706.8 [d]
O 1s	O^{2-}	529.98 [a], 530.2 [b], 530.2 [c], 530.1 [d]
	OH^-	531.4 [a], 531.5 [b], 531.5 [c], 531.7 [d]
	H_2O	533.6 [a], 532.5 [c], 533.3 [d]

[a] K. Asami and K. Hashimoto [77]

[b] P. Keller and H.-H. Strehblow [82]

[c] I. V. Sieber et al. [66]

[d] R.-H. Jung et al. [83]

Auger electron spectroscopy (AES) is a surface analysis technique similar to XPS; it analyzes Auger electrons that have escaped from a sample surface, using an electron beam as a probe. Thus, AES can analyze a micro-region with a diameter of a few nanometers by focusing an electron beam. Taking advantage of the small area of analysis, the chemical composition of a local sample surface was analyzed by AES [27,84]. An AES depth profile of the passive film formed on iron in neutral borate solution showed a significant amount of boron in the outer part of the film [85], though this was inconsistent with the results using XPS [66]. Since AES injects a high-energy electron beam into a sample, the possibility of the alteration and decomposition of the sample by the incident electron beam must be considered.

Vacuum analysis is a powerful technique to define the chemical composition and structure of a passive film; however, it requires transferring a sample from the electrolyte solution in which the passive film formed into a vacuum environment. It cannot be denied that adsorbed species such as water molecules disappear in vacuum and that the chemical states of cations and anions may change. Thus, the results obtained from vacuum analysis should be treated with caution when considering changes in film properties.

1.3.2. Optical measurements

Using light as a probe, optical measurement techniques enable the analysis of a sample surface without any destruction of chemical species and do not require a specific experimental environment. Taking advantage of these characteristics, several optical measurement techniques have been developed and applied to the analysis of oxide films formed on iron.

Raman spectroscopy investigates the vibrational structure of a substance, generally using visible light as a probe (Fig. 1.10) to identify the composition of the substance by comparing it with standards. The composition of a passive film on iron was studied by means of Raman spectroscopy, with Raman peaks assigned to a hydrated form of Fe_3O_4 and γ-Fe_2O_3 or $Fe_{3-\delta}O_4$ [86]. However, observation of clear Raman peaks in the passive film and *in situ* observation were difficult due to its ultrathin structure. This obstacle has been overcome by a SERS technique that enhances Raman scattering of substances by nanostructures of a substrate surface, which enables *in situ* measurements of Raman spectra. The passive film on iron was investigated by means of *in situ* SERS by depositing nanoparticles of silver [54] and gold [56]. Recently, confocal Raman spectroscopy that confines measurement area to ca. 1 μm in a diameter has been performed to investigate a local sample surface; Raman mapping was also conducted [87].

Ellipsometry is an effective method for determining the thickness and optical constants of a thin oxide layer on a flat substrate. The principle of ellipsometry is described in Chapter 2. Due to its high thickness resolution of sub-nanometers, ellipsometry has been intensively used to investigate the thicknesses and structures of anodic oxide films on metals [88–90]. A relatively thin thermal oxide film formed on an interstitial free steel has also been reported [91]. Since ellipsometry is a non-destructive technique, it is suitable for *in situ* measurements of the formation and degradation of oxide films on metals and alloys. An ellipsometer combined with an electrochemical cell observed *in situ* optical changes of an iron surface during potentiostatic anodic polarization and galvanostatic cathodic reduction [92]. The structure of a passive film on iron was precisely revealed by *in situ* ellipsometry [93]. *In situ* ellipso-microscopy observed local film degradation of a passive film on titanium [27]. By using a laser as a probe light, the spot area on a sample surface can be confined to several micrometers in diameter. Laser-probed ellipsometry with high lateral resolution has enabled the visualization of the two-dimensional (2D) distribution of ellipsometric parameters of the sample surface. For example, the thickness distributions of organic thin films on a gold substrate [94] and a ZnO film on a silicon wafer [95] were observed by 2D ellipsometry. This technique is a promising method for elucidating the surface heterogeneity of oxidized polycrystalline metals. Thus, *in situ* 2D ellipsometry, which is a combination of 2D ellipsometry and electrochemical measurements, is thought to be an effective technique for investigating the surface heterogeneity of oxidized polycrystalline metals.

1.3.3. Micro-electrochemical measurement methods

For the purpose of investigating the local electrochemical behavior of polycrystalline

metals and alloys, several micro-electrochemical measurement techniques have been developed by researchers [96–99]. The two major techniques, scanning electrochemical microscopy (SECM) and a micro-capillary cell (MCC) method, are outlined.

SECM is a kind of scanning probe microscopy developed by Bard et al. [96,97] as a tool for imaging the electrochemical activity of a sample electrode surface. The probe tip of a micro-electrode moves normally to the sample surface (in the *z* direction) to evaluate the diffusion layer on the surface, or can be scanned at constant *z* across the surface (in the *x*-*y* directions) to achieve an image map of electrochemical reactivity of the surface. This technique was applied to evaluate the heterogeneity of an anodic passive film formed on polycrystalline metals [15,17,23]. When SECM is conducted in tip-generation/substrate-collection (TG/SC) mode (Fig. 1.11), the oxidation and reduction of a redox couple mediator such as $Fe(CN)_6^{4-}/Fe(CN)_6^{3-}$ occur respectively at the tip and substrate kept at constant potential. The mediator is oxidized at the tip and the oxidized mediator is reduced at a passive film formed on the substrate metal. The probe current reflects the generation rate of reduced species on the film and thus depends on the electron tunneling through the passive film. Since the tunneling current is affected by the electronic property and thickness of the film, SECM can evaluate the heterogeneity of the electronic property and/or thickness of a passive film formed on a whole polycrystalline metal surface.

The MCC (also called a capillary microcell or a micro-droplet cell) method was developed independently by Böhni et al. [98] and Lohrengel et al. [99] in the late 1990s. It uses a narrow capillary filled with electrolyte solution and places a small droplet on a sample surface. The contact area of the droplet represents the working electrode in an electrochemical cell. The tip diameter of the capillary varies from 20 μm to a few millimeters and defines the electrode diameter of the MCC. Usually, insulating narrow tubes of glasses or polymers are used for the capillary, while at times metallic tubes of platinum, gold, and stainless steel are used for the capillary, which also works as a counter electrode. MCC has the following advantages comparing with ordinary macro-electrochemical cells: (i) pretreatment of a sample with insulating coating, resin-embedding, or the like is not necessary; (ii) an electrochemical measurement is conducted only at a desired micro-region of a sample electrode; (iii) it consumes only a small amount of electrolyte solution for a single measurement (on the order of micro-liters). The MCC technique is divided into two groups, according to the structure of a capillary tip/sample electrode interface. Figure 1.12a shows the cell structure of a meniscus type MCC [98]. A capillary tip maintains a constant distance from a substrate and makes a droplet as a micro-electrode between the tip and the substrate surface. Since the capillary tip does not contact the substrate directly, it is possible to scan the micro-electrode laterally during electrochemical measurements. However, it is difficult to keep the electrode area constant, because the shape of the droplet is governed by the surface tension and wettability of the electrolyte solution. Figure 1.12b shows a gasket type MCC [99]. A silicone rubber is placed on the tip and the capillary directly contacts the substrate surface. A micro-electrode is formed in the confined area made up of the capillary, gasket, and sample

substrate. Although it is difficult to scan gasket type MCCs, they realize a constant electrode area at each measurement.

1.4. Previous study on orientation-dependent corrosion of iron

The corrosion behavior of iron has been studied heavily, as outlined above; it has been reported that surface crystallographic orientation affected corrosion behavior [4–6]. However, the progress of orientation-dependent corrosion of iron is difficult to explain using previous corrosion theories and has been frequently overlooked when researchers have examined the corrosion reactions of iron. The orientation-dependent corrosion behavior of iron low Miller indices' planes has been reported by several researchers [5,6,17–20,100–106] using single crystals or single grains on a polycrystalline substrate as sample electrodes. The currently reported corrosion tendency of the iron planes are summarized in Table 1.4.

The dissolution rate of iron {0 0 1}, {1 0 1}, and {1 1 1} planes has been reported using several evaluation methods and solutions. Although the sequence shows some scattering, it can be classified according to the acidity of solution, with the following relation is thought to be a major suggestion: the dissolution rate becomes larger in the order of {0 0 1} > {1 1 1} > {1 0 1} in acidic solution and {1 1 1} > {1 0 1} > {0 0 1} in neutral or base solutions. In acidic solution, Schreiber et al. [19] observed by atomic force microscopy that electropolishing led to the occurrence of positive, barely visible or step-like grain boundaries on polycrystalline iron, whereas chemical polishing led to the occurrence of negative and step-like grain boundaries. Fushimi et al. [20] concluded that the decomposed d-valence charge at the outermost surface could explain the sequence. For neutral and base solutions, Chiba and Seo [100] explained that the difference in anodic dissolution rates was due to the surface atom density ρ_{surf}; that of the {1 0 1} plane is 1.42 times larger than that of the {0 0 1} plane. Schreiber et al. [18] suggested that electrochemical behavior of three iron planes correlated with ρ_{surf} (Table 1.2); they believed that the closer distance between the uppermost and second atom layers provided stronger bonding and resulted in a surface stable against active dissolution.

An oxidation rate in air was greatly affected by the substrate structure below 843 K, at which recrystallization of iron is very slow and FeO does not form due to its thermodynamic instability [107]. The orientation dependency of the oxidation rate in dry air has been reported at low oxygen partial pressure and at a temperature range of 473–623 K. Boggs et al. [5] observed the oxidation behavior of four iron planes and concluded that the formation rate of outer α-Fe_2O_3 on the surface of inner Fe_3O_4 reduced the overall oxidation rate, depending on the anisotropic growth of both oxides. This finding was supported by Ramasubramanian et al. [101]. On the other hand, Graham and Hussey [102] showed that surface pretreatment greatly affected the oxidation behavior, rather than the substrate orientation, due to the formation of vacancies that caused a

separation of the metal-oxide interface.

The orientation dependency on the thickness of a passive film on iron single crystals was reported by Davenport et al. [6], who conducted *in situ* XRD to identify the detailed structure of the passive film. The thickness difference was explained by the epitaxial relationship between the film and the substrate iron. Fushimi et al. [17] observed the heterogeneous thickness of the passive film formed on polycrystalline iron surface by means of SECM, observing the same grain dependency as reported by Davenport et al. and indicating that the dependency was caused by ρ_{surf} of substrate iron and/or the epitaxial relationship between the film and the substrate.

As introduced above, the rough trends of orientation-dependent corrosion of iron have been clarified. However, the relationship between the crystallographic orientations of an iron surface and corrosion behavior has not been sufficiently studied, and the detailed mechanism of orientation-dependent corrosion remains unclear. It is thus necessary to examine orientation-dependent corrosion behavior in detail and to establish a new corrosion model to explain it.

1.5. Purpose of this dissertation

As described above, oxide films formed on polycrystalline iron show heterogeneous behavior and property due to the orientation-dependent corrosion of substrate iron. The characteristics of the orientation-dependent corrosion of low Miller indices' iron planes have been partially studied, but there is still no clear understanding that connects the oxidation behavior and oxide property of each grain with the heterogeneity of the oxide film formed on whole polycrystalline substrate. With the aim at connecting them, two measurement techniques were developed in this dissertation. Micro-electrochemistry with an improved MCC was used to study the passivation behavior and oxide property of single grains on a polycrystalline iron surface. *In situ* 2D ellipsometry was applied to investigate the heterogeneity of the thickness and the degradation behavior of oxide film formed on whole polycrystalline iron surface. Finally, the heterogeneity of oxide films formed on polycrystalline iron was discussed from the viewpoints of both single grains and the whole surface of polycrystalline iron.

Table 1.4. Sequence of orientation-dependent corrosion activity of iron for low Miller indices' planes.

Property	Sequence	Surrounding	Condition	Ref.
Dissolution rate	{0 1 1} > {1 1 1} > {0 0 1}	5 M ammonium nitrate solution	Dynamic polarization	[104]
	{1 1 1} > {1 0 1}, {0 0 1}	0.5 M sulfuric acid	Galvanostatic polarization	[105]
	{1 1 0}, {1 1 1} > {1 0 0}	Sulfate solution (pH 2.3)	Potentiostatic at −0.1 V (SHE)	[103]
	(1 1 0) > (0 0 1)	Borate buffer (pH 8.4)	Dynamic polarization	[106]
	(1 1 0) > (1 0 0)	Borate buffer (pH 8.4)	Potentiostatic at 0.25 V (SSE)	[100]
	(1 1 1), (1 0 1) > (1 0 0)	Acetate buffer (pH 6.0)	Dynamic polarization	[18]
	(1 0 0) > (1 0 1), (1 1 1)	CH_3COOH : $HClO_4$: H_2O = 95 : 3.5 : 1.5 (vol%)	Electropolishing at 0.3 A cm^{-2}	[19]
	(1 0 0) > (1 0 1), (1 1 1)	1 M $(COOH)_2$ 28 cm^3 + 9 M H_2O_2 4 cm^3 + H_2O 80 cm^3	Immersion	[19]
	(1 1 1) > (1 0 1) > (1 0 0)	5 M sodium nitrate solution	Electrochemical machining	[19]
	{0 0 1} > {1 1 1} > {1 0 1}	0.05 M sulfuric acid	Dynamic polarization	[20]

Table 1.4. (Continued) Sequence of orientation-dependent corrosion activity of iron for low Miller indices' planes.

Property	Sequence	Surrounding	Condition	Ref.
Oxidation rate	(0 0 1) > (1 1 2) > (1 1 1) > (0 1 1)	Oxygen gas ($1.33–1.33 \times 10^3$ Pa)	at 623 K	[5]
	(0 0 1) > (1 1 2)	Oxygen gas (2.66×10^3 Pa)	at 623 K	[101]
	(0 0 1) > (1 1 2)	Oxygen gas (0.655 Pa)	at 473–513 K (Electropolished)	[102]
	(1 1 2) > (0 0 1)	Oxygen gas (0.655 Pa)	at 533–573 K (Preoxidated)	[102]
	(1 1 2) > (0 0 1)	Oxygen gas (0.655 Pa)	at 533–573 K (Electropolished)	[102]
Passive film thickness	{1 0 0} > {1 1 0}, {1 1 1}	Borate buffer (pH 8.4)	Potentiostatic at 1.0 V (SHE)	[17]
	(0 0 1) > (1 1 0)	Borate buffer (pH 8.4)	Potentiostatic at 0.4 V (MSE)	[6]
	{1 0 0} > {1 1 0}, {1 1 1}	Borate buffer (pH 8.4)	Potentiostatic at 1.0 V (SHE)	[103]

References

[1] P. W. Atkins and J. De Paula, *Atkins' Physical Chemistry*, 10th Ed., Oxford University Press, Oxford (2014).

[2] Committee on Cost of Corrosion in Japan, *Zairyo-to-Kankyo*, **50**, 490 (2001).

[3] Z. Xia, Y. Kang, and Q. Wang, *J. Magn. Magn. Mater.*, **320**, 3229 (2008).

[4] P. B. Sewell, C. D. Stockbridge, and M. Cohen, *J. Electrochem. Soc.*, **108**, 933 (1961).

[5] W. E. Boggs, R. H. Kachik, and G. E. Pellissier, *J. Electrochem. Soc.*, **112**, 32 (1967).

[6] A. J. Davenport, L. J. Oblonsky, M. P. Ryan, and M. F. Toney, *J. Electrochem. Soc.*, **147**, 2162 (2000).

[7] S. I. Ali and G. C. Wood, *Corros. Sci.*, **8**, 413 (1968).

[8] W. Wang and A. Alfantazi, *Electrochim. Acta*, **131**, 79 (2014).

[9] S. Kudelka, A. Michaelis, and J. W. Schultze, *Electrochim. Acta*, **41**, 863 (1996).

[10] D. Abayarathna, E. B. Hale, T. J. O'Keefe, Y.-M. Wang, and D. Radovict, *Corros. Sci.*, **32**, 755 (1991).

[11] J. T. Clemens, *Bell Labs Techn. J.*, **2**, 76 (1997).

[12] P. Caron and T. Khan, *Aerosp. Sci. Technol.*, **3**, 513 (1999).

[13] H. Krawiec and Z. Szklarz, *Electrochim. Acta*, **203**, 426 (2016).

[14] J.-M. Song, Y.-S. Zou, C.-C. Kuo, and S.-C. Lin, *Corros. Sci.*, **74**, 223 (2013).

[15] E. Martinez-Lombardia, Y. Gonzalez-Garcia, L. Lapeire, I. De Graeve, K. Verbeken, L. Kestens, J. M. C. Mol, and H. Terryn, *Electrochim. Acta*, **116**, 89 (2014).

[16] E. Martinez-Lombardia, V. Maurice, L. Lapeire, I. De Graeve, K. Verbeken, L. Kestens, P. Marcus, and H. Terryn, *J. Phys. Chem. C*, **118**, 25421 (2014).

[17] K. Fushimi, K. Azumi, and M. Seo, *ISIJ Int.*, **39**, 346 (1999).

[18] A. Schreiber, J. W. Schultze, M. M. Lohrengel, F. Kármán, and E. Kálmán, *Electrochim. Acta*, **51**, 2625 (2006).

[19] A. Schreiber, C. Rosenkranz, and M. M. Lohrengel, *Electrochim. Acta*, **52**, 7738 (2007).

[20] K. Fushimi, K. Miyamoto, and H. Konno, *Electrochim. Acta*, **55**, 7322 (2010).

[21] M. Liu, D. Qiu, M.-C. Zhao, G. Song, and A. Atrens, *Scr. Mater.*, **58**, 421 (2008).

[22] G.-L. Song and Z. Xu, *Corros. Sci.*, **63**, 100 (2012).

[23] K. Fushimi, T. Okawa, K. Azumi, and M. Seo, *J. Electrochem. Soc.*, **147**, 524 (2000).

[24] U. König and B. Davepon, *Electrochim. Acta*, **47**, 149 (2001).

[25] M. Hoseini, A. Shahryari, S. Omanovic, and J. A. Szpunar, *Corros. Sci.*, **51**, 3064 (2009).

[26] M. Schneider, S. Schroth, J. Schilm, and A. Michaelis, *Electrochim. Acta*, **54**, 2663 (2009).

[27] K. Fushimi, K. Kurauchi, Y. Yamamoto, T. Nakanishi, Y. Hasegawa, and T. Ohtsuka, *Electrochim. Acta*, **144**, e56 (2014).

[28] C. J. Park, M. M. Lohrengel, T. Hamelmann, M. Pilaski, and H. S. Kwon, *Electrochim. Acta*, **47**, 3395 (2002).

[29] J. W. Schultze, M. Pilaski, M. M. Lohrengel, and U. Konig, *Faraday Discuss.*, **121**, 211

(2002).

[30] B. D. B. Aaronson, C.-H. Chen, H. Li, M. T. M. Koper, S. C. S. Lai, and P. R. Unwin, *J. Am. Chem. Soc.*, **135**, 3873 (2013).

[31] World Steel Association, *Steel Statistical Yearbook 2016*.

[32] The Research Institute of Innovative Technology for the Earth (RITE), 地球環境国際研究推進事業（脱地球温暖化と持続的発展可能な経済社会実現のための対応戦略の研究）成果報告書, (2011).

[33] F. W. Clarke and H. S. Washington, *The composition of the Earth's crust*, Government Printing Office, Washington (1924).

[34] H. W. King, in *CRC Handbook of Chemistry and Physics*, W. M. Haynes and D. R. Lide, Editors, p. 12–15, CRC Press, New York (2011).

[35] B.-Q. Fu, W. Liu, and Z.-L. Li, *Appl. Surf. Sci.*, **255**, 8511 (2009).

[36] J. Radilla, G. E. Negrón-Silva, M. Palomar-Pardavé, M. Romero-Romo, and M. Galván, *Electrochim. Acta*, **112**, 577 (2013).

[37] P. Błoński and A. Kiejna, *Surf. Sci.*, **601**, 123 (2007).

[38] A. J. Bard and L. R. Faulkner, *Electrochemical Methods: Fundamentals and Applications*, 2nd ed., John Wiley & sons, New York (2001).

[39] U. R. Evans, *Metallic Corrosion, Passivity and Protection*, E. Arnold & Co., London (1937).

[40] J. O. Bockris, D. Drazic, and A. R. Despic, *Electrochim. Acta*, **4**, 325 (1961).

[41] K. E. Heusler, *Berichte der Bunsengesellschaft für Phys. Chemie*, **62**, 582 (1958).

[42] F. Hibert, Y. Miyoshi, G. Eichkorn, and W. J. Lorenz, *J. Electrochem. Soc.*, **118**, 1919 (1971).

[43] F. Hibert, Y. Miyoshi, G. Eichkorn, and W. J. Lorenz, *J. Electrochem. Soc.*, **118**, 1927 (1971).

[44] H. Schweickert and W. J. Lorenz, *J. Electrochem. Soc.*, **127**, 1693 (1980).

[45] M. Pourbaix, *Atlas of Electrochemical Equilibria in Aqueous Solution*, 2nd English ed., p. 307, National Association of Corrosion Engineers, Houston (1974).

[46] N. Cabrera and N. F. Mott, *Rep. Prog. Phys.*, **12**, 163 (1949).

[47] G. T. Burstein and A. J. Davenport, *J. Electrochem. Soc.*, **136**, 936 (1989).

[48] C. Y. Chao, L. F. Lin, and D. D. Macdonald, *J. Electrochem. Soc.*, **128**, 1187 (1981).

[49] D. D. MacDonald, *Electrochim. Acta*, **56**, 1761 (2011).

[50] M. Nagayama and M. Cohen, *J. Electrochem. Soc.*, **109**, 781 (1962).

[51] K. Kuroda, B. D. Cahan, G. Nazri, E. Yeager, and T. E. Mitchell, *J. Electrochem. Soc.*, **129**, 2163 (1982).

[52] N. Sato, K. Kudo, and R. Nishimura, *J. Electrochem. Soc.*, **123**, 1419 (1976).

[53] S. C. Tjong and E. Yeager, *J. Electrochem. Soc.*, **128**, 2251 (1981).

[54] L. J. Oblonsky and T. M. Devine, *Corros. Sci.*, **37**, 17 (1995).

[55] L. J. Oblonsky, S. Virtanen, V. Schroeder, and T. M. Devine, *J. Electrochem. Soc.*, **144**,

1604 (1997).

[56] V. Schroeder, *J. Electrochem. Soc.*, **146**, 4061 (1999).

[57] A. J. Davenport and M. Sansone, *J. Electrochem. Soc.*, **142**, 725 (1995).

[58] A. J. Davenport, J. A. Bardwell, and C. M. Vitus, *J. Electrochem. Soc.*, **142**, 721 (1995).

[59] P. Schmuki, *J. Electrochem. Soc.*, **143**, 574 (1996).

[60] M. P. Ryan, R. C. Newman, and G. E. Thompson, *J. Electrochem. Soc.*, **142**, L177 (1995).

[61] E. E. Rees, M. P. Ryan, and D. S. McPhail, *Electrochem. Solid-State Lett.*, **5**, B21 (2002).

[62] Y. Mori, M. Hashimoto, and J. Liao, *ISIJ Int.*, **53**, 1057 (2013).

[63] C. Zhang, Z.-W. Zhang, and L. Liu, *Electrochim. Acta*, **210**, 401 (2016).

[64] N. Sato and G. Okamoto, in *Comprehensive Treatise of Electrochemistry Vol. 4: Electrochemical Materials Science*, J. O. M. Bockris, B. E. Conway, E. Yeager, and R. E. White, Editors, p. 193, Plenum Press, New York and London (1981).

[65] R. Nishimura and N. Sato, *ISIJ Int.*, **31**, 177 (1991).

[66] I. V. Sieber, H. Hildebrand, S. Virtanen, and P. Schmuki, *Corros. Sci.*, **48**, 3472 (2006).

[67] H. Deng, H. Nanjo, P. Qian, A. Santosa, I. Ishikawa, and Y. Kurata, *Electrochim. Acta*, **52**, 4272 (2007).

[68] K. Azumi, T. Ohtsuka, and N. Sato, *Trans. Jpn. Inst. Met.*, **27**, 382 (1986).

[69] T. Yamamoto, K. Fushimi, S. Miura, and H. Konno, *J. Electrochem. Soc.*, **157**, C231 (2010).

[70] K. Azumi, T. Ohtsuka, and N. Sato, *J. Electrochem. Soc.*, **134**, 1352 (1987).

[71] E. B. Castro and J. R. Vilche, *Electrochim. Acta*, **38**, 1567 (1993).

[72] M. Büchler, P. Schmuki, H. Böhni, T. Stenberg, and T. Mäntylä, *J. Electrochem. Soc.*, **145**, 378 (1998).

[73] Ž. Petrović, M. Metikoš-Huković, and R. Babi, *Electrochim. Acta*, **75**, 406 (2012).

[74] S. Hendy, B. Walker, N. Laycock, and M. Ryan, *Phys. Rev. B*, **67**, 85407 (2003).

[75] S. C. Hendy, N. J. Laycock, and M. P. Ryan, *J. Electrochem. Soc.*, **152**, B271 (2005).

[76] C. Albu, S. Van Damme, L. C. Abodi, A. S. Demeter, J. Deconinck, and V. Topa, *Electrochim. Acta*, **67**, 119 (2012).

[77] K. Asami and K. Hashimoto, *Corros. Sci.*, **17**, 559 (1977).

[78] E. McCafferty, M. K. Bernett, and J. S. Murday, *Corros. Sci.*, **28**, 559 (1988).

[79] J. Banas, B. Mazurkiewicz, and B. Stypuła, *Electrochim. Acta*, **37**, 1069 (1992).

[80] S. Suzuki, Y. Ishikawa, M. Isshiki, and Y. Waseda, *Mater. Trans.*, **38**, 1004 (1997).

[81] L. A. Toledo-Matos and M. A. Pech-Canul, *J. Solid State Electrochem.*, **15**, 1927 (2011).

[82] P. Keller and H.-H. Strehblow, *Corros. Sci.*, **46**, 1939 (2004).

[83] R.-H. Jung, H. Tsuchiya, and S. Fujimoto, *Corros. Sci.*, **58**, 62 (2012).

[84] J.-S. Lee, Y. Kitagawa, T. Nakanishi, Y. Hasegawa, and K. Fushimi, *J. Electrochem. Soc.*, **162**, C685 (2015).

[85] M. Seo, M. Sato, J. B. Lumsden, and R. W. Staehle, *Corros. Sci.*, **17**, 209 (1977).

[86] T. Ohtsuka, *Mater. Trans.*, **37**, 67 (1996).

[87] M. López-López, J. L. Ferrando, and C. García-Ruiz, *Anal. Chem.*, **85**, 2595 (2013).

[88] N. Sato, K. Kudo, and T. Noda, *Corros. Sci.*, **10**, 785 (1970).

[89] S. H. Kim, W.-K. Paik, and J. O'M. Bockris, *Surf. Sci.*, **33**, 617 (1972).

[90] T. Ohtsuka, M. Masuda, and N. Sato, *J. Electrochem. Soc.*, **132**, 787 (1985).

[91] V. Goossens, J. Wielant, S. Van Gils, R. Finsy, and H. Terryn, *Surf. Interface Anal.*, **38**, 489 (2006).

[92] N. Sato and K. Kudo, *Electrochim. Acta*, **16**, 447 (1971).

[93] R. Nishimura, K. Kudo, and N. Sato, *Surf. Sci.*, **96**, 413 (1980).

[94] A. Furchner, G. Sun, H. Ketelsen, J. Rappich, and K. Hinrichs, *Analyst*, **140**, 1791 (2015).

[95] D. C. Look, K. D. Leedy, and D. L. Agresta, *Appl. Phys. Lett.*, **104**, 242107 (2014).

[96] A. J. Bard, F.-R. F. Fan, J. Kwak, and O. Lev, *Anal. Chem.*, **61**, 132 (1989).

[97] A. J. Bard, F.-R. F. Fan, D. T. Pierce, P. R. Unwin, D. O. Wipf, and F. Zhou, *Science*, **254**, 68 (1991).

[98] H. Böhni, T. Suter, and A. Schreyer, *Electrochim. Acta*, **40**, 1361 (1995).

[99] M. M. Lohrengel, *Electrochim. Acta*, **42**, 3265 (1997).

[100] M. Chiba and M. Seo, *J. Electorchemical Soc.*, **150**, B525 (2003).

[101] N. Ramasubramanian, P. B. Sewell, and M. Cohen, *J. Electrochem. Soc.*, **115**, 12 (1968).

[102] M. J. Graham and R. J. Hussey, *Oxid. Met.*, **15**, 407 (1981).

[103] K. Fushimi and M. Seo, *Electrochim. Acta*, **47**, 121 (2001).

[104] J. Mieluch and M. Smialowski, *Corros. Sci.*, **4**, 237 (1964).

[105] G. P. Cammarota, L. Felloni, G. Palombarini, and S. Sostero Traverso, *Corrosion*, **129**, 129 (1970).

[106] M. Seo and M. Chiba, *Electrochim. Acta*, **47**, 319 (2001).

[107] R. Y. Chen and W. Y. D. Yuen, *Oxid. Met.*, **59**, 433 (2003).

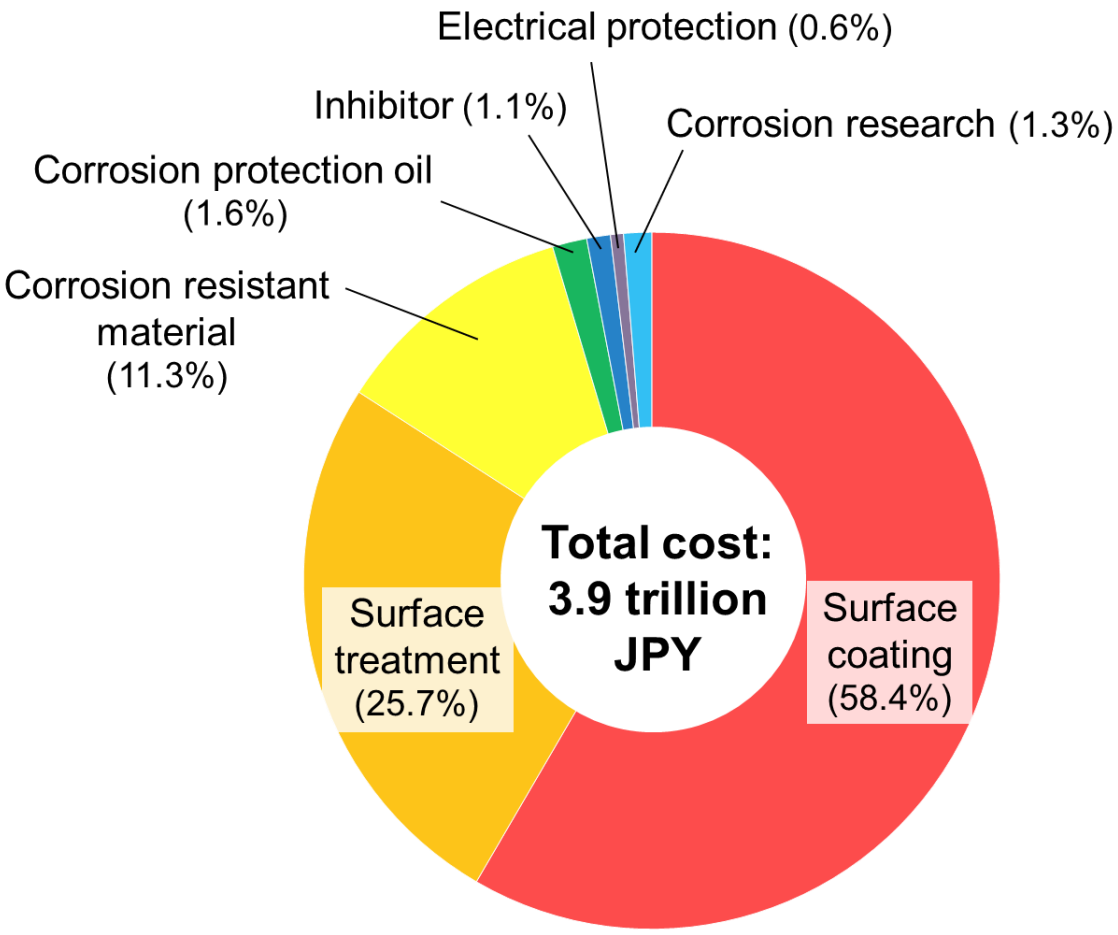

Figure 1.1. Breakdown of corrosion costs in Japan in 1997, estimated with the Uhlig method.

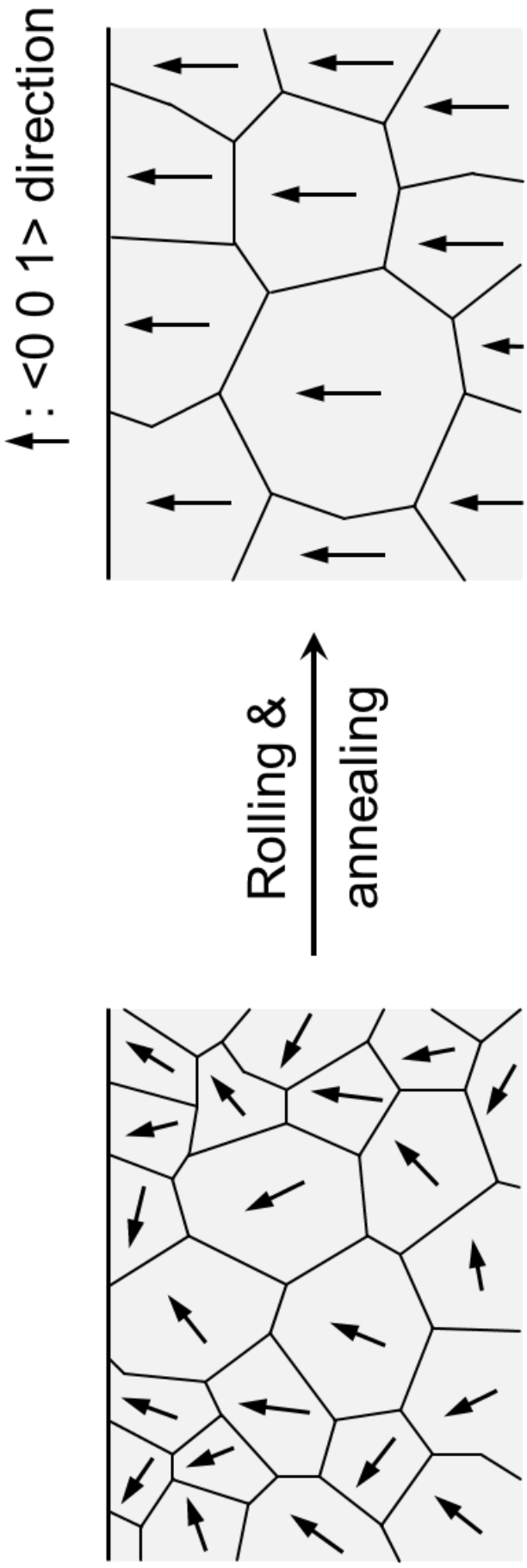

Figure 1.2. Schematic illustration of fabrication of electrical steel.

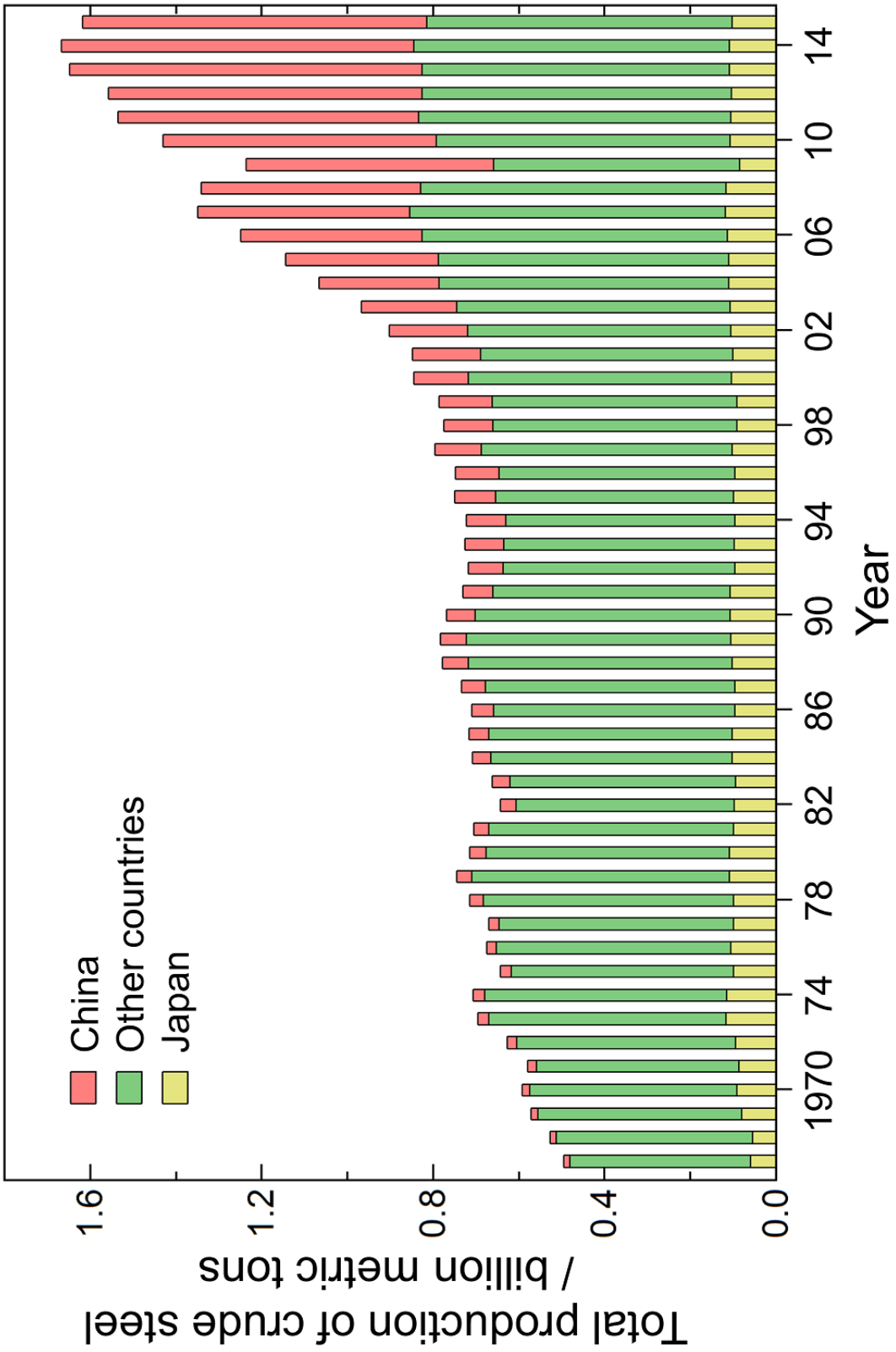

Figure 1.3. Total global production of crude steel from 1967 to 2015.

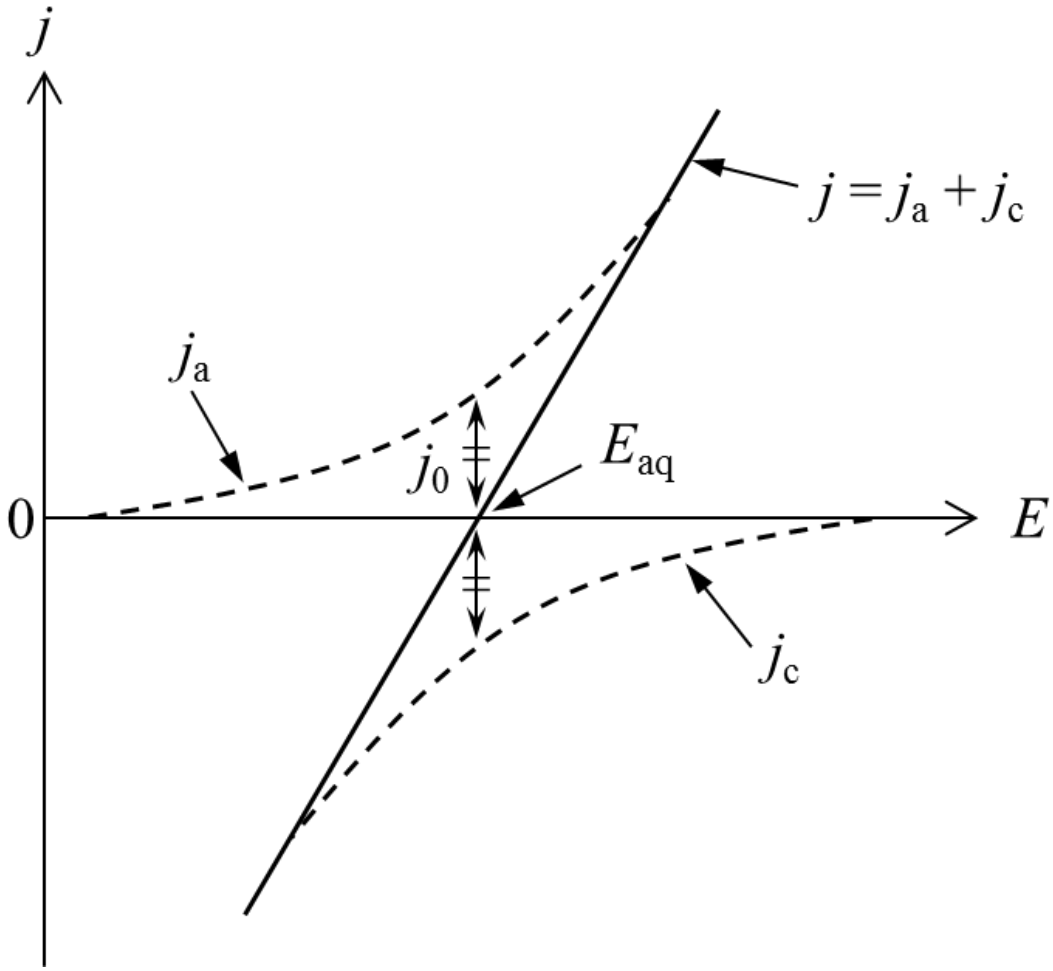

Figure 1.4. Polarization curve of current versus overpotential for the system in Eq. 1.1.

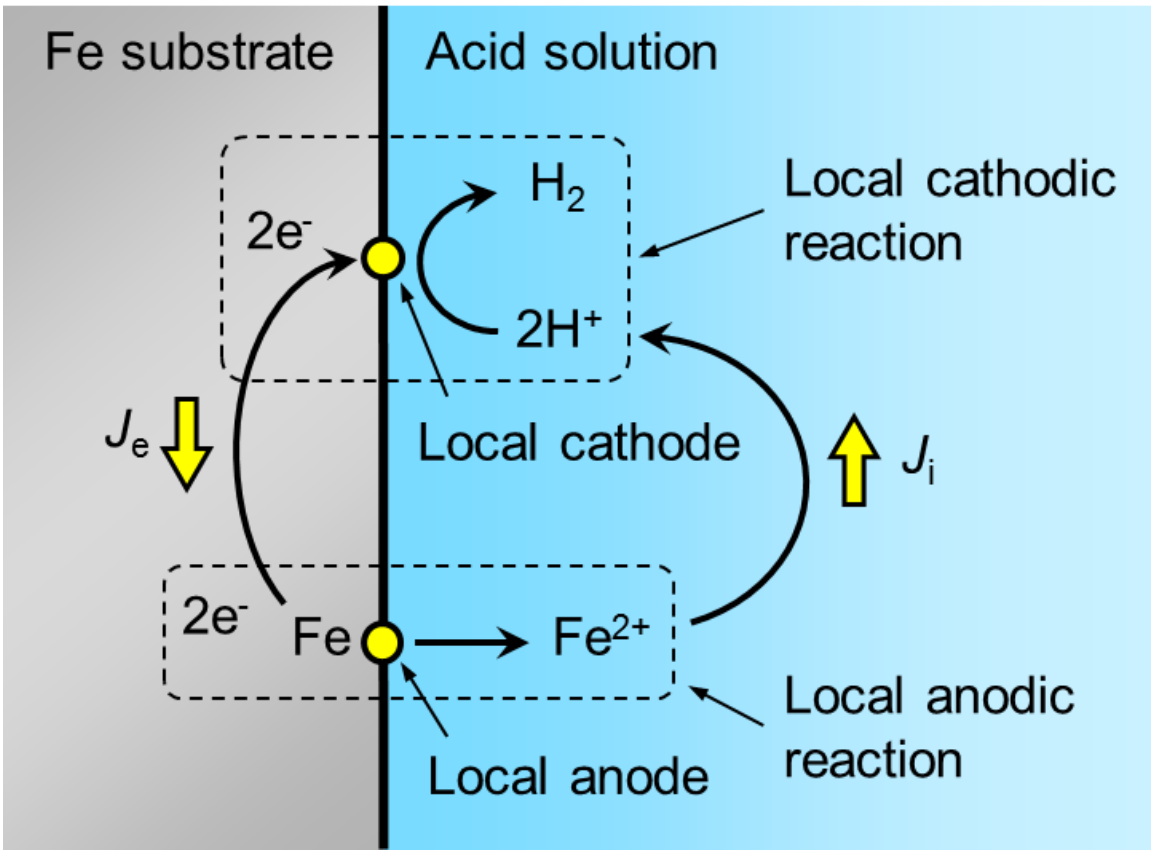

Figure 1.5. Schematic illustration of local cell reactions at an iron substrate/acid solution interface.

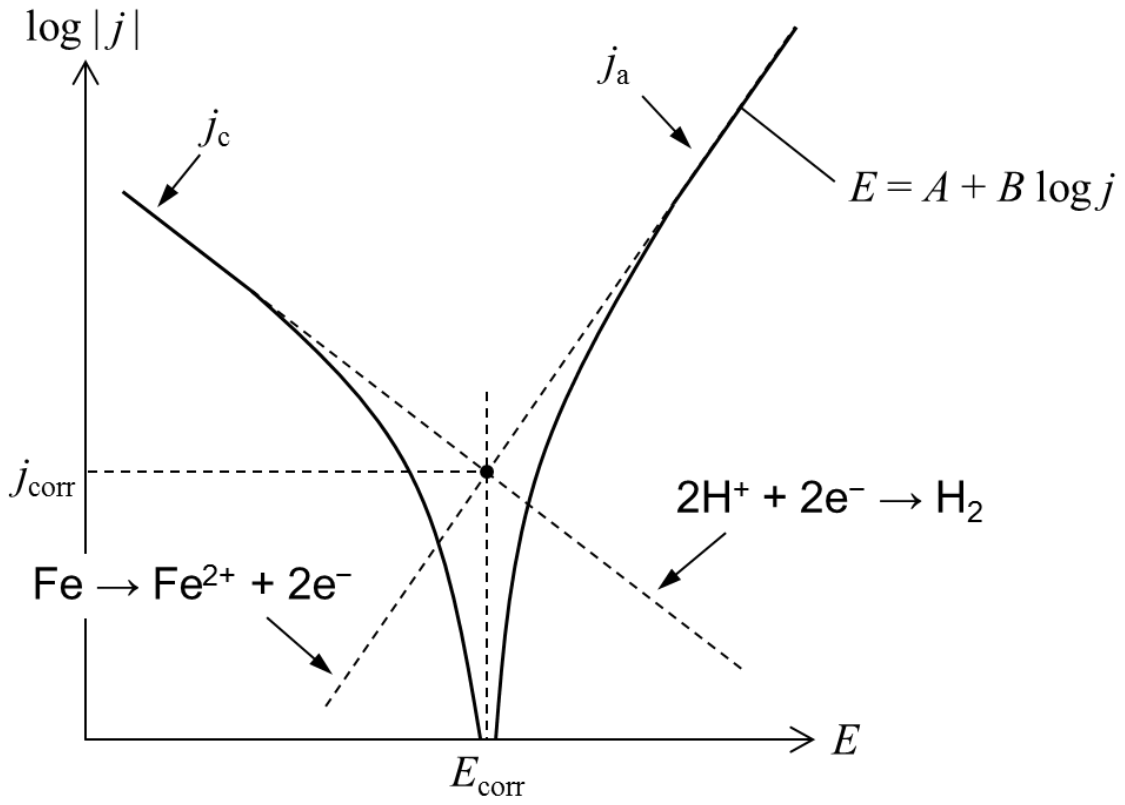

Figure 1.6. Tafel plots for the dissolution of iron and the reduction of hydrogen.

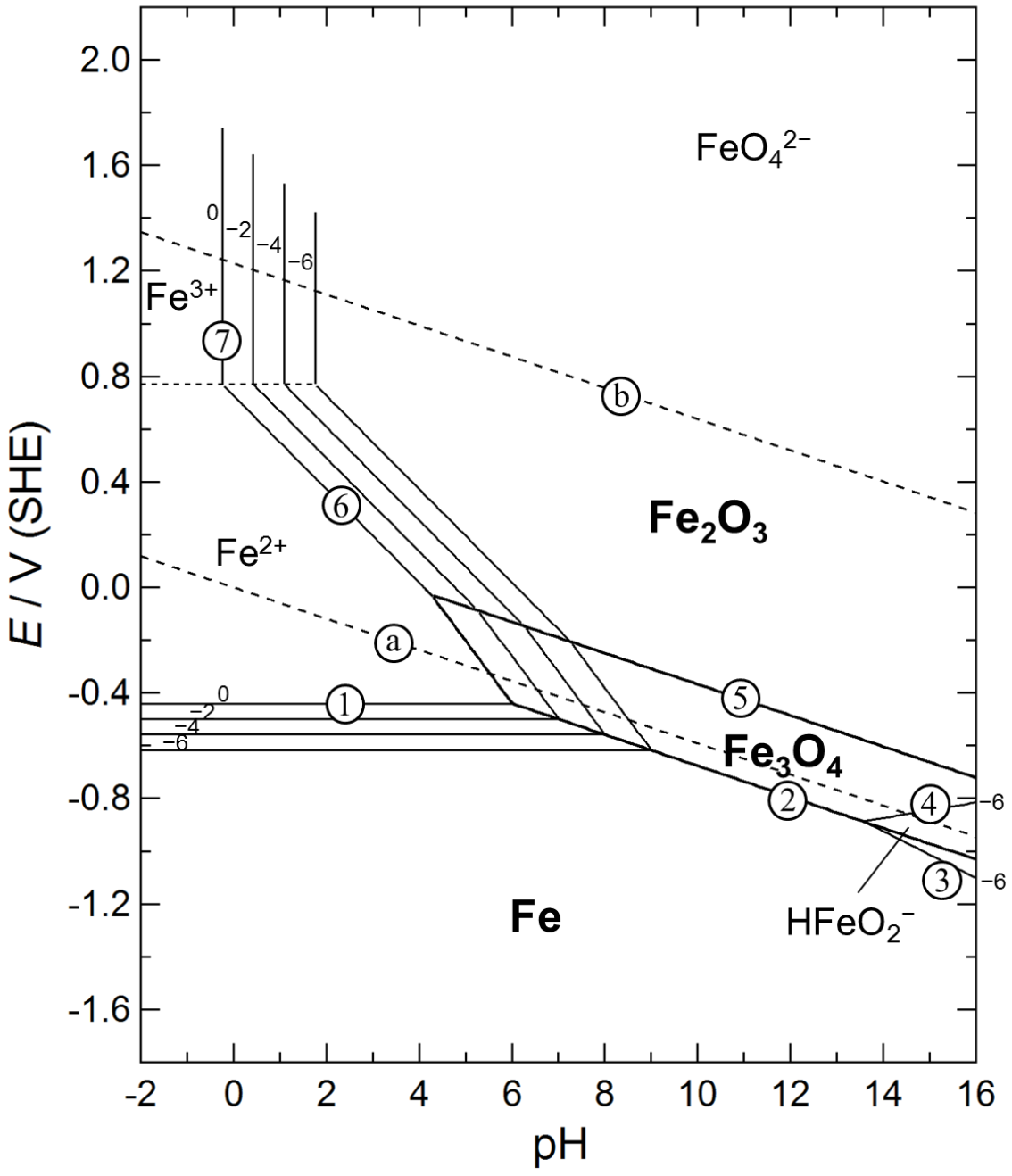

Figure 1.7. Potential-pH (Pourbaix) diagram for the system iron-water at 298 K, considering only Fe, Fe_2O_3, and Fe_3O_4 as solid substances.

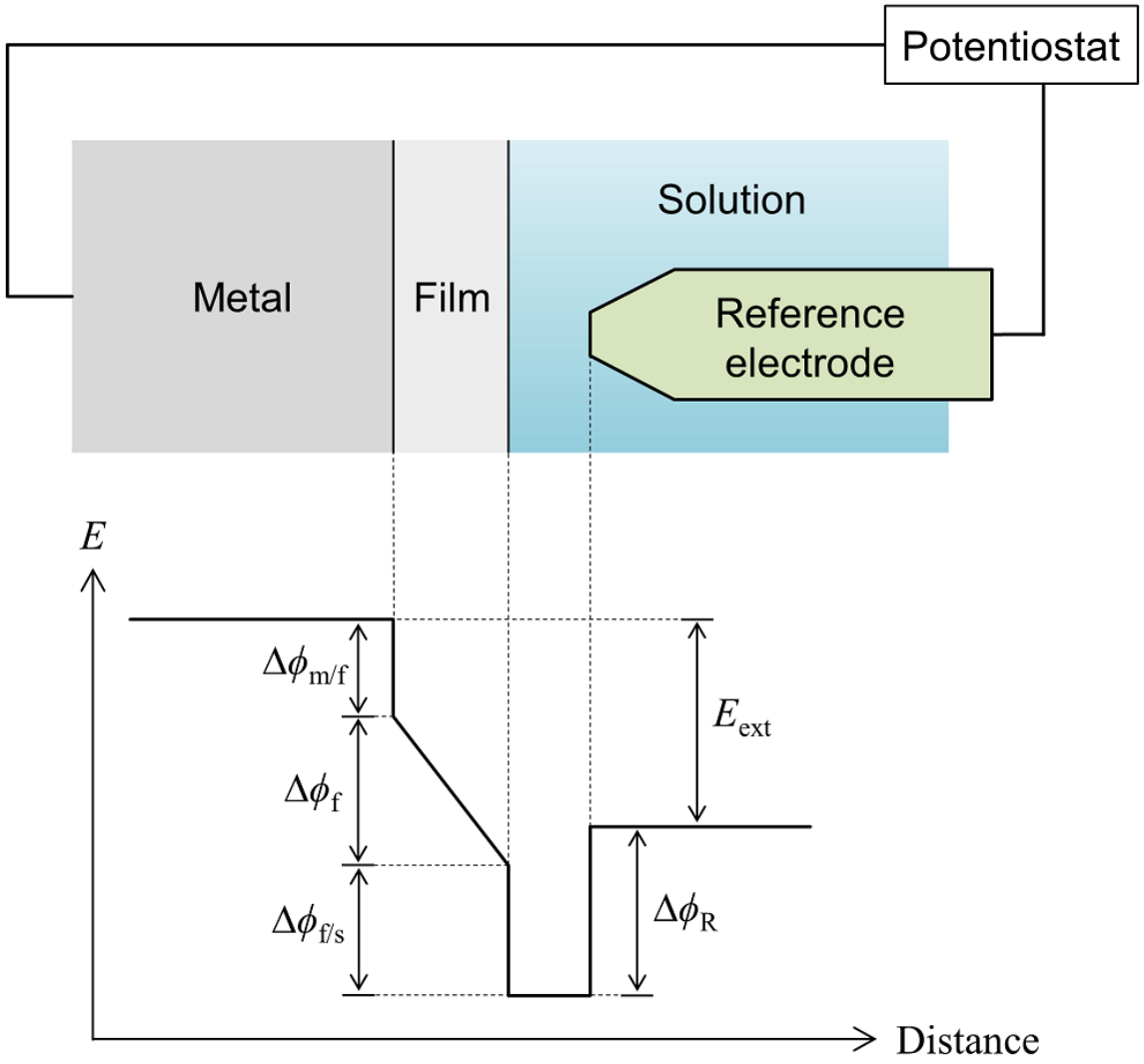

Figure 1.8. Schematic image of working and reference electrodes in an electrochemical cell and the corresponding potential-distance relationships, where $\Delta\phi_{m/f}$, $\Delta\phi_{f/s}$, and $\Delta\phi_R$ are potential drops at metal/film, film/solution, and solution/reference electrode interfaces, respectively, $\Delta\phi_f$, is the potential drop across the film, and E_{ext} is the external potential.

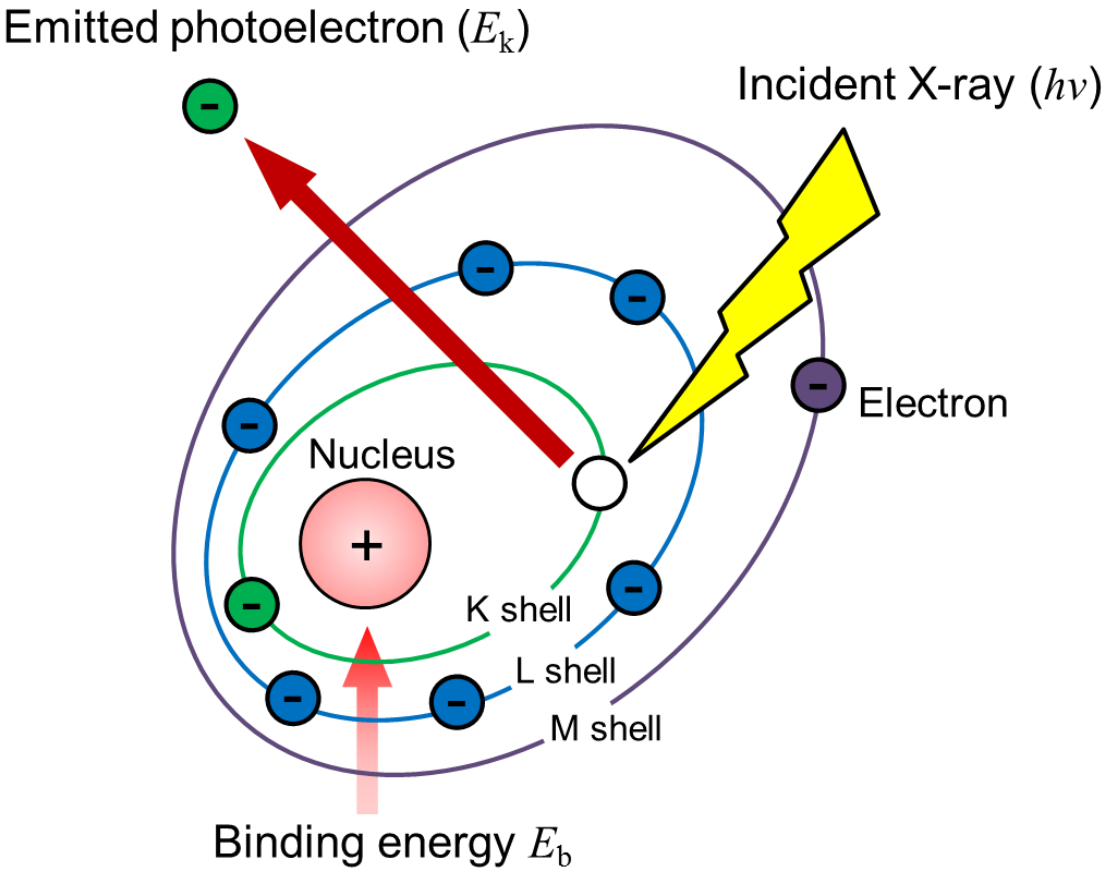

Figure 1.9. Emission of photoelectron by incident X-ray.

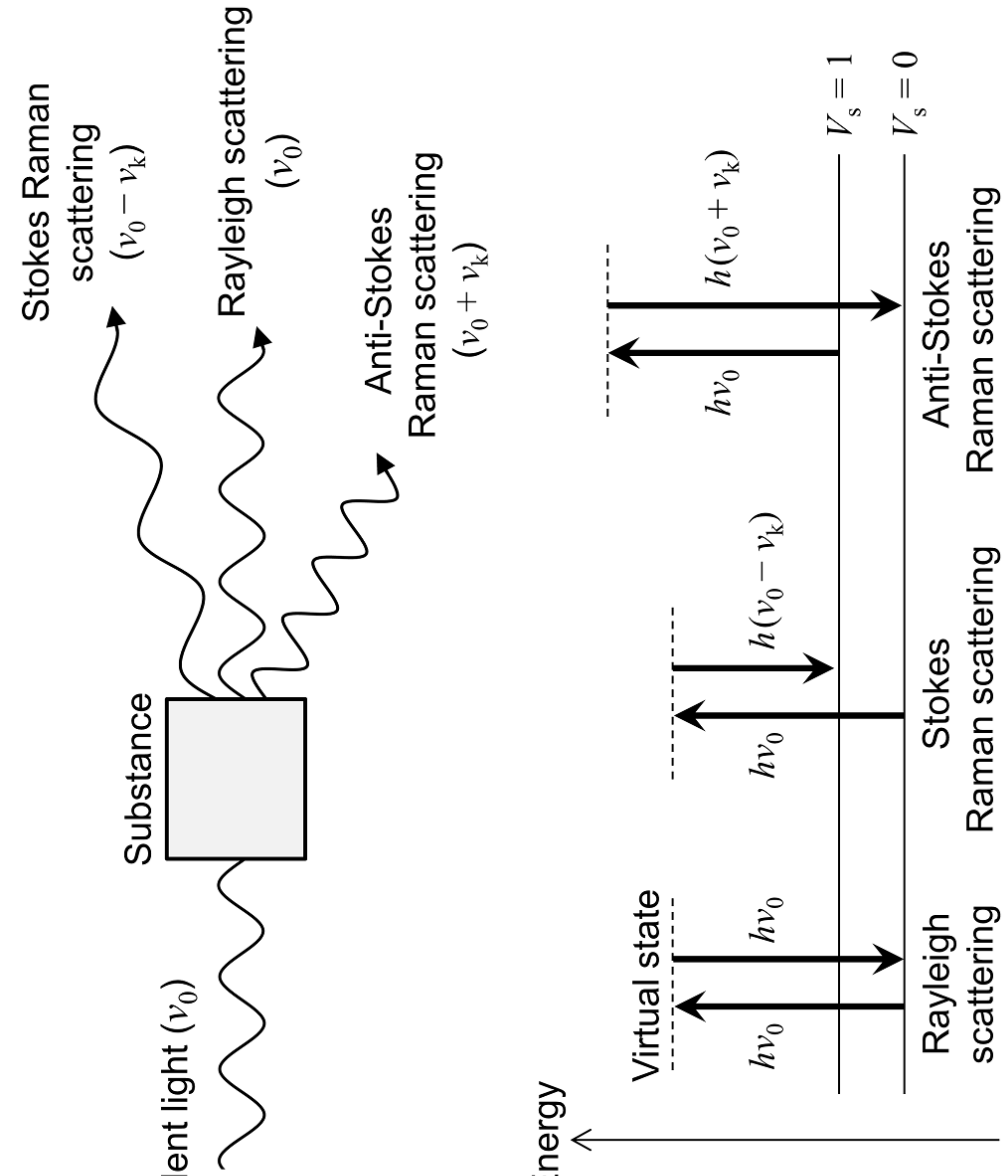

Figure 1.10. (a) Schematic image and (b) energy states of light scattering caused by a substance; V_s is the vibrational state of the substance and $h\nu_k$ is the energy gap between the vibrational states 0 and 1.

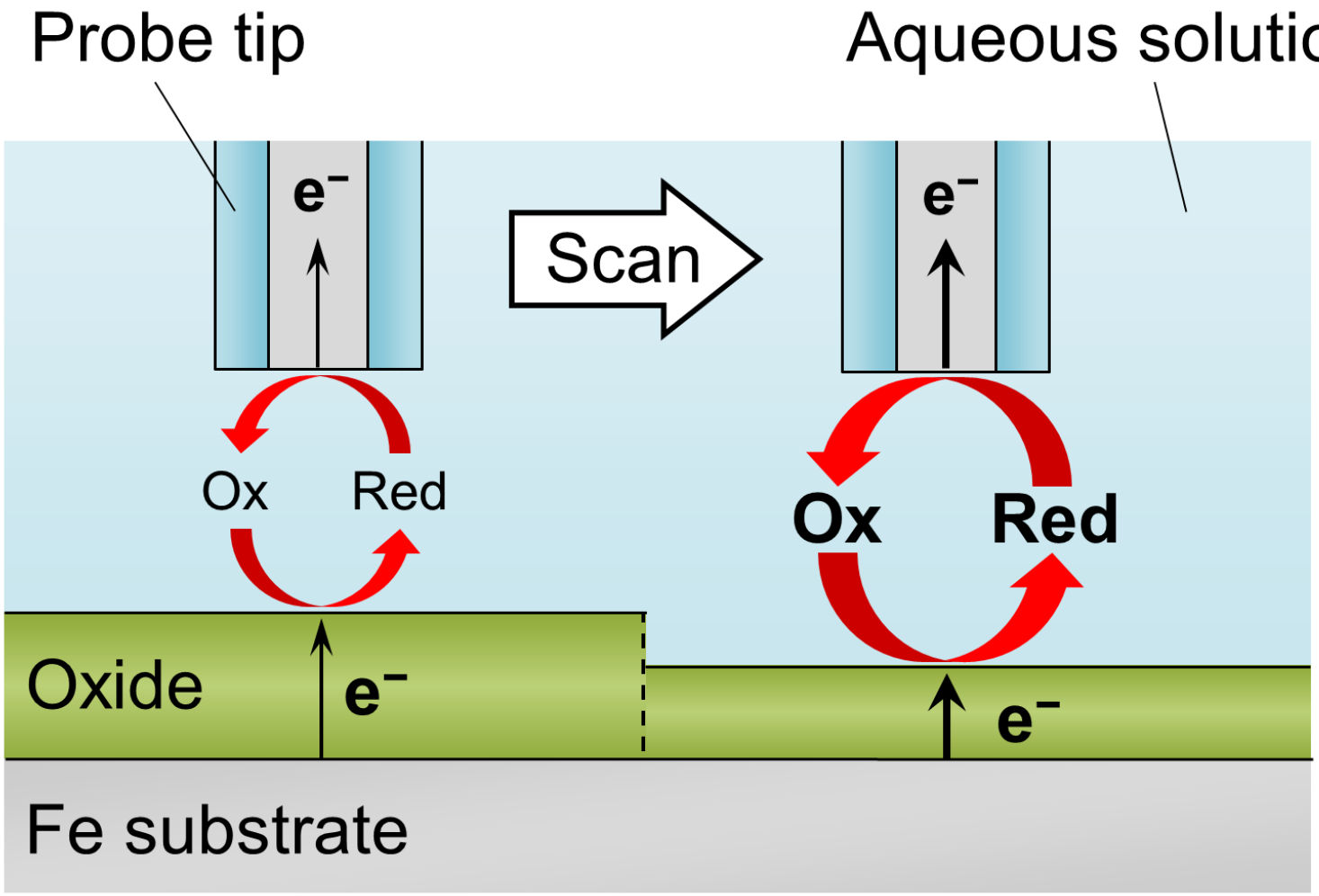

Figure 1.11. Schematic illustration of TG/SC mode SECM. Ox and Red are the oxidized and reduced mediators respectively.

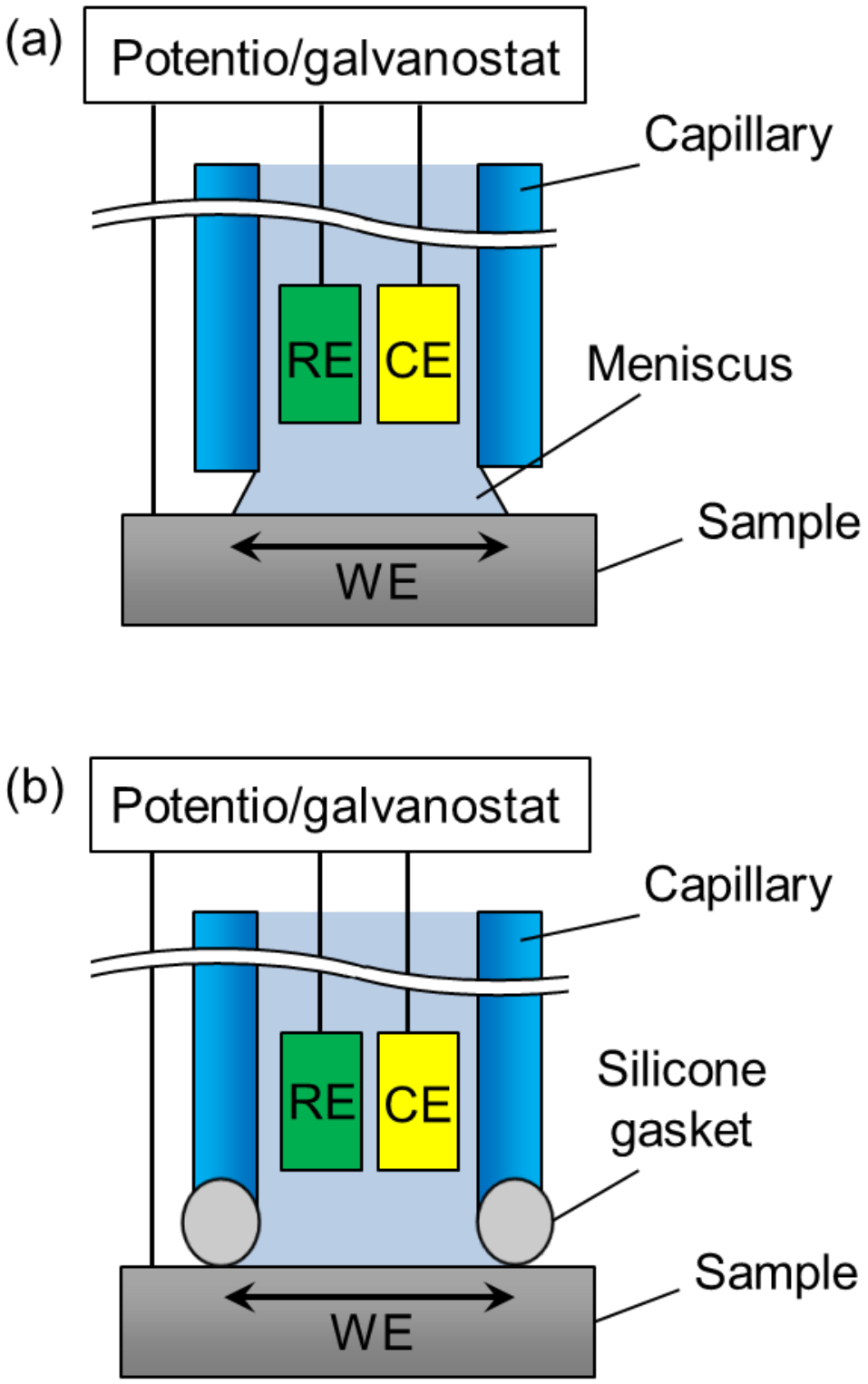

Figure 1.12. Schematic illustrations of (a) meniscus and (b) gasket type micro-capillary cells.

Chapter 2
Experimental techniques and setups

2.1. Sample preparation

The sample used in this study was a polycrystalline iron plate (purity: 99.99%) provided by Nippon Steel and Sumitomo Metal corporation. The sample was cut into small pieces (10 mm × 5 mm × 2 mm) by a refine saw (RCO-961, Refinetec) and subjected to the following treatments.

2.1.1. Grain coarsening

When a metal undergoes plastic deformation by rolling processes, dislocations and lattice defects are induced inside the metal. Since metals and alloys with a distorted lattice structure have higher strain energy than a well-ordered lattice structure, the former are thermodynamically unstable and show different reaction behaviors than the latter. Distortion in metals should be removed for the precise investigation of corrosion behavior, since the atomic arrangement of a metal surface affects corrosion behavior. For the purpose of releasing lattice distortion and coarsening crystal grains, the annealing of a sample specimen was performed.

The sample iron pieces were vacuum-encapsulated into a quartz glass tube to avoid contamination by oxygen and inserted into a tubular furnace. Figure 2.1 shows the sequence of the annealing. At first, the sample was heated to 1253 K for 3 h and kept at that temperature for 1 h; it was then cooled to 603 K for 48 h. The transformation point of iron from α-phase to γ-phase is at 1185 K (Table 1.1). This process of crossing the transformation point introduces lattice disarrangement to the sample as a driving force for the growth of crystal grains. It is known that the correct temperature for the growth of crystal grains is about approximately one-third to one-half of the melting point (degrees K basis) of metals [1], or 603–904 K for iron. The following procedure was then repeated three times: the sample was heated to 1053 K for 4 h, kept there for 2 h, and cooled to 603 K for 24 h. Finally, the sample was cooled to room temperature. The upper temperature limit at 1053 K was set to take into account the temperature difference between the sample and a thermocouple in the furnace.

2.1.2. Surface polishing

The sample specimen was mounted in acrylic resin (Technovit 5071, Heraeus Kulzer) and

ground with the conditions in Table 2.1 by using an auto-grinding machine (LaboForce-3, Struers). After mirror-like polishing with colloidal SiO_2 particles with a diameter of 0.04 μm, the sample was etched in 10 vol% HNO_3 ethanol solution for 10 s to remove the mechanically damaged layer generated by rough grinding processes. Then, the sample was polished again with the colloidal silica particles to make the roughened sample surface flat and washed ultrasonically in distilled water for 60 s. Finally the sample was removed from the resin by breaking it mechanically and washed ultrasonically in each of acetone and ethanol for 60 s.

Table 2.1. Conditions of mechanical polishing for a sample specimen. Tap water was used as lubricant for all processes.

Order	1	2	3	4	5
Abrasive	MD-Piano 220*	SiC-paper	SiC-paper	SiC-paper	MD-chem*
Particle	Diamonds	SiC	SiC	SiC	SiO_2
Grit	-	#800	#1500	#4000	0.04 μm
Rotating rate (rpm)	300	150	150	150	150
Applied force (N)	30	10	10	10	15
Time (s)	to be flat	180	300	420	180

*Abrasive disc produced by Struers

2.1.3. Identification of surface crystallographic orientation

The crystallographic orientation of a polycrystalline iron surface was identified by electron backscattering diffraction (EBSD) patterning, which is a surface characterization technique to study the metallographic structure, crystallographic orientation, and phase of crystalline materials. When an electron beam is incident to a sample tilted 70 degrees in the chamber of a scanning electron microscope (SEM), an electron diffraction pattern called the Kikuchi pattern is projected on a phosphor screen serving as a detector (Fig. 2.2). The crystallographic orientation of the sample surface is determined by indexing pattern bands projected on the screen. Since the escape depth of diffracted electrons is about 50 nm depending on the measurement conditions, such as the acceleration voltage and atomic number of a sample, it is important for accurate patterning to prepare a flat sample surface without a grinding-affected layer. A crystallographic orientation is described by three Euler angles (φ_1, Φ, φ_2) as misorientation angles between crystal and sample frames (Fig. 2.3). The line of node N_{CS} is defined as the intersection of the *xy* and *XY* coordinate planes. A crystallographic orientation is visually represented by a pole figure and an inverse pole figure (IPF). When one focuses on a certain crystal plane of a sample, a pole figure provides helpful information; Fig. 2.4a shows the formation of the pole figure of the {0 0 1} plane of a sample with cubic crystal symmetry. Intersections between the sphere centered at the sample lattice and {0 0 1} normal directions (NDs) of the sample are projected on a stereographic projection plane, which is a pole figure. Figures 2.4b–d indicate that the {0 0 1} plane of the

sample is perpendicular to the sample ND and that other {0 0 1} planes are perpendicular to the sample rolling direction (RD) and transverse direction (TD). On the other hand, when one focuses on the crystallographic orientation of a sample surface, an IPF is beneficial for optimizing the orientation. Figure 2.5a shows the IPF on a stereographic projection plane when the sample (0 0 1) plane is parallel to the sample ND. Figures 2.5b–c indicate when the {1 2 2} and {1 2 3} planes are perpendicular to the sample ND and the equivalent planes of a sample with cubic crystal symmetry can be expressed on the shaded unit triangle. In this study, the crystallographic orientation of the sample surface was displayed by the colors of the unit triangle (Fig 2.5d).

The crystallographic orientation of a polycrystalline iron specimen was identified by an EBSD apparatus (SC-200, TSL Solutions) incorporated in a field emission Auger electron microprobe (JAMP-9500F, JEOL) and measurement software (OIM Data Collection 5.31, TSL Solutions). The conditions of Kikuchi pattern projection and background subtraction are summarized in Table 2.2. The crystallographic orientation of the sample surface was collected at a magnification of ×100 with a scanning step of 10 μm. Obtained orientation images were cleaned under the cleanup parameters of a grain tolerance angle of 5 degrees and a minimum grain size of 5 pixels, using OIM Analysis 5.31 software (TSL Solutions). Figure 2.6 shows the EBSD IPF map of a typical polycrystalline iron specimen. The annealed sample consists of many grains with diameters ranging from a few micrometers to 1 mm. Relatively large grains with approximated {0 0 1}, {1 0 1}, and {1 1 1} planes within a misorientation angle of 10 degrees were used for micro-electrochemical measurements as working electrodes.

Table 2.2. Typical conditions of Kikuchi pattern projection and background subtraction for EBSD measurements.

Acceleration voltage (kV)	Probe current (nA)	Working distance (mm)	Gain	Black	Exposure (ms)	Flames
20	1	25	−2.0	1.0	7.74	30

2.2. Electrochemical measurements with micro-capillary cell

There are two types of MCCs, depending to the geometry of a capillary tip/sample electrode interface, as introduced in 1.3.3. In this study, the gasket type MCC was adopted and developed to conduct electrochemical measurements with a constant electrode area in which the scanning of the MCC was not necessary.

2.2.1. Fabrication of micro-capillary

A 10 cm-long Pylex glass tube with inner and outer diameters of 3 and 5 mm respectively

was divided by hot-stretching of the middle part with a gas flame; the hot stretched end of the glass tube with a narrow tip was bent to an L-shape (Fig. 2.7a). The opposite end of the glass tube was capped with a Luer fitting (VFUP6, Isis) that had a hole with a diameter of 5.5 mm by adhesive (Araldite Rapid, Huntsman Materials). The narrow tip of the glass was ground by a micro-pipet grinder (EG-400, Narishige); a hole with an inner diameter of 70–250 μm was achieved (Fig. 2.7b). The thickness of the wall of the capillary tip was reduced by SiC paper into ca. 100 μm (Fig. 2.7c). The capillary was then washed ultrasonically in distilled water and ethanol and dried by compressed air. Finally, silicone glue (RTV 118, Momentive) was placed on the capillary tip (Fig. 2.7d).

2.2.2. Micro-reference electrode

In order to reduce electrolyte resistance between a working electrode and a reference electrode, the electrodes should be installed as close as possible to each other. However, ordinary reference electrodes are too large to insert into the micro-capillary. Here, a suitable micro-reference electrode [2] for an MCC was fabricated. A silver wire with a diameter of 300 μm (purity: 99.99%, Niraco) was cut into 10-cm length pieces and immersed in nitric acid for 2 s to remove a native oxide film. The silver wire was first cleaned and roughened by cycling 10 times between 0.5 and −0.1 V (SHE) with a scan rate of 10 mV s^{-1} in 0.1 mol dm^{-3} KCl aqueous solution. Then, AgCl was deposited by potentiostatic polarization at 0.1 V (SHE) for 120 s and finally at 0.3 V (SHE) for 600 s. After rinsing with water, the wire was kept in saturated KCl solution for at least one day. Meanwhile, a glass tube with an outer diameter of 2 mm was cut into 7 cm-long pieces and a platinum wire with a diameter of 300 μm (purity: 99.98%, Niraco) was embedded in an one end of the glass tube by a gas flame. The Ag/AgCl wire was inserted into the glass tube with saturated KCl solution at ca. 333 K and closed by Araldite adhesive (Fig. 2.8a). Figure 2.8b shows potential-time transients of the micro-Ag/AgCl electrode (SSE) versus a commercial Ag/AgCl reference electrode (HS-205C, TOA DKK). The colors of curves indicate saving periods since the micro-electrode was fabricated. After one day, the electrode potential was 100 mV less than that of the commercial electrode and increased about 8 mV for 50 ks. After 16 days, the electrode potential did not show any obvious change for 100 ks, so the micro-electrode could be used as a stable reference electrode for this time range. After 167 days, the micro-electrode showed a constant potential at –74 mV (SSE), indicating that a stable reference electrode for long-term experimentation had been achieved. Finally, the tip of the micro-electrode was wrapped with a platinum wire as a counter electrode.

2.2.3. Setup of micro-capillary cell

The main body of an MCC was fabricated from a polycarbonate polymer block. The body had a simple structure with three holes. An adapter fitting (VFU306, Isis) and a flon tube (King

Works) were jointed on an upper hole of the block as a solution inlet. A cylinder pump (Aladdin-1000, World Precision Instruments) was connected to the tube via a three-way stopcock (VXB1079, Isis) to enable precise adjustment of water pressure in the cell. A micro-capillary fabricated in 2.2.1 was attached to the polymer block from the left side and a micro-reference electrode fabricated in 2.2.2 was attached from the right side. Figure 2.9 shows a photograph and the schematic setup of the MCC. The combination of an optical microscope and the cell enabled precise determination of a measurement point on a polycrystalline sample surface. A differential interferometer was equipped on the optical microscope to identify crystal grains on the mirror-like polished sample surface. An objective lens (M-Plan Apo 20x, Mitutoyo) had a focal distance of 20 mm and enabled operating the glass capillary between the lens and the sample. A CMOS camera (L-835, Hozan) was attached to the microscope and collected sample images after electrochemical measurements with the MCC. An auto-*xy* stage (TSDM40-15, Sigma Koki), an auto-*z* stage (SGSP40-5ZF, Sigma Koki), and a force sensor (KD24s 2N, Meβsysteme GmbH) were controlled with a LabVIEW program (National Instruments). This enabled placing the MCC on a sample surface with high position accuracy with 0.1-μm unit. A tool scope (TS-C-2-10-4, Chuo Precision Industrial) was positioned in front of the sample stage and used to observe the surface of electrolyte droplet coming out from the capillary tip.

2.2.4. Measurement procedure

Before the installation of the MCC, the inside of the glass capillary was filled with electrolyte solution coming from the solution inlet. First, a measurement point of a sample surface was established in the middle of a scope of the optical microscope. The capillary tip was then moved to the space between the measurement point and the objective lens by moving the auto-*xy* stage. The water level of a droplet surface was adjusted to match the plane of the ground capillary tip by the cylinder pump and observation with the tool scope. Adjusting the water level was important in order to avoid the contamination of bubbles at the sample/solution interface and the leakage of electrolyte solution outside of the capillary tip caused by excessive water pressure. Finally, the MCC was installed on the sample surface by moving down the auto-*z* stage; an electrochemical measurement was immediately performed. After the measurement, the MCC was moved away from the sample surface and the inside of the cell was washed by fresh electrolyte solution coming from the solution inlet.

In this study, all electrochemical measurements were performed by a potentiostat (FAS2 Femtostat) and measurement software (Gamry Framework 6.04) produced by Gamry Instruments.

2.3. Two-dimensional ellipsometry

2.3.1. Principle of ellipsometry

Ellipsometry is an optical technique that analyzes the polarization of light reflected at a sample surface and measures the optical constant of the sample or the thickness of a thin film on the sample surface. In this section, the principle of ellipsometry required to calculate the thickness of thin films on flat substrate is introduced [3].

The refractive index n is given by

$$n = c / s, \tag{2.1}$$

where c and s are the speed of light in vacuum and in a medium. When a light with the wavelength λ travels in a medium, the wave number K is described as

$$K = 2\pi n / \lambda. \tag{2.2}$$

The propagation of plane waves in an isotropic absorbing medium is described by the complex refractive constant N, which is written as

$$N = n - ik, \tag{2.3}$$

where i is the imaginary number ($i^2 = -1$) and k is the extinction coefficient of the medium. Figure 2.10 shows the optical interference caused by the thin film on a flat substrate. The phase change α_p caused by the optical path-length difference between primary and secondary light is written by using Eq. 2.2 as follows:

$$\alpha_p = \frac{2\pi N_1}{\lambda}(l_{AB} + l_{BC}) - \frac{2\pi N_0}{\lambda} l_{AD}\,, \tag{2.4}$$

where N_x is the complex refractive index of a medium x and l_{XY} is the distance between points X and Y in Fig. 2.10. It is also recognized that $l_{AD} = l_{AC} \sin\theta_0$ and $l_{AC} = 2d \tan\theta_1$, where θ_0 and θ_1 are the incident and refraction angles respectively and d is the thickness of the thin layer. By using Snell's law ($N_x \sin\theta_x = N_y \sin\theta_y$), Eq. 2.4 is transformed into

$$l_{AD} = 2d \frac{\sin^2\theta_1}{\cos\theta_1} \frac{N_1}{N_0}. \tag{2.5}$$

From Eqs. 2.4 and 2.5 and $l_{AB} = l_{BC} = d \cos\theta_1$,

$$\alpha_p = \frac{4\pi d N_1}{\lambda}\cos\theta_1. \tag{2.6}$$

Finally, the film phase thickness β_p (= $\alpha_p/2$) is described as

$$\beta_p = \frac{2\pi d}{\lambda} N_1 \cos\theta_1. \tag{2.7}$$

When the incident light is linearly polarized, the electric vector is divided into two components, the electric vectors vibrating parallel (p) and perpendicular (s) to the plane of

incidence. They are denoted as p- and s-polarizations. Let (E_{ip}, E_{is}), (E_{rp}, E_{rs}) and (E_{tp}, E_{ts}) represent the complex amplitudes of the components of the electric vectors of incident, reflected, and transmitted waves, respectively, at opposite points immediately above and below the interface of media 0 and 1 (Fig. 2.10). Thus, the Fresnel complex-amplitude reflection and transmission coefficients for the p- and s-polarizations $r_{01,p}$, $r_{01,s}$, $t_{01,p}$, and $t_{01,s}$ are expressed as

$$r_{01,\mathrm{p}} = \frac{E_{\mathrm{rp}}}{E_{\mathrm{ip}}} = \frac{N_1\cos\theta_0 - N_0\cos\theta_1}{N_1\cos\theta_0 + N_0\cos\theta_1}, \tag{2.8}$$

$$r_{01,\mathrm{s}} = \frac{E_{\mathrm{rs}}}{E_{\mathrm{is}}} = \frac{N_0\cos\theta_0 - N_1\cos\theta_1}{N_0\cos\theta_0 + N_1\cos\theta_1}, \tag{2.9}$$

$$t_{01,\mathrm{p}} = \frac{E_{\mathrm{tp}}}{E_{\mathrm{ip}}} = \frac{2N_0\cos\theta_0}{N_1\cos\theta_0 + N_0\cos\theta_1}, \tag{2.10}$$

$$t_{01,\mathrm{s}} = \frac{E_{\mathrm{ts}}}{E_{\mathrm{is}}} = \frac{2N_0\cos\theta_0}{N_0\cos\theta_0 + N_1\cos\theta_1}. \tag{2.11}$$

Figure 2.11 shows the optical interference model of multiple reflections at the thin film/substrate interface. The amplitude reflection coefficient of a primary light is r_{01}. The phase change caused by the optical path length of a secondary light is expressed as $\exp(-i2\beta_p)$. Thus, the secondary light is given by the multiplicity of the phase change and coefficients at each interface as $t_{01}t_{10}r_{12}\exp(-2\beta_p i)$. The amplitude reflection coefficient r_{012} at medium/thin film/substrate is described by summarizing all high-order reflected light as

$$r_{012} = r_{01} + t_{01}t_{10}r_{12}\exp\left(-i2\beta_{\mathrm{p}}\right) + t_{01}t_{10}r_{10}r_{12}^{\,2}\exp\left(-i4\beta_{\mathrm{p}}\right) + t_{01}t_{10}r_{10}^{\,2}r_{12}^{\,3}\exp\left(-i6\beta_{\mathrm{p}}\right) + \cdots. \tag{2.12}$$

Using the infinite series $y = a + ar + ar^2 + ar^3 + \cdots = a/(1 - r)$, one obtains

$$r_{012} = r_{01} + \frac{t_{01}t_{10}r_{12}\exp\left(-i2\beta_{\mathrm{p}}\right)}{1 - r_{10}r_{12}\exp\left(-i2\beta_{\mathrm{p}}\right)}. \tag{2.13}$$

If the substitutions $r_{01} = -r_{01}$ and $t_{01}t_{10} = 1 - r_{10}^{\,2}$ are derived from Eqs. 2.8–11, Eq. 2.13 is transformed into

$$r_{012} = \frac{r_{01} + r_{12}\exp\left(-i2\beta_{\mathrm{p}}\right)}{1 + r_{01}r_{12}\exp\left(-i2\beta_{\mathrm{p}}\right)}. \tag{2.14}$$

Likewise, the amplitude transmission coefficient t_{012} is

$$t_{012} = \frac{t_{01}t_{12}\exp\left(-i\beta_{\mathrm{p}}\right)}{1 + r_{01}r_{12}\exp\left(-i2\beta_{\mathrm{p}}\right)}. \tag{2.15}$$

From Eqs. 2.14 and 2.15, the amplitude reflection and transmission for p- and s-polarizations are written as

$$r_{012,\mathrm{p}} = \frac{r_{01,\mathrm{p}} + r_{12,\mathrm{p}}\exp\left(-i2\beta_{\mathrm{p}}\right)}{1 + r_{01,\mathrm{p}}r_{12,\mathrm{p}}\exp\left(-i2\beta_{\mathrm{p}}\right)}, \tag{2.16a}$$

$$r_{012,\mathrm{s}} = \frac{r_{01,\mathrm{s}} + r_{12,\mathrm{s}}\exp\left(-i2\beta_{\mathrm{p}}\right)}{1 + r_{01,\mathrm{s}}r_{12,\mathrm{s}}\exp\left(-i2\beta_{\mathrm{p}}\right)}, \tag{2.16b}$$

$$t_{012,\mathrm{p}} = \frac{t_{01,\mathrm{p}}\, t_{12,\mathrm{p}}\exp\left(-i\beta_{\mathrm{p}}\right)}{1 + r_{01,\mathrm{p}}\, r_{12,\mathrm{p}}\exp\left(-i2\beta_{\mathrm{p}}\right)}, \tag{2.17a}$$

$$t_{012,\mathrm{p}} = \frac{t_{01,\mathrm{p}}\, t_{12,\mathrm{p}}\exp\left(-i\beta_{\mathrm{p}}\right)}{1 + r_{01,\mathrm{p}}\, r_{12,\mathrm{p}}\exp\left(-i2\beta_{\mathrm{p}}\right)}. \tag{2.17b}$$

Optical interference caused by a multi-layer film is also explained by using Fresnel coefficients. Figure 2.12 shows an optical model that has a bi-layer thin film on a substrate. The amplitude reflection coefficient r_{123} at a thin layer 2/substrate interface is given by

$$r_{123} = \frac{r_{12} + r_{23}\exp\left(-i2\beta_{\mathrm{p2}}\right)}{1 + r_{12}r_{23}\exp\left(-i2\beta_{\mathrm{p2}}\right)}, \tag{2.18}$$

where β_{p2} is the film phase thickness ($= 2\pi d_2 N_2 \cos\theta_2/\lambda$) and d_2 is the thickness of the thin layer 2. Finally, the total amplitude reflection coefficient r_{0123} is obtained by using Eq. 2.18

$$r_{0123} = \frac{r_{01} + r_{123}\exp\left(-i2\beta_{\mathrm{p1}}\right)}{1 + r_{12}r_{123}\exp\left(-i2\beta_{\mathrm{p1}}\right)}. \tag{2.19}$$

where β_{p1} is the film phase thickness ($= 2\pi d_1 N_1 \cos\theta_1/\lambda$) and d_1 is the thickness of the thin layer 1. As described above, the multi-layer film is calculated layer by layer from the substrate by using the Fresnel coefficients.

The reflection ellipsometry used in this study measures the ratio P of the complex Fresnel reflection coefficients for the p- and s-polarizations,

$$P = \frac{r_{\mathrm{p}}}{r_{\mathrm{s}}} = \tan\Psi\exp(i\Delta), \tag{2.20}$$

where Ψ and Δ are the differential changes in amplitude and phase between the vibrations of p- and s-polarizations (Fig. 2.13). If the complex Fresnel coefficients are expressed in polar coordinates, P is described as

$$P = \frac{|r_{\mathrm{p}}|}{|r_{\mathrm{s}}|}\exp\{i(\delta_{\mathrm{rp}} - \delta_{\mathrm{rs}})\}, \tag{2.21}$$

where δ_{rp} and δ_{rs} are the arguments of r_p and r_s, respectively. From Eqs. 2.20 and 2.21, it is readily seen that

$$\tan\Psi = \frac{|r_p|}{|r_s|}, \tag{2.22}$$

$$\Delta = \delta_{rp} - \delta_{rs} \ (-180 < \Delta \leq 180 \text{ degrees}). \tag{2.23}$$

An angle range of Δ can be converted to $0 < \Delta \leq 360$ degrees by adding 360 degrees to the region $-180 < \Delta < 0$ degrees.

As an example of the calculation of Ψ and Δ using the principle of ellipsometry introduced above, ideal curves of Ψ and Δ were demonstrated by using the bi-layered optical model shown in Fig. 2.14a as a model case; a bi-layered oxide film with an outer α-Fe_2O_3 layer and an inner Fe_3O_4 layer was formed on Fe substrate in air. The parameters of $\theta_0 = 70$ degrees and $\lambda = 636$ nm, $N_0 = 1.00$, $N_1 = 2.64 - 0.01i$, $N_2 = 2.28 - 0.45i$ and $N_3 = 2.87 - 3.36i$ were used for the calculation. Figures 2.14b–c show ideal curves of Ψ and Δ as a function of d_1, the thickness of the outer α-Fe_2O_3 layer. The value of Ψ fluctuates at a constant cycle and gradually decreases with increasing d_1, decreasing with increasing d_2 the thickness of the inner Fe_3O_4. On the other hand, Δ decreases continuously. The relations between Ψ and Δ for various d_1 and d_2 are summarized in Fig. 2.14d.

2.3.2. Two-dimensional ellipsometry measurement

An ellipsometer (SE-101, Photonic Lattice) detected polarization of light by using a photonic crystal array (PCA) equipped in front of a CCD camera (Fig. 2.15) instead of rotating an analyzer and a photo-detector. The wavelength λ of an incident light was 636 nm. A line profile of P of light reflected at the sample surface with an incident angle of 70 degrees at 23.25 μm intervals was measured by a 112 imaging channel aligned in the x-direction on the sensor, which was combined the PCA with the CCD camera. The LabVIEW program enabled mapping of Ψ and Δ by controlling an auto y-axis stage (SGSP20-20, Sigma Koki) at an interval distance of 23 μm during ellipsometric measurements. The thickness d of the thin layer on a sample surface was determined by the least-squares method to obtain the minimum value X:

$$X = (\Psi - \Psi_{ideal})^2 + (\Delta - \Delta_{ideal})^2, \tag{2.24}$$

where Ψ_{ideal} and Δ_{ideal} are the theoretical values of Ψ and Δ calculated from any given values of d by using a single layer optical model (Fig. 2.11). The most suitable d that could give the minimum value of X was obtained by trial and error with the LabVIEW program. The thicknesses d_1 and d_2 of the outer and inner oxide layers in a bi-layered thin film (Fig. 2.12) respectively were simultaneously determined by Eq. 2.24. The most suitable combination of d_1 and d_2 that could give the minimum value of X was also obtained by trial and error with that program.

2.3.3. Setup of electrochemical cell for *in situ* 2D ellipsometry

First, a sample specimen was mounted on an epoxy resin holder with the Araldite Rapid adhesive. A brass screw in contact with the back side of the sample was used to obtain an electric contact with the potentiostat. The sample was put in an electrochemical cell designed for *in situ* 2D ellipsometry, as shown in Fig. 2.16. A platinum wire was used as a counter electrode and an Ag/AgCl/saturated KCl reference electrode was connected to the cell via a Luggin-Haber capillary and a salt-bridge of solidified agar with KNO_3. The cell was connected with two glass bottles filled with pH 6.5 and pH 8.4 borate buffer solutions (0.293 mol dm^{-3} boric acid and 0.00188 mol dm^{-3} sodium borate, and 0.150 mol dm^{-3} boric acid and 0.0375 mol dm^{-3} sodium borate solutions, respectively.). These solutions were deaerated with bubbling of pure Ar gas and injected into the cell by the pressure of the Ar gas, thus avoiding the contamination by air of the cell.

References

[1] 古林英一　著、材料学シリーズ　再結晶と材料組織、内田老鶴圃 (2000).

[2] A. W. Hassel, K. Fushimi, and M. Seo, *Electrochem. commun.*, **1**, 180 (1999).

[3] R. M. A. Azzam and N. M. Bashara, *Ellipsometry and Polarized Light*, p. 269, North-Holland Personal Library, Amsterdam (1987).

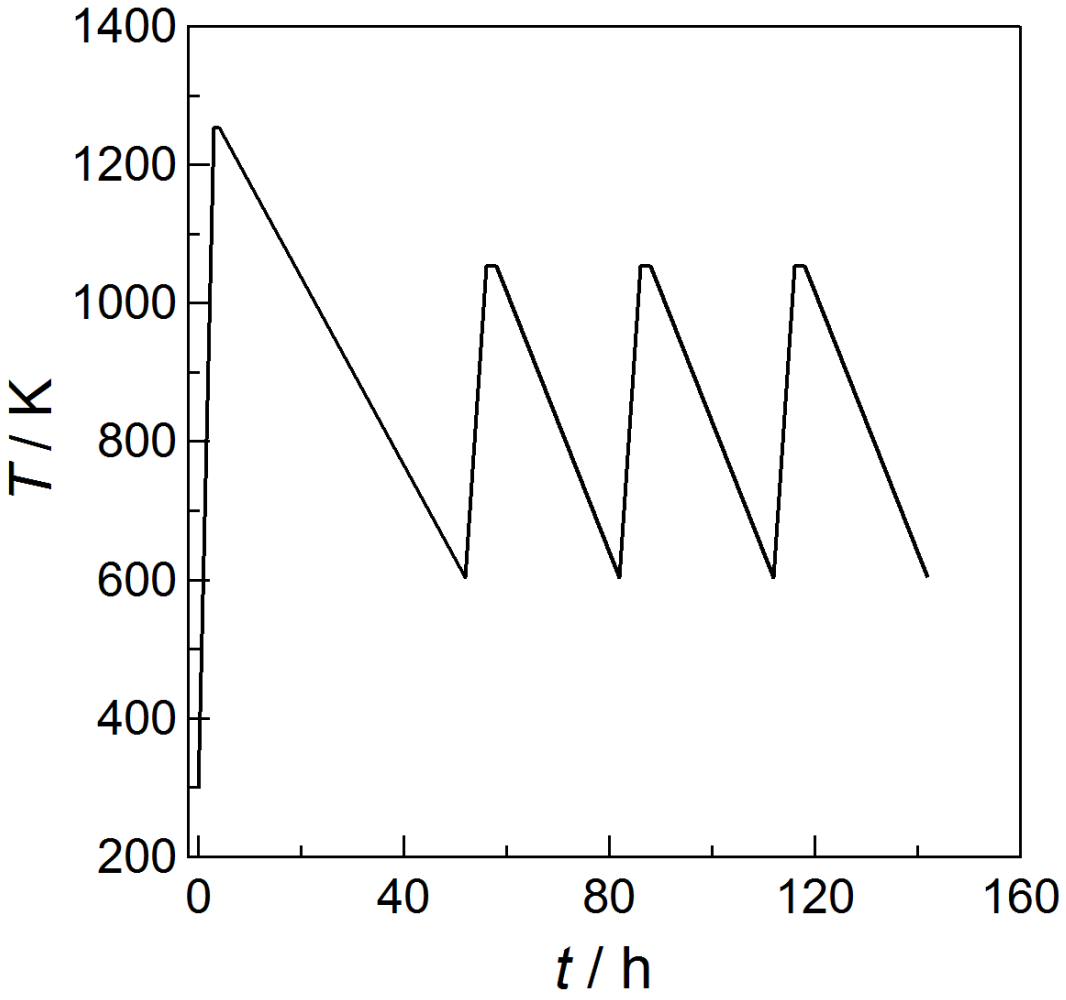

Figure 2.1. Annealing condition for polycrystalline iron substrate.

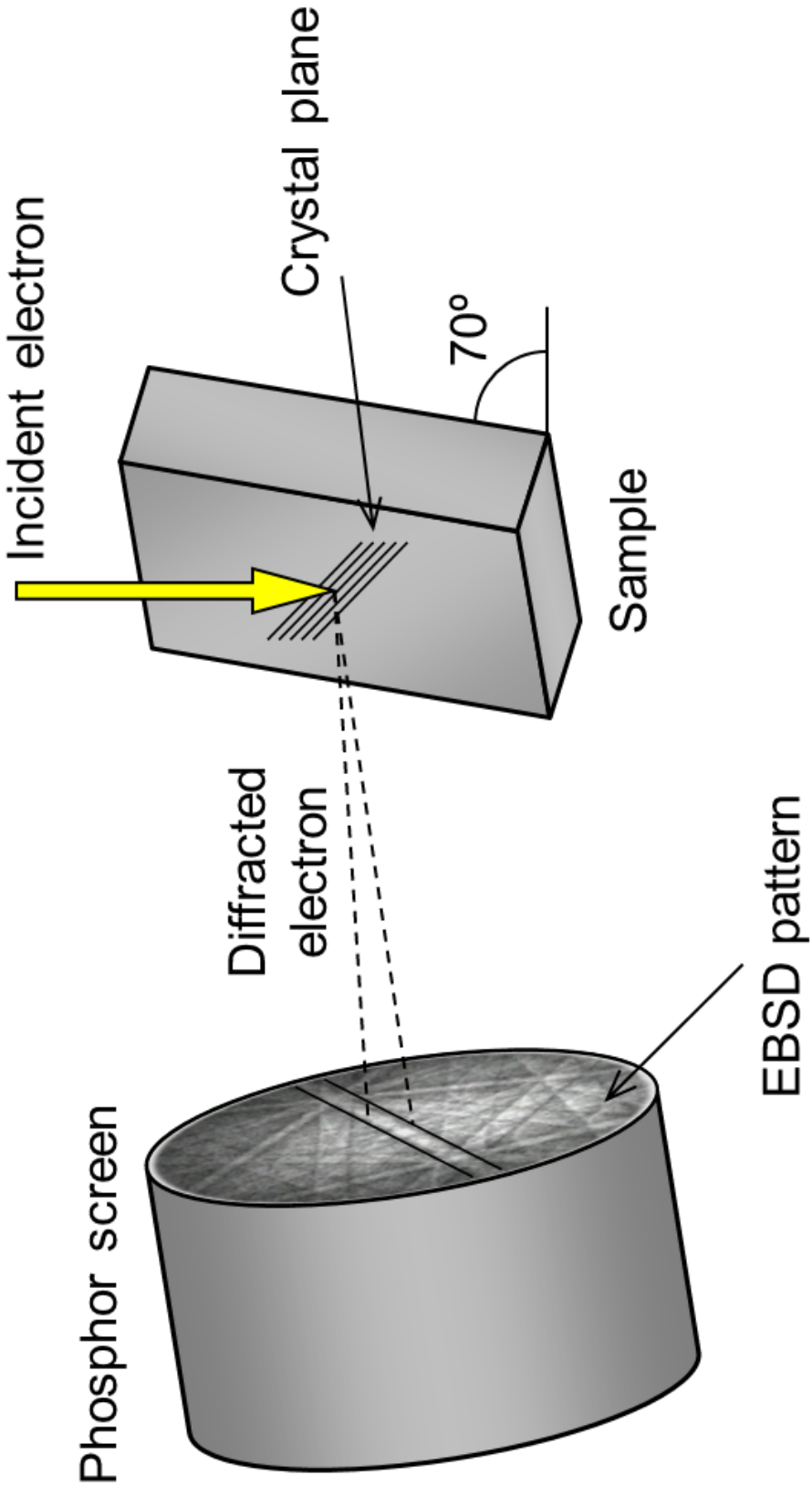

Figure 2.2. Projection of EBSD pattern (Kikuchi pattern) by incident electron beam.

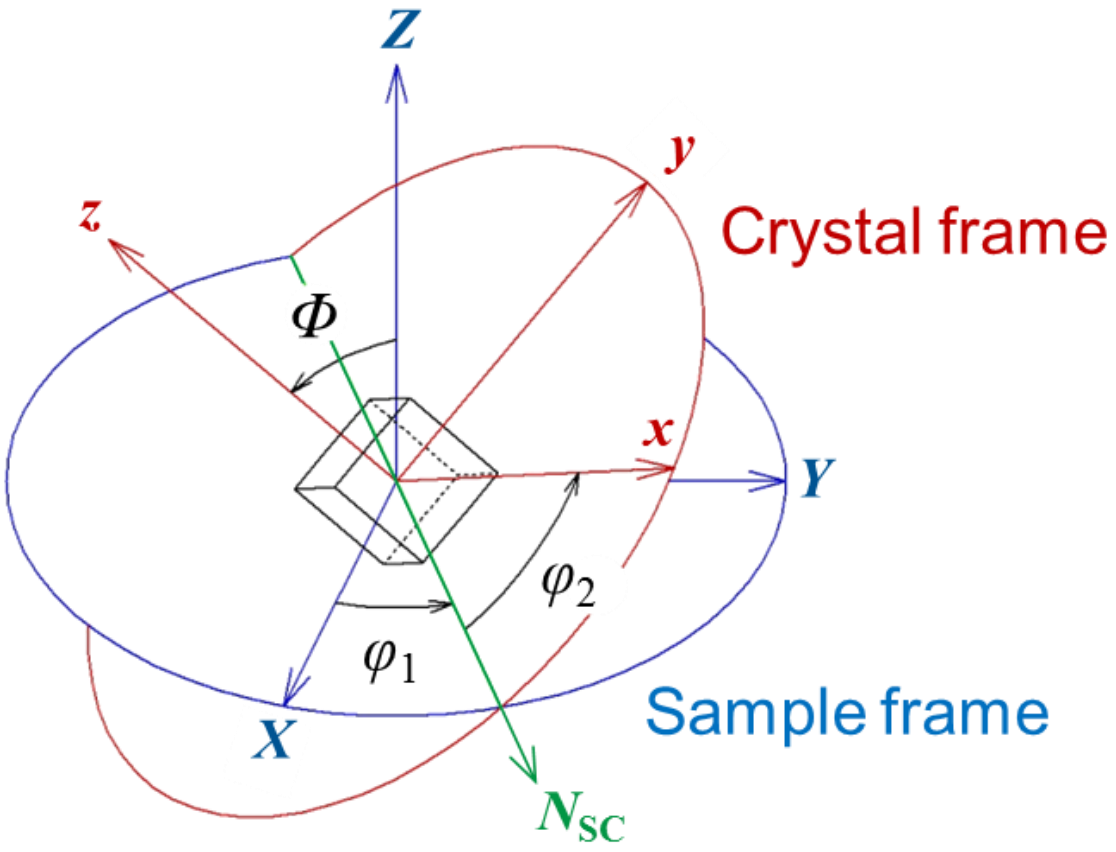

Figure 2.3. Description of crystallographic orientation by three Euler angles (φ_1、Φ、φ_2). The line of node N_{CS} is defined as the intersection of the *xy* and *XY* coordinate planes.

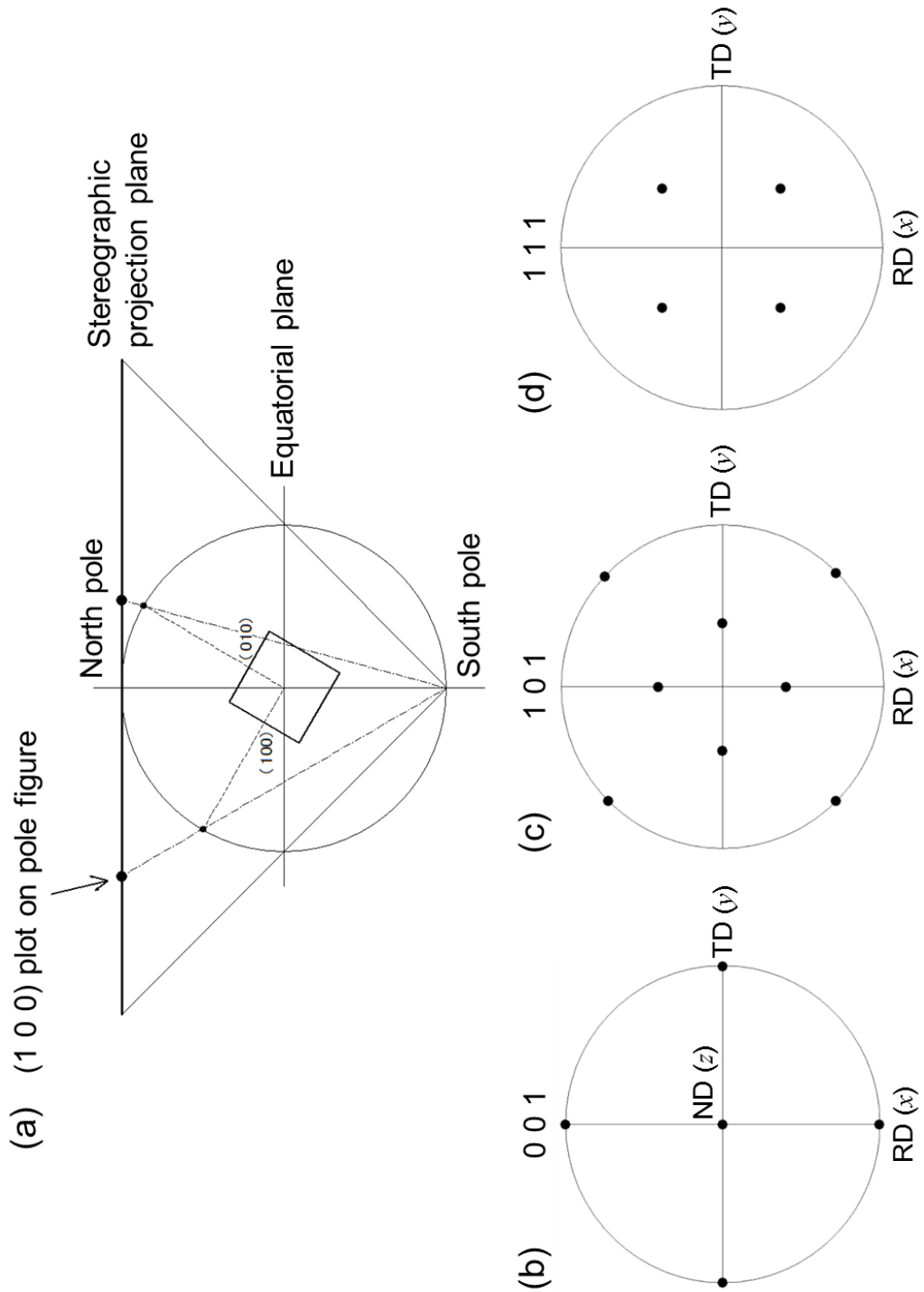

Figure 2.4. (a) Stereographic projection for the formation of the pole figure for a sample with cubic crystal symmetry; (b) {0 0 1}, (c) {1 0 1}, and (d) {1 1 1} pole figures for a sample that shows {0 0 1} plane.

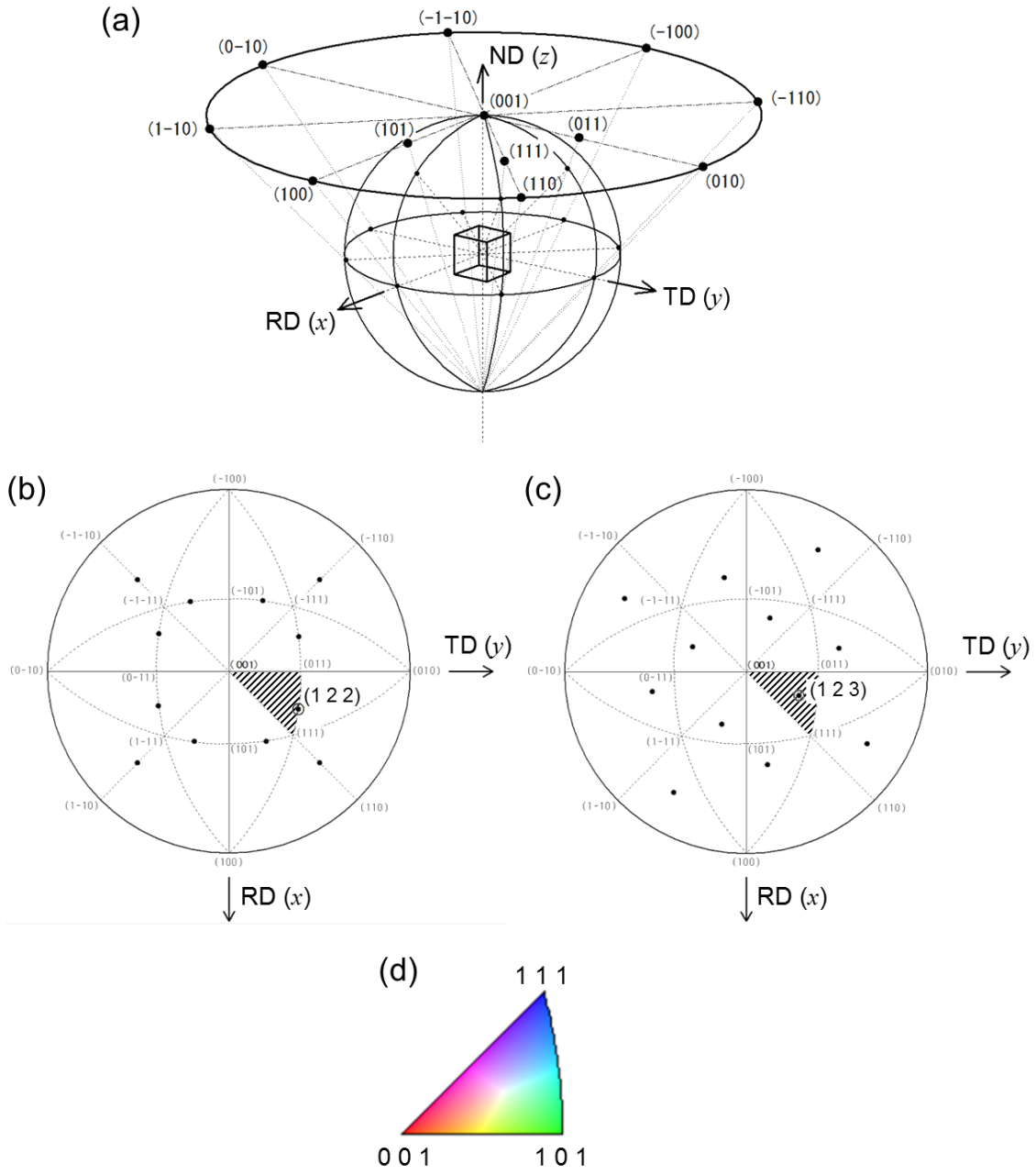

Figure 2.5. (a) Stereographic projection for the formation of an IPF of a sample ND; (b) {1 2 2} and (c) {1 2 3} planes are perpendicular to the sample ND; (d) IPF color-coded map of the unit triangle for a sample with cubic crystal symmetry.

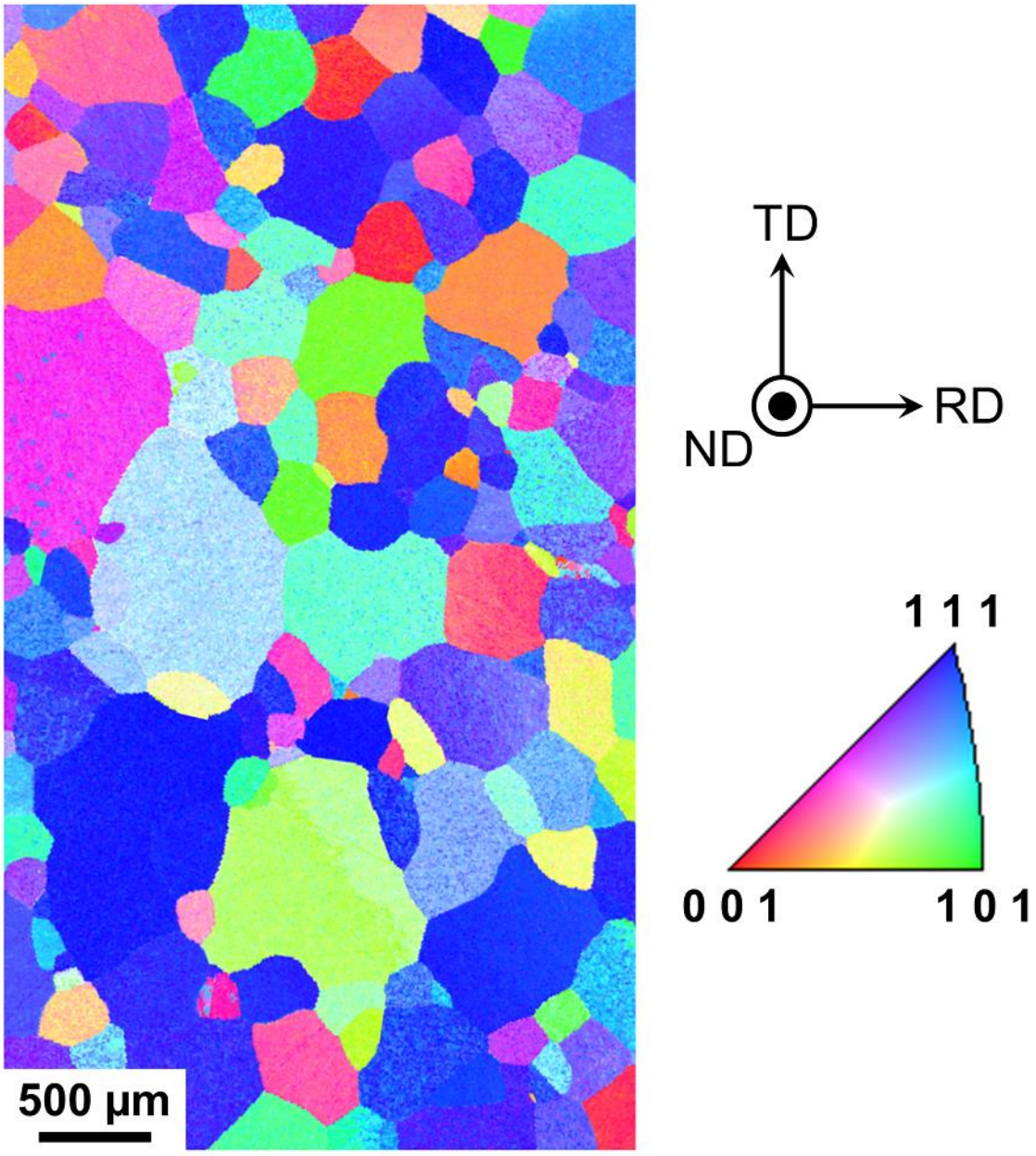

Figure 2.6. EBSD IPF map of a typical polycrystalline iron specimen.

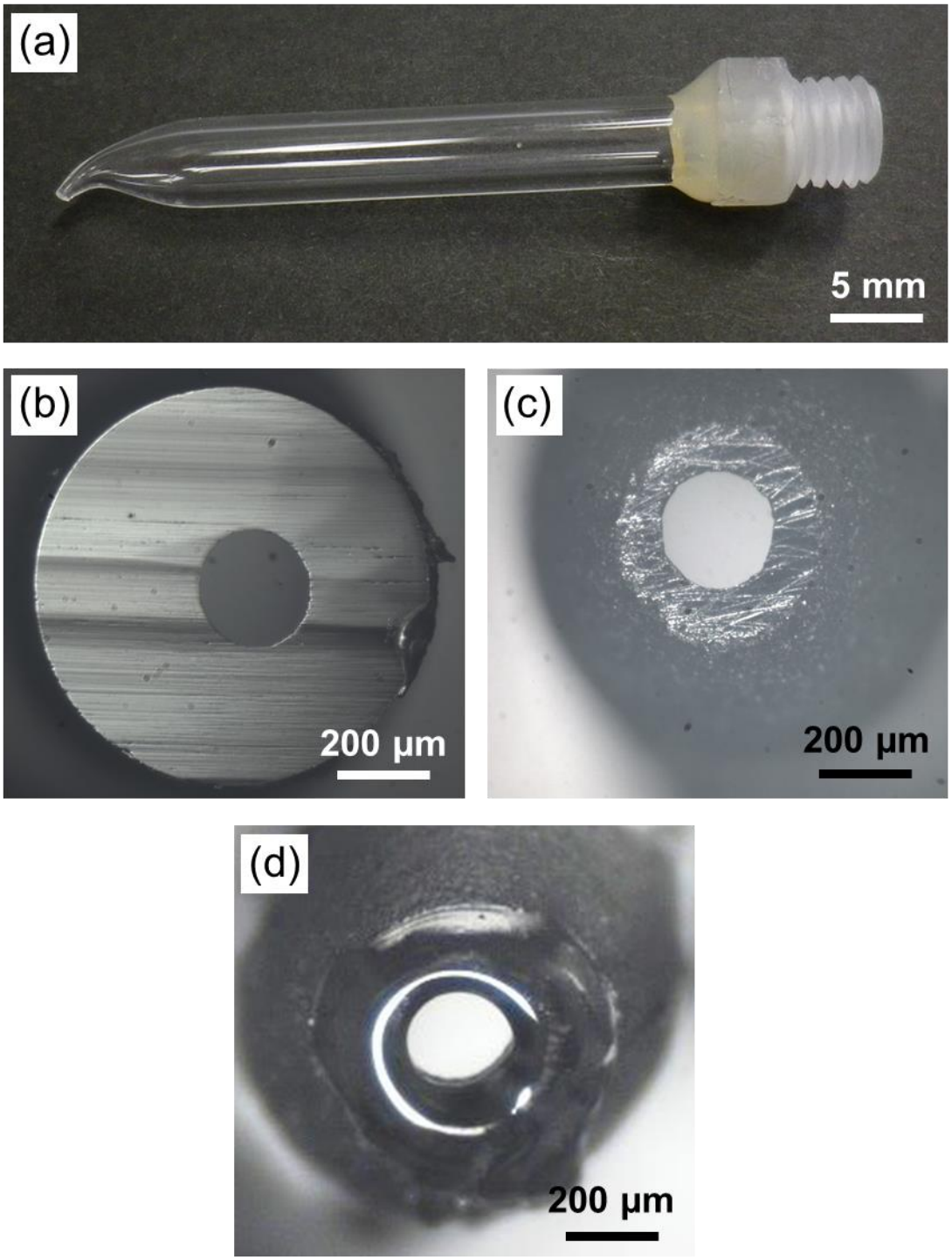

Figure 2.7. Optical micrographs of (a) total image, (b) ground, (c) feathered, and (d) glued tip of the glass capillary.

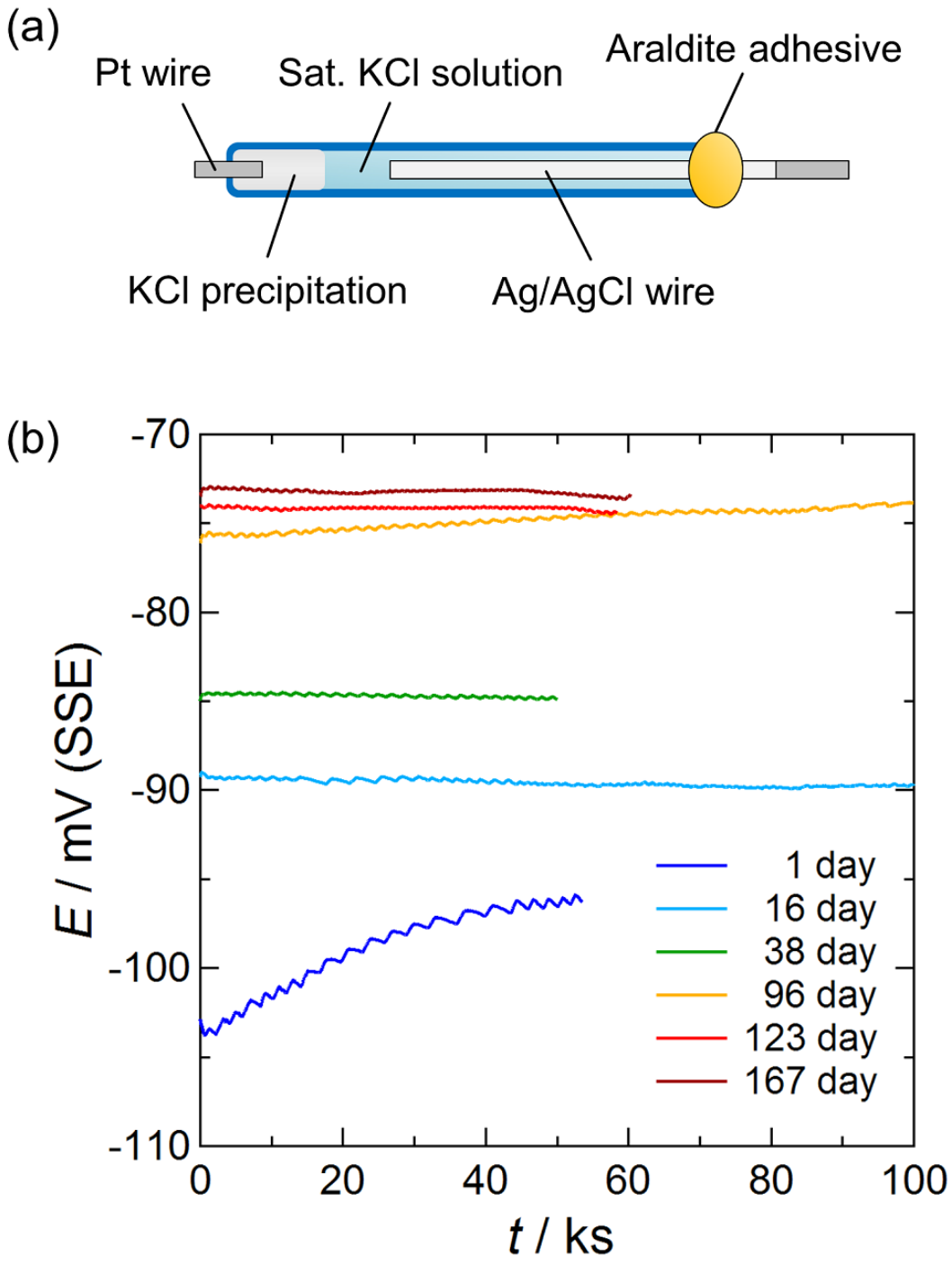

Figure 2.8. (a) Schematic illustration of a micro-Ag/AgCl reference electrode and (b) potential-time transients of the electrode against the commercial Ag/AgCl reference electrode; the potentials were measured on several different days after the micro-electrode was fabricated.

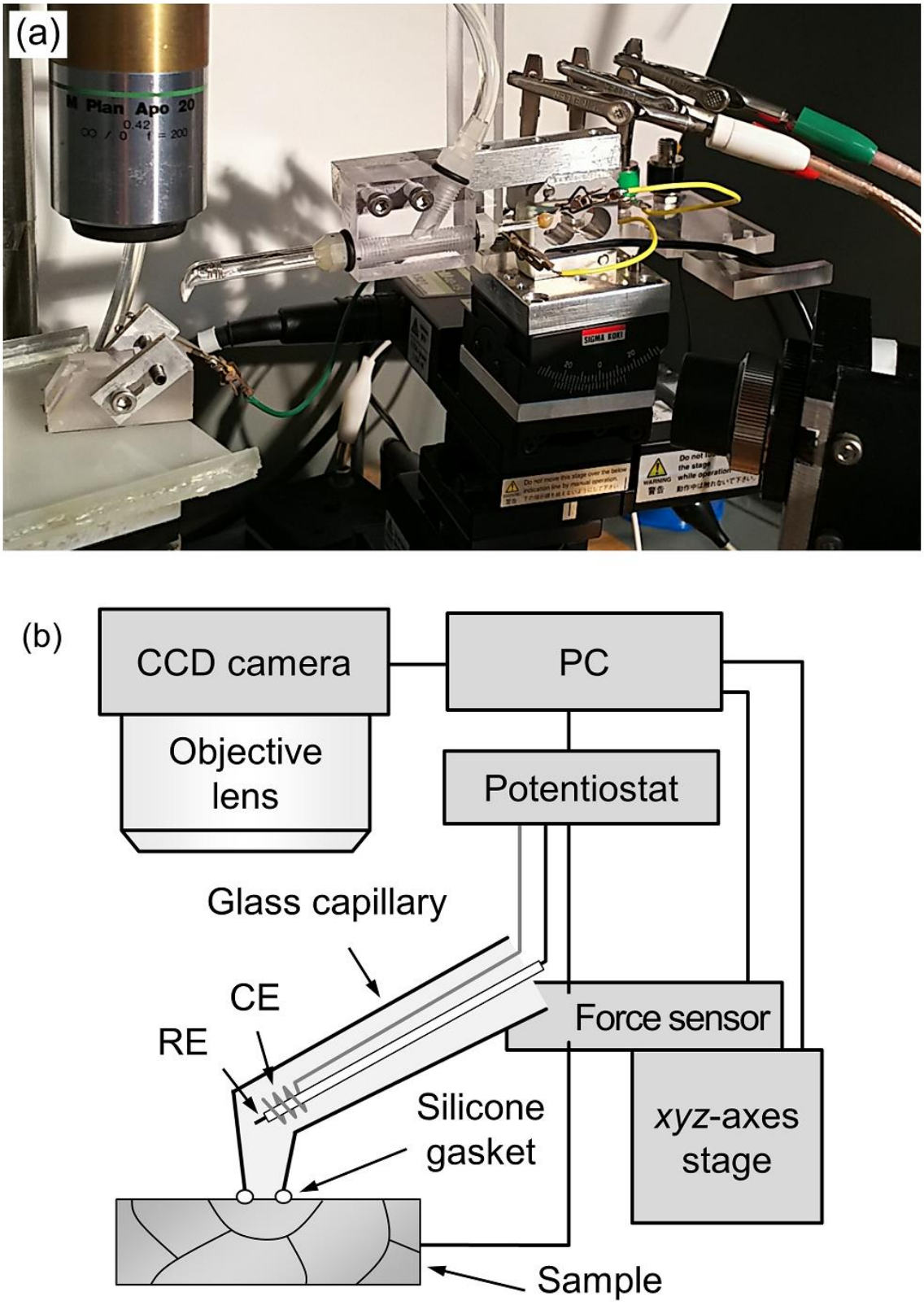

Figure 2.9. (a) Photograph and (b) schematic setup of the MCC.

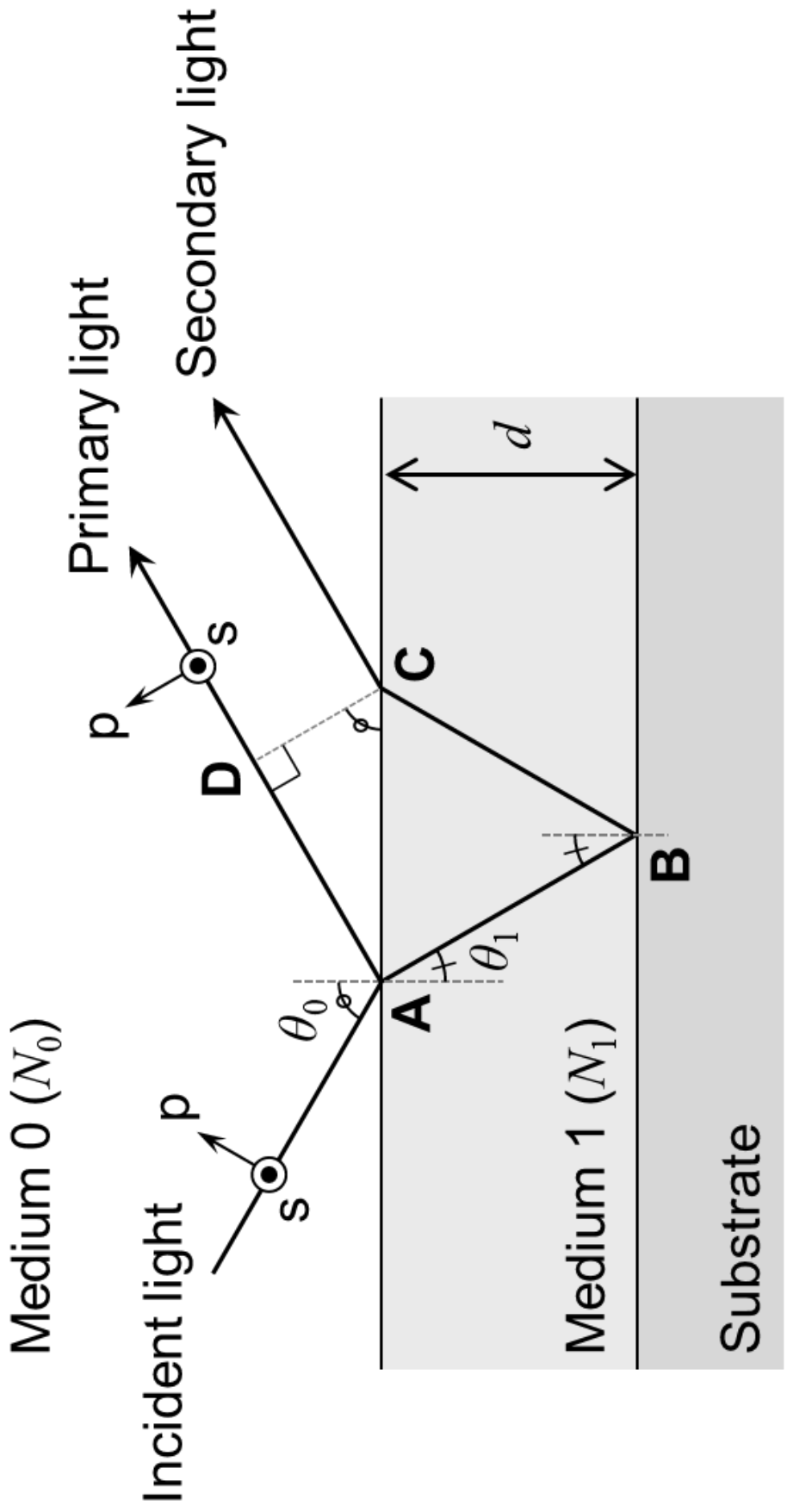

Figure 2.10. Optical interference caused by the thin film (Medium 1) on a substrate.

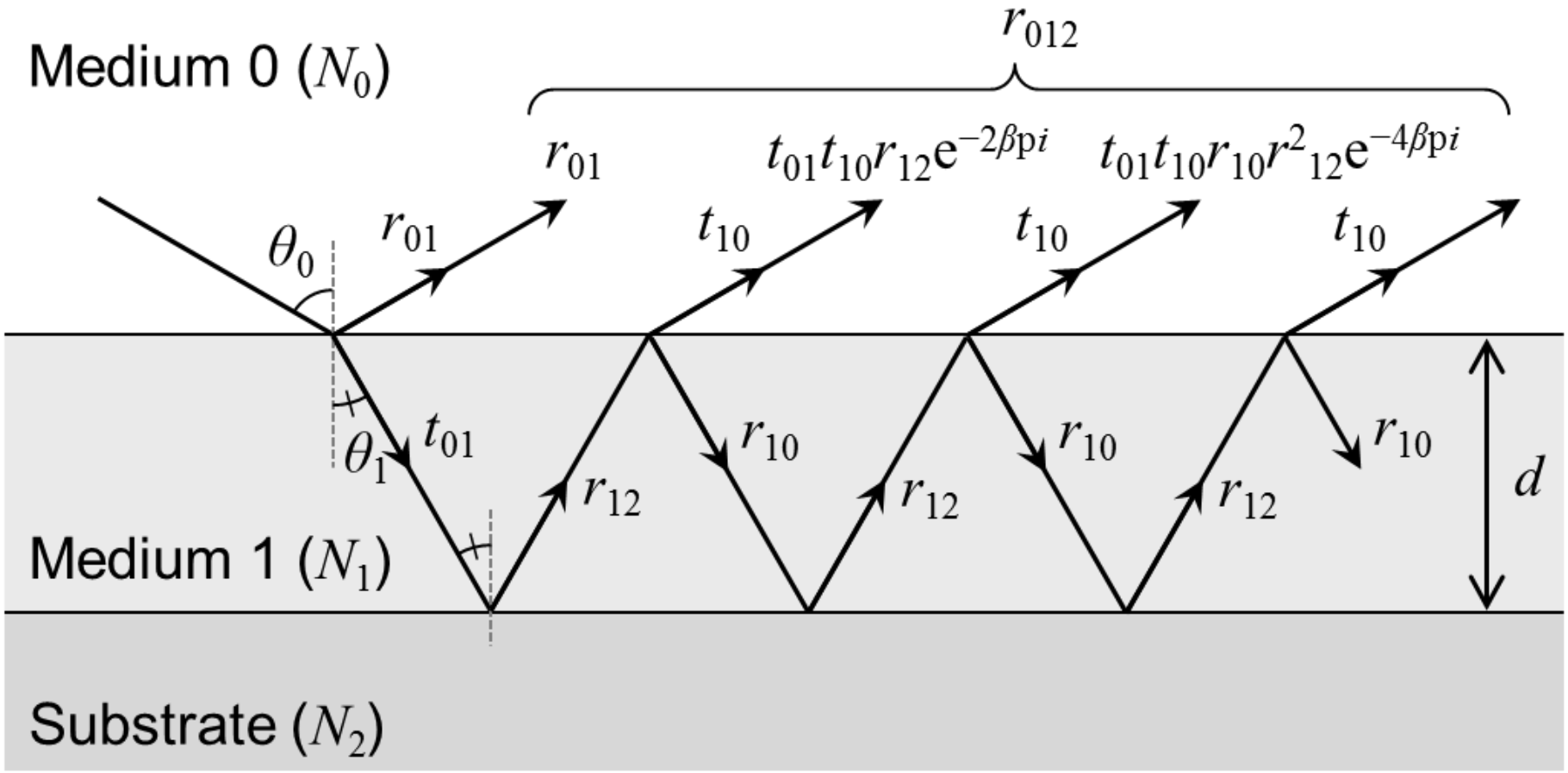

Figure 2.11. Optical interference model of the multiple reflections at the thin film (Medium 1)/substrate interface.

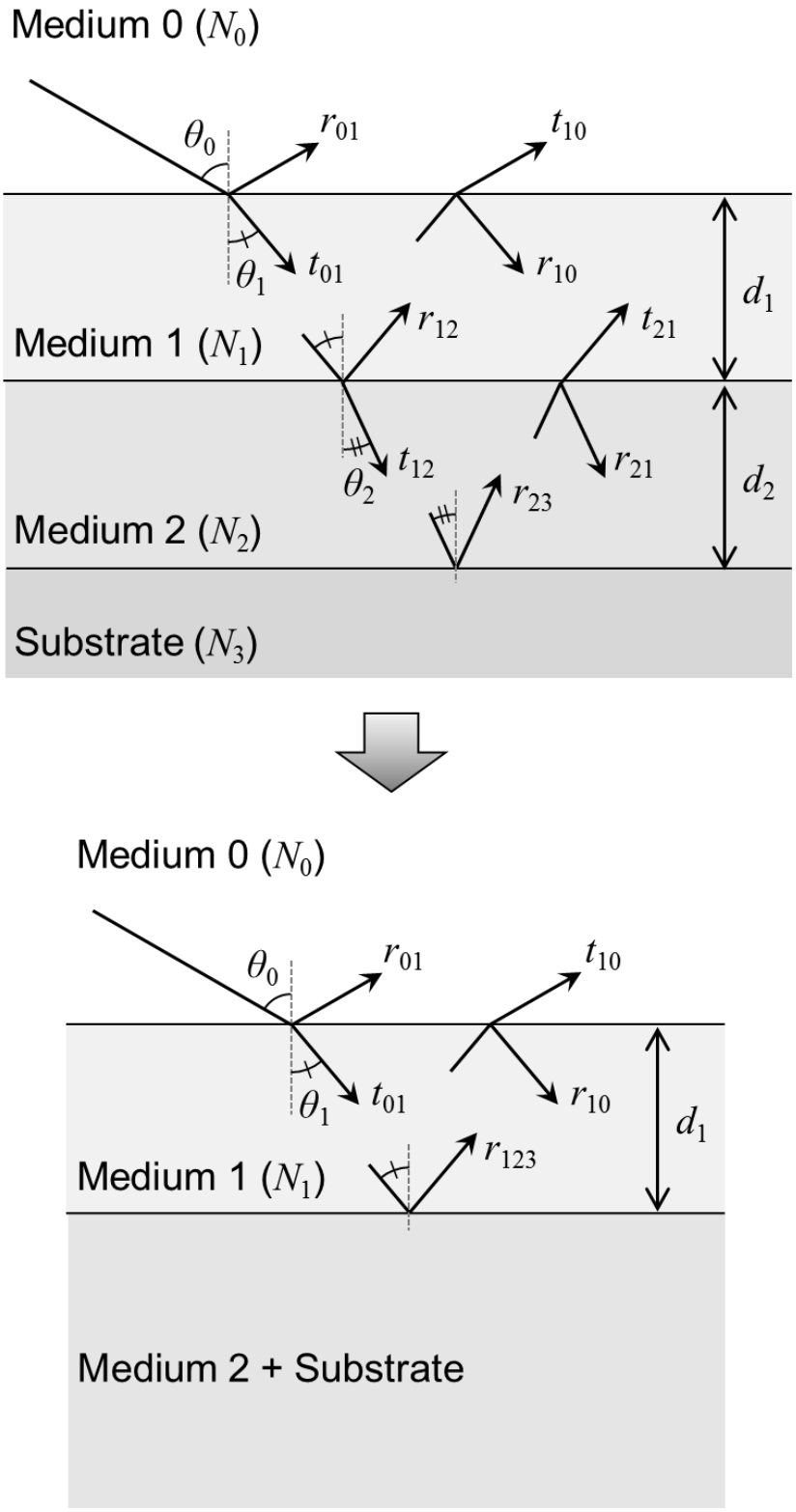

Figure 2.12. Concept of the calculation of optical interference caused by the bi-layered thin film on a substrate.

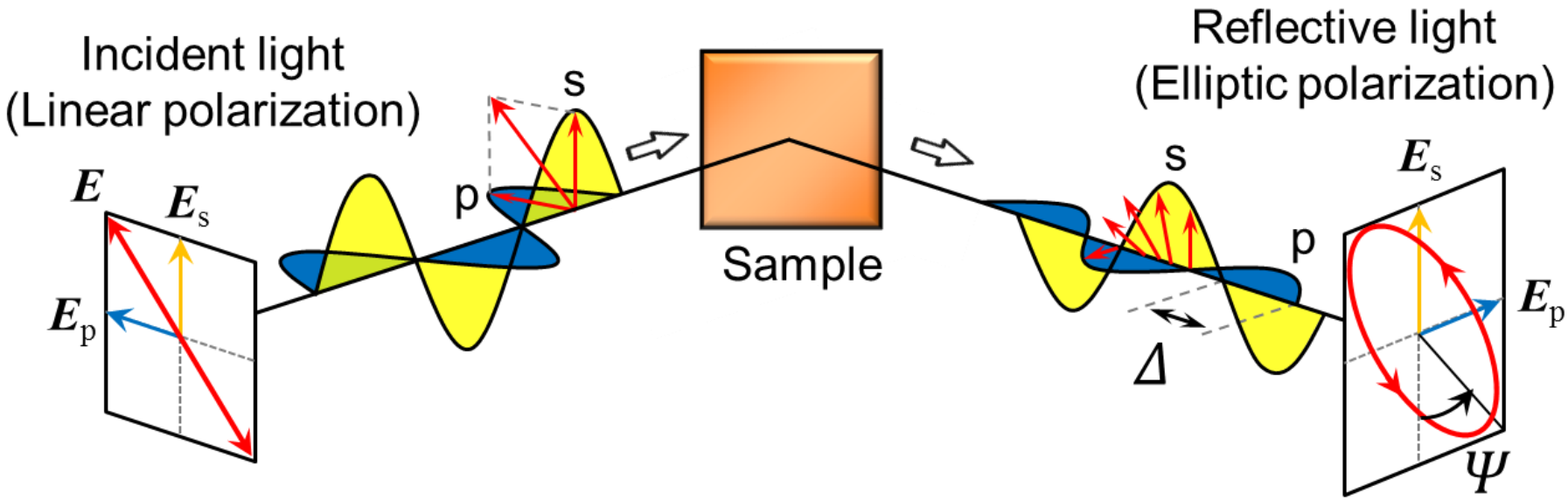

Figure 2.13. Schematic model of reflection ellipsometry; linear-polarized light turns to elliptic-polarized light by reflection on a sample surface because the amplitude and phase of p- and s-polarizations change differently.

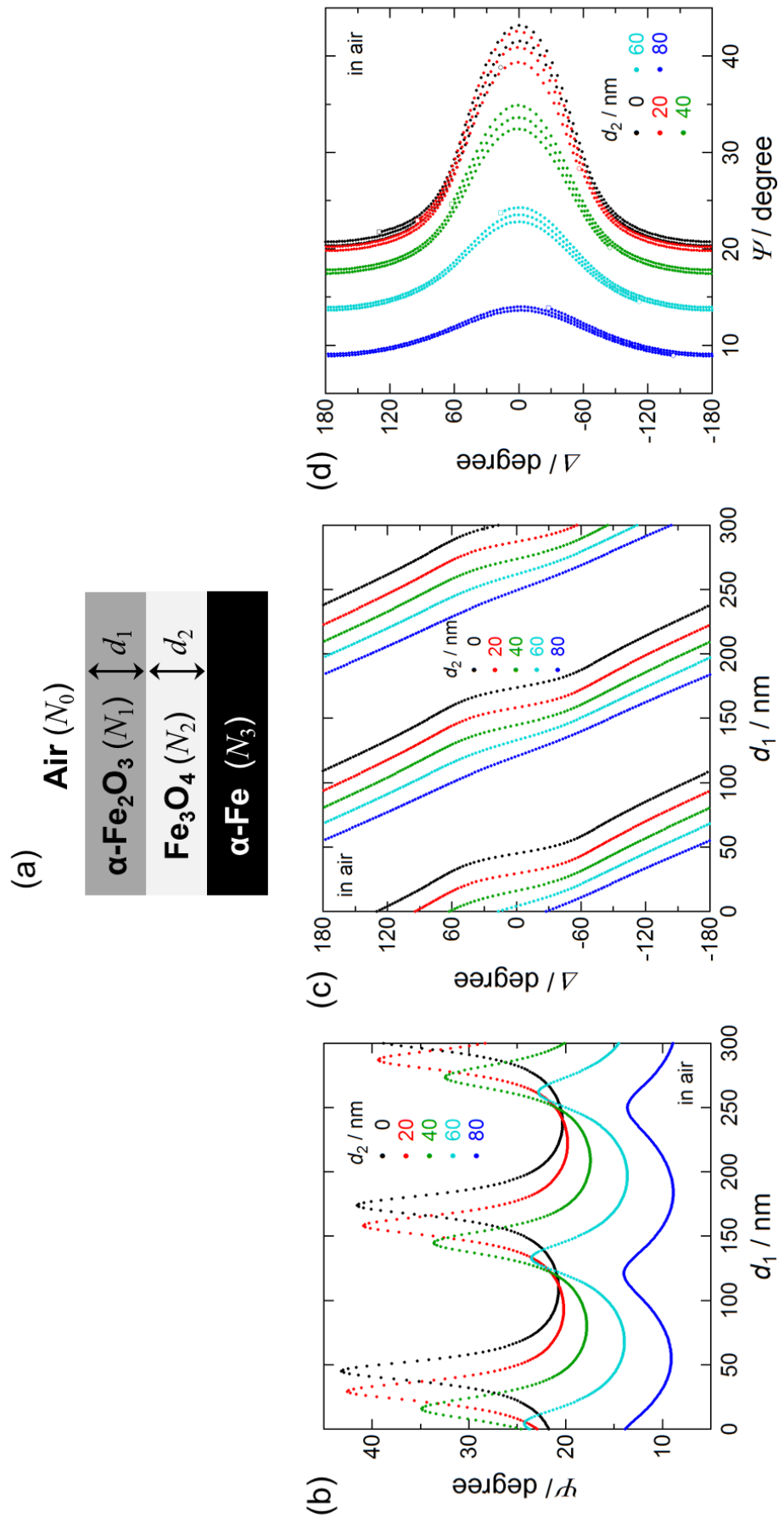

Figure 2.14. (a) Optical model used for the calculation of ideal values of Ψ and Δ; d_1 and d_2, thickness of outer α-Fe_2O_3 and inner Fe_3O_4 layers, respectively; (b–d) ideal curves of Ψ and Δ as a function of d_1 when d_2 is constant at 0, 20, 40, 60, and 80 nm, respectively—the dots in the ideal curves are plotted at 1-nm intervals: $\theta_0 = 70$ degrees, $\lambda = 636$ nm, $N_0 = 1.00$, $N_1 = 2.64 - 0.01i$, $N_2 = 2.28 - 0.45i$, and $N_3 = 2.87 - 3.36i$ were used for the calculation.

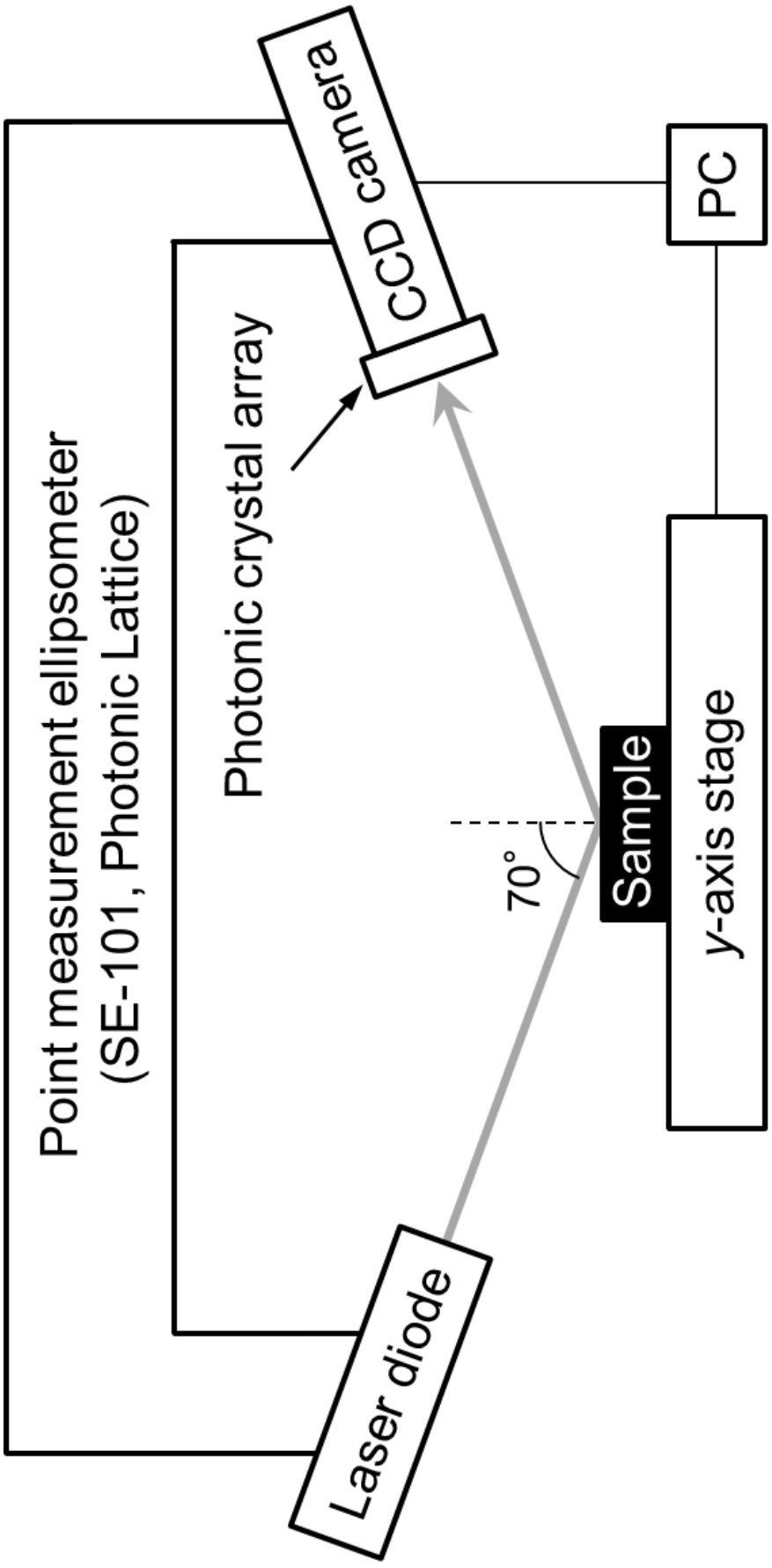

Figure 2.15. Schematic illustration of the 2D ellipsometer.

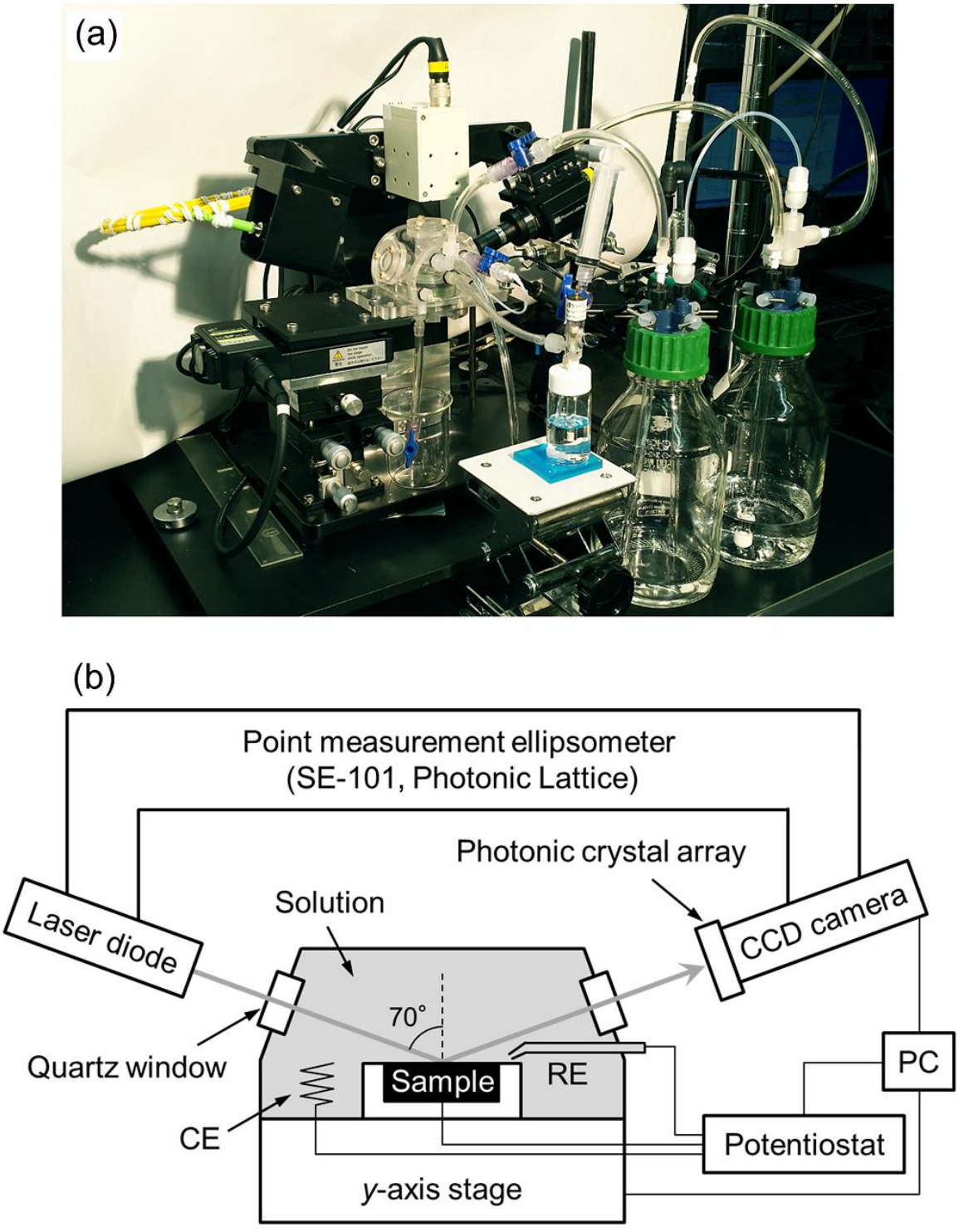

Figure 2.16. (a) Photograph and (b) schematic setup of the electrochemical cell designed for *in situ* 2D ellipsometry.

Chapter 3
Grain-dependent oxidation behavior in sulfuric acid measured by micro-capillary cell

3.1. Introduction

The polarization behavior of iron depends on the pH of the electrolyte solution [1,2]. Anodic currents in active and passive states increase with decreasing pH. In the passive state, the anodic current is suppressed by the formation of a passive oxide film and the steady state current increases with decreasing the solution pH due to the dissolution of iron ions into the solution through the passive film. The passive film thickness at steady state is a linear function of the applied potential. Ellipsometric measurement revealed that the structure of the passive film formed in acid solution was a bi-layered barrier film of inner Fe_3O_4 and outer γ-Fe_2O_3, and photoelectric potential measurements demonstrated the n-type semiconductive property of the passive oxide.

The orientation-dependent corrosion of iron in acid solution was observed through its dissolution rate (Table 1.4). The anisotropic dissolution of iron has been examined by means of several measurement methods by researchers and the tendencies of the dissolution rate have been clarified. Grain-dependent dissolution of polycrystalline iron was reported by Fushimi and Seo [3], who conducted SECM in pH 2.3 sulfate solution. In such an environment, it is expected that iron will also show orientation dependency in passivation behavior; however, there is no published research that investigated the orientation dependency of the passive film formed in acid solution, and the mechanism of grain-dependent passivation remains unclear. In order to elucidate the precise corrosion reaction that occurs on a polycrystalline iron surface, it is necessary to examine both the passivation behavior and the dissolution behavior of each grain on the polycrystalline substrate.

In this chapter, the grain-dependent oxidation behavior of iron single grains in sulfuric acid was investigated using an MCC method in order to reveal how the surface orientation determines passive film formation.

3.2. Experimental

3.2.1. Micro-electrochemical measurements

Micro-electrochemical measurements were carried out by using the MCC developed in section 2.2. In this section, three glass capillaries with different tip geometry were used for the MCC. Figure 3.1 presents optical images of the glass capillaries; their sizes are summarized in Table 3.1. The tips have different inner diameters and widths of silicone rubber. All potentials measured versus SSE were converted into potentials versus RHE. The inside of the capillary was filled with an electrolyte of 0.05 mol dm^{-3} H_2SO_4 aqueous solution (pH 1.3), deaerated by bubbling of pure Ar gas before measurement. Crystal grains for which crystallographic orientation could be approximated to {0 0 1}, {1 0 1}, and {1 1 1} planes within an Euler angle disparity of 10 degrees were used as sample electrodes.

Table 3.1. Sizes of capillary tips of MCCs; A_{MCC}, achieved electrode area.

No.	Inner diameter (μm)	Silicone gasket	A_{MCC} (cm^2)	Tip image
C1	93	thick and wide	6.8×10^{-5}	Fig. 3.1a
C2	70	thin and narrow	3.7×10^{-5}	Fig. 3.1b
C3	250	thin and narrow	5.1×10^{-4}	Fig. 3.1c

After E_{corr} measurement for 300 s, potentiodynamic polarization was performed from (E_{corr} − 0.1 V) to 1.9 V (RHE) at a potential sweep rate of 5 mV s^{-1} with the capillary C1 or C2. The morphology of the sample surface after potentiodynamic polarization was observed with a field-emission SEM (JSM-6500F, JEOL). On a fresh sample surface, potentiostatic polarization was carried out at 1.2 V (RHE) for 1 h with the capillary C3 and the current transient was recorded. Immediately after the potentiostatic polarization, EIS was performed at 1.2 V (RHE) with an ac voltage amplitude of ±10 mV in a frequency range of 10^5 to 10^{-2} Hz. Curve fitting of impedance spectrum was done by using a suitable equivalent electronic circuit (EEC) with analysis software (Echem Analyst 6.04, Gamry Instruments). Furthermore, after the potentiostatic polarization at 1.2 V (RHE), impedance measurements for MS analysis were conducted in a potential range from 1.2 to 0.5 V (RHE) with an ac voltage amplitude of ±10 mV at the frequency of 100 Hz. Separately, the sample polarized at 1.2 V (RHE) for 1 h was galvanostatically reduced at −6 μA cm^{-2} [4] and the potential transient of the sample electrode was recorded. All electrochemical measurements were conducted in an air-conditioned room at 295 K.

3.2.2. X-ray photoelectron spectroscopy

After potentiostatic polarization by the MCC with the capillary C3, the samples were immediately rinsed with ethanol and dried with clean air. The chemical state of the polarized

sample surface was studied by XPS. Photoelectron spectra were recorded using a JPS-9200 photoelectron spectrometer (JEOL) with Al Kα radiation operating at 100 W (10 kV, 10 mA). This photoelectron spectrometer can analyze a micro-region by adjusting the angle-limiting aperture and the field view aperture, which select photoelectrons captured into the electrostatic lens and the analyzer, instead of focusing an X-ray. Here, we confined the detection area of photoelectrons to 200 μm in a diameter by adjusting the two apertures to analyze the small sample area polarized with the MCC. The acquisition of each spectrum was repeated 100 times due to the small photoelectron intensity obtained from the small detection area. In this study, no sputtering to remove contamination on the surface was carried out to avoid reduction of oxidized iron species [5]. Photoelectron spectra were analyzed by using SpecSurf software (JEOL). The C 1s peak from contaminant carbon at 285.1 eV was used as a reference for charge correction [6]. After background subtraction using Shirley's method [7], the spectra were separated into different oxidation states by deconvolution.

3.3. Results

3.3.1. Corrosion potential and dynamic polarization

Since the diameter of the MCCs was smaller than the grains on the sample, a micro-electrode could be set on a single grain. Just after the installation of the MCC, the sample surface showed a relatively noble rest potential; however, it shifted immediately to a steady state value of E_{corr} (Fig. 3.2), suggesting that a native oxide film that had formed on the sample surface was removed due to the acidity of the electrolyte.

Figure 3.3 shows dynamic polarization curves measured on the iron {0 0 1}, {1 0 1}, and {1 1 1} grains using the capillary C1. The polarization curves show active, passive, and trans-passive states of iron. All samples show similar E_{corr} values of ca. −0.22 V (RHE), though this is more positive than previous results [8] obtained in a sufficiently deaerated solution using an ordinary electrochemical cell. The obscure difference and the positive shift of E_{corr} are likely due to contamination of oxygen dissolved from the tip of the glass capillary before the installation of the MCC. Compared with ordinary macro-cells, an MCC is sensitive to contamination of the solution because of its small volume. Regardless of the similar E_{corr} values, an anodic current flowing in the active state from E_{corr} to ca. 0.76 V is due to active dissolution and was slightly dependent on the surface crystallographic orientation. The electric charge q_a consumed in the active state was in the order of {1 1 1} > {1 0 1} > {0 0 1} grains (Table 3.2). Subsequently, a small current flowed on each grain in the passive state from ca. 0.76 to 1.46 V (RHE), due to passivation of the surface. The current included fluctuations on the {1 0 1} and {1 1 1} grains but no fluctuation on the {0 0 1} grain. The electric charge q_p consumed in the passive state was also in the order of {1 1 1} > {1 0 1} > {0 0 1} grains associated with the current fluctuations (Table

Table 3.2. Experimental parameters of potentiodynamic polarization at 5 mV s^{-1} in 0.05 mol dm^{-3} sulfuric acid with the capillary C1; q_a and q_p, charge density consumed in active and passive states, respectively.

Surface	q_a (C cm^{-2})	q_p (10^{-3} C cm^{-2})
{0 0 1}	6.8 ± 0.86	15 ± 1.7
{1 1 1}	10 ± 0.29	53 ± 34
{1 0 1}	8.8 ± 0.70	34 ± 17

3.2). After potentiostatic polarization reached 1.1 V (RHE), a number of facets over the whole electrode surface in the active state were observed with SEM (Fig. 3.4), depending on the substrate orientation. The {0 0 1} grain showed a flat surface and the {1 0 1} and {1 1 1} grains had rough surfaces composed of a number of facets with heights of several tens to hundreds of nanometers, depending on crystallographic orientation. These surface morphologies indicate that active dissolution of iron is selectively advanced in the direction of <0 0 1>.

Figure 3.5 shows polarization curves of the surface of a bi-grain including {0 0 1} and {1 1 1} grains, where a_{111} is the relative area of the {1 1 1} grain, defined as the ratio of an area A_{111} of the {1 1 1} grain part to the entire electrode area in the MCC as follows:

$$a_{111} = A_{111} / A_{MCC}. \quad (3.1)$$

It is clear that polarization curves of bi-grains were approximately the same and between the curves of two single grains. Figure 3.6 shows optical and SEM images of the surface of the bi-grain electrode after potentiodynamic polarization. The dark part of the bi-grain electrode in optical images (Fig. 3.6a) increases with increasing a_{111} due to a number of facets forming on the {1 1 1} grain part (Fig. 3.6b). In a high magnification SEM image of the bi-grain electrode (Fig. 3.7), the vicinity of the grain boundary between the {0 0 1}/{1 1 1} grains shows a relatively smooth surface. Figure 3.8 plots q_a, q_p, and L_{GB}, the length of grain boundary in bi-grain electrodes, as a function of a_{111}. The value of q_a shows a linear relation with a_{111}, while the relation between q_p and a_{111} shows a concave curve and L_{GB} displays a convex curve against a_{111}, indicating that the reactivity of the bi-grain electrode is suppressed due to the existence of the grain boundary in the electrode.

In contrast to the polarization behavior described above, current fluctuations in a passive state were not observed for the {1 0 1} and {1 1 1} grains when the capillary C2 was used to perform potentiodynamic polarization (Fig. 3.9). A very stable passivity-maintaining current of ca. 10^{-4} A cm^{-2} flowed in the passive state for all grains, although the shape of the curve resembles those in Figs. 3.3 and 3.5. In the active state, the steady state current density observed in Fig. 3.9 is about twice of that in Figs. 3.3 and 3.5, and q_a is quite similar among the three grains (Table 3.3), with similar currents flowing in the trans-passive state. The values of q_p for the {1 0 1} and {1 1 1} grains are smaller than half of what was measured by the capillary C1, and the standard deviations become significantly small. Furthermore, the magnitude order of q_p changed to {0 0 1}

Table 3.3. Experimental parameters of potentiodynamic polarization at 5 mV s^{-1} in 0.05 mol dm^{-3} sulfuric acid with the capillary C2; q_a and q_p, charge density consumed in active and passive state, respectively.

Surface	q_a (C cm^{-2})	q_p (10^{-3} C cm^{-2})
{0 0 1}	17 ± 1.2	21 ± 2.1
{1 1 1}	17 ± 1.1	18 ± 1.3
{1 0 1}	17 ± 1.5	16 ± 1.4

> {1 1 1} > {1 0 1}. After potentiodynamic polarization using the capillary C1, the morphology of the polarized sample surface became inhomogeneous (Figs. 3.10a and 3.10c). The middle part of the sample surface showed a number of facets that appear as dark parts in an optical image; however, the outside of the sample surface, which was laid under the silicone gasket during polarization, showed no facets. On the contrary, after the polarization using the capillary C2, a number of facets were formed over the entire electrode surface and the morphology of the surface was homogeneous (Figs. 3.10b and 3.10d).

It is obvious that the transients of anodic currents depend on the geometry of the MCC. Localized concentration of dissolved iron species at the solution/electrode interface induces precipitation of iron oxides or iron hydroxides, and acidification of the solution simultaneously, resulting in current oscillations in active to passive transition [9]. In this sense, it is considered that the thick and wide silicone gasket rubber of the capillary C1 makes a tiny space between the rubber and the sample surface in the MCC. Diffusion of ferrous ions generated at the sample surface in an active state to bulk electrolyte is limited in the tiny space and the ions are highly concentrated. This results in a decrease in local pH due to hydrolysis by the formation of iron hydroxides, leading the destabilization of passivity. A smaller steady current in the active state with the capillary C1 suggests that the diffusion of dissolved species is partially limited. The current fluctuation observed in the passive state with the capillary C1 is probably related to a roughness of the specimen surface under the silicone gasket. The concentration gradient of ferrous ions on a rough surface destabilizes passivity rather than that on a smooth surface. Thus, it is also thought that a relatively smooth surface in the vicinity of a grain boundary stabilizes the passivity of the bi-grain electrode. In any cases, corrosion behavior in both active and passive states on bi-grain electrodes seems to be explained by that on single grains. These results indicate that the geometry of an MCC greatly affects electrochemical behavior of local surfaces.

During polarization in acidic media, the surface condition of an electrode is altered chemically and electrochemically. The electrochemical behavior of the electrode surface significantly suffers from the previous polarization under the condition of potentiodynamic polarization. In this sense, the iron species generated in an active state affect the electrode behavior in a passive state. The MCC is much more susceptible than macro-electrochemical cells to dissolved species due to its small solution volume. Although there are some qualitative grain

dependencies on polarization curves such as current fluctuation in the passive state, it is thought that the potentiodynamic polarization curve obtained by using the MCC is less suitable for quantitative investigation of grain-dependent passivation.

3.3.2. Potentiostatic polarization

The potentiostatic polarization was conducted by using the capillary C3 that showed no current fluctuation in the passive state on the iron {1 1 1} grain during potentiodynamic polarization. Figure 3.11 shows a double logarithmic plot for current-time transients of the three iron grains during potentiostatic polarization at 1.2 V (RHE) in 0.05 mol dm^{-3} sulfuric acid. In the initial period of polarization, an anodic current of ca. 0.2 A cm^{-2} that is independent of the substrate orientation flowed due to charging of the double layer and subsequent active dissolution of the iron surface. The independence of the charging current for all grains indicates that the single grain samples had the same actual electrode area. The faradaic current started to decrease dramatically in a short period t_{pa} of a few seconds, corresponding to the commencement of oxide formation on the surface. The sequence of t_{pa} on the three grains is in the order of {1 1 1} > {1 0 1} > {0 0 1}. This order is the same as that of the surface atom density ρ_{surf} (Table 1.2). The total electric charge density q_t consumed during the polarization for 1 h depended on the orientation associated with t_p (Table 3.4). The values of q_t are quite small compared with the charge density of ca. 17 C cm^{-2} consumed in an active state under potentiodynamic polarization at 5 mV s^{-1} (Fig. 3.9), suggesting that the amount of dissolved species in the active state under potentiostatic polarization is very small. After polarization for ca. 10 s, the current decreased exponentially against polarization time with a slope ($-\mathrm{d}\log j / \mathrm{d}\log t$) of ca. 0.65. The decrease in current was caused by the formation of an insulating oxide on the substrate. However, it competes with oxide film dissolution and/or substrate dissolution through the film [10] since the slope is not unity like the film formation in a high field mechanism in which the dissolution is negligible [11]. While the {1 0 1} grain maintained a constant slope until 1 h, the slopes on the {0 0 1} and {1 1 1} grains gradually decreased after 500 s. The slope on the {0 0 1} grain became almost zero after 3000 s. Therefore, the current density j_f at 1 h was strongly dependent on the substrate orientation (Table 3.4), although the values of j_f are in the order of {0 0 1} > {1 1 1} > {1 0 1} grains, which is a different sequence from t_p. This suggests that the three grains exhibited different

Table 3.4. Experimental parameters of potentiostatic polarization at 1.2 V (RHE) in 0.05 mol dm^{-3} sulfuric acid; t_{pa}, passivating time; q_t, total charge density consumed for 1 h; j_f, current density at 1 h.

Surface	t_{pa} (s)	q_t (C cm^{-2})	j_f (10^{-6} A cm^{-2})
{0 0 1}	3.7 ± 1.5	0.54 ± 0.33	2.9 ± 0.50
{1 1 1}	5.2 ± 1.1	1.2 ± 0.11	1.9 ± 0.21
{1 0 1}	4.6 ± 1.2	0.85 ± 0.38	1.3 ± 0.12

activities in the initial formation and the following aging of the oxide film.

3.3.3. Electrochemical impedance spectroscopy

Under the condition of the potentiostatic polarization for 1 h in 0.05 mol dm^{-3} sulfuric acid, about 5% of the j_f decreased during the last 500 s. It was considered that the formation and dissolution of the oxide film were almost in a steady state during this period, and that the film property was not changed significantly. Although the measurement period of 460 s was necessary to take an impedance spectrum, immediately after the potentiostatic polarization with the MCC, EIS with the MCC was carried out on single grains to investigate the electric property of the electrode surface polarized at 1.2 V (RHE). In a Bode plot (Fig. 3.12a), the three grains show almost the same shapes in the whole range of the frequency *f*. The phase shift θ determined by the capacity reactance of the oxide film shows a single peak at ca. 50 Hz. However, the impedance magnitude $|Z|$ depends on the grain orientation at frequencies lower than 0.1 Hz, and $|Z|$ on the {1 0 1} grain is the largest among the three grains. In a Nyquist plot (Fig. 3.12b), which plots the imaginary part of impedance Z_{Im} as a function of the real part of impedance Z_{Re}, a single capacitive semicircle was observed for all grains. The diameter of the semicircle significantly depends on the substrate orientation and becomes in the order of {1 0 1} > {1 1 1} > {0 0 1} grains. Since no other semicircles are observed in the higher frequency region in the Nyquist plot, the electrode process can be described by an EEC with a single time constant. Figure 3.13 shows a so-called Randles type EEC representing an electrode interface where R_{el} and R_{ct} are electrolyte resistance and charge transfer resistance, respectively, and CPE is a constant phase element. Since the impedance spectra were measured at the film formation potential, R_{ct} includes ionic and electronic resistances corresponding to the film formation and dissolution. The CPE can be substituted with the interfacial capacitance *C* as follows [12]:

$$C = Q^{1/p}\left(\frac{1}{R_{el}} + \frac{1}{R_{ct}}\right)^{(p-1)/p}, \tag{3.2}$$

where *Q* and *p* are the CPE constant and coefficient, respectively. The values of R_{ct} and *C* obtained by curve fitting of the impedance spectra with the EEC are summarized in Table 3.5. The grain dependency on R_{ct} is remarkable, becoming greater in the order of {1 0 1} > {1 1 1} > {0 0 1}, and the {1 0 1} grain shows about a 2.5-times larger value of R_{ct} than that of the {0 0 1} grain. However, the values of R_{ct} are less than half of that (210 kΩ cm^2) of a passive film formed on iron in neutral borate solution [13]. It is thought that the lower solution pH gives greater reactivity for a charge transfer reaction such as dissolution of an oxide film and substrate iron through the film. On the other hand, the values of *C* for the three grains are similar. Since the electrode surface (Fig. 3.14) after an EIS measurement following potentiostatic polarization shows no facets that observed after potentiodynamic polarization (Fig. 3.4), actual electrode area during the EIS measurement is similar among the three grains. It is also considered that the

Table 3.5. Experimental parameters obtained from EIS. R_{ct}, charge transfer resistnce; C, interfacial capacitance; E_{fb}, flat band potential; N_D, donor density calculated by MS equation assuming $\varepsilon = 40$ [13].

Surface	R_{ct} ($10^3\ \Omega\ cm^2$)	C (10^{-6} F cm^{-2})	E_{fb} (V (RHE))	N_D (10^{20} cm^{-3})
{0 0 1}	43 ± 6.6	12 ± 0.41	0.46	5.3
{1 1 1}	69 ± 6.2	11 ± 0.26	0.49	4.7
{1 0 1}	110 ± 11	11 ± 0.60	0.48	5.1

thickness of the oxide film formed on each grain was almost constant.

The MS equation for an n-type semiconductor is [14,15]

$$C_{SC}^{-2} = \left(\frac{2}{eN_D\varepsilon\varepsilon_0}\right)\left(E - E_{fb} - \frac{k_B T}{e}\right), \tag{3.3}$$

where C_{SC} is the space charge layer capacitance, e is the electron charge, N_D is the donor density, ε is the dielectric constant of the semiconductor, ε_0 is the permittivity in vacuum, E_{fb} is the flat band potential, and k_B is the Boltzmann constant. The value of C_{SC} is derived from C and the Helmholtz layer capacitance C_H [16],

$$C = \left(\frac{1}{C_{SC}} + \frac{1}{C_H}\right)^{-1}. \tag{3.4}$$

The values of C_H of 2.3–2.5 mF cm^{-2} were reported for iron electrode in sulfuric acid [17,18]. Assuming C_H = 2.3 mF cm^{-2}, C_{SC} became similar to C as measured within the difference of less than 1%. Thus, C as measured can be regarded as C_{SC} in this study.

It is well known that an oxide film formed on an iron surface displays an n-type semiconductive property [19,20]. Azumi et al. reported that the values of E_{fb} and N_D of passive films formed on iron in pH 6.5 borate or phosphate solutions at 1.2 V (RHE) were ca. 0.5 V (RHE) and 6–10 × 10^{20} cm^{-3}, respectively [19]. MS analysis with the MCC was conducted for the passive oxide film formed on the iron single grains. Figure 3.15a shows MS plots of {0 0 1}, {1 0 1}, and {1 1 1} grains polarized at 1.2 V (RHE) for 1 h in 0.05 mol dm^{-3} sulfuric acid measured at the frequency of 100 Hz. A linear relationship between C_{SC}^{-2} and potential E can be found at a potential range from 0.6 to 0.8 V (RHE). Extrapolation and the slope of the relationship give E_{fb} and N_D summarized in Table 3.5. The values of E_{fb} become greater in the order of {1 0 1} > {0 0 1} > {1 1 1} with ca. 20-mV intervals, and N_D is similar to those reported for polycrystalline iron as described above. However, the values of N_D are slightly larger than that of a passive film formed in a neutral borate solution [19,21], suggesting that the film formed in acidic solution with the MCC has more defects, which behaves as donors for electron transfer, than those of a passive film formed in a neutral solution.

On the other hand, potentiodynamic polarization in the cathodic direction was conducted at a potential sweep rate of –10 mV s^{-1}, which is a potential change rate similar to that in the MS

analysis, in 0.05 mol dm^{-3} sulfuric acid with the MCC after potentiostatic polarization at 1.2 V (RHE) for 1 h. The whole sample surface allowed a cathodic current in a potential region from 0.53 to 0.90 V (RHE) as shown in Fig. 3.15b, suggesting that reduction of the oxide film was possible during the MS analysis. In this potential region, a relatively large scattering of standard deviation is observed in the MS plot. Although the values of E_{fb} and N_D show some grain dependencies, the reliability of MS analysis in this experiment is not superior. In order to evaluate the grain dependency in the semiconductive properties of oxide films more precisely, MS analysis under milder conditions in which no reduction of the oxide film occurs might be necessary.

3.3.4. Galvanostatic reduction of the passive film

Separately from EIS, cathodic reduction of the passive oxide film was performed immediately after potentiostatic polarization at 1.2 V (RHE) for 1 h in 0.05 mol dm^{-3} sulfuric acid. Figure 3.16 shows changes in electrode potential when {0 0 1}, {1 0 1}, and {1 1 1} grains were galvanostatically reduced at –6 μA cm^{-2} using the MCC. Initially, the potential declined steeply from ca. 1.0 V (RHE) and reached a plateau potential at ca. 0.6 V (RHE). Subsequently, the potential dropped when the cathodic charge density q_c in Table 3.6 was consumed on the three iron grains. The deviations of q_c were less than 4% for five measurements, and the reproducibility was quite excellent.

According to the Pourbaix diagram (Fig. 1.7) [22], the backward reaction of Eq. 1.23 occurs at potentials less than

$$E^{o}\ (\mathrm{RHE}) = 0.569 - 0.0591 \log[Fe^{2+}]\ . \qquad (3.5)$$

When the electrode covered with Fe_2O_3 is at the potential of 1.0 or 0.6 V (RHE), the concentration of ferrous ions $[Fe^{2+}]$ at an electrode interface is equal to 5.1×10^{-8} or 0.3 mol dm^{-3}, respectively. Ferrous ions in the solution are derived from the substrate iron by potentiostatic and galvanostatic polarizations. Therefore, changes in electrode potential during the reduction indicate that the electrolyte solution was not so highly concentrated with ferrous ions at the end of the potentiostatic polarization, although $[Fe^{2+}]$ at the oxide/solution interface increased during the galvanostatic polarization.

Oblonsky et al. [23] explained on the basis of results of an *in situ* XANES study that the

Table 3.6. Experimental parameters obtained from cathodic reduction and XPS analysis of the passive film; q_c, cathodic charge density consumed for the reduction of the passive film.

Surface	q_C (10^{-4} C cm^{-2})	Peak intensity ratio: Fe^{2+}/Fe^{3+}
{0 0 1}	2.1 ± 0.075	0.80 ± 0.06
{1 1 1}	1.9 ± 0.0053	0.47 ± 0.04
{1 0 1}	1.5 ± 0.024	0.26 ± 0.03

plateau potential under galvanostatic reduction of the passive film formed on iron in acetate buffer represented the simultaneous reduction of Fe_2O_3 to Fe_3O_4 and Fe^{2+} as follows:

$$2Fe_2O_3 + 4H^+ + 2e^- \rightarrow Fe_3O_4 + Fe^{2+} + 2H_2O. \quad (3.6)$$

Fe_3O_4 dissolves chemically in an acidic solution [22]. When the substrate iron is partially exposed to the solution, the remaining oxide (including Fe_2O_3 and Fe_3O_4) seems to be removed rapidly since an electrochemical dissolution of the substrate Fe can drive an electrochemical reduction of the oxide. As a result, the potential shifts immediately to another plateau where hydrogen evolution reaction on the substrate iron is dominant.

It is thought that the order of q_c corresponds to the grain dependency on the amount of Fe_2O_3 in the film. From Eq. 3.6, a charge density of 0.29 mC cm^{-2} was required to reduce a Fe_2O_3 layer with a thickness of 1 nm that was contained in the oxide film formed in an acidic solution [4]. However, the values of q_c are less than that required to reduce all of the Fe_2O_3. This indicates that a chemical dissolution of the oxide film proceeded in parallel with the electrochemical reactions of Eqs. 1.23 and/or 3.6 in an acidic solution [23]. Although q_c indicates that the relative thickness of the Fe_2O_3 layer becomes in the order of {0 0 1} > {1 1 1} > {1 0 1} grains, the chemical dissolution make it difficult to estimate quantitatively the amount of Fe_2O_3 in the film from the cathodic polarization in this study.

3.3.5. X-ray photoelectron spectroscopy

After potentiostatic polarization of a single grain with the MCC that has a tip diameter of ca. 250 μm, XPS analysis of the polarized surface was conducted with a photoelectron detection diameter of 200 μm. Figure 3.17 shows Fe $2p_{3/2}$ photoelectron spectra obtained from the surfaces of iron {0 0 1}, {1 0 1}, and {1 1 1} grains polarized at 1.2 V (RHE) for 1 h in 0.05 mol dm^{-3} sulfuric acid. Although several deconvolution components for iron oxides have been reported for analyzing photoelectron spectra of passive oxide films on iron [24–26], Fe^{2+} and Fe^{3+} ions were focused on for oxidized iron species in order to identify the grain dependency on the oxidation state of iron atoms in the passive film. The spectra after background subtraction were deconvoluted into three curves that represent different oxidation states of iron species, Fe^{3+}, Fe^{2+}, and Fe^0, using the XPS peak energies for the standards reported by Keller and Strehblow [25]. A relatively large peak of Fe^0 observed in Fig. 3.17 probably indicate that the thickness of the passive film is similar or smaller than the escape depth of photoelectrons since an in elastic mean free path of Fe at Kα radiation [27] is ca. 2 nm. Therefore, the intensity of Fe^0 should be excluded to discuss the grain dependency of the oxide film. The ratio Fe^{2+}/Fe^{3+} of peak intensity in Table 3.6 clearly depends on the substrate orientation. This indicates that the film composition depends on the substrate orientation and that the relative quantity of Fe^{2+} in the film was larger in the order of {0 0 1} > {1 1 1} > {1 0 1} grains.

3.4. Discussion

A bi-layered structure of the passive film, an inner Fe_3O_4 layer and an outer γ-Fe_2O_3 layer [4], was reported by Nishimura et al., who conducted ellipsometry and galvanostatic polarization in pH 1.85 phosphate solution. When the oxide film formed on iron in sulfuric acid has a bi-layer structure, grain-dependent layer structures as shown in Fig. 3.18 can be assumed. While both oxide films have similar thicknesses, since the interfacial capacitance C is independent of substrate orientation, they show different ratios in the thickness of the inner Fe_3O_4 layer and the outer γ-Fe_2O_3 layer. On the {0 0 1} grain (Fig. 3.18a), for which the largest q_c was consumed during galvanostatic polarization among the three grains, the outer γ-Fe_2O_3 layer accounted for a larger proportion of the film than did that of the {1 0 1} grain (Fig. 3.18c). The film structure of the iron {1 1 1} grain is considered such that the ratio of Fe_3O_4/γ-Fe_2O_3 represents a value between those of the iron {0 0 1} and {1 0 1} grains (Fig. 3.18b). Since the electrical resistivity ρ of Fe_3O_4 is significantly smaller than that of γ-Fe_2O_3 ($\rho = 10^{-4}$ Ω m [28] and 10^5–10^7 Ω m [29–31] for Fe_3O_4 and γ-Fe_2O_3 respectively.), most of the potential drop in the oxide film during potentiostatic polarization exists in the γ-Fe_2O_3 layer, and R_{ct} expresses the resistance to the migration of ions driven by the potential drop. However, the magnitude order of R_{ct} and q_c showed inverse correlation, even though thicker oxide typically shows higher electric or ionic resistances. XPS analysis demonstrated that the Fe^{3+}/Fe^{2+} ratio in the oxide became greater in the same order as that of R_{ct}. Thus, the concentration of defects that trap Fe^{2+} ions as impurities and provide the ionic conduction pass of the oxide becomes larger in the order of {0 0 1} > {1 1 1} > {1 0 1}.

Generation of Fe_3O_4, which introduces Fe^{2+} ions into the oxide film, is thermodynamically spontaneous in γ-Fe_2O_3. For example, at the metal/film interface, the following reaction progresses, since the Gibbs energy ΔG is equal to –133.0 kJ mol^{-1}:

$$Fe + 4\gamma\text{-}Fe_2O_3 \rightarrow 3Fe_3O_4, \tag{3.7}$$

where the ΔG of the formation of Fe_3O_4 and γ-Fe_2O_3 are –1014.88 kJ mol^{-1} and –727.9 kJ mol^{-1} respectively [28,32]. Here, the surface energy γ of a bcc lattice structure is greater in the order of {0 0 1} > {1 1 1} > {1 0 1} grains (Table 1.2). It is reasonable that the {1 0 1} grain of bcc iron has a low activity for Eq. 3.7 and is more impoverished in Fe^{2+} than the other grains.

Greater ionic defects in the oxide film allow a larger ionic current, and oxide ions [33] and/or alternative cations [34] carry the ionic current in the anodic oxide film on iron. Davenport et al. conducted *in situ* surface XRD and suggested that the passive film formed on the iron (0 0 1) face was less defective than that formed on the iron (1 0 1) face due to the larger grain size and fewer antiphase boundaries of the oxide film on the (1 0 1) face [35]. Their results measured in pH 8.4 borate solution indicate that the {0 0 1} grain shows a higher ionic resistance than that of the {1 0 1} grain. However, the {1 0 1} grain exhibited the largest R_{ct}. This inconsistency can be caused by the difference of the acidity of electrolyte solution. Under potentiostatic anodic polarization in a passive state, the dissolution of an oxide film and/or substrate iron through the

oxide film occurs in acidic solution, whereas it is negligible in neutral solution. Thus, it is considered that the passive oxide film formed in pH 1.3 sulfuric acid has different defect concentration due to the dissolution compared with that formed in neutral solution. The defect concentration is the largest for the oxide film formed on the {0 0 1} grain and is the smallest for that on the {1 0 1} grain. As a result, the migration rate of ions thorough the defect and the dissolution rate of the oxide and substrate become greater in the order of {0 0 1} > {1 1 1} > {1 0 1} grains, that is the inverse order of R_{ct}. The dominant defects in the oxide film are considered to be oxygen vacancies and/or iron interstitials [36], and grain boundaries between grains of the oxide. It is thought that the grain-dependent defect structure is caused by different γ and epitaxial relation between the substrate and oxide.

3.5. Conclusions

Grain-dependent passivation of iron single grains in sulfuric acid was investigated individually with an MCC. Under the condition of potentiostatic polarization, iron {0 0 1}, {1 0 1}, and {1 1 1} grains showed different passivation behavior, and the current density after polarization for 1 h became larger in the order of {0 0 1} > {1 1 1} > {1 0 1}. EIS following the passivation revealed that the charge transfer resistance of the passive film formed on the iron single grains greatly depended on the substrate orientation and exhibited a larger value in the order of {1 0 1} > {1 1 1} > {0 0 1}. It was considered from galvanostatic reduction and XPS analysis that the structure of the passive film formed on iron depended on the substrate orientation due to the different surface energy of bcc iron. Considering that the structure of the oxide film formed in sulfuric acid was bi-layered with an inner Fe_3O_4 layer and an outer γ-Fe_2O_3 layer, the ratio of these two oxide layers depended on the substrate orientation. However, the thickness of a highly-resistive γ-Fe_2O_3 layer and the charge transfer resistance inversely correlated. It was considered that the defect concentration depends on the substrate orientation due to different surface energy and/or epitaxial relation between the substrate and oxide.

References

[1] N. Sato, in *Passivity of metals*, R. P. Frankental and J. Kruger, Editors, p. 29, The Electrochemical Society Inc., Princeton, NJ (1978).

[2] N. Sato and G. Okamoto, in *Comprehensive Treatise of Electrochemistry Vol. 4: Electrochemical Materials Science*, J. O. M. Bockris, B. E. Conway, E. Yeager, and R. E. White, Editors, p. 193, Plenum Press, New York and London (1981).

[3] K. Fushimi and M. Seo, *Electrochim. Acta*, **47**, 121 (2001).

[4] R. Nishimura, K. Kudo, and N. Sato, *Surf. Sci.*, **96**, 413 (1980).

[5] T. J. Chuang, C. R. Brundle, and K. Wandelt, *Thin Solid Films*, **53**, 19 (1978).

[6] E. Desimoni, G. I. Casella, A. M. Salvi, T. R. I. Cataldi, and A. Morone, *Carbon*, **30**, 527 (1992).

[7] D. A. Shirley, *Phys. Rev. B*, **5**, 4709 (1972).

[8] K. Fushimi, K. Miyamoto, and H. Konno, *Electrochim. Acta*, **55**, 7322 (2010).

[9] B. Rush and J. Newman, *J. Electrochem. Soc.*, **142**, 3770 (1995).

[10] K. J. Vetter and F. Gorn, *Electrochim. Acta*, **18**, 321 (1973).

[11] G. T. Burstein and A. J. Davenport, *J. Electrochem. Soc.*, **136**, 936 (1989).

[12] G. J. Brug, A. L. G. van den Eeden, M. Sluyters-Rehbach, and J. H. Sluyters, *J. Electroanal. Chem. Interfacial Electrochem.*, **176**, 275 (1984).

[13] K. Azumi, T. Ohtsuka, and N. Sato, *Trans. Jpn. Inst. Met.*, **27**, 382 (1986).

[14] N. F. Mott, *Proc. R. Soc. London A*, **171**, 27 (1939).

[15] W. Schottky, *Zeitschrift für Phys.*, **113**, 367 (1939).

[16] J. W. Schultze and M. M. Lohrengel, *Electrochim. Acta*, **45**, 2499 (2000).

[17] N. Krithivasan, T. Tsuru, and S. Haruyama, *Boshoku Gijutsu*, **29**, 275 (1980).

[18] C. Jeyaprabha, S. Sathiyanarayanan, and G. Venkatachari, *Appl. Surf. Sci.*, **246**, 108 (2005).

[19] K. Azumi, T. Ohtsuka, and N. Sato, *J. Electrochem. Soc.*, **134**, 1352 (1987).

[20] J. Wielant, V. Goossens, R. Hausbrand, and H. Terryn, *Electrochim. Acta*, **52**, 7617 (2007).

[21] T. Yamamoto, K. Fushimi, S. Miura, and H. Konno, *J. Electrochem. Soc.*, **157**, C231 (2010).

[22] M. Pourbaix, *Atlas of Electrochemical Equilibria in Aqueous Solution*, 2nd English ed., p. 307, National Association of Corrosion Engineers, Houston (1974).

[23] L. J. Oblonsky, M. P. Ryan, and H. S. Isaacs, *Corros. Sci.*, **42**, 229 (2000).

[24] K. Asami and K. Hashimoto, *Corros. Sci.*, **17**, 559 (1977).

[25] P. Keller and H.-H. Strehblow, *Corros. Sci.*, **46**, 1939 (2004).

[26] R.-H. Jung, H. Tsuchiya, and S. Fujimoto, *Corros. Sci.*, **58**, 62 (2012).

[27] T. Nagatomi, S. Tanuma, and K. Goto, *Surf. Interface Anal.*, **42**, 1537 (2010).

[28] G. V. Samsonov, *The Oxide Handbook*, p. 272, IFI/Plenum, New York (1973).

[29] K. Iwauchi, *Jpn. J. Appl. Phys.*, **10**, 1520 (1971).

[30] K. S. Rane, A. K. Nikumbh, and A. J. Mukhedkar, *J. Mater. Sci.*, **16**, 2387 (1981).

[31] V. A. Hiremath and A. Venkataraman, *Bull. Mater. Sci.*, **26**, 391 (2003).

[32] J. Majzlan, K.-D. Grevel, and A. Navrotsky, *Am. Mineral.*, **88**, 855 (2003).

[33] N. Sato and T. Noda, *Electrochim. Acta*, **22**, 839 (1977).

[34] S. C. Hendy, N. J. Laycock, and M. P. Ryan, *J. Electrochem. Soc.*, **152**, B271 (2005).

[35] A. J. Davenport, L. J. Oblonsky, M. P. Ryan, and M. F. Toney, *J. Electrochem. Soc.*, **147**, 2162 (2000).

[36] S. Ahn and H. Kwon, *J. Electroanal. Chem.*, **579**, 311 (2005).

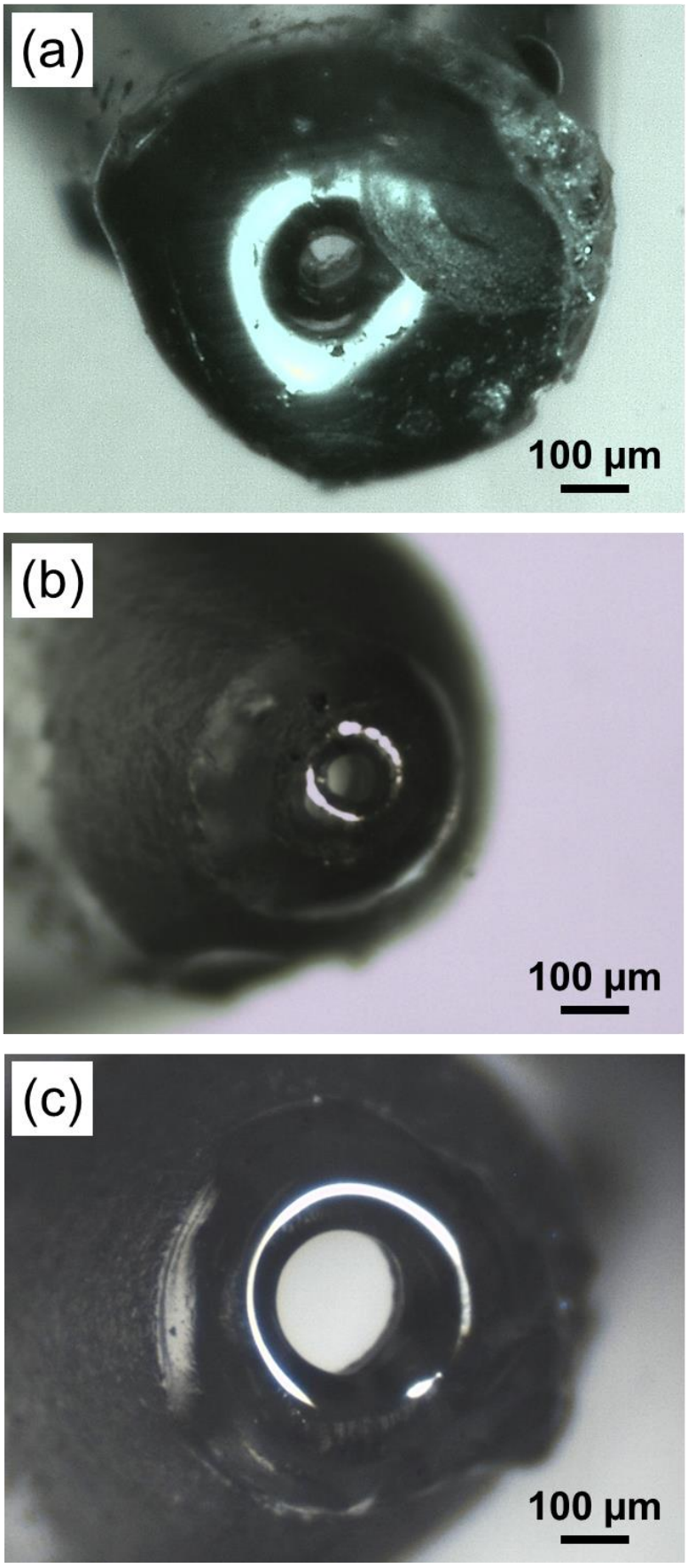

Figure 3.1. Optical images of capillary tips: (a) C1, (b) C2, and (c) C3.

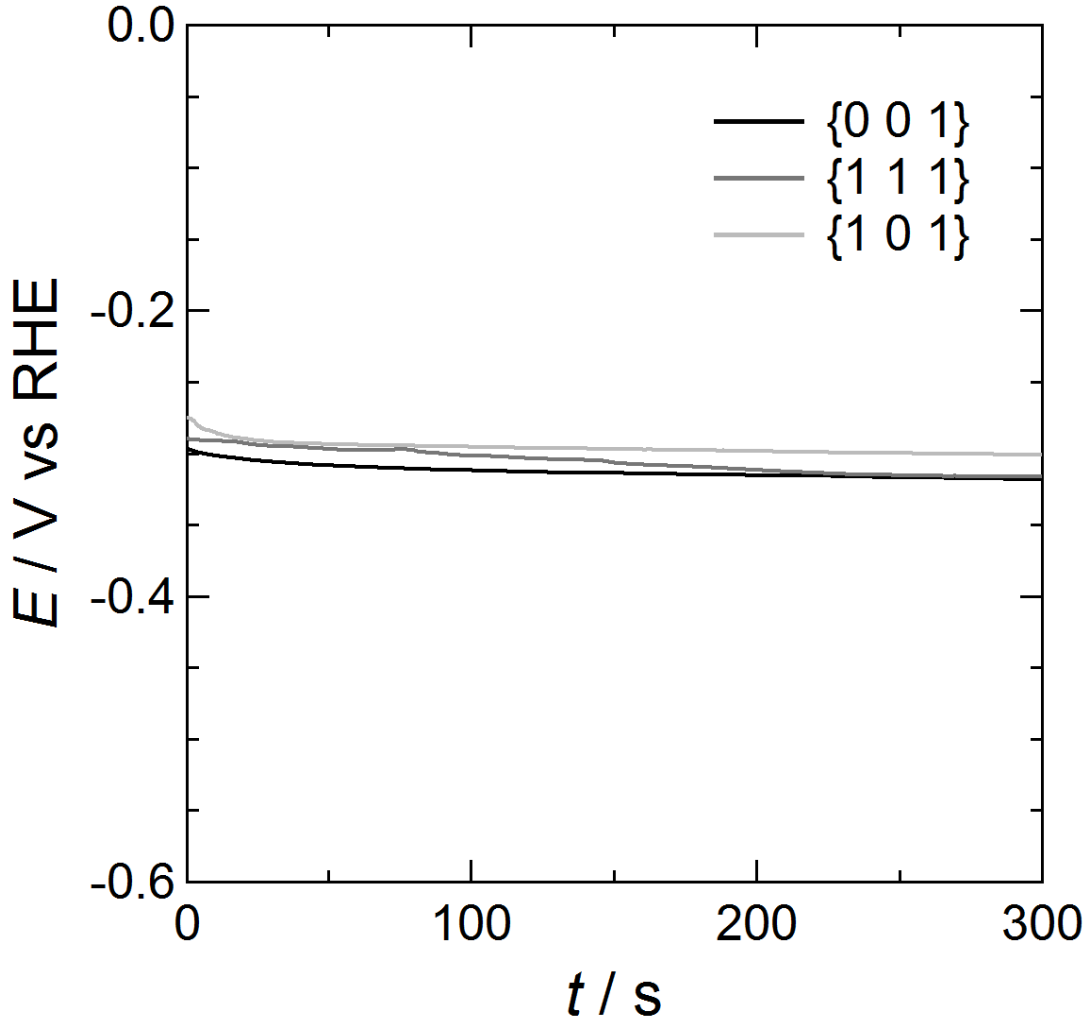

Figure 3.2. Potential-time transients of iron {0 0 1}, {1 0 1}, and {1 1 1} grains during E_{corr} measurements in 0.05 mol dm^{-3} sulfuric acid.

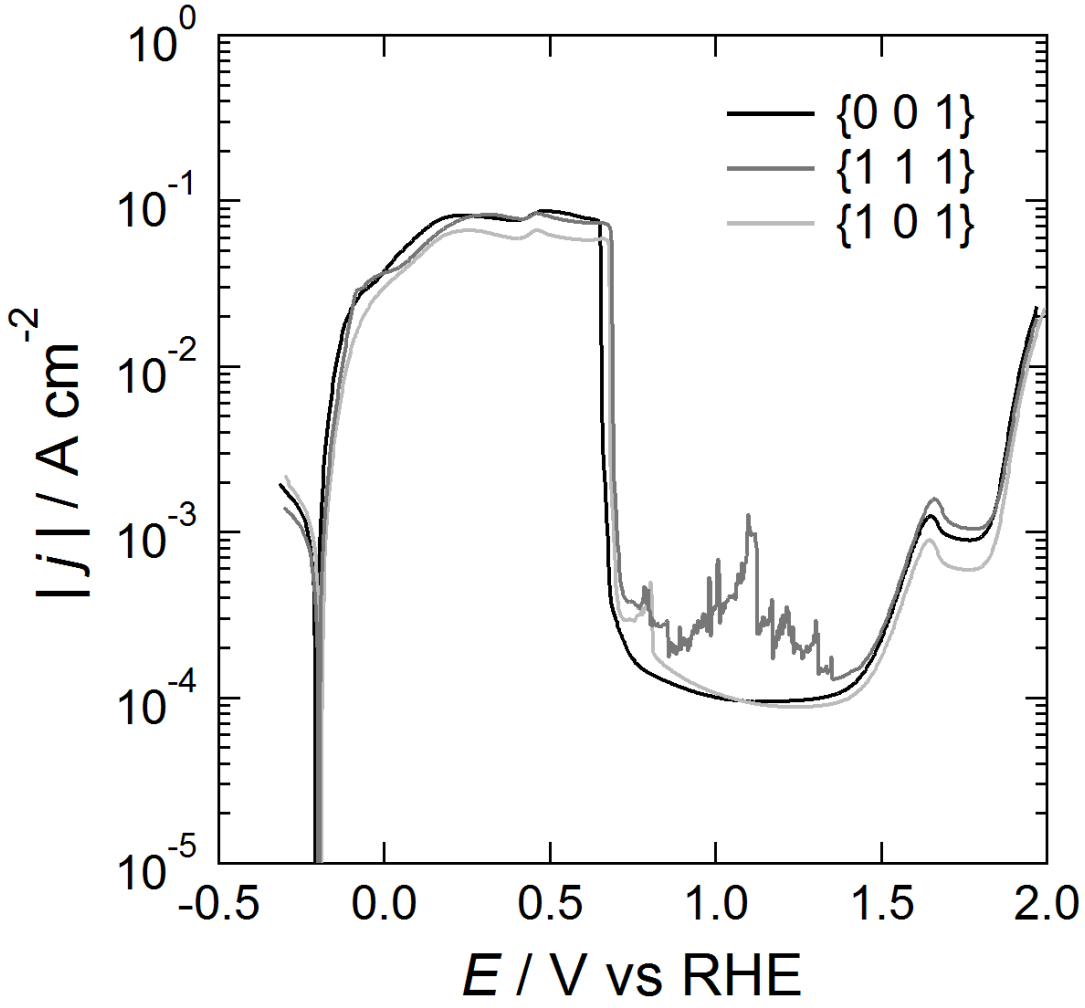

Figure 3.3. Anodic polarization curves of iron {0 0 1}, {1 0 1}, and {1 1 1} grains in 0.05 mol dm^{-3} sulfuric acid measured by using the capillary C1; the potential was scanned at 5 mV s^{-1}.

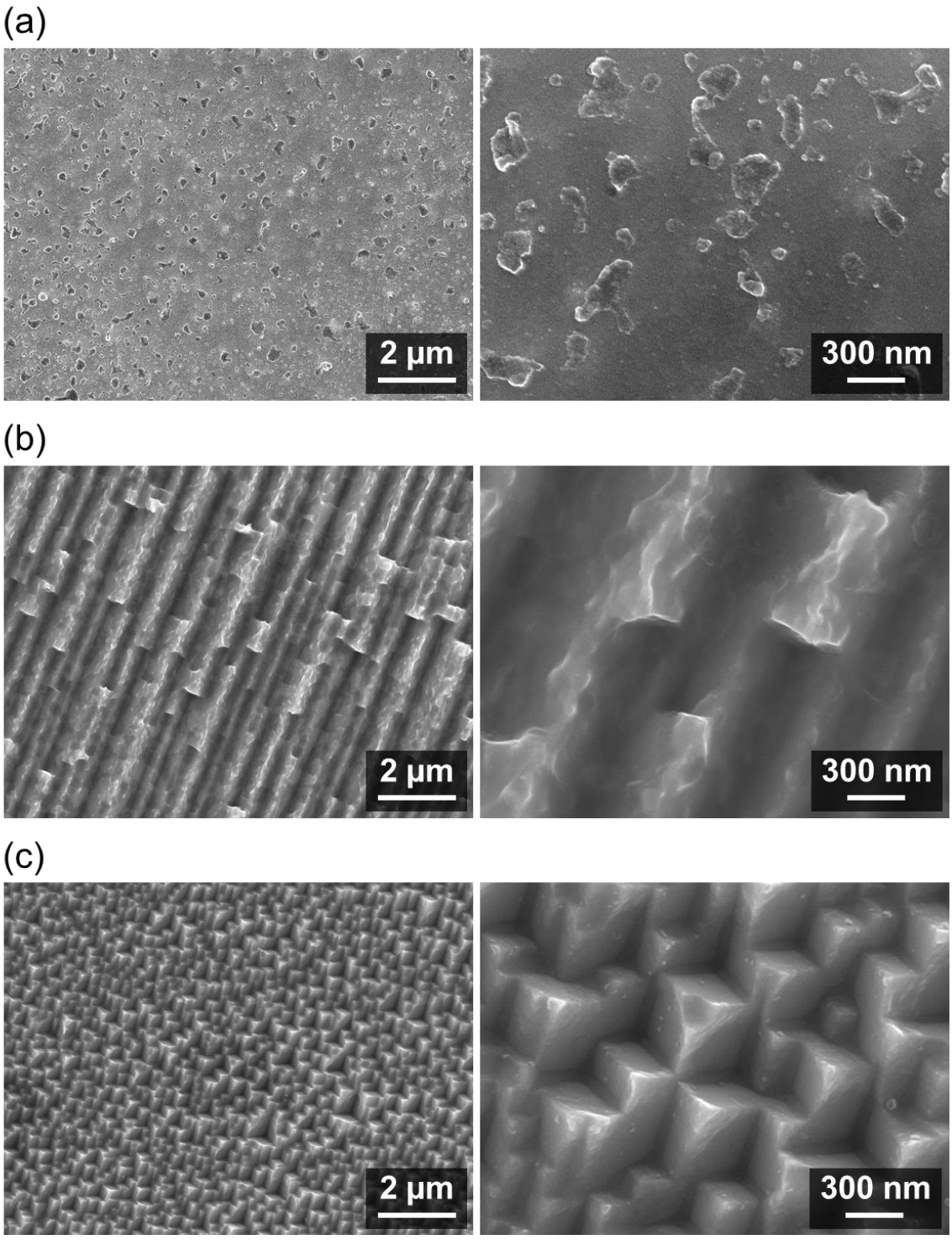

Figure 3.4. SEM images of the surface of iron (a) {0 0 1}, (b) {1 0 1}, and (c) {1 1 1} grains after the potentiodynamic polarization until 1.1 V (RHE).

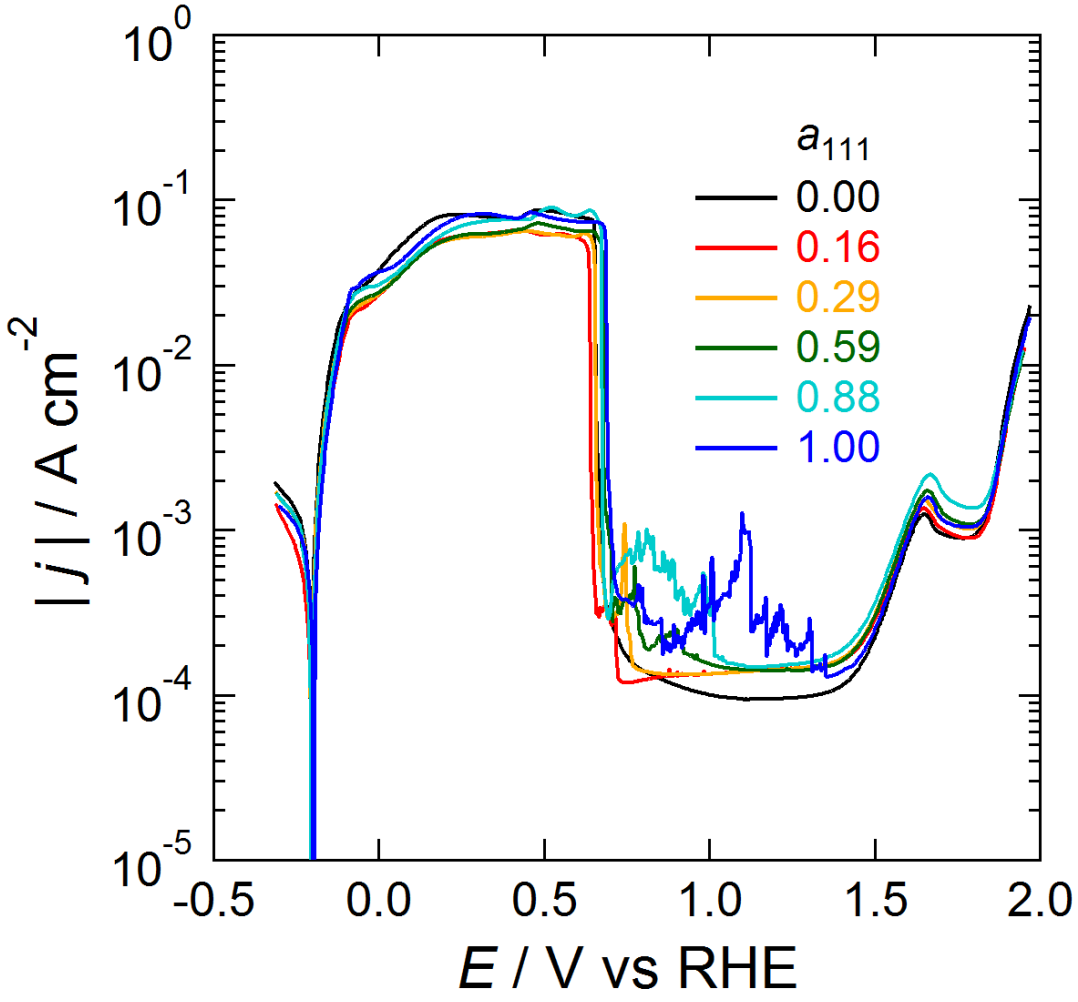

Figure 3.5. Anodic polarization curves of iron {0 0 1}/{1 1 1} bi-grains measured by using the capillary C1 in 0.05 mol dm^{-3} sulfuric acid with the potential sweep rate of 5 mV s^{-1}; the relative area a_{111} of the {1 1 1} grain was defined as the ratio of the area of the {1 1 1} grain part to the total electrode area.

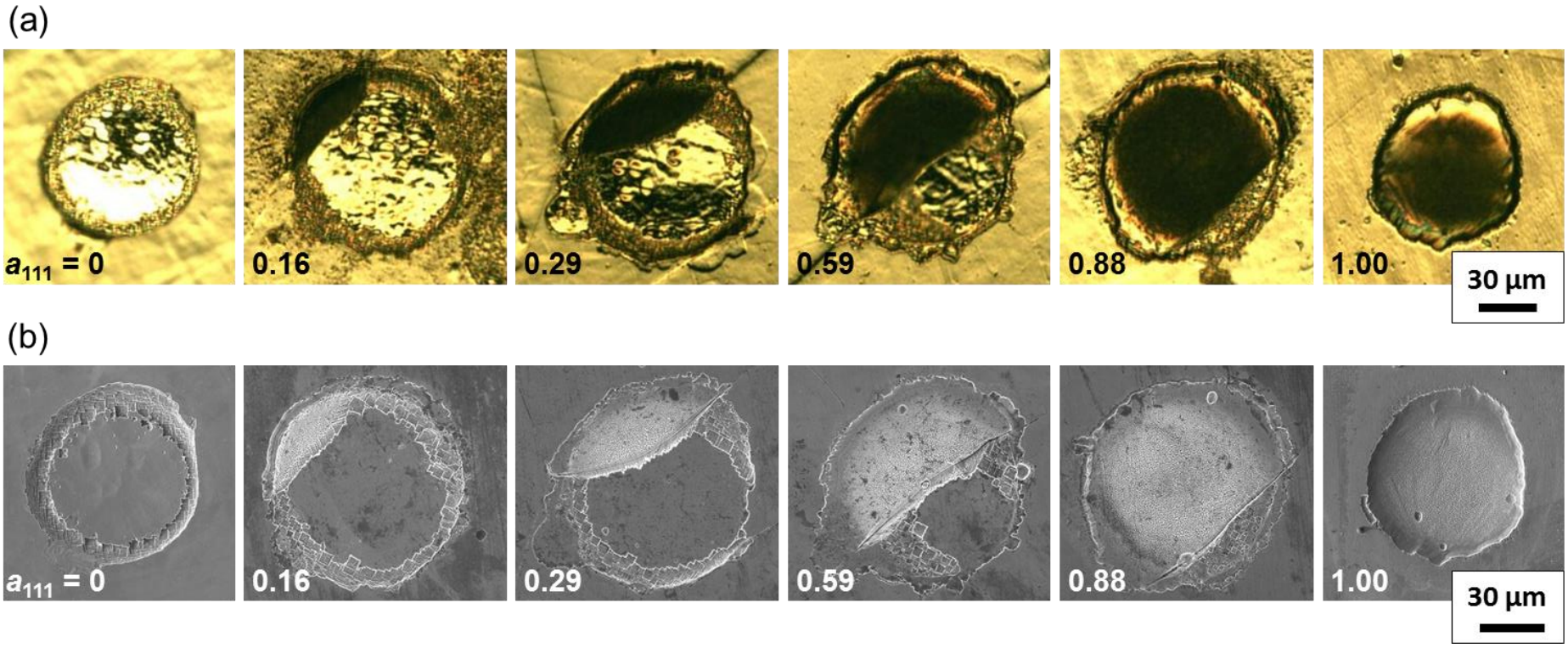

Figure 3.6. (a) Optical microscopic images and (b) SEM images of iron {0 0 1}/{1 1 1} bi-grain electrodes after the potentiodynamic polarization shown in Fig. 3.5, with the value in the bottom left of each image displaying a_{111} the relative area of the {1 1 1} grain.

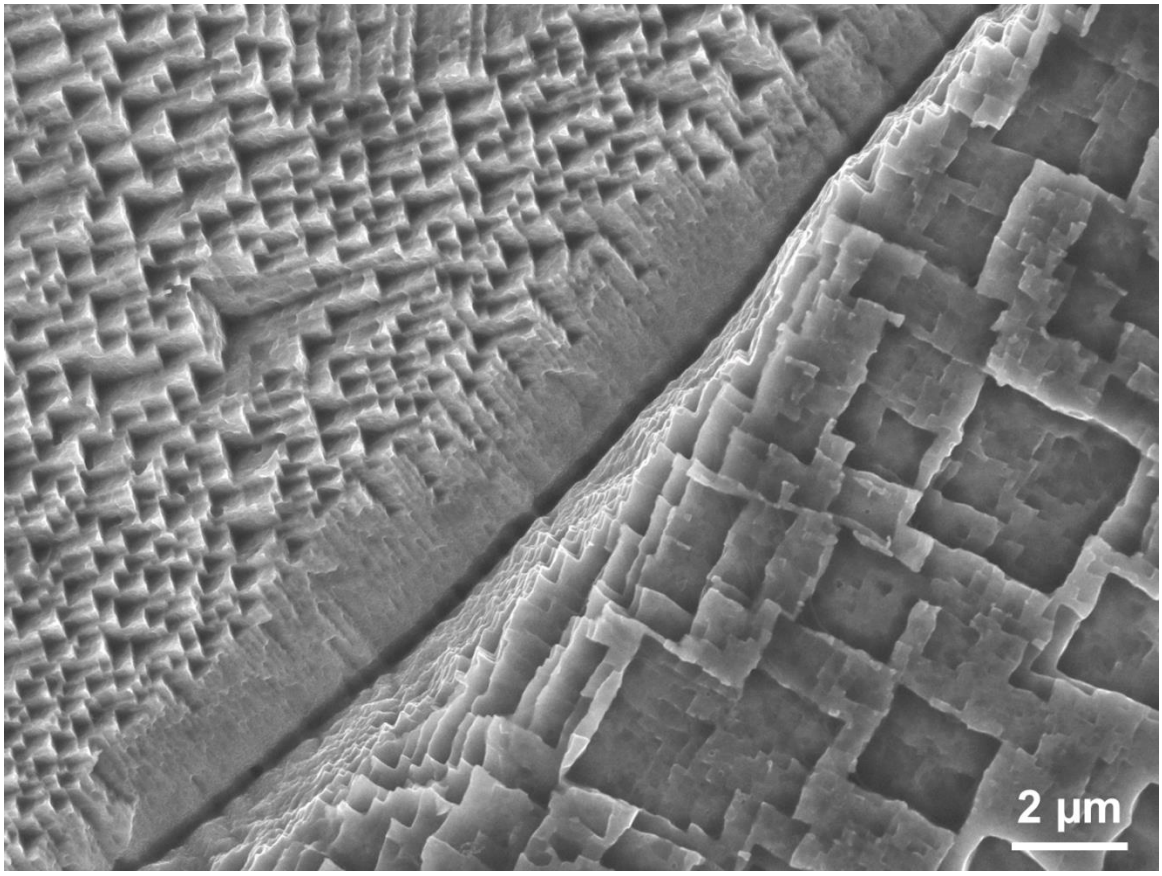

Figure 3.7. High magnification SEM image of the grain boundary in the {0 0 1}/{1 1 1} bi-grain electrode (a_{111} = 0.88) after the potentiodynamic polarization with the capillary C1; the upper left part is the {0 0 1} grain and the lower right part is the {1 1 1} grain.

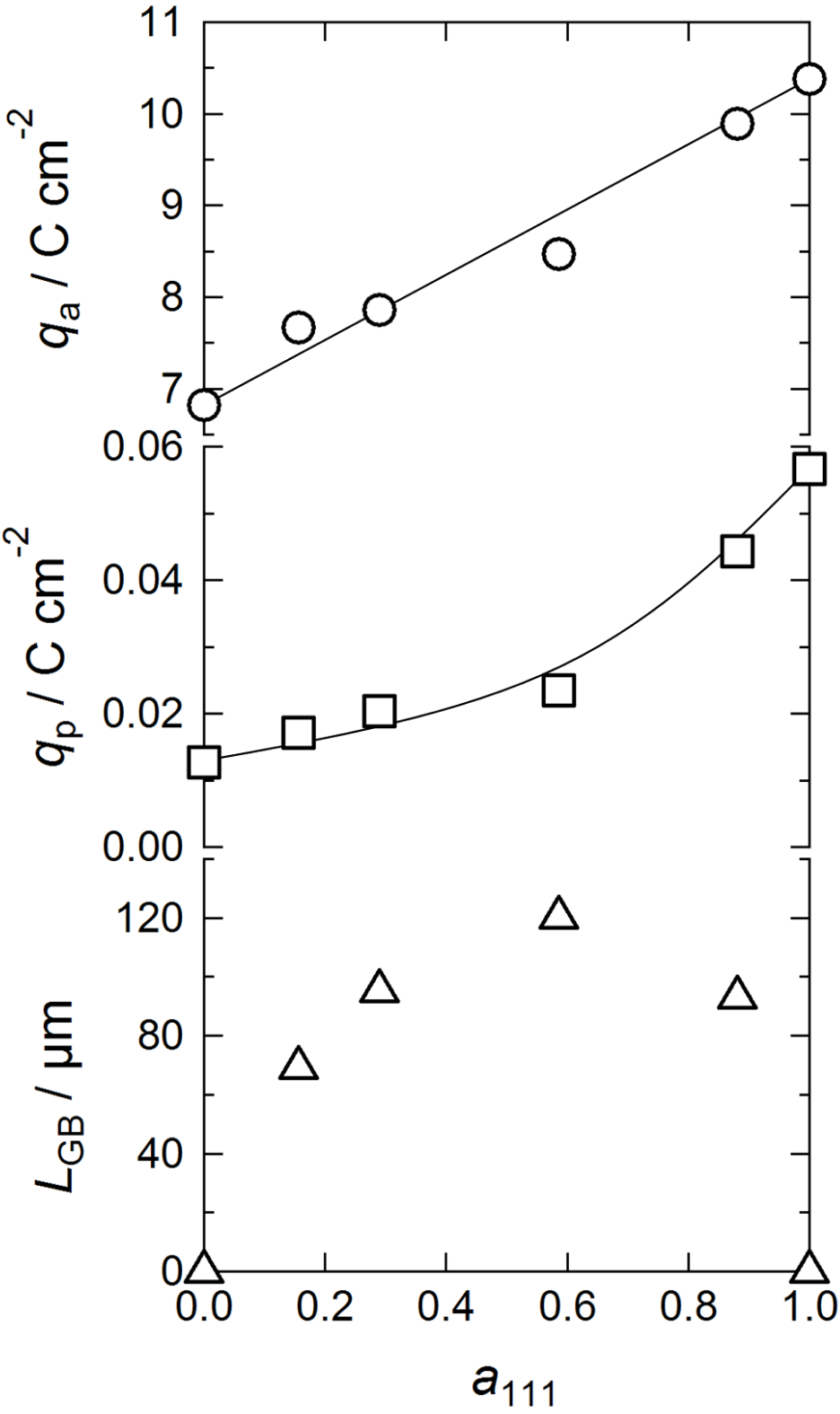

Figure 3.8. Electric charge densities q_a and q_p consumed in active and passive states, respectively, and length of a grain boundary L_{GB} in bi-grain electrodes as a function of a_{111}; the values of q_a and q_p were obtained from the integration of the polarization curves shown in Fig. 3.5 in potential ranges from E_{corr} to 0.76 V (RHE) and from 0.76 to 1.46 V (RHE) respectively.

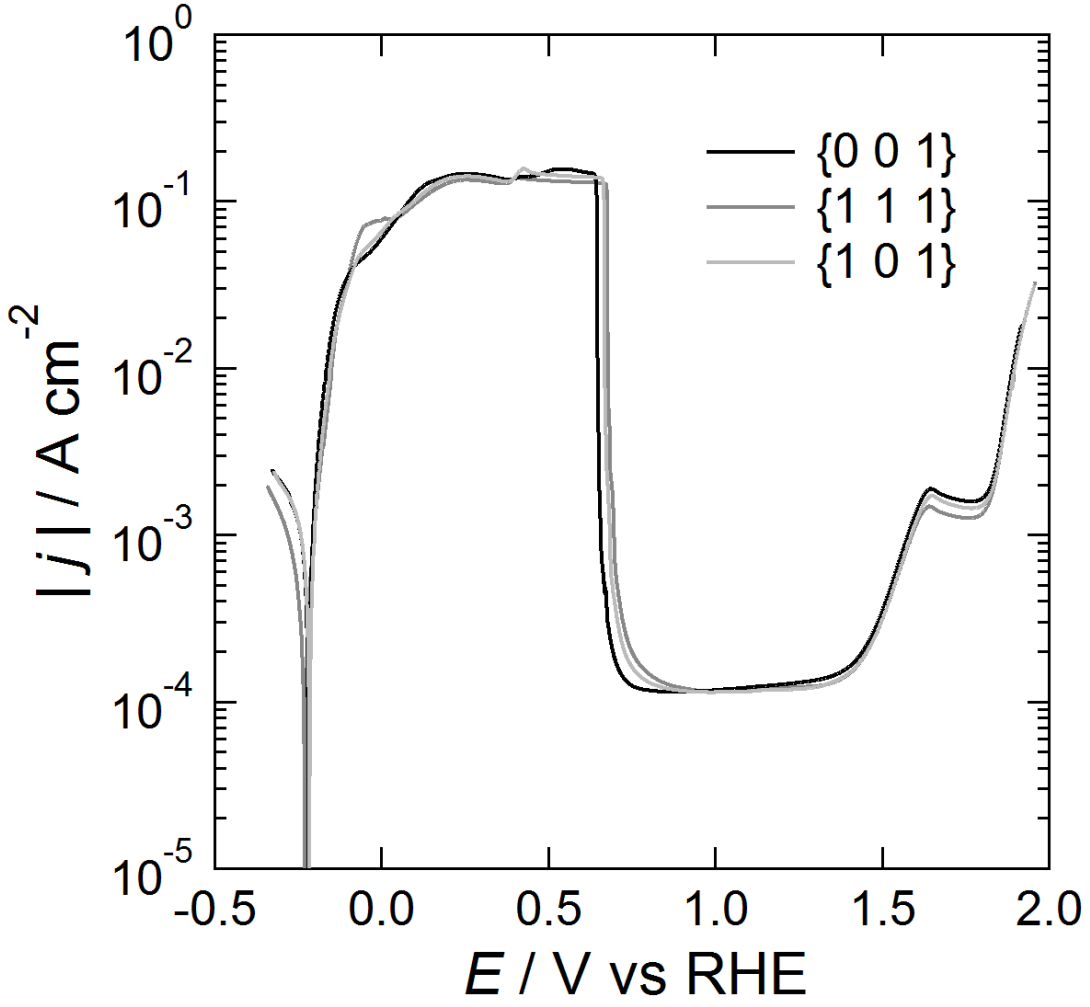

Figure 3.9. Anodic polarization curves of iron {0 0 1}, {1 0 1}, and {1 1 1} grains in 0.05 mol dm^{-3} sulfuric acid measured by using the capillary C2; the potential was scanned at 5 mV s^{-1}.

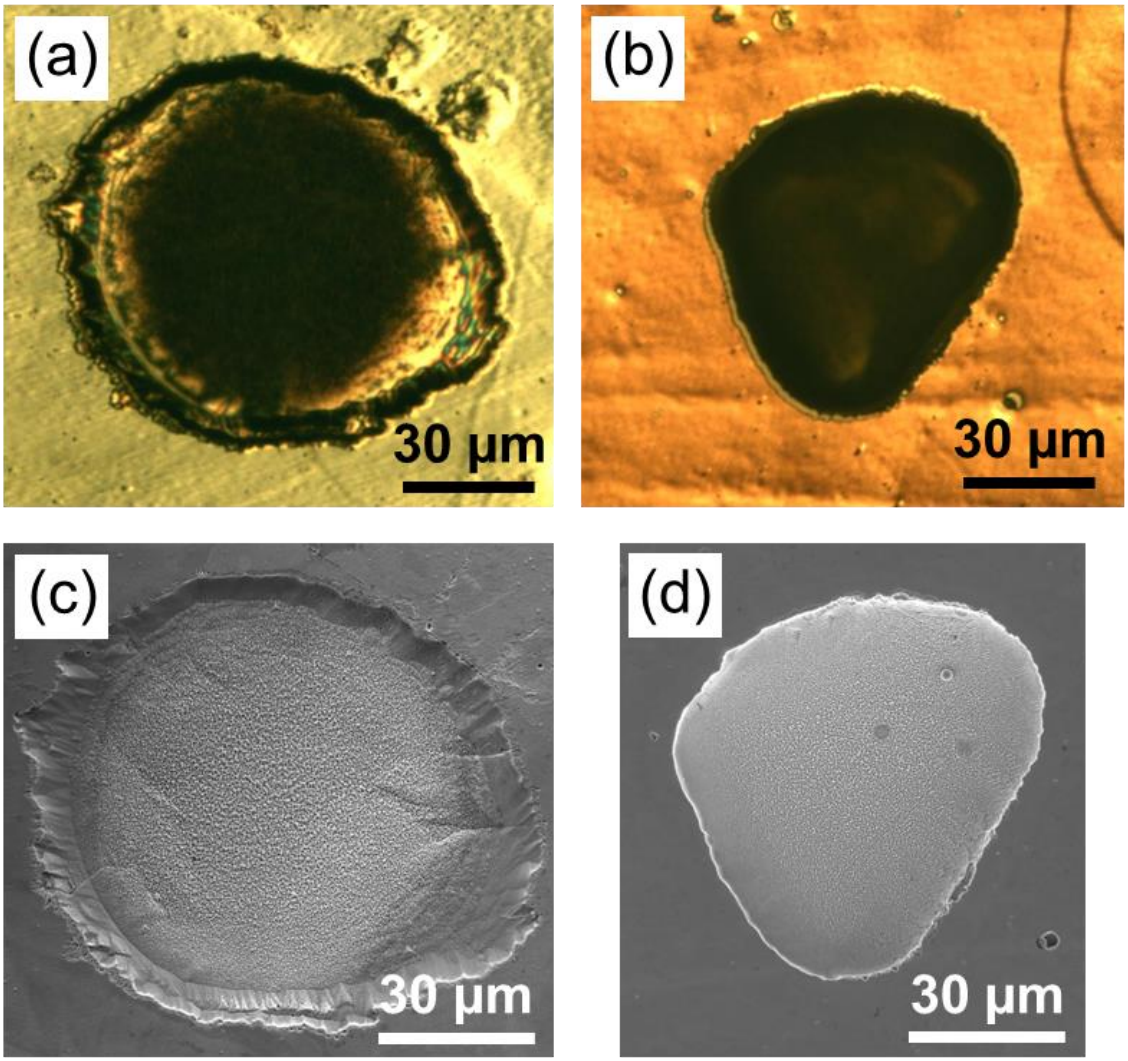

Figure 3.10. (a, b) Optical microscopic images and (c, d) SEM images of the iron {1 1 1} grain surface after potentiodynamic polarization by the MCC with (a, c) capillary C1 and (b, d) C2.

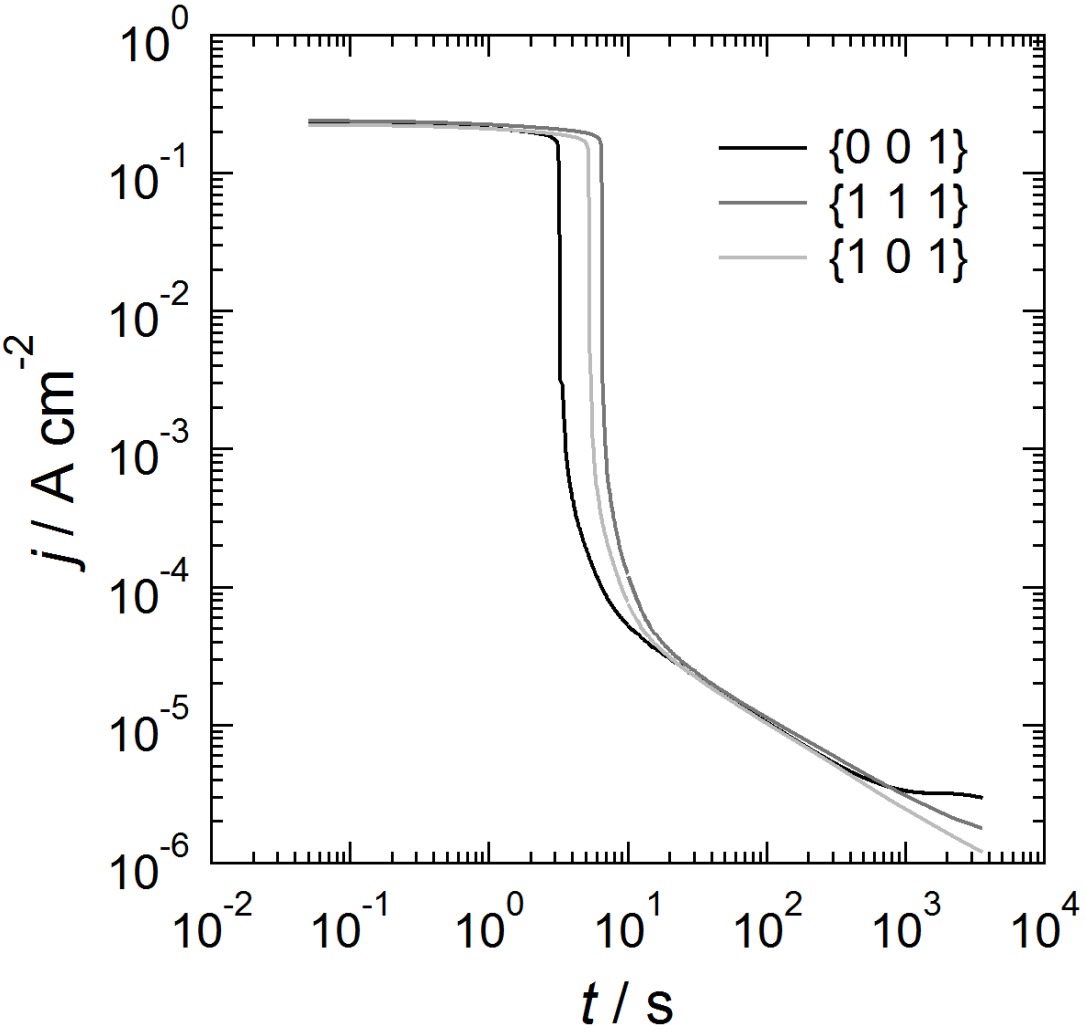

Figure 3.11. Double logarithmic plots of current-time transients of iron {0 0 1}, {1 0 1}, and {1 1 1} grains under the condition of potentiostatic polarization in 0.05 mol dm^{-3} sulfuric acid at 1.2 V (RHE) for 1 h.

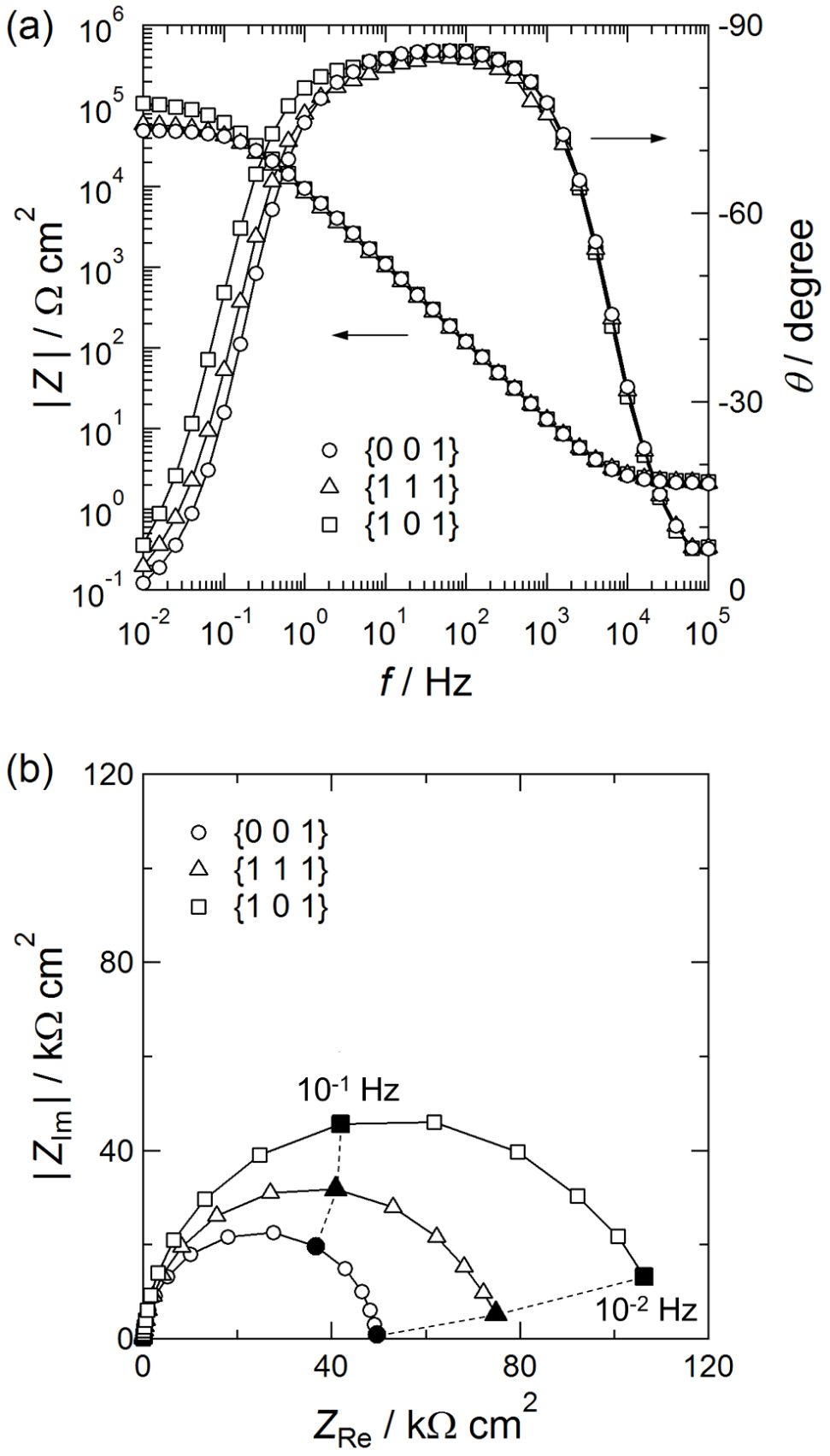

Figure 3.12. (a) Bode plot and (b) Nyquist plot of iron {0 0 1}, {1 0 1}, and {1 1 1} grains polarized at 1.2 V (RHE) for 1 h in 0.05 mol dm^{-3} sulfuric acid.

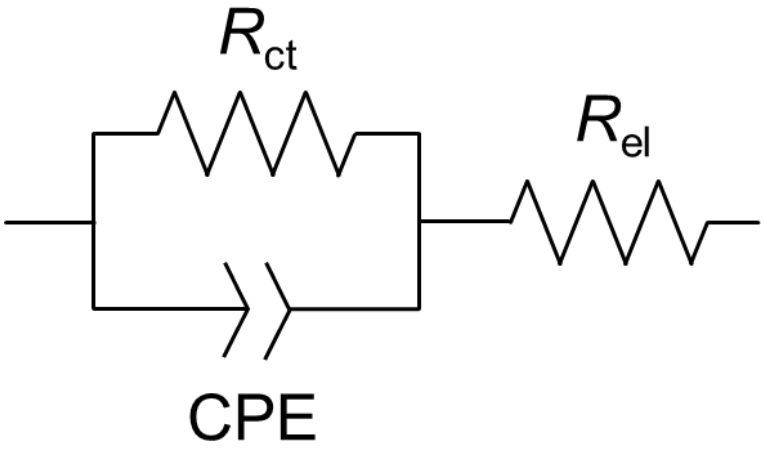

Figure 3.13. Equivalent electronic circuit used to fit the EIS data, where R_{ct} is charge transfer resistance, R_{el} is electrolyte resistance, and CPE is used instead of a capacitor.

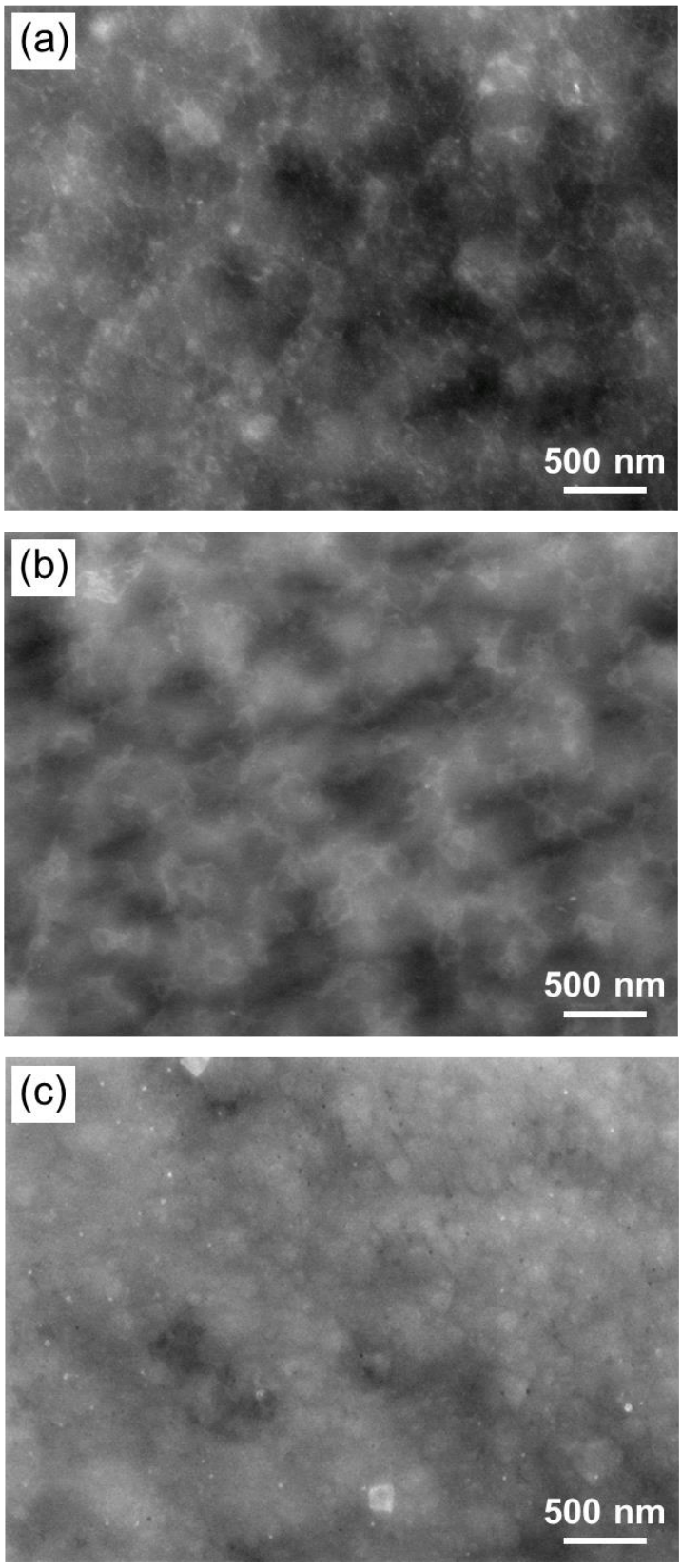

Figure 3.14. SEM images of the surface of iron (a) {0 0 1}, (b) {1 0 1}, and (c) {1 1 1} grains after EIS measurements following the potentiostatic polarization at 1.2 V (RHE) for 1 h in 0.05 mol dm^{-3} sulfuric acid with the MCC (capillary C3).

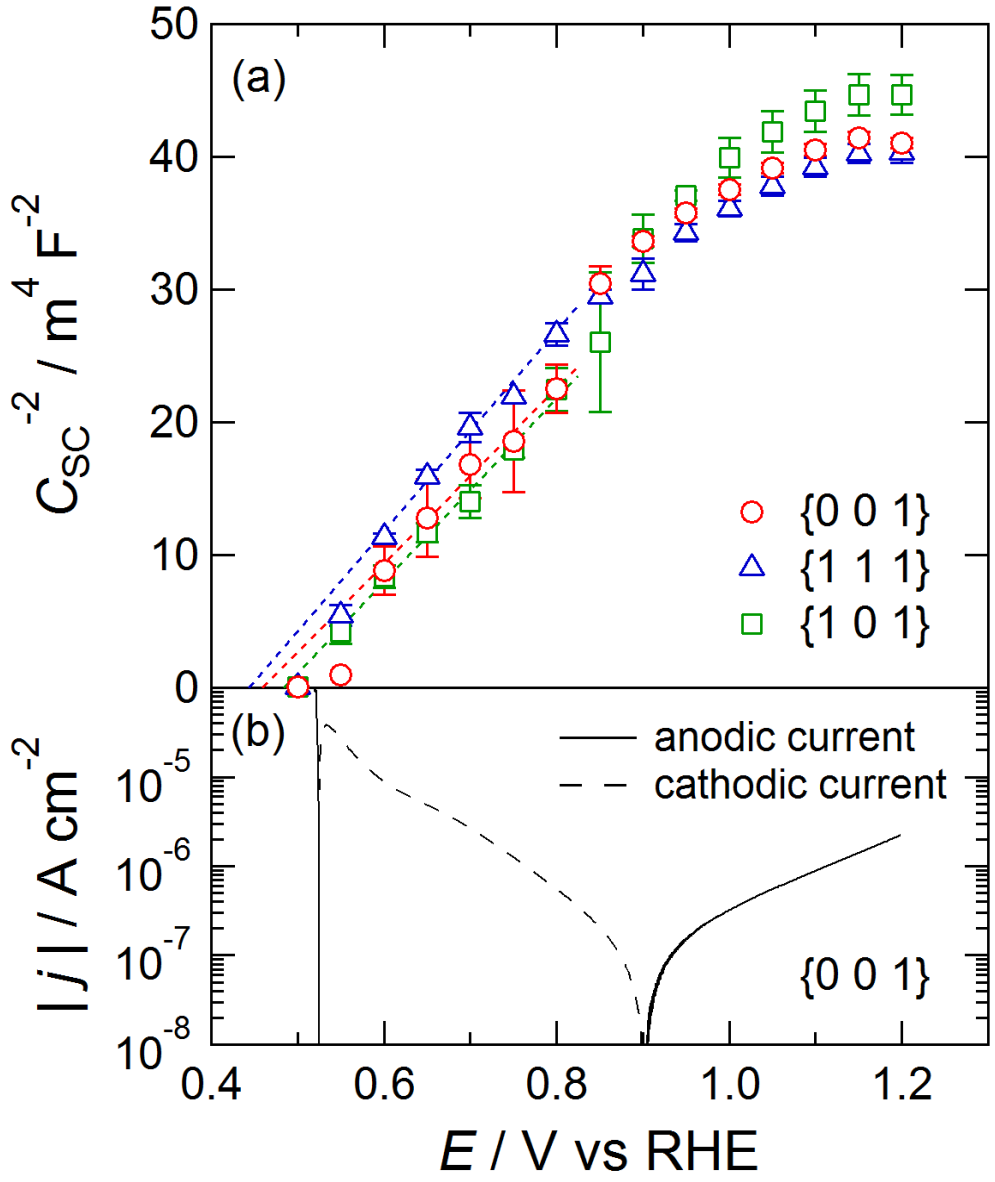

Figure 3.15. (a) Mott-Schottky plot for passive oxide films formed on iron {0 0 1}, {1 0 1}, and {1 1 1} grains measured at 100 Hz; (b) cathodic polarization curve of the iron {0 0 1} grain in 0.05 mol dm^{-3} sulfuric acid following potentiostatic polarization at 1.2 V (RHE) for 1 h, with the potential sweep rate of –10 mV s^{-1}.

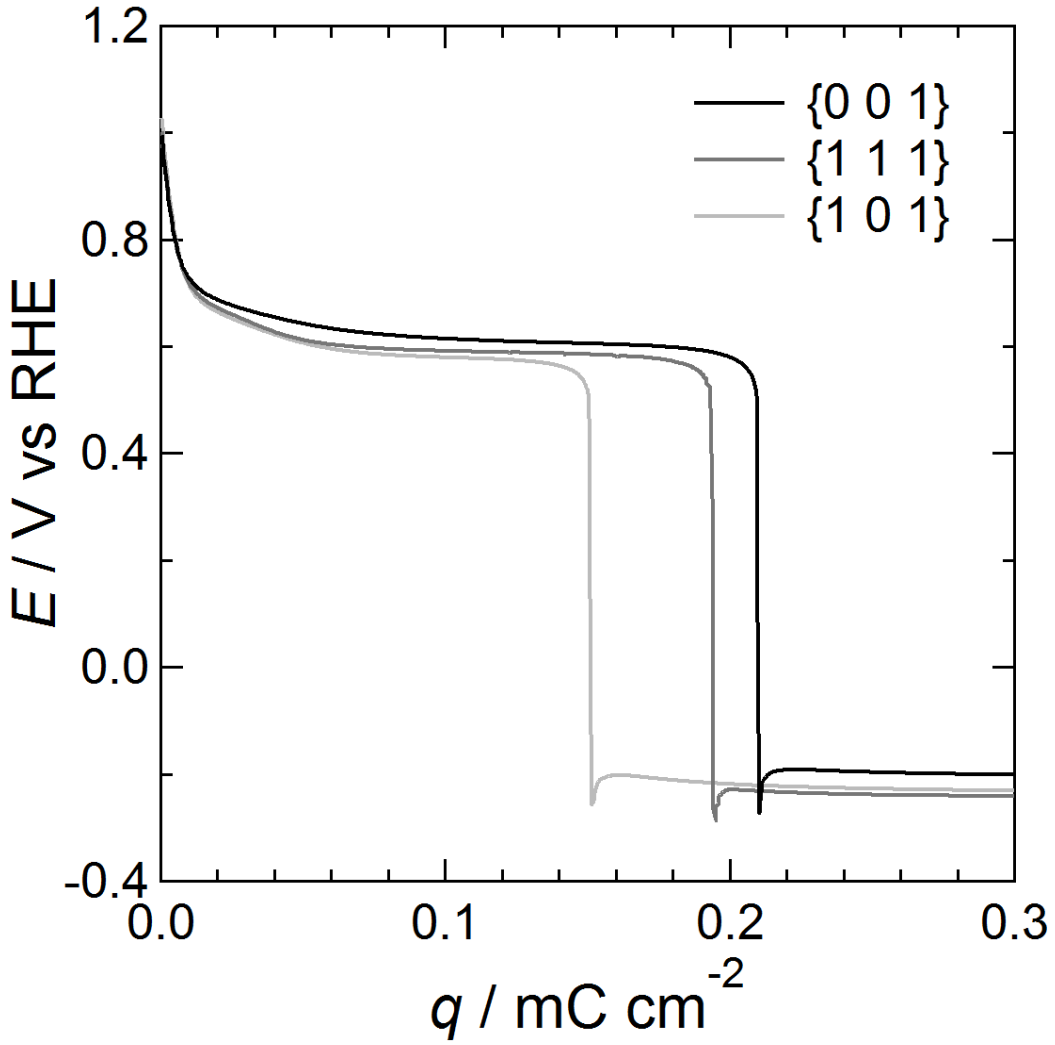

Figure 3.16. Changes in potential as a function of electric charge *q* during galvanostatic reduction of iron {0 0 1}, {1 0 1}, and {1 1 1} grains with a cathodic current density of −6 μA cm^{-2} after potentiostatic polarization at 1.2 V (RHE) for 1 h in 0.05 mol dm^{-3} sulfuric acid.

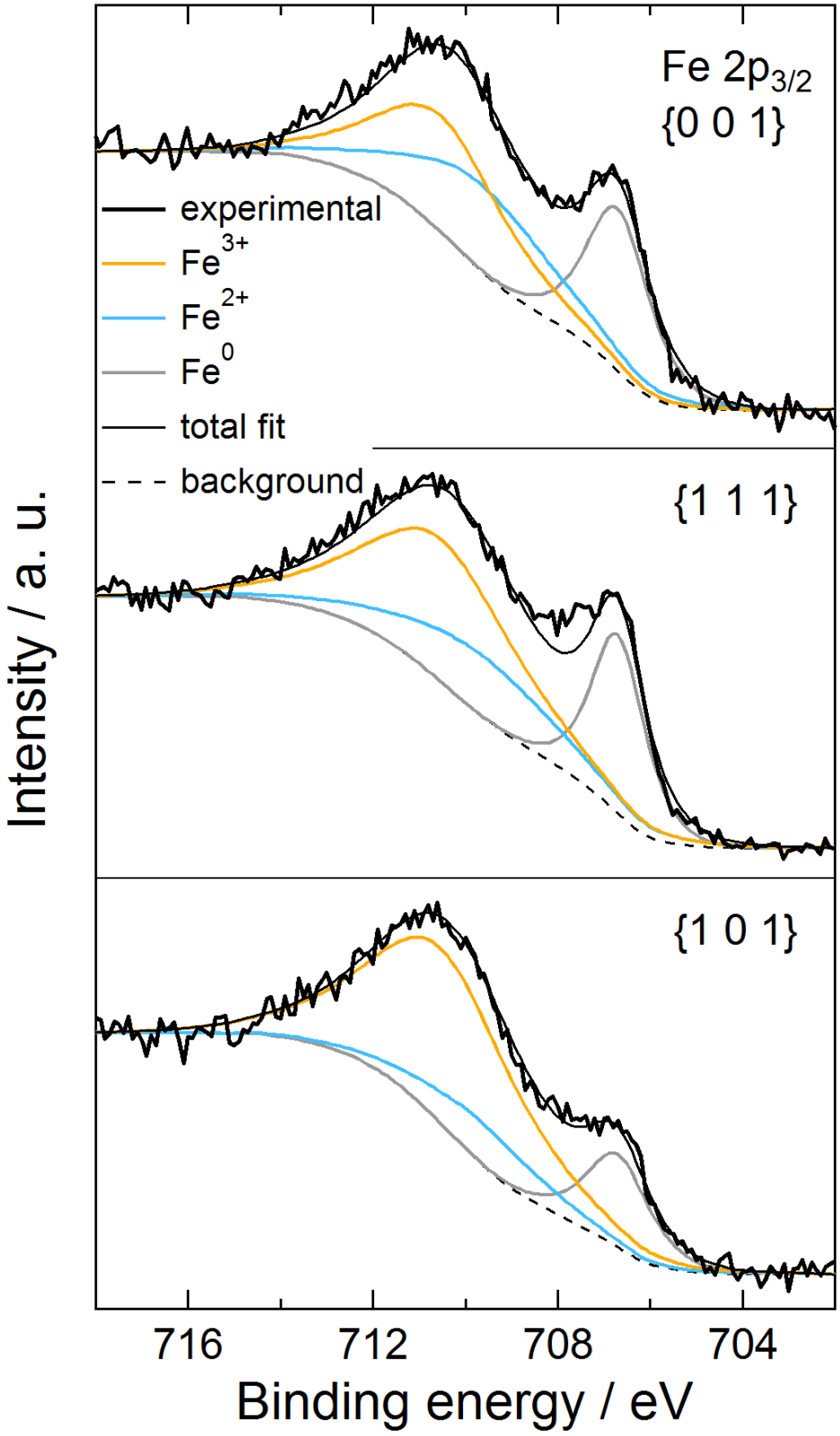

Figure 3.17. Fe $2p_{3/2}$ photoelectron spectra of iron {0 0 1}, {1 0 1}, and {1 1 1} single grains polarized at 1.2 V (RHE) for 1 h in 0.05 mol dm^{-3} sulfuric acid.

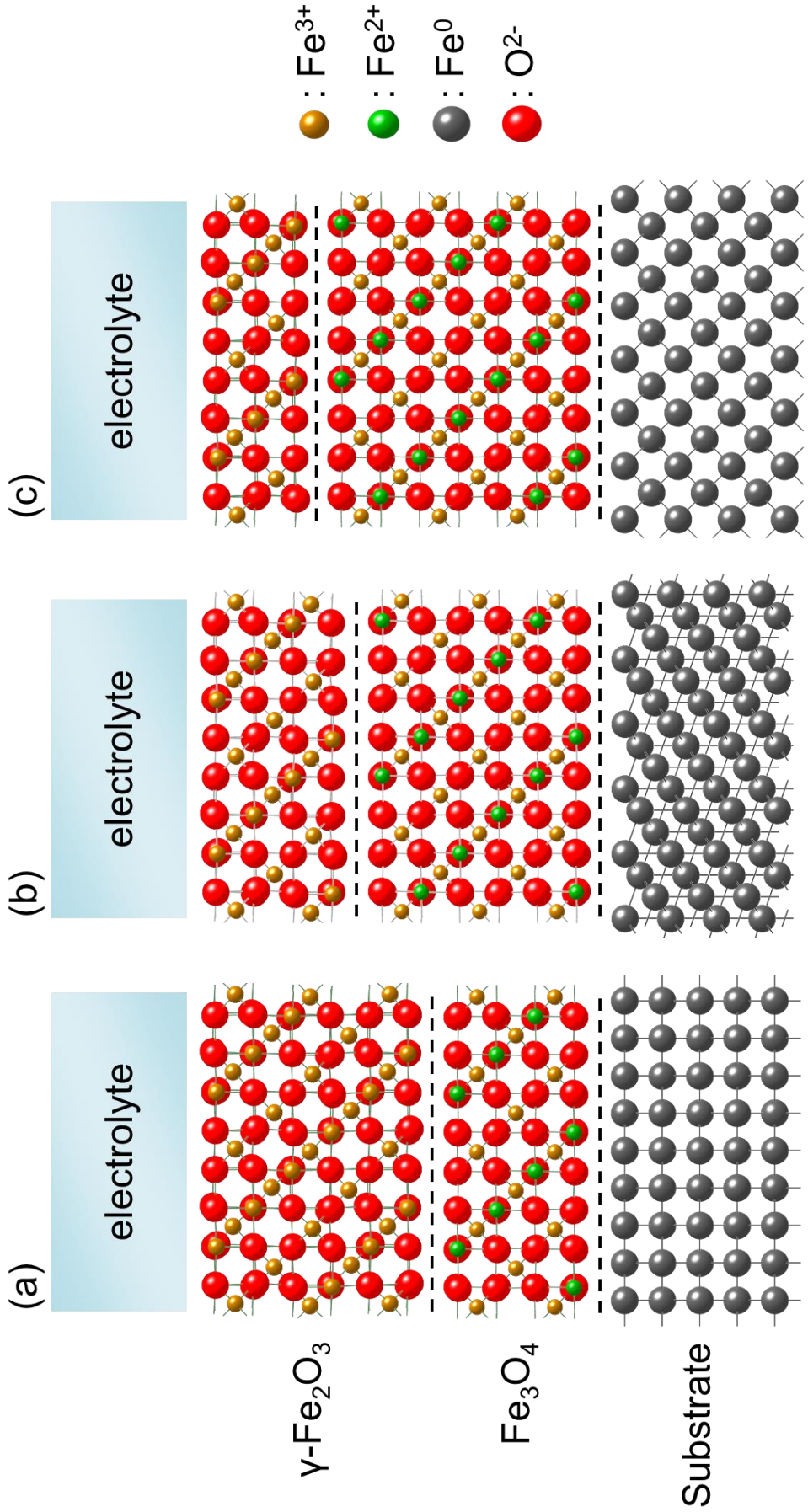

Figure 3.18. Schematic diagram of iron (a) {0 0 1}, (b) {1 1 1}, and (c) {1 0 1} grain surfaces after potentiostatic polarization in sulfuric acid.

Chapter 4
Heterogeneity of thermally grown oxide film observed by two-dimensional ellipsometry

4.1. Introduction

A thermal oxide film grows on the surface of metals and alloys when it is exposed to a high temperature atmosphere. Chemical characteristics of oxide such as corrosion resistance generally differ from those of base metals. Thus, it is important to know the characteristics of the thermally oxidized surface of metals and alloys to avoid undesired degradation of metallic materials. It has been shown that thermally grown oxides formed on pure iron have characteristic composition, structure, and thickness depending on oxidation conditions such as temperature, oxygen partial pressure, and the presence of water vapor [1–3]. The crystallographic orientation of the iron surface is also one of the factors that influence the rate of formation of thermal oxides. Orientation-dependent formation of an oxide on an iron single crystal has been reported [4–6]. It has been shown that the surface orientation greatly affects oxide formation at temperatures of 473 to 623 K、a temperature range at which recrystallization of iron is very slow and FeO does not form due to its thermodynamic instability [7]. Orientation dependence on oxide thickness was observed during an oxidation period of less than 1 h. Steels are generally used as polycrystalline substances with surfaces consisting of numerous grains with different orientations and it is apparent that the characteristics of a thermally oxidized polycrystalline iron surface are heterogeneous. Pryor and Evans observed non-uniform dissolution of thermally grown oxide on iron in dilute hydrochloric acid due to the heterogeneity of oxide thickness [8]. When the oxide locally degrades and the substrate is partially exposed to a corrosive environment, localized corrosion can occur. However, the heterogeneity of the oxidized surface was overlooked when researchers investigated the characteristics and growth behavior of thermal oxides formed on iron. For example, the thickness of an oxide layer on polycrystalline iron was usually reported as an average value of the whole surface [9]; the distribution of oxide thicknesses that depended on the each grain of a polycrystalline iron surface was not considered. The requirement to average characteristics of a surface oxide was partly due to the lack of a measurement technique to investigate both the numerous crystallographic orientations on a polycrystalline surface and the characteristics of all of the oxides formed on each grain of the polycrystalline surface. Recently,

EBSD patterning has been used for the identification of surface crystallographic orientations of polycrystalline metals as applied to iron in 2.1.3. Precise crystal structures of relatively thick thermal oxides, so-called “oxide scales”, formed on low-carbon steel [10] and pure iron [11] were also determined by EBSD. However, despite the development of high-precision measurement techniques, there has still been no report on the heterogeneous thermally oxidized surface of polycrystalline iron.

In Chapter 3, the MCC fabricated in Chapter 2 successfully demonstrated the grain-dependent electric properties of passive films formed on iron in sulfuric acid. In this chapter, the heterogeneity of a thermally oxidized polycrystalline iron surface was visualized using 2D ellipsometry, with the characteristics of the oxidized surface of each grain investigated by the MCC method. Furthermore, grain-dependent degradation of the oxidized surface was observed by means of *in situ* 2D ellipsometry and orientation-dependent growth of the thermal oxide film was discussed.

4.2. Experimental

4.2.1. Sample preparation

After mirror-like polishing and EBSD patterning as described in section 2.1, the sample was oxidized in a muffle furnace (KDF-S70, Denken-Highdental) at 573 K in air for 1 h. This temperature is suitable for both MCC measurements and ellipsometry, since thick oxide films formed at temperatures above 573 K showed too much electronic resistance and impedance measurement became difficult, while thin oxide films formed below 573 K showed less grain dependency. Finally, the sample was cooled to ambient temperature in open air.

4.2.2. Characterization of the oxidized surface

The oxidized surface of each grain was characterized by using a confocal Raman microscope (XploRA, HORIBA) with a probe area of ca. 1 μm in diameter. A diode laser with a wavelength of 532 nm was used for the excitation of Raman scattering. The power of the incident laser was confined to 2 mW by filtering to avoid any change in the composition of the sample surface, and a single Raman spectrum was scanned 64 times. In fact, no visual change was observed on the sample surface after a Raman spectroscopic measurement for 280 s.

The oxidized surface was also characterized with XPS. The JPS-9200 photoelectron spectrometer with Al Kα radiation operating at 100 W (10 kV, 10 mA) collected photoelectrons emitted from the oxidized polycrystalline substrate and α-Fe_2O_3 powder (purity: 99.9%, Wako Pure Chem. Ind., Ltd.) on a conductive carbon tape as a reference.

The morphology of the oxidized surface was observed with the JSM-6500F field-emission

SEM and secondary electron (SE) images were collected. Furthermore, in order to observe the cross-sectional structure of the oxidized sample surface, the sample was prepared by a cross section polisher (CP) (SM-09010, JEOL) as follows. The sample specimen mounted in acrylic resin was ground parallel to the sample ND with #800 SiC paper, and a sample cross section was fabricated by using an Ar ion beam with an acceleration voltage of 6 kV. The cross section of the sample was observed with a field-emission SEM (JSM-7001FA, JEOL). Backscattered electron (BE) images were collected to observe the compositional distribution in the oxidized surface.

4.2.3. Two-dimensional ellipsometry

The thickness distribution of an oxidized layer on the sample specimen was measured in air with the 2D ellipsometer described in 2.3. Furthermore, the changes in Ψ and Δ were investigated during degradation of the oxidized sample by galvanostatic polarization. First, the oxidized sample specimen was mounted on an epoxy resin holder with Araldite adhesive. A brass screw in contact with the back side of the sample was used to obtain electric contact with the potentiostat. The sample was put in an electrochemical cell designed for *in situ* 2D ellipsometry as shown in Fig. 2.16. The cell was filled with pure Ar gas before measurements. A pH 8.4 borate buffer deaerated with bubbling of pure Ar gas was injected into the cell. After open circuit potential (OCP) measurement for 1 h, which was sufficient to obtain a stable electrode potential within scattering of ±1 mV per 100 s, galvanostatic polarization was performed at −6 μA cm^{-2} and a potential transient of the sample electrode was recorded. Ellipsometric measurements were conducted every 300 s during the galvanostatic polarization.

4.2.4. Micro-electrochemistry

Local electrochemical measurements of the oxidized sample surface were conducted with the MCC developed in section 2.2 that had a capillary tip with an inner diameter of 200 μm and a thin silicone gasket. The tip of the cell achieved an electrolyte contact area of 3.1×10^{-4} cm^2 on the sample surface. The inside of the capillary was filled with an electrolyte of pH 8.4 borate buffer solution. After OCP measurement for 1 h, EIS was performed at a rest potential, which was the final potential of the OCP measurement, with an ac voltage amplitude of ±10 mV in a frequency range of 10^5 to 10^{-2} Hz. Subsequently, the sample electrode was kept at OCP for 1800 s and MS analysis was conducted in a potential range from 0.3 to −0.4 V (SSE) with an ac voltage of ±10 mV at a frequency of 0.1 Hz. All electrochemical measurements were conducted in an air-conditioned room at 296 K.

4.3. Results

4.3.1. Inhomogeneous growth of oxide on polycrystalline iron

Figure 4.1a shows an EBSD IPF map of a typical iron sample surface before thermal oxidation. It is clear that the sample surface consists of many grains with diameters larger than 100 μm. Figure 4.1b is an optical microscopic image of the same sample surface after thermal oxidation in air at 573 K for 1 h. The distribution of surface colors is clearly related to the substrate metallographic structure. The iron {0 0 1}, {1 0 1}, and {1 1 1} grains turned white, light pink, and blue, respectively. These colors are produced by the interference of light reflected at the sample surface. When light waves reflect at the top and bottom of a thin film (Fig, 4.2a), the condition for interference is described as

$$2nd\sin\theta_1 = (2m+1)\frac{\lambda}{2} \tag{4.1}$$

for constructive interference of reflected light and

$$2nd\sin\theta_1 = 2m\frac{\lambda}{2} \tag{4.2}$$

for destructive interference of reflected light, where n is the refractive index of the thin film, d is the thickness of the film, θ_1 is the reflex angle at the bottom of the film, m is an integer, and λ is the wavelength of incident light. Figure 4.2b shows the relation of d and the interference color of a thin film when a single layer of α-Fe_2O_3 is formed (n = 2.64 for α-Fe_2O_3, which formed on an interstitial free steel substrate at 523 K [12]). Film colors change vibrantly with increasing d, implying that the oxide thicknesses on the sample surface vary around 170–250 nm and become larger in the order of the {0 0 1} > {1 1 1} > {1 0 1} planes.

Figure 4.3 shows Raman spectra measured on iron {0 0 1}, {1 0 1}, and {1 1 1} grains after thermal oxidation. Raman bands at 225, 245, 295, 415, 500, 615, and 1320 cm^{-1} and those at 540 and 665 cm^{-1} were assigned to α-Fe_2O_3 and Fe_3O_4, respectively [13]. The Raman spectra indicate that the oxidized sample surface consists of both α-Fe_2O_3 and Fe_3O_4. The ratio of Raman scattering intensity between α-Fe_2O_3 and Fe_3O_4 depends on the substrate orientation. For example, the intensity ratios of Fe_3O_4 at 665 cm^{-1} to α-Fe_2O_3 at 1320 cm^{-1} were 1.8, 0.59 and 0.33 for iron {0 0 1}, {1 1 1}, and {1 0 1} grains, respectively. This suggests that the proportion of Fe_3O_4 in the oxide becomes larger in the order of {0 0 1} > {1 1 1} > {1 0 1} grains.

Figure 4.4 shows SEM SE images of the oxidized sample surface of {0 0 1}, {1 0 1}, and {1 1 1} grains. The {0 0 1} grain shows a homogeneous morphology with a nanometer-scale structure. However, the {1 0 1} grain shows a netted pattern with a diameter of ca. 1 μm on the whole grain surface. The surface of the {1 1 1} grain has a morphology similar to the {1 0 1} grain, although the netted pattern is broken. A cross-sectional SEM BE image of the oxidized sample surface of a {1 2 5} grain is shown in Fig. 4.5. Vertical stripes in the image are traces of

Ar ions with a CP and are not originated from mechanical grinding. The BE image with compositional contrast clearly distinguishes the oxide layer from the iron substrate. The oxide layer seems to adhere to the iron substrate without any voids at their interfaces. The image contrast in the oxide layer implies that the oxide has a multi-layered structure. The thickness of the oxide layer shown in Fig. 4.5 was 154 nm. Photoelectron spectra of the oxidized surface and standard α-Fe_2O_3 powder (Fig. 4.6) coincide well in their shape and peak energies (Fe $2p_{3/2}$ and Fe $2p_{1/2}$ at 711.0 and 724.6 eV, respectively, and satellite peak for Fe $2p_{3/2}$ at 718.8 eV [14]), indicating that the outermost layer of the sample consisted of Fe_2O_3. The results of Raman spectroscopy and XPS suggest that the oxide layer has a bi-layered structure with inner Fe_3O_4 and outer α-Fe_2O_3. This bi-layer structure agrees well with the reported structure of a thermal oxide layer on pure iron that grew at 573 K [15].

4.3.2. Two-dimensional ellipsometry in air

As noted in 4.3.1, cross-sectional SEM observation enabled to determine the oxide thickness directly. However, fabrication and observation of cross sections of all grains on a polycrystalline substrate are not a realistic approach since it requires cumbersome and numerous number of experimental trials. In order to investigate the distribution of oxide thicknesses on a polycrystalline iron surface, 2D ellipsometry was conducted in air. A bi-layer optical model shown in Fig. 4.7a was used for the ellipsometry. Although the optical constant N of oxides would be dependent on the condition for preparation and morphology of samples, the N values of $2.28 - 0.45i$ and $2.64 - 0.01i$ for Fe_3O_4 and α-Fe_2O_3, respectively, at λ = 636 nm for a thermal oxide formed on an interstitial free steel substrate at 523 K [12] were used as well as other values for air (1.00) and metal Fe ($2.87 - 3.36i$) [16]. In ellipsometry, furthermore, it has been reported that the maximum possible depth d_p of a sample is inversely proportional to the absorption coefficient α_a ($= 4\pi k/\lambda$) as follows [17]:

$$d_p \sim 5\alpha_a^{-1}. \qquad (4.3)$$

In the case of λ = 636 nm, d_p for α-Fe_2O_3, Fe_3O_4, and Fe are 2.53×10^4, 562, and 75.3 nm, respectively. This assures that the oxide layers formed at 573 K for 1 h are sufficiently thin and that the iron substrate is thick enough to prevent reflection from the backside of the substrate. The thicknesses of inner Fe_3O_4 and outer α-Fe_2O_3, d_{IL} and d_{OL}, respectively, were simultaneously calculated according to Eq. 2.24.

Figures 4.7b–d show thickness distribution maps of the oxidized sample surface (Fig. 4.1) obtained by 2D ellipsometry in air using the bi-layer model shown in Fig. 4.7a. Thickness scales for all of the maps are displayed with the constant range of 60 nm. Stripe noises in the maps are artifacts originating from the differences in sensitivity of the imaging channels of the ellipsometer. The patch pattern corresponding to the thickness distribution strongly depends on the metallographic structure of the substrate (Fig. 4.1a). The value of d_{IL} is smaller than that of d_{OL}

everywhere on the sample surface and is clearly dependent on the crystal grains compared with that of d_{OL}, which shows poorer thickness contrast. The total oxide thickness d_{total} (= d_{IL} + d_{OL}) shown in Fig. 4.7d is clearly related to the interference color of the surface (Fig. 4.1b). The thickness distribution of d_{total} is more similar to that of d_{IL} than to that of d_{OL}, indicating that the substrate orientation strongly affects growth of the inner Fe_3O_4 layer.

Figure 4.8 shows the relation between crystallographic orientation of the substrate iron surface and thickness of the oxide film formed on the substrate. The ellipsometric thicknesses in Figs. 4.7b-d were plotted in an IPF for a bcc lattice structure and linearly complemented. Crystal planes are expressed by three Euler angles (φ_1, Φ, φ_2) as rotations from the sample frame to crystal frame. The Euler angles of {0 0 1}, {1 0 1}, and {1 1 1} planes at the corner of the IPF are (0°, 0°, 0°), (0°, 45°, 0°), and (0°, 55°, 45°), respectively. The values of d_{IL} and d_{total} decrease with increase in Φ and increase slightly with increase in φ_2 when Φ is larger than 45 degrees. Focusing on the corner of the IPF, d_{IL} and d_{total} become larger in the order of {0 0 1} > {1 1 1} > {1 0 1}. The order of d_{IL} is the same as that of the Raman intensity ratio of Fe_3O_4 to α-Fe_2O_3. On the other hand, d_{OL} does not show an apparent gradient of thickness (Fig. 4.8b), suggesting that the substrate orientation has little influence on the thickness of the outer α-Fe_2O_3 layer. The ellipsometric thicknesses of oxide formed on {1 2 5} are very similar to those observed with SEM, proving that these results for d_{IL}, d_{OL}, and d_{total} sufficiently correspond to the absolute thickness of the oxide layers. The combination of EBSD and 2D ellipsometry is thought to be an effective approach for obtaining the relation between oxide layer thickness and crystallographic orientation of a polycrystalline surface.

4.3.3. *In situ* 2D ellipsometry during galvanostatic polarization

Figure 4.9 shows the transient of the electrode potential during galvanostatic reduction of the oxidized iron sample in pH 8.4 borate solution. Immediately after the polarization commences, the potential declines steeply from ca. −0.33 V (SSE) and shows a plateau at ca. −0.80 V (SSE). The potential gradually decreases after 2100 s and finally reaches a steady state potential of ca. −0.88 V (SSE) after 3300 s. *Ex situ* Raman spectroscopy after polarization for 800 s revealed that the sample surface was still covered by oxide composed of α-Fe_2O_3 and Fe_3O_4 (Fig. 4.10). The Raman bands of α-Fe_2O_3 disappeared, but the single band of Fe_3O_4 at 665 cm^{-1} was observed after the electrode potential showed −0.88 V (SSE). The disappearance of the α-Fe_2O_3 layer indicates that the outer oxide is reduced at −0.80 V (SSE) by the backward reaction of Eq. 1.23 that is dominant at potentials lower than

$$E\,(\mathrm{SSE}) = -0.960 - 0.0591 \log[Fe^{2+}] \qquad (4.4)$$

according to the Pourbaix diagram (Fig. 1.7) [18]. The appearance of the second plateau corresponds to complete reduction of the α-Fe_2O_3 layer and to exposure of the Fe_3O_4 layer to the electrolyte solution. The electrode potential did not significantly change even after polarization

for 7200 s. *Ex situ* Raman spectroscopy also showed the presence of Fe_3O_4 on the surface after polarization for 7200 s (Fig. 4.10). Therefore, Fe_3O_4 cannot be completely reduced under the polarization conditions used in 4.2.3. This agrees with the results of a previous study showing that an Fe_3O_4 layer on an iron substrate was not cathodically reduced in pH 7.65 buffer solution [19]. Since the redox potential of H^+/H_2 in pH 8.4 solution is −0.695 V (SSE), it is thought that hydrogen revolution reaction is in competition with oxide reduction reactions. If an α-Fe_2O_3 layer with a thickness of 148 nm (Fig. 4.8b) was reduced by the reaction of Eq. 1.23, an electric charge of 84 mC cm^{-2} would have been required. However, the charge of 20 mC cm^{-2} was consumed during polarization for 3300 s, when the electrode potential reached the second plateau potential. This apparent difference in the charge would be due to an autoreduction process, which is simultaneous reactions of the reduction of Fe_2O_3 (Eq. 1.23) and anodic dissolution of the iron substrate (Eq. 1.18) when no external potential is applied to the substrate. This process could occur during the cathodic reduction at a low current density in neutral buffered solution [20].

Reduction behavior of the thermally oxidized specimen surface was also observed by *in situ* 2D ellipsometry. Figure 4.11 shows a series of Δ and Ψ images of the polycrystalline iron specimen surface during galvanostatic polarization in pH 8.4 solution. The n value of borate buffer solution (n = 1.335) was measured by an Abbe refractometer (NAR-1T, Atago). Two-dimensional imaging of oxide thickness was not performed for *in situ* 2D ellipsometry, since changes in the optical parameters n and k of oxides could occur during the polarization and calculated oxide thickness became inaccurate. When each pair of Δ and Ψ images was constructed by 112 × 112 measurement spots with 23-μm steps, it took 235 s to scan from bottom to top in the y-direction. This time period was sufficiently short to observe the reduction process of the oxidized surface. The patch pattern shown in Fig. 4.11 corresponds to heterogeneous oxide film thickness that depends on the metallographic structure of the substrate iron. It is clear from the images that the reduction process changes the oxide film non-uniformly. The value of Δ increases on the whole specimen surface as the polarization progresses. On the other hand, Ψ increases or decreases depending on the substrate grains. The changes in Δ and Ψ on iron {0 0 1}, {1 0 1}, and {1 1 1} grains under the galvanostatic polarization are plotted in Fig. 4.12. The values of Δ and Ψ were measured at every 300 s, and the dotted lines are ideal curves derived from the bi-layer optical model in borate solution (Fig. 4.7a) when d_{OL} changes with a constant d_{IL}. According to the ideal curves, Δ increases with decreasing d_{OL} and Ψ increases or decreases with decreasing d_{OL} and increases with decreasing d_{IL}. The plots at t = 0 s differ among the grains since initial oxide thicknesses are not the same. The values of Δ increase for all grains as the polarization progresses, indicating that the thickness of the outer α-Fe_2O_3 layer is decreased by cathodic reduction. However, the transient of Δ and Ψ is too small for complete reduction of α-Fe_2O_3 and does not follow the ideal curve if d_{IL} does not change. This suggests that alteration of oxide properties such as n and k and change in d_{IL} are caused by cathodic currents in an aqueous solution and hydrogen evolution reaction in parallel with reductive dissolution of α-Fe_2O_3. Since bulk Fe_3O_4 shows much

higher electric conduction than that of α-Fe_2O_3 (electrical conductivity σ = ca. 10^{-12} and 10^4 Ω^{-1} m^{-1} for α-Fe_2O_3 and Fe_3O_4, respectively [21,22].), it is reasonable to expect that the reduction of α-Fe_2O_3 to Fe_3O_4 occurs at their interface. *Ex situ* electron diffraction patterning disagreed with the formation of Fe_3O_4 as a reduction product of α-Fe_2O_3 [19], but there is a great possibility that the reduction could be observed by *in situ* measurement. Furthermore, the values of Δ and Ψ show different behavior depending on the substrate orientation. All of the plots shift to the direction of decrease in d_{OL}.; however, their trajectories do not show the same shapes. After polarization for 3300 s when the electrode potential showed the second plateau, plot intervals for {0 0 1} do not change remarkably, whereas those for {1 0 1} and {1 1 1} become obviously smaller. It suggests that the oxidized surface of the {0 0 1} grain with a thicker Fe_3O_4 layer is more susceptible than that of other grains to alteration of oxide properties by the cathodic polarization.

4.3.4. Electric properties of the thermal oxide film

The electric behavior of the oxidized specimen surface was investigated with EIS by means of the MCC. Figure 4.13 shows a Bode plot measured on the oxidized iron {0 0 1}, {1 0 1}, and {1 1 1} grains. The impedance magnitude $|Z|$ shows similar transients in the whole frequency range, and identical values are not observed in the low frequency region. The phase shift θ shows a single peak at ca. 10 Hz for all grains. The small negative shift of θ in the high frequency region around 10^5 Hz is an artifact, which is originated from the reference electrode [23]. Since EIS in a frequency range from 10^5 to 10^{-2} Hz did not show features of more than two time constants, the so-called Randles type $R_{ox}C$-R_{el} EEC (Fig. 3.13) was used to represent an electrode/solution interface, where R_{ox} is an ohmic resistance of the oxidized sample surface. In order to describe a non-ideal behavior of the electrode interface, CPE was introduced to the EEC instead of C. The space charge capacitance C_{SC} of the oxide film without frequency-dependent capacitance behavior is expressed using the following equation [24]:

$$C_{SC} = \frac{-1}{\left(2\pi\frac{f}{f_0}\right)^p |Z| \sin\theta}, \tag{4.5}$$

where f is the evaluation frequency, f_0 is the reference frequency. The value of f_0 was arbitrarily set to 1 Hz. Here, C_{SC} is a component that constitutes C with C_H as written in Eq. 3.4. According to Hsu and Mansfeld, the value of C is derived from CPE parameters as [25]

$$C = Q\,(\omega''_m)^{p-1}, \tag{4.6}$$

where ω''_m is the frequency at which the imaginary part of the impedance Z shows a maximum value. The average error between calculated C_{SC} and measured C was ca. 10%. Although there appears to be a slight difference in the two capacitance values, C was considered to be C_{SC} here.

In order to clarify the grain-dependent electric property of the thermally oxidized surface, MS analysis was performed at the frequency of 0.1 Hz, where θ showed grain dependency in the

Bode plot. Figure 4.14 shows MS plots measured on thermally oxidized iron {0 0 1}, {1 0 1}, and {1 1 1} grains. Capacitance behavior shows an obvious grain dependency at potentials higher than −0.15 V (SSE). The value of C_{SC}^{-2} decreases with decreasing applied electrode potential. A linear relation between C_{SC}^{-2} and E is found at a potential range from −0.15 to 0.00 V (SSE). The positive slope in this potential region indicates that the thermal oxide film has an n-type semiconductive property. The values of E_{fb} and N_D were estimated from the slope by applying the MS equation described in Eq. 3.3. Since the outermost layer of the specimen consisted of α-Fe_2O_3, ε = 12 of α-Fe_2O_3 [26] was used for the calculation of N_D. The calculated values of E_{fb} and N_D are summarized in Table 4.1. Although the values of E_{fb} are ca. 100 mV positive from that reported by Wielant et al. [27] and N_D of the {0 0 1} grain is in agreement with their report, N_D clearly shows a variance among the three grains. The N_D values of {1 0 1} and {1 1 1} grains are 6.85% and 13.5% of that of the {0 0 1} grain. The thickness of the space charge layer d_{SC} in the oxide is expressed as follows:

$$d_{SC} = \varepsilon\varepsilon_0 / C_{SC}. \quad (4.7)$$

At 0.3 V (SSE), d_{SC} values of 0.53, 1.3, and 2.1 nm were calculated for iron {0 0 1}, {1 1 1}, and {1 0 1} grains, respectively. This means that the space charge layer exists only in the outer α-Fe_2O_3 layer. Büchler et al. found that N_D of a passive film on iron correlated with Fe^{2+} content in an iron oxide [24]. Thus, the content of the doping species Fe^{2+} in α-Fe_2O_3 is assumed to be one of the factors that determine N_D of the thermally oxidized iron surface.

Table 4.1. Flat band potential E_{fb} and donor density N_D of the thermally oxidized surface of iron {0 0 1}, {1 0 1}, and {1 1 1} grains estimated from MS analysis.

Surface	E_{fb} (V (SSE))	N_D (10^{20} cm^{-3})
{0 0 1}	−0.22 ± 0.014	13 ± 1.6
{1 1 1}	−0.18 ± 0.026	1.8 ± 0.040
{1 0 1}	−0.19 ± 0.0072	0.89 ± 0.19

4.4. Discussion

The bi-layered oxide structure was constructed by two-step oxidation [3]. It has been reported that the growth of the inner Fe_3O_4 layer is controlled by iron ion diffusion from the substrate iron, whereas the growth of the outer α-Fe_2O_3 layer is governed by oxide ion diffusion from gas phase [28,29]. At first, Fe_3O_4 grows at the iron/air interface. Then α-Fe_2O_3 platelets start to form on the Fe_3O_4 layer and finally cover the entire surface, resulting in reduction of the oxidation rate by reducing the flux of iron ions from the substrate. Therefore, the growth rate of the Fe_3O_4 layer in the initial period of oxidation and/or the surface coverage rate of the α-Fe_2O_3

layer can determine the total oxide thickness. Two-dimensional ellipsometry revealed that d_{IL} became larger in the order of {0 0 1} > {1 1 1} > {1 0 1} grains. This relation accords with the calculated value of surface energy γ for bcc iron (Table 1.2). Thus, it is reasonable that a thicker oxide layer grows at crystal planes with greater γ, i.e., the surface activity for oxidation. The little grain dependency in d_{OL} can be explained by the following: (i) the growth of α-Fe_2O_3 was controlled by oxide ion diffusion from gas phase and had little dependency on substrate crystallographic orientation and (ii) the oxidation period of 1 h was insufficient to observe an obvious difference at the reduced oxidation rate.

On the other hand, the preferred growth direction of oxides affects the oxidation rate. Boggs et al. suggested that anisotropic growth of oxides resulted in the characteristic geometry at Fe/Fe_3O_4 and Fe_3O_4/α-Fe_2O_3 interfaces [4]. They found that the lateral spread of α-Fe_2O_3 was faster when the angles between the (1 1 1) plane of Fe_3O_4 and the surface plane of iron was closer since α-Fe_2O_3 preferentially grew on the Fe_3O_4 (1 1 1) plane. This mechanism is explained by the growth directions of both oxides. Figure 4.15 shows a schematic diagram of the iron/Fe_3O_4 interface. The presence of a thin γ-Fe_2O_3 layer at the Fe_3O_4/α-Fe_2O_3 interface reported by Buob et al. [19] is not discussed here. Since γ-Fe_2O_3 and Fe_3O_4 have the same oxygen close-packed spinel structure with similar lattice constants (8.34 Å for γ-Fe_2O_3 and 8.40 Å for Fe_3O_4 [31]), it is assumed that γ-Fe_2O_3 has little influence on the growth of α-Fe_2O_3. The misorientation angles between the iron surface and Fe_3O_4 (1 1 1) plane are 55, 39 and 75, and 0 degrees for iron {0 0 1}, {1 1 1}, and {1 0 1} planes, respectively. It is thought that the α-Fe_2O_3 layer covers the relatively flat Fe_3O_4 surface on the iron {1 0 1} plane more rapidly than on the other planes, and d_{IL} and d_{total} become the smallest for the iron {1 0 1} grain. The misorientation angles also indicate that the vector components to the sample ND for iron {0 0 1} and {1 1 1} planes become 0.57 and 0.78, respectively, when the vector of the Fe_3O_4 <1 1 1> direction is set to unity. This difference is related to the formation rate of Fe_3O_4 and is assumed to correlate with d_{IL}. It is thought that the anisotropic growth of the inner Fe_3O_4 layer has a great role in the thermal oxidation of iron, and the thermally grown oxide on polycrystalline iron becomes heterogeneous in d_{IL} and d_{total}.

MS analysis with the MCC revealed that N_D of the oxidized iron surface became greater in the order of {0 0 1} > {1 1 1} > {1 0 1} grains. Since N_D here represents the density of defects in the outer α-Fe_2O_3 layer rather than that of the inner Fe_3O_4 layer, it is expected that the anisotropic growth of oxides affects the grain dependency in N_D. Since the volume ratio of α-Fe_2O_3 to Fe_3O_4 is 1.02 [32], the α-Fe_2O_3 layer on the iron {1 0 1} grain grows with less compressive stress in it and shows lower N_D than those of the other grains. However, the growth direction of α-Fe_2O_3 on iron {0 0 1} and {1 1 1} planes is not perpendicular to the sample ND (Fig. 4.15), and α-Fe_2O_3 also grows in the lateral direction. The lateral component of the growth direction causes compressive stress in α-Fe_2O_3 with its growth, resulting in large defects, such as oxygen ion vacancies and high Fe^{2+} content, and in high N_D. When the vector of the Fe_3O_4 <1 1 1> direction is set to unity, the sums of two opposite vectors parallel to the surface plane of iron are 1.64 and

1.52 for the iron {0 0 1} and {1 1 1} planes, respectively, whereas that for the iron {1 0 1} plane is zero. These values suggest that α-Fe_2O_3 formed on iron {0 0 1} grains contains the highest defect concentration. Moreover, N_D and d_{IL} for each iron grain showed a positive relation. The grain dependency in both N_D and d_{IL} was considered to be the anisotropic growth of oxides. It is thought that the contour plot of d_{IL} (Fig. 4.8a) indirectly shows the relation between N_D of the oxidized surface and crystallographic orientation of the substrate iron.

4.5. Conclusions

The heterogeneity of a thermally oxidized polycrystalline iron surface was investigated by using 2D ellipsometry and an MCC. The thermally grown oxides on an iron specimen had a bi-layered structure with an inner Fe_3O_4 layer and an outer α-Fe_2O_3 layer. The 2D ellipsometry demonstrated that the thickness d_{IL} of the inner Fe_3O_4 layer clearly depended on substrate orientation, whereas the thickness d_{OL} of the outer α-Fe_2O_3 layer did not show obvious grain dependency. Two-dimensional imaging of oxide thicknesses on the polycrystalline iron specimen enabled the construction of contour maps of d_{IL} and d_{OL} on an IPF map of bcc iron. The thickness gradient on the IPF could be explained by using Euler angles Φ and φ_2. *In situ* observation of the specimen surface by 2D ellipsometry was conducted during galvanostatic cathodic polarization, and it was revealed that the transient of ellipsometric parameters Δ and Ψ showed different behavior depending on the substrate orientation. This grain-dependent degradation behavior was considered to be mainly due to changes in optical properties of the oxide layers caused by cathodic reaction including hydrogen evolution reaction. MS analysis with the MCC on iron was also carried out. The donor density N_D of α-Fe_2O_3 obviously depended on the substrate orientation and was greater in the order of {0 0 1} > {1 1 1} > {1 0 1} grains. The anisotropic growth of oxides was considered to be a key factor that caused the grain dependency on d_{IL} and N_D. The results suggested that the surface coverage rate of the outer α-Fe_2O_3 layer determined d_{IL} and that the lateral component of the growth direction generated more defects in α-Fe_2O_3.

References

[1] E. J. Caule, K. H. Buob, and M. Cohen, *J. Electrochem. Soc.*, **108**, 829 (1961).

[2] W. E. Boggs, R. H. Kachik, and G. E. Pellissier, *J. Electrochem. Soc.*, **112**, 539 (1965).

[3] R. Y. Chen and W. Y. D. Yuen, *Oxid. Met.*, **59**, 433 (2003).

[4] W. E. Boggs, R. H. Kachik, and G. E. Pellissier, *J. Electrochem. Soc.*, **112**, 32 (1967).

[5] N. Ramasubramanian, P. B. Sewell, and M. Cohen, *J. Electrochem. Soc.*, **115**, 12 (1968).

[6] M. J. Graham and R. J. Hussey, *Oxid. Met.*, **15**, 407 (1981).

[7] H. Okamoto, *Desk Handbook Phase Diagrams for Binary Alloys*, 2nd ed., p. 384, ASM

International, Ohio (2010).

[8] M. J. Pryor and U. R. Evans, *J. Chem. Soc.*, 1259 (1950).

[9] P. B. Sewell, C. D. Stockbridge, and M. Cohen, *J. Electrochem. Soc.*, **108**, 933 (1961).

[10] B.-K. Kim and J. A. Szpunar, *Scr. Mater.*, **44**, 2605 (2001).

[11] C. Juricic, H. Pinto, D. Cardinali, M. Klaus, C. Genzel, and A. R. Pyzalla, *Oxid. Met.*, **73**, 15 (2010).

[12] V. Goossens, J. Wielant, S. Van Gils, R. Finsy, and H. Terryn, *Surf. Interface Anal.*, **38**, 489 (2006).

[13] T. Ohtsuka, K. Kubo, and N. Sato, *Corrosion*, **42**, 476 (1986).

[14] T. Yamashita and P. Hayes, *Appl. Surf. Sci.*, **254**, 2441 (2008).

[15] H. Sakai, T. Tsuji, and K. Naito, *J. Nucl. Sci. Technol.*, **21**, 844 (1984).

[16] J. H. Weaver and H. P. R. Frederikse, in *CRC Handbook of Chemistry and Physics*, W. H. Haynes and D. R. Lide, Editors, p. 12–126, CRC Press, New York (2011).

[17] M. Wakagi, H. Fujiwara, and R. W. Collins, *Thin Solid Films*, **313**–**314**, 464 (1998).

[18] M. Pourbaix, *Atlas of Electrochemical Equilibria in Aqueous Solution*, 2nd English ed., p. 307, National Association of Corrosion Engineers, Houston (1974).

[19] K. H. Buob, A. F. Beck, and M. Cohen, *J. Electrochem. Soc.*, **105**, 74 (1958).

[20] H. G. Oswin and M. Cohen, *J. Electrochem. Soc.*, **104**, 9 (1957).

[21] F. J. Morin, *Phys. Rev.*, **83**, 1005 (1951).

[22] G. V. Samsonov, *The Oxide Handbook*, p. 272, IFI/Plenum, New York (1973).

[23] F. Mansfeld, S. Lin, Y. C. Chen, and H. Shih, *J. Electrochem. Soc.*, **135**, 906 (1988).

[24] M. Büchler, P. Schmuki, H. Böhni, T. Stenberg, and T. Mäntylä, *J. Electrochem. Soc.*, **145**, 378 (1998).

[25] C. H. Hsu and F. Mansfeld, *Corrosion*, **57**, 747 (2001).

[26] K. F. Young and H. P. R. Frederikse, *J. Phys. Chem. Ref. Data*, **2**, 313 (1973).

[27] J. Wielant, V. Goossens, R. Hausbrand, and H. Terryn, *Electrochim. Acta*, **52**, 7617 (2007).

[28] M. H. Davies, M. T. Simnad, and C. E. Birchenall, *J. Met.*, **3**, 889 (1951).

[29] M. H. Davies, M. T. Simnad, and C. E. Birchenall, *J. Met.*, **5**, 1250 (1953).

[30] B.-Q. Fu, W. Liu, and Z.-L. Li, *Appl. Surf. Sci.*, **255**, 8511 (2009).

[31] W. A. Deer, R. A. Howie, and J. Zussman, *An Introduction to the Rock-Forming Minerals*, 3rd ed., p. 402, The Mineralogical Society, London (2013).

[32] S. D. Cramer and B. S. Covino Jr., *ASM Handbook Volume 13A: Corrosion: Fundamentals, Testing, and Protection*, p. 93, ASM International, Ohio (2004).

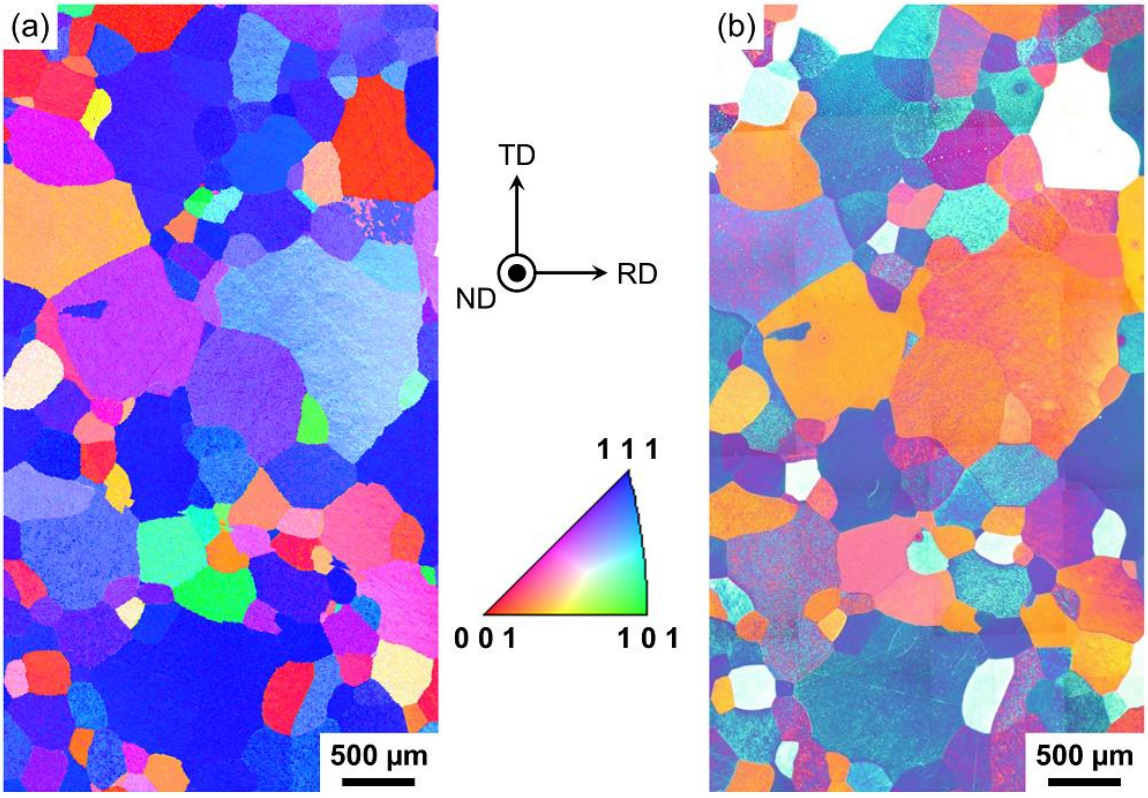

Figure 4.1. (a) Inverse pole figure map of the substrate iron surface and (b) optical image of the iron surface after thermal oxidation at 573 K in air for 1 h.

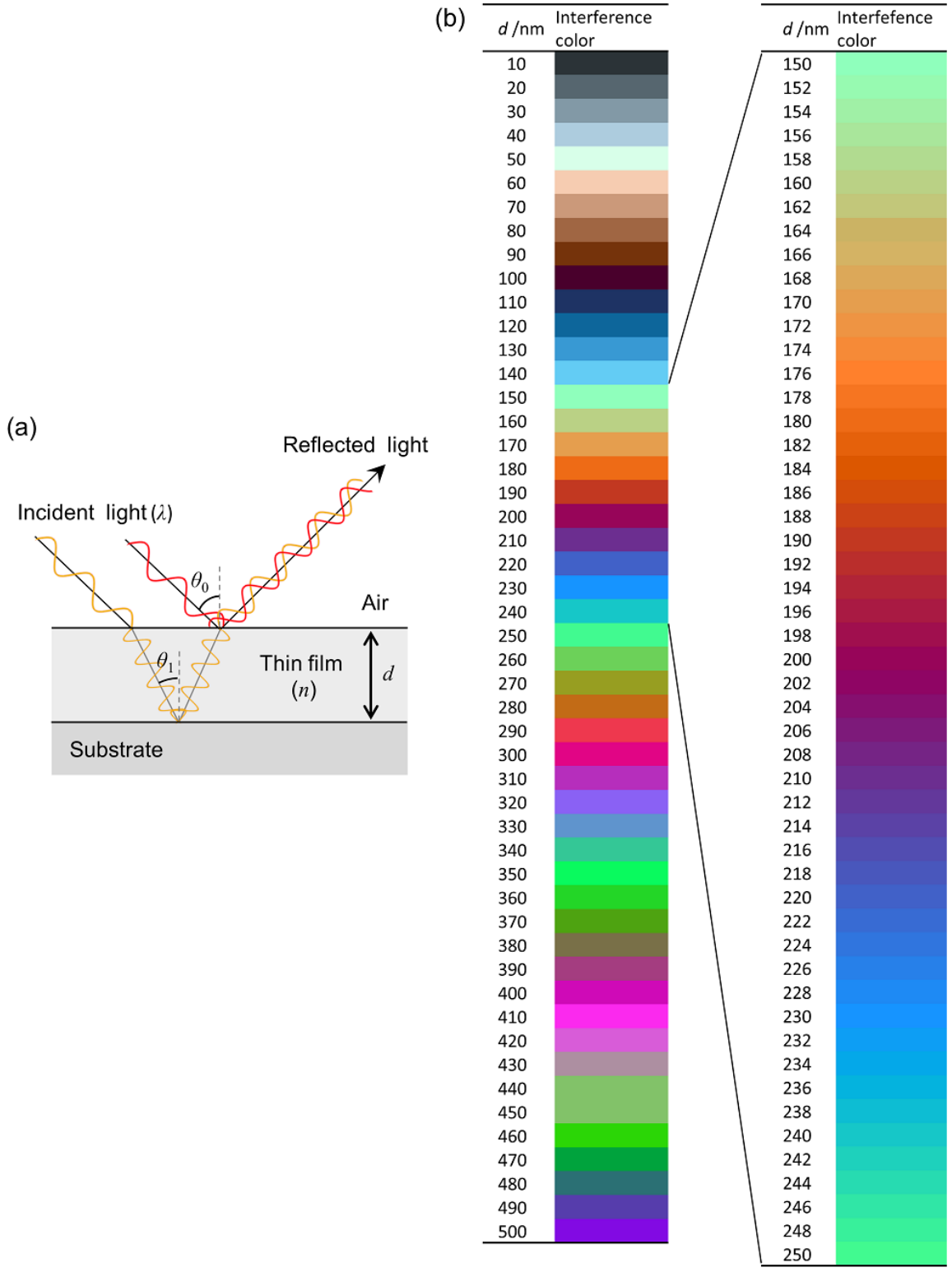

Figure 4.2. (a) Optical model of interference of light caused by a thin film on a flat substrate; (b) relation between the thickness of a thin film *d* and the color of the thin film caused by interference of light.

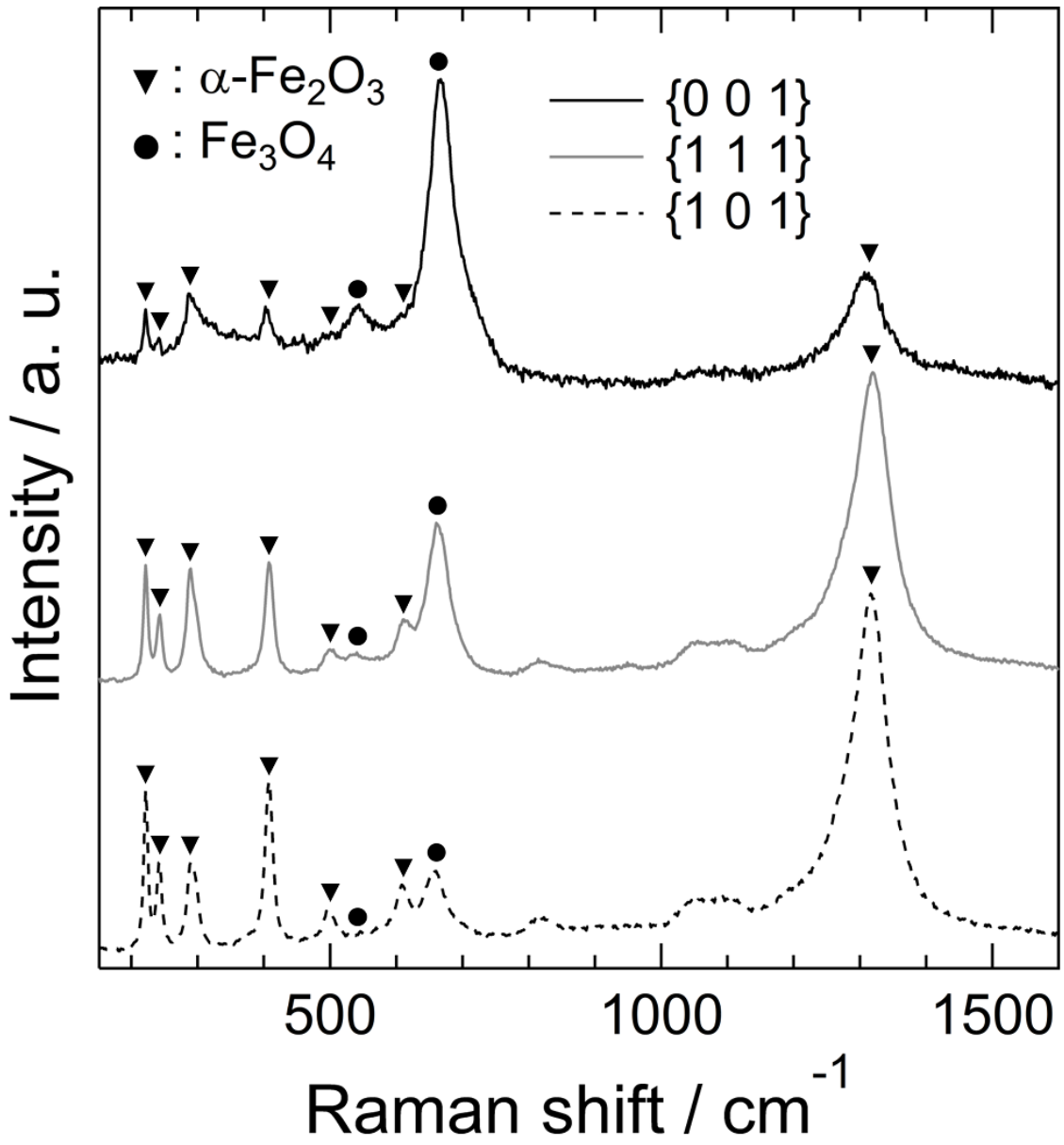

Figure 4.3. Raman spectra measured on thermally oxidized iron {0 0 1}, {1 0 1}, and {1 1 1} grains. The Raman shifts of α-Fe_2O_3 and Fe_3O_4 are marked with inverse triangles and solid circles respectively.

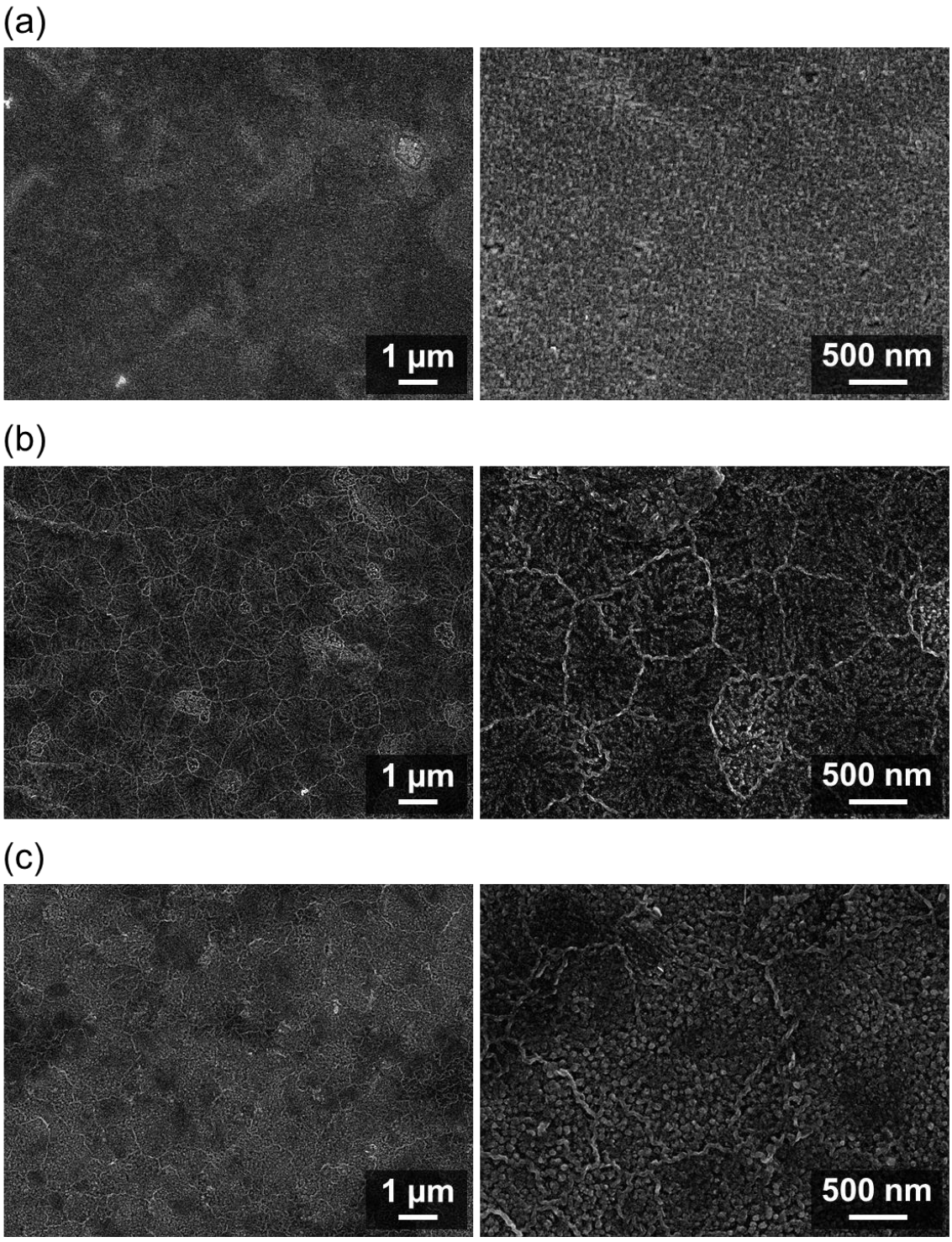

Figure 4.4. SEM SE images of the oxidized surface of iron (a) {0 0 1}, (b) {1 0 1}, and (c) {1 1 1} grains.

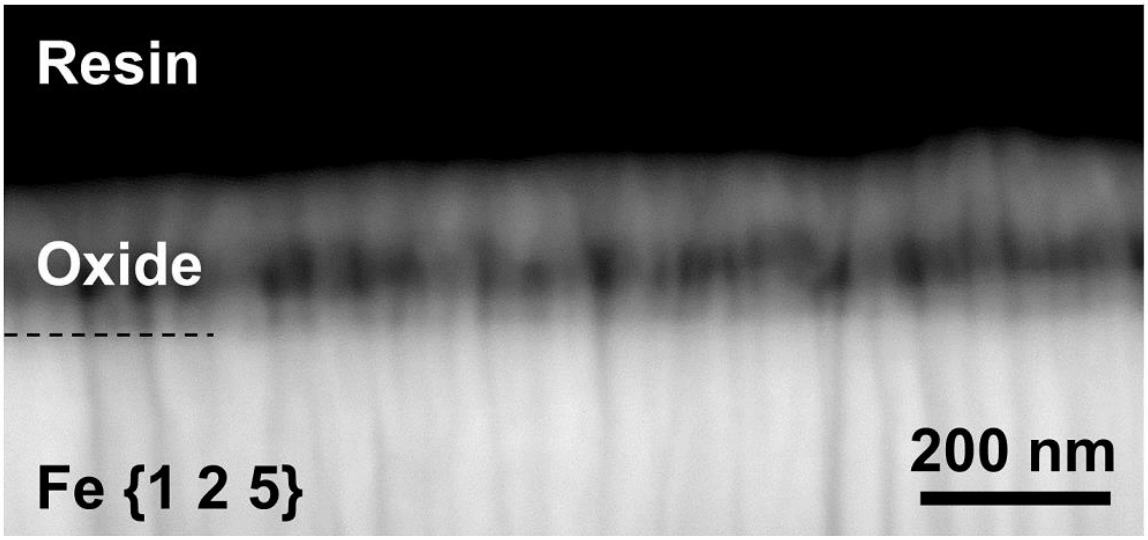

Figure 4.5. SEM cross-sectional image of the oxidized surface of an iron {1 2 5} grain (BE image with compositional contrast).

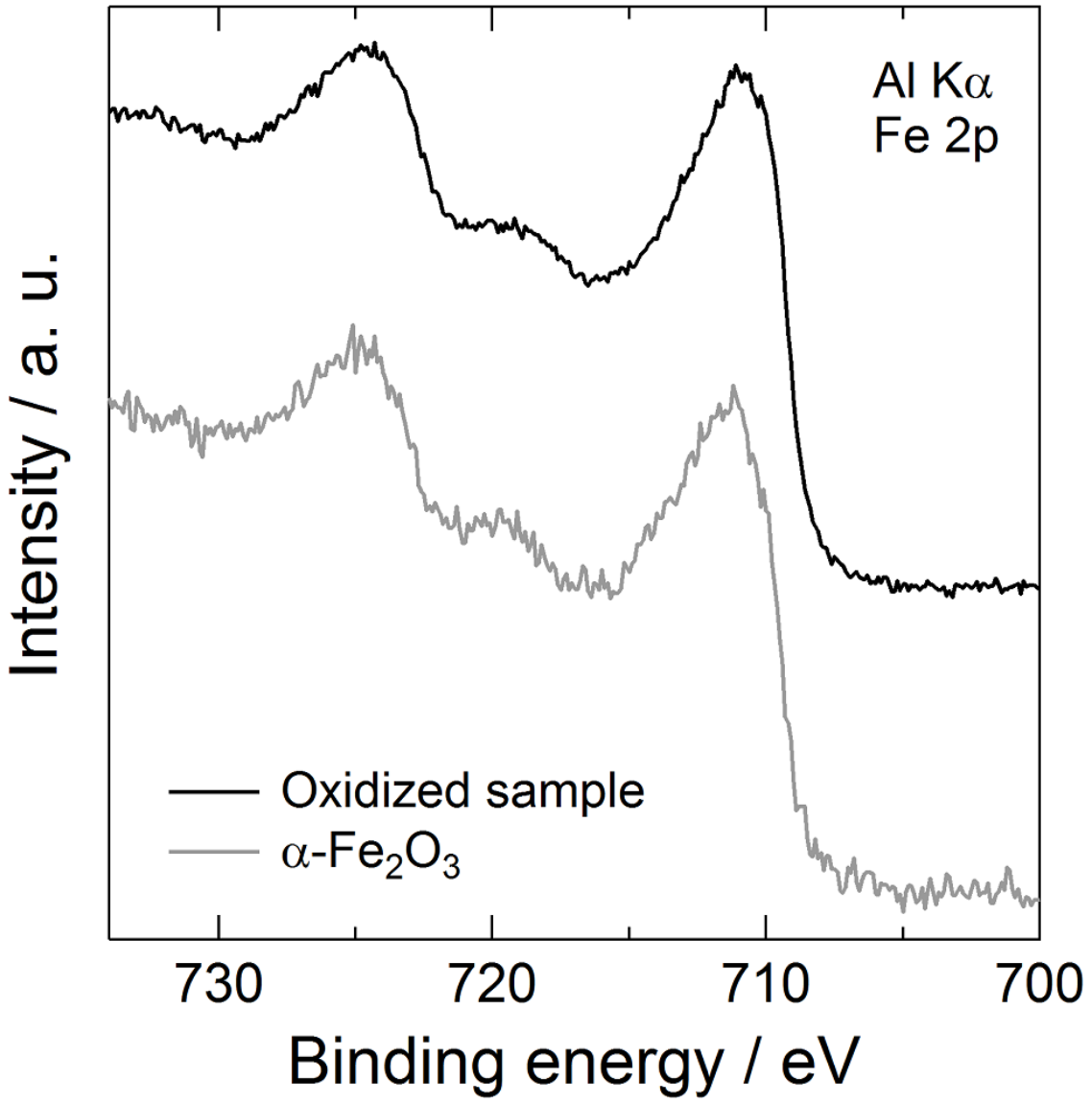

Figure 4.6. Fe 2p photoelectron spectra of the oxidized polycrystalline iron surface and α-Fe_2O_3 powder.

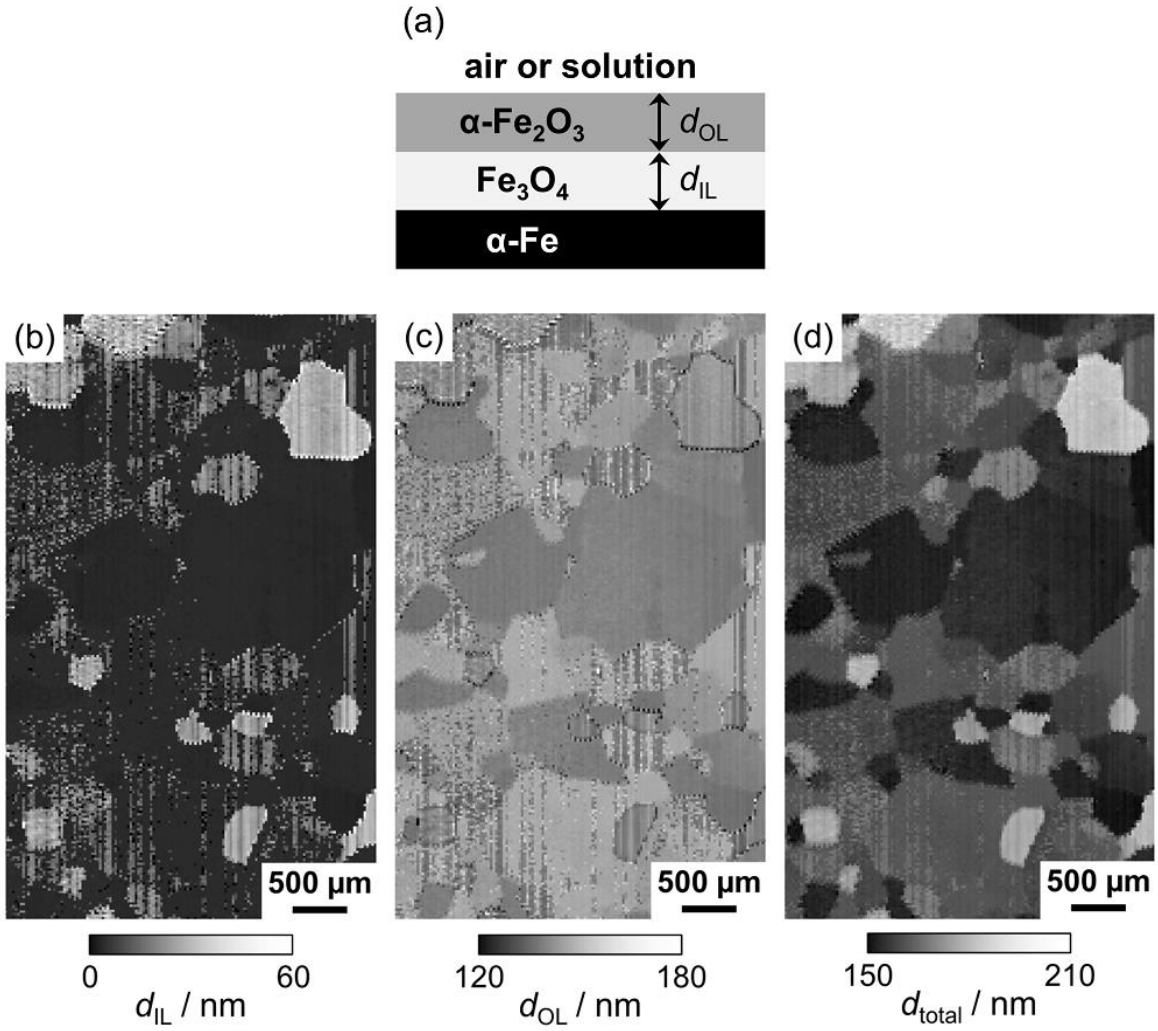

Figure 4.7. (a) Optical model used for 2D ellipsometry; d_{IL} and d_{OL}, thickness of the inner Fe_3O_4 layer and that of the outer α-Fe_2O_3 layer respectively; (b–d) 2D maps of d_{IL} and d_{OL}, and total layer thickness d_{total} (= d_{IL} + d_{OL}), with these maps showing the same sample surface as that shown in Fig. 4.1.

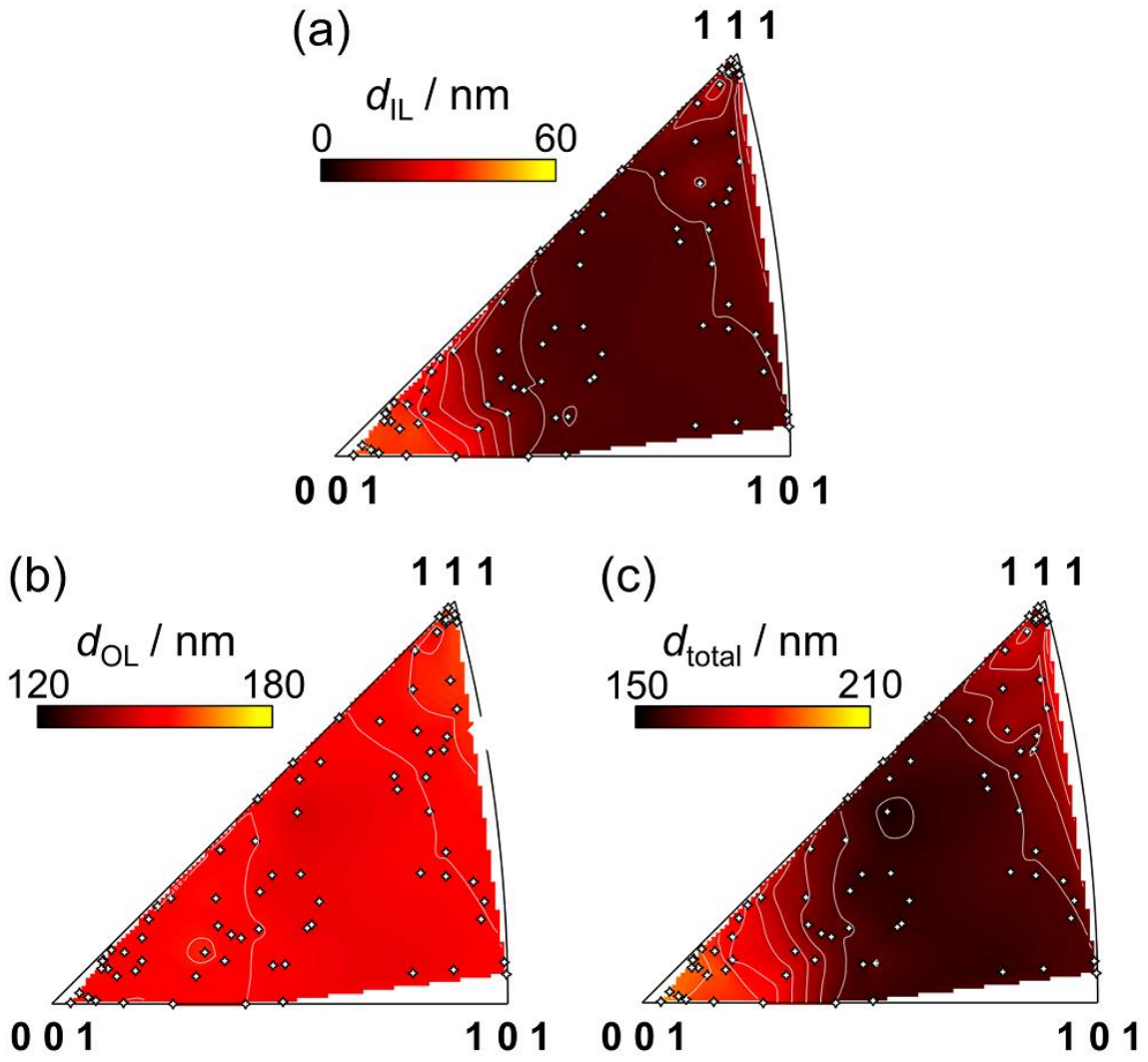

Figure 4.8. Contour maps of oxide thickness: (a) inner Fe_3O_4 layer, (b) outer α-Fe_2O_3 layer, and (c) sum of the two oxide layers. Thicknesses measured by a 2D ellipsometer were plotted as open stars to the surface crystallographic orientation of the substrate iron. The thickness gradient in the contour maps was complemented by Igor Pro 6 software (WaveMetrics) and contour lines were drawn at 5-nm intervals.

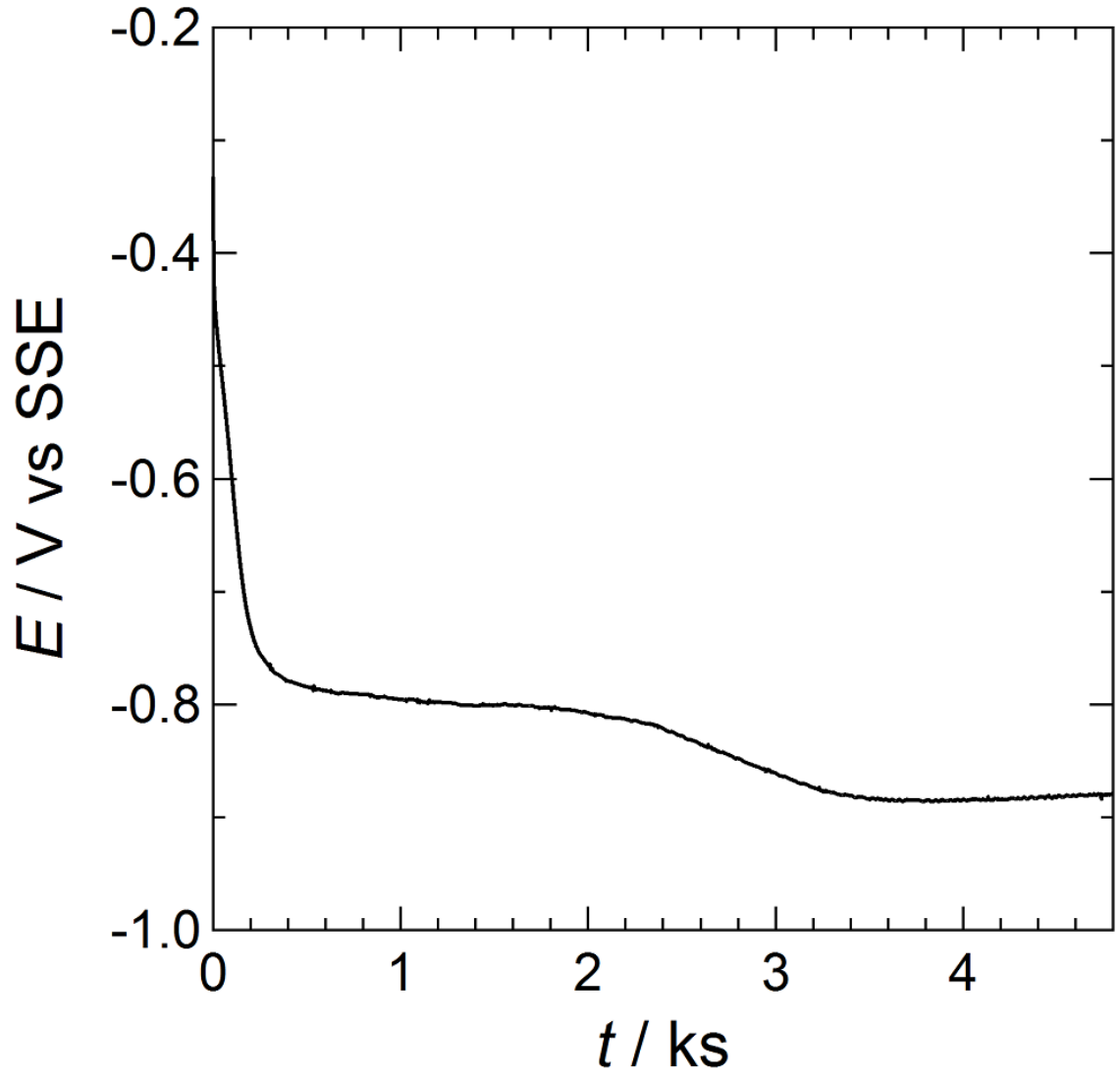

Figure 4.9. Changes in electrode potential during galvanostatic polarization of the thermally oxidized polycrystalline iron; the polarization was conducted in pH 8.4 boric acid-borate sodium solution with a current density of −6 μA cm^{-2}.

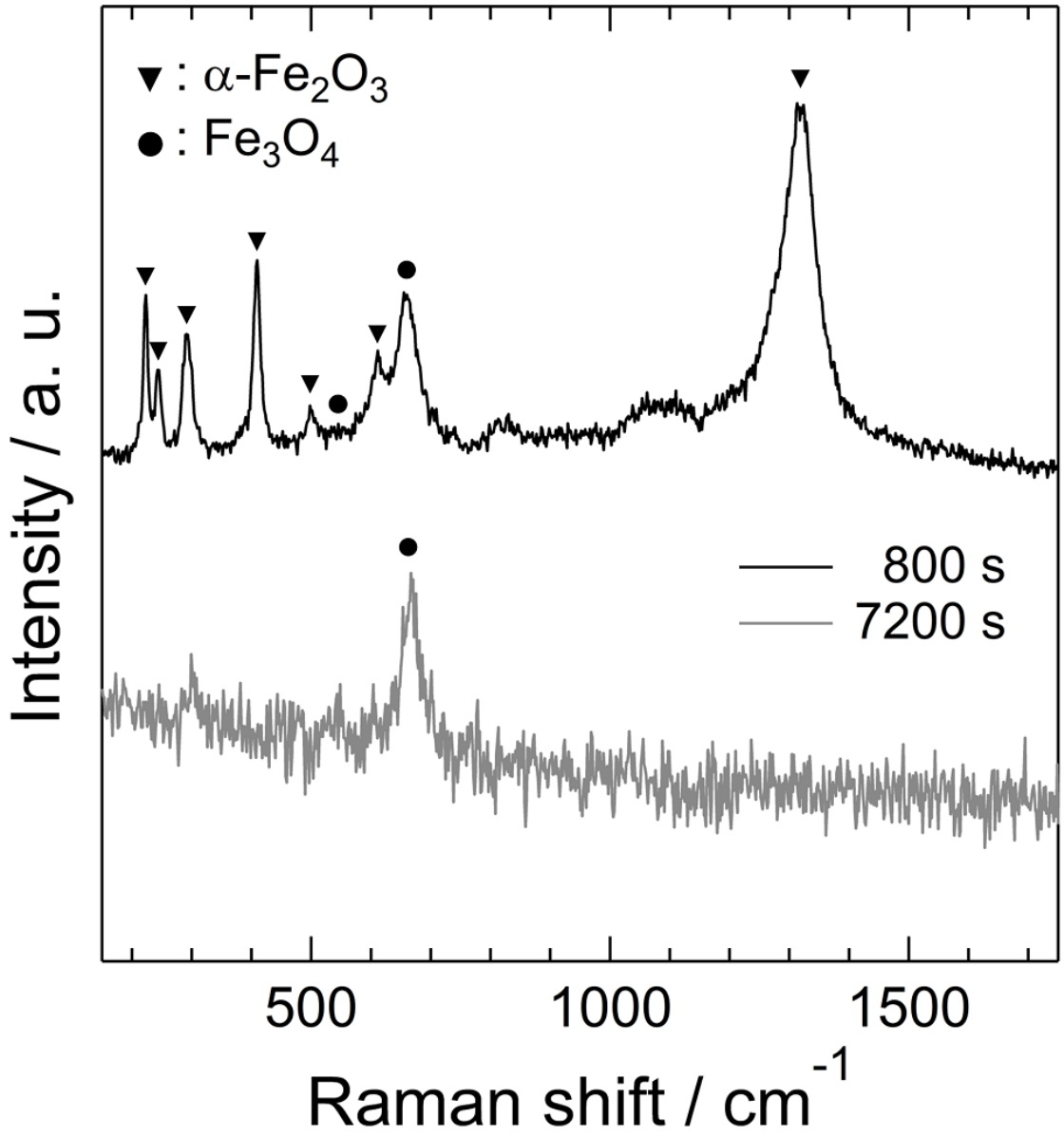

Figure 4.10. Raman spectra measured on the thermally oxidized iron surface after galvanostatic polarization for 800 s and 7200 s; the Raman shifts of α-Fe_2O_3 and Fe_3O_4 are marked with inverse triangles and solid circles respectively.

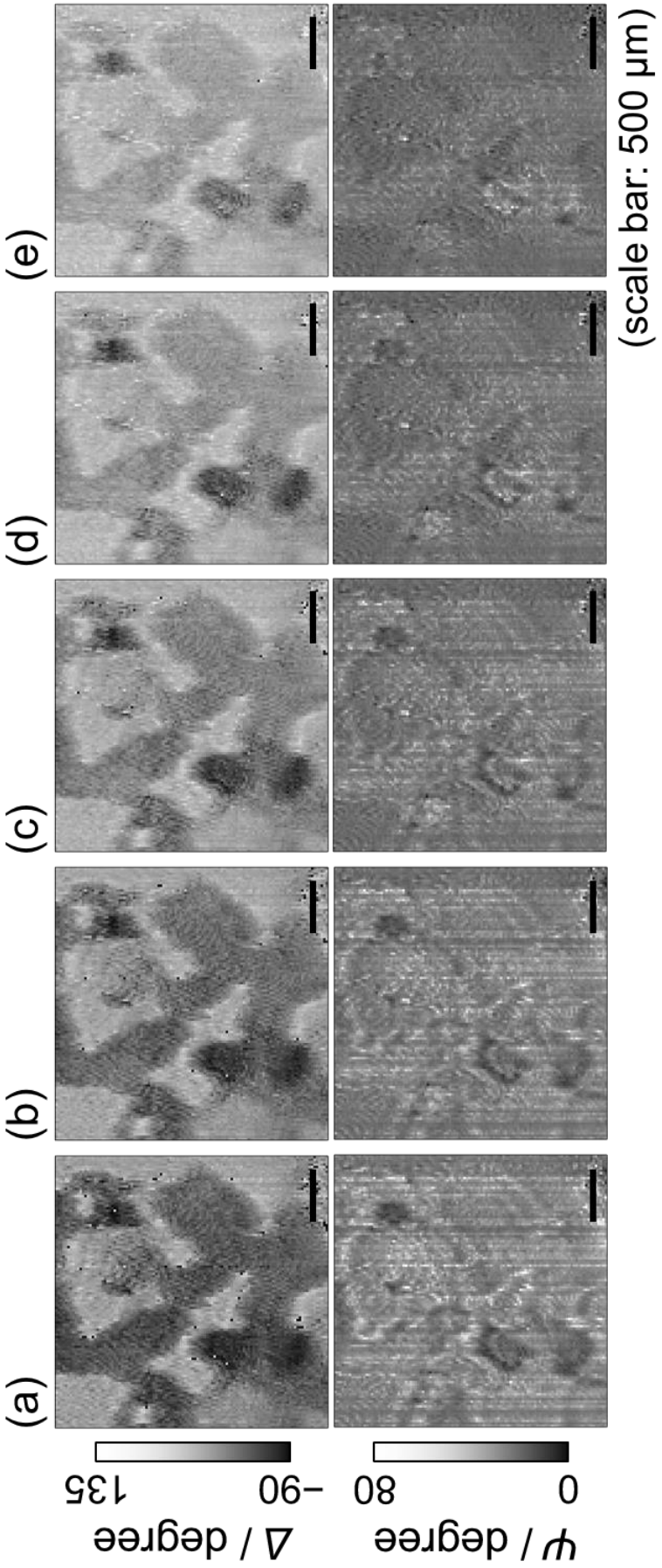

Figure 4.11. Two-dimensional images of Ψ and Δ measured on the iron specimen surface measured by 2D ellipsometry during galvanostatic polarization for (a) 0, (b) 900, (c) 1800, (d) 2700, and (e) 3600 s with a current density of −6 μA cm^{-2} in pH 8.4 boric acid-borate sodium solution.

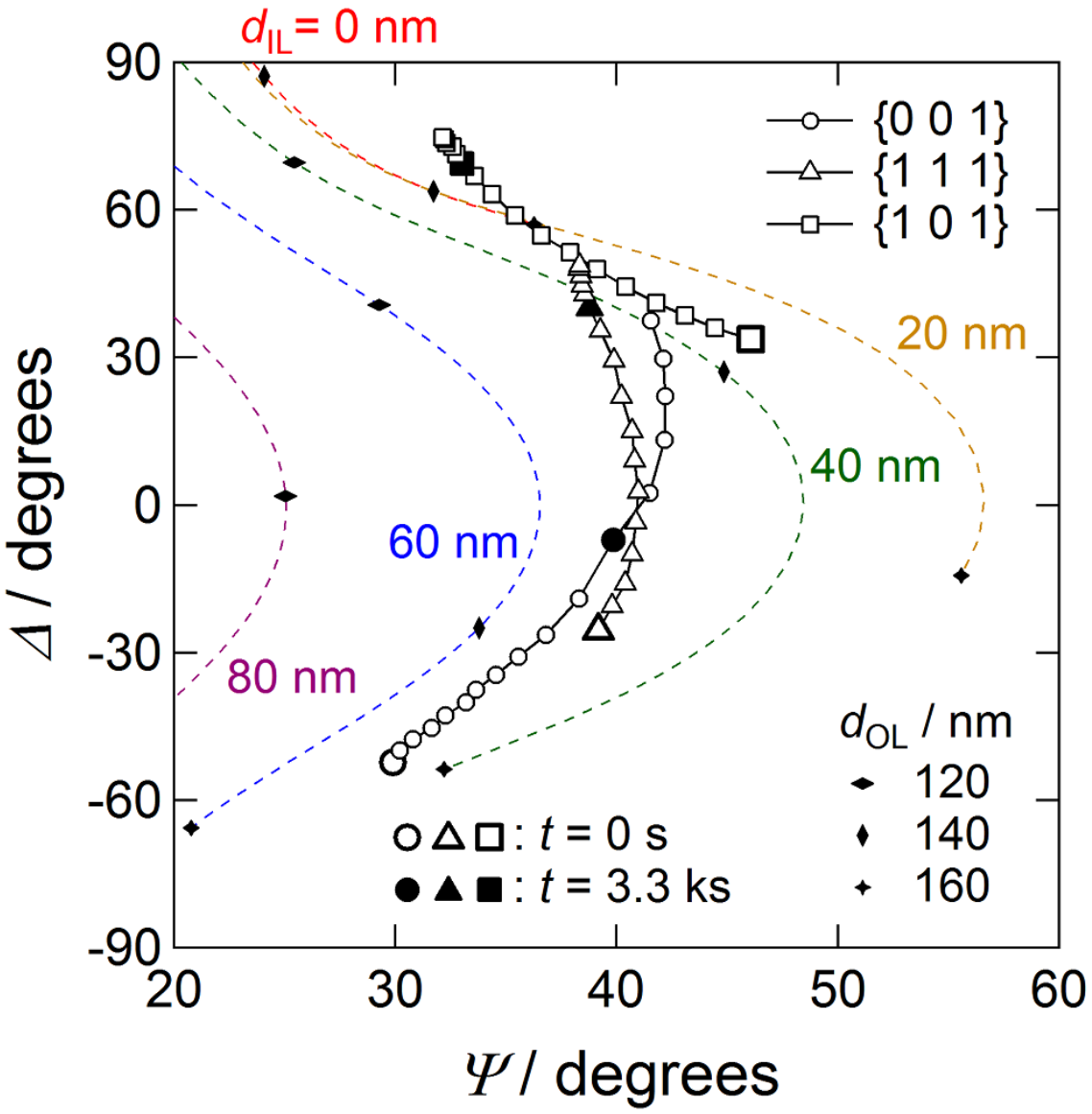

Figure 4.12. Changes in Ψ and Δ of the thermally oxidized iron surface measured at every 300 s during galvanostatic polarization. The transients of Ψ and Δ on iron {0 0 1}, {1 1 1}, and {1 0 1} grains are plotted as circles, triangles, and squares, respectively. Bold and solid markers indicate the plots at the polarization time t = 0 and 3300 s. Colored lines between dots are ideal curves calculated with the bi-layered optical model in borate solution (Fig. 4.7a) as functions of the thickness d_{OL} of an outer α-Fe_2O_3 layer when the thickness d_{IL} of an inner Fe_3O_4 layer is constant at 0, 20, 40, 60, and 80 nm, respectively. The dots in the ideal curves are plotted at 1-nm intervals and emphasized at d_{OL} = (♦) 120, (+) 140, and (x) 160 nm, respectively.

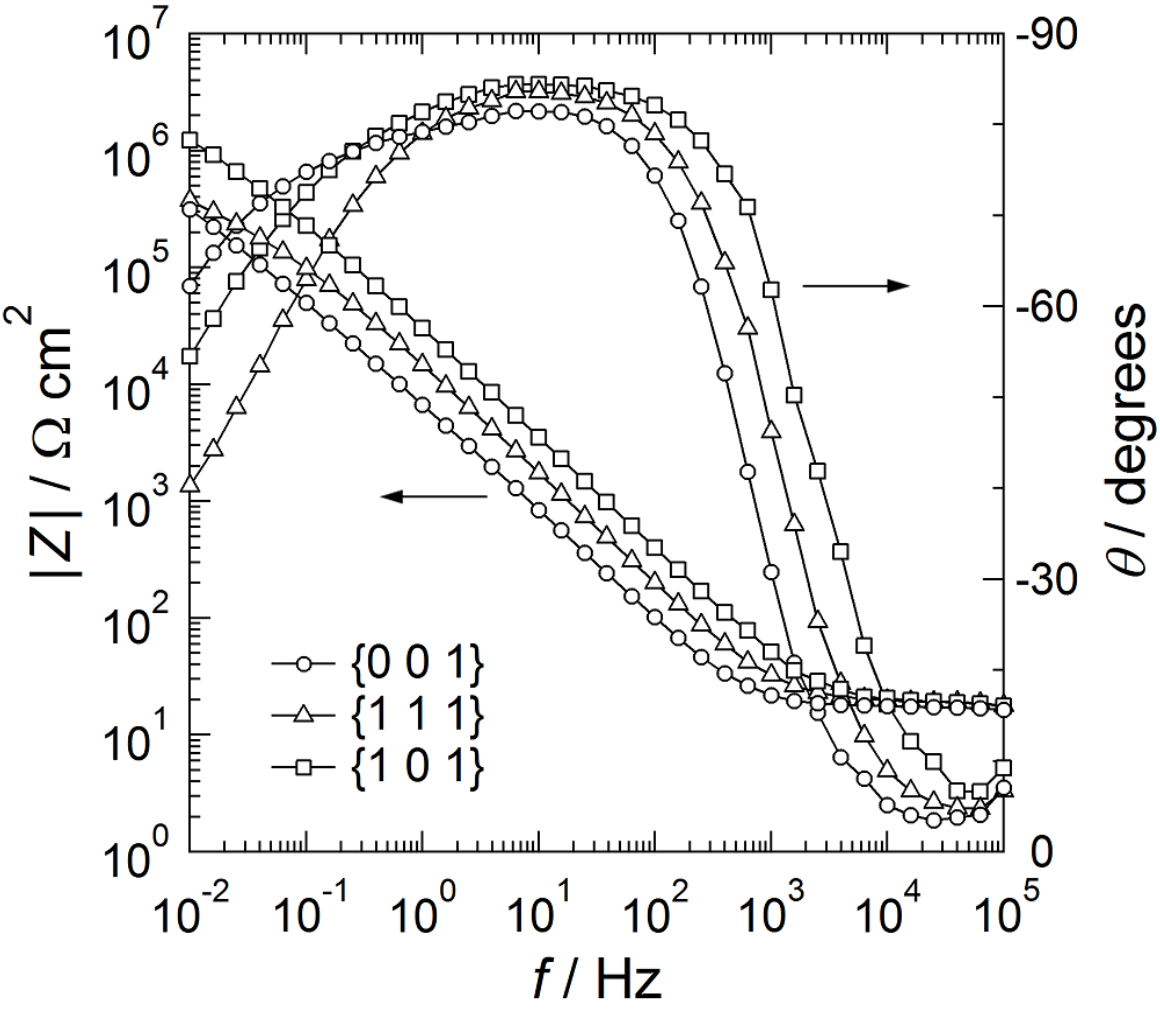

Figure 4.13. Bode plot of thermally oxidized iron {0 0 1}, {1 0 1}, and {1 1 1} grains measured by the MCC in pH 8.4 borate buffer solution.

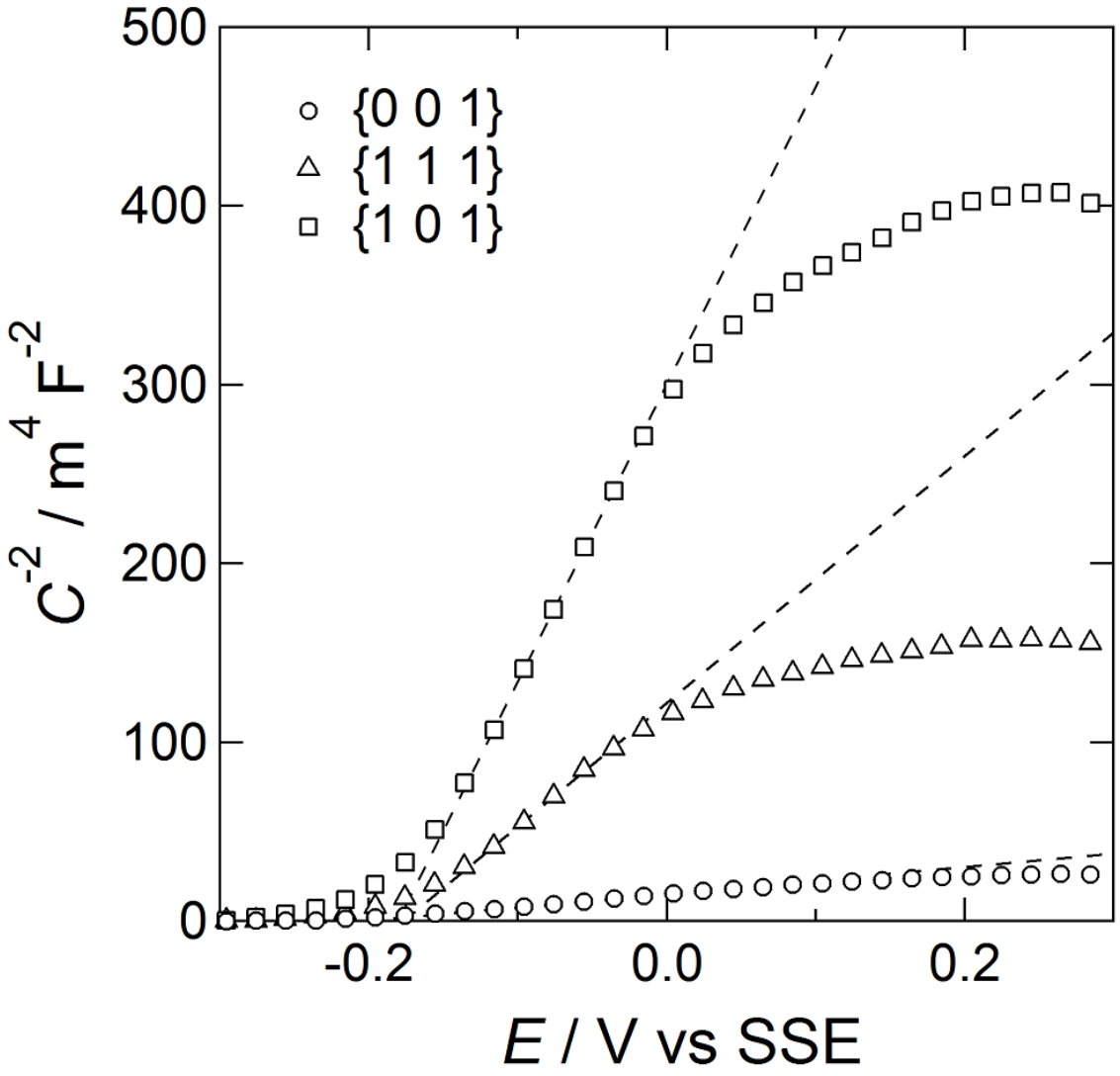

Figure 4.14. Mott-Schottky plot for thermally oxidized iron {0 0 1}, {1 0 1}, and {1 1 1} grains measured by the MCC at 0.1 Hz.

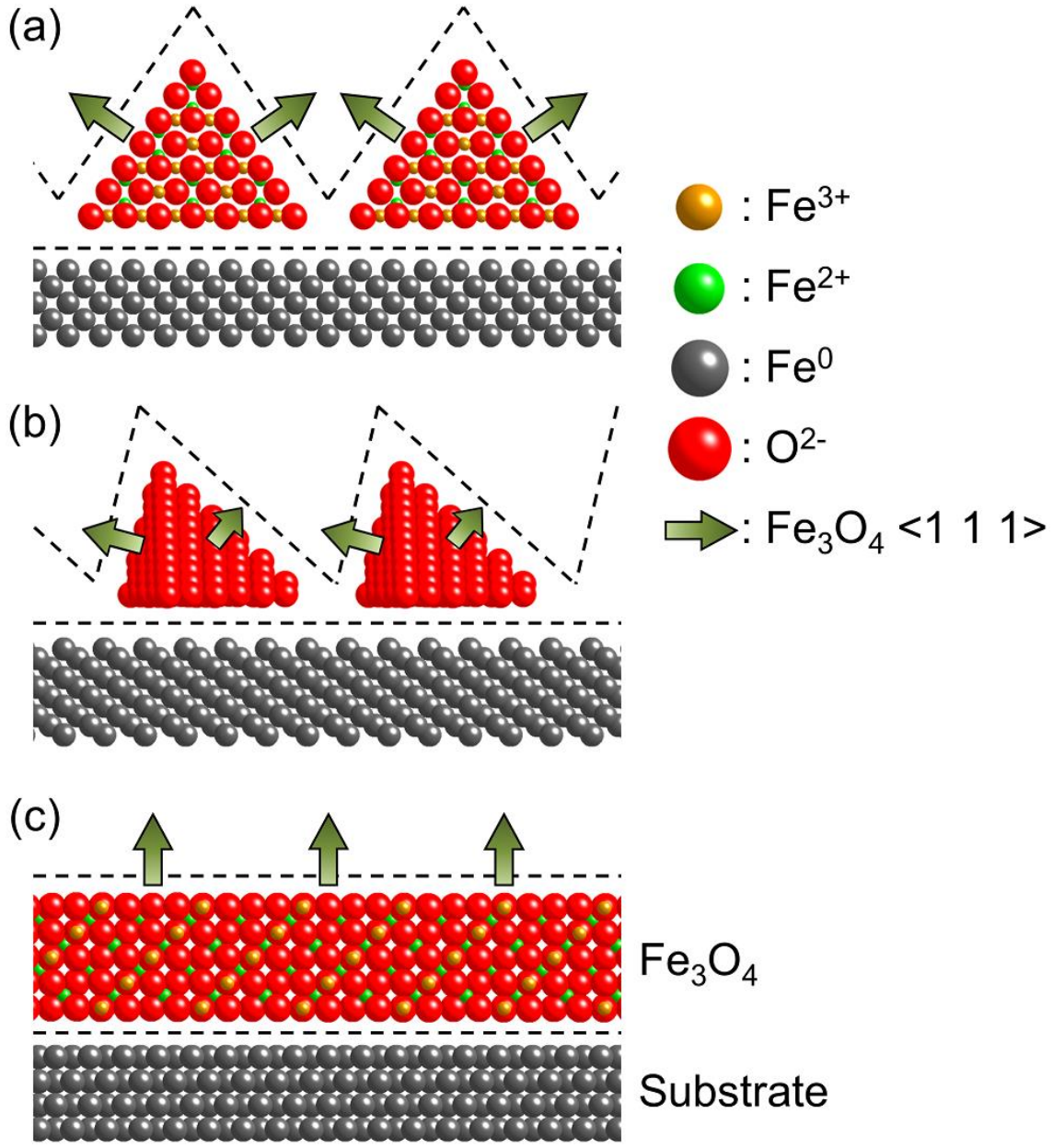

Figure 4.15. Schematic diagrams of the iron/Fe_3O_4 interface on iron (a) {0 0 1}, (b) {1 1 1}, and (c) {1 0 1} grains.

Chapter 5
Grain-dependency of passive film formed in neutral borate solution investigated by MCC and 2D ellipsometry

5.1. Introduction

As noted in Chapter 1, the structure, thickness, and characteristics of a passive film formed on iron have been intensively studied in neutral borate buffer solution, in which the dissolution of the film and/or the substrate into the solution is negligible. However, most previous studies on passive film have used a polycrystalline electrode, thus overlooking heterogeneous passivation behavior that might occur on the polycrystalline substrate due to the grain-dependent passivation that is affected by the various crystallographic orientations of surface grains.

Davenport et al. [1], who conducted *in situ* XRD, observed that the structure of the passive film depended on the surface crystallographic orientation. They used single crystals as sample specimens and explained that the difference in the structure of the passive film was due to the epitaxial relationship between the film and the substrate. The heterogeneity of the passive film formed on whole polycrystalline iron surface was examined by Fushimi et al. [2], who performed SECM in pH 8.4 borate buffer solution. The probe current, which reflected the tunneling current through the passive film, obviously depended on the substrate grains and the current flowed above the grain surface oriented to the {1 0 0} plane was less than that above the grain surface oriented to the {1 1 0} and {1 1 1} planes, indicating that the electronic resistivity of the film differed among the substrate grains. They ascribed their results largely to the difference in thickness of the passive films.

As noted above, the heterogeneity of the passive film formed on a polycrystalline iron surface has been reported. However, the passivation behavior of each grain has not been studied and the mechanism that leads to the grain dependency of the film remains unclear. In Chapter 3, grain-dependent passivation in pH 1.3 sulfuric acid was clearly demonstrated with an MCC technique. In Chapter 4, the heterogeneous thickness distribution and degradation behavior of the oxide film formed on whole polycrystalline substrate were successfully observed by *in situ* 2D ellipsometry. Thus, the combination of these techniques is expected to clarify the precise

mechanism of grain-dependent passivation of polycrystalline iron by examining the passivation behavior of both single grains and whole surface of a polycrystalline substrate.

In this chapter, the passivation behavior of polycrystalline iron in pH 8.4 borate buffer solution was investigated by means of *in situ* 2D ellipsometry and an MCC method. Furthermore, the electric property of a passive film formed on each grain was evaluated by EIS with the MCC.

5.2. Experimental

5.2.1. *In situ* 2D ellipsometry

The sample specimen of polycrystalline iron prepared in section 2.1 was mounted on an epoxy resin holder and placed in an electrochemical cell designed for *in situ* 2D ellipsometry (Fig. 2.16). At first, a native oxide film that formed on the sample surface was removed by galvanostatic polarization at −6 μA cm^{-2} in pH 6.5 borate buffer for 400 s. After the electrolyte solution was changed to fresh solution of pH 8.4 borate buffer solution, E_{corr} was measured for 10 s and followed by potentiodynamic polarization from (E_{corr} − 0.05 V) to 1.1 V (SSE) at a potential sweep rate of 1 mV s^{-1} or potentiostatic polarization at 0.9 V (SSE) for 24 h. In parallel with the potentiostatic polarization, *in situ* 2D ellipsometry was conducted at the polarization periods of 0, 1, 6, 12, and 24 h. The changes in Ψ and Δ were measured during the potentiostatic polarization. Separately, EIS measurements were taken after the potentiostatic polarization at 0.9 V (SSE) for 1, 6, 12, and 24 h with an ac voltage amplitude of ±10 mV in the frequency range of 10^5 to 10^{-2} Hz.

5.2.2. Micro-electrochemistry

Micro-electrochemical measurements were conducted with an MCC that had a capillary tip with an inner diameter of 200 μm. The fabrication of the MCC was described in section 2.2. The tip of the cell had an electrolyte contact area of 3.1×10^{-4} cm^2 on the sample surface. An electrolyte solution of pH 8.4 borate buffer solution filled the inside of the capillary. The capillary tip was placed on a grain of the polycrystalline iron sample and potentiostatic polarization was performed at 0.9 V (SSE) for 1 h. Immediately after potentiostatic polarization, EIS was performed at 0.9 V (SSE) with an ac voltage amplitude of ±10 mV with a frequency range of 10^5 to 10^{-2} Hz. Separately, MS analysis was performed immediately after the potentiostatic polarization in a potential range from 0.4 to −0.4 V (SSE) with an ac voltage of ±5 mV at a frequency of 10 Hz.

5.2.3. Characterization of the passive film

After the potentiostatic polarization, the sample surface was examined by means of Raman spectroscopy and XPS. Raman spectra were measured on a grain of the polycrystalline substrate

by the XploRA confocal Raman microscope with a probe area of ca. 1 μm in diameter. A laser diode with a wavelength of 532 nm was used for the excitation of Raman scattering. The power of the incident laser was confined to 1 mW, and a Raman spectrum was scanned 64 times. Photoelectron spectra were measured by the JPS-9200 photoelectron spectrometer with Al Kα radiation operating at 100 W (10 kV, 10 mA). The diameter of the photoelectron detection area was confined to 200 μm by adjusting the detection apertures of the spectrometer in order to collect photoelectrons escaped from a grain on the polycrystalline substrate. The C 1s peak from contaminant carbon at 285.1 eV [3] was used as a reference for charge correction.

5.3. Results

5.3.1. *In situ* 2D ellipsometry

The entire surface of the polycrystalline iron specimen was used as a working electrode for *in situ* 2D ellipsometry. Figure 5.1 shows a dynamic polarization curve measured at a potential sweep rate of 1 mV s^{-1}. Active and passive states of iron were observed from −0.62 to 0.95 V (SSE), followed by oxygen evolution. Thus, the potential of 0.9 V (SSE) was chosen as the E_{app} value for the potentiostatic polarization at which no oxygen evolution occurs and the formation rate of a passive film was expected to be significant.

Figure 5.2 shows a double logarithmic plot for the current-time transient of the polycrystalline iron specimen under potentiostatic polarization at 0.9 V (SSE). The current decreased exponentially due to the formation of an insulating passive oxide film on the specimen. After polarization for ca. 10 s, the transient showed a constant slope (−d log j / d log t) of 0.99. When an anodic oxide film grows under high electric field in which dissolution of the oxide is negligible, the slope becomes unity [4], which suggests that the current efficiency of the film formation is close to 100% and that the film grows without dissolution of the oxide and the substrate iron. Subsequently, the slope declined to 0.67 after a few hundred seconds, likely because the dominant anodic reaction shifted from the growth to the aging of the passive oxide film.

Figure 5.3 shows an ideal curve of Δ vs Ψ when a passive oxide film formed on iron has a uniform single layer. The ideal curve for a single barrier layer of thickness d and an imaginary refractive index N of 2.50 – 0.30i [5] is drawn as a dotted line. The values of N for borate buffer solution (1.335) and metal Fe (2.87 − 3.36i [6]) were also used to draw the ideal curve, which indicates that the growth of a passive film leads to a decrease in Δ and an increase in Ψ. Figure 5.4 shows a series of 2D images of Δ and Ψ obtained from *in situ* 2D ellipsometry. Ellipsometric parameters were scanned from bottom to top of each pair of Δ and Ψ images; it took 235 s to

obtain the pair and the value in the bottom left of each image shows the average value of that image. At t = 0 s after the reduction of a native oxide film, Δ and Ψ were in good agreement with the ideal values of d = 0 nm (Δ and Ψ are 113.0 and 28.4 degrees, respectively.). The value of Δ decreased from 113.5 to 107.3 degrees at 1 h and finally decreased to 105.8 degrees at 24 h. By contrast, Ψ increased from 28.2 to 28.5 degrees at 1 h and did not show any further increase for the remaining polarization periods. Impedance spectra of the passive film (Fig. 5.5) show that the electric resistance at the electrode surface increases as polarization progress, suggesting that the thickness of the passive film increases or that the aging of the film progresses in 24-h polarization. According to the least-squares calculation in Eq. 2.24, the thickness of the passive film formed at 24-h polarization was derived as 3.1 nm, which is slightly thinner than the reported thickness (ca. 4.5 nm) [7] and is likely due to the absence of grain boundaries on a single grain electrode or a difference in λ used in the ellipsometer. Although the growth of an oxide film was observed, heterogeneous transients that correspond to the metallographic texture of the substrate iron (Fig. 2.6) were not clearly observed in the 2D images.

5.3.2. Characterization of the passive film

Figure 5.6 shows *ex situ* Raman spectra measured on iron {0 0 1}, {1 0 1}, and {1 1 1} grains after potentiostatic polarization. All spectra show no clear Raman peaks except for a broad peak at ca. 670 cm^{-1}; this broad peak corresponds to strong Raman shifts of γ-Fe_2O_3 and Fe_3O_4 (at 645, 670 and 715 cm^{-1}, and 665 cm^{-1} [8]). The shapes of the Raman spectra are quite similar to those of a passive film formed on iron in same media [9]. The oxide composition assigned from the broad peak is in agreement with the reported bi-layer structure—an inner Fe_3O_4 layer and an outer γ-Fe_2O_3 layer [10,11]—of the passive film formed on iron. Figure 5.7 shows photoelectron spectra obtained from iron {0 0 1}, {1 0 1}, and {1 1 1} grains after potentiostatic polarization. The photoelectron peak corresponding to Fe^{3+} is observed at 710.9 eV in Fe $2p_{3/2}$ spectra, although it is shifted by 0.4 eV from the standard reported peak [12]. However, a peak of Fe^{2+} that is 0.9 eV negative from Fe^{3+} is not clearly observed in the spectra. The small peak around 707 eV is assigned to substrate Fe^0, indicating that the thickness of the passive film is similar to the escape depth of photoelectrons, since an inelastic mean free path of Fe at Al Kα radiation [13] is ca. 2 nm. On the other hand, a peak corresponding to O^{2-} is observed at 530.2 eV in the O 1s spectra. The broad bottom of the peak at higher energies indicates the presence of hydroxides on the outermost layer of the passive film. In any case, the three grains show quite similar spectra of both Raman scattering and photoelectrons, indicating that the composition of the oxide film is independent of the substrate orientation.

5.3.3. Micro-electrochemical measurements

Figure 5.8 shows a double logarithmic plot for current-time transients of three iron grains

during potentiostatic polarization at 0.9 V (SSE), as measured with the MCC. In the initial period of polarization of a few seconds, a relatively large current flowed due to charging of the double layer and subsequent active dissolution of the iron surface; it became greater in the order of iron {1 0 1} > {1 1 1} > {0 0 1} grains. This grain dependency is thought to be due to the differences in the surface atom density ρ_{surf} and the work function Φ_w (Table 1.2). The lower ρ_{surf} provides stronger bonding between the uppermost and second atom layers and leads to a surface that is more stable against active dissolution [14–16], while the higher Φ_w causes a larger potential drop at the electrode/solution interface, providing a greater driving force to the dissolution. The current then decreased exponentially for all grains due to the formation of an insulating oxide film on the sample surface. After polarization for ca. 10 s, the slopes of the transients became constant at 0.98, 0.99, and 0.93 for iron {0 0 1}, {1 0 1}, and {1 1 1} grains respectively through the end of the polarization. This suggests that the passive films on a single grain measured with MCC grow with almost 100% current efficiency. However, the slope of the {1 1 1} grain is slightly gentler than those of the other grains, and the current density j_f at 1 h became greater in the order of {1 1 1} > {1 0 1} > {0 0 1} grains (Table 5.1). The magnitude order of the total charge density q_t summarized in Table 5.1 does not correlate with the j_f values of the three grains due to the large current in the initial period of the polarization. Although the presence of a native oxide film before polarization cannot be completely neglected, the grain dependency on j_f appears to be significant.

Table 5.1. Experimental parameters of potentiostatic polarization at 0.9 V (SSE) in pH 8.4 borate buffer solution.; j_f, current density at 1 h; q_t, total charge density consumed for 1 h.

Surface	j_f (10^{-9} A cm^{-2})	q_t (10^{-3} C cm^{-2})
{0 0 1}	64 ± 8.6	1.7 ± 0.22
{1 1 1}	100 ± 5.2	2.1 ± 0.16
{1 0 1}	97 ± 4.5	2.5 ± 0.070

Figure 5.9 shows a Bode plot and a Nyquist plot measured by EIS immediately after the 1-h potentiostatic polarization of three iron grains with the MCC. The values of the impedance magnitude $|Z|$ and the phase shift θ show almost the same spectra for the three grains. Since impedance spectra in the frequency region from 10^5 to 10^{-2} Hz do not show a significant feature of more than two time constants, it is reasonable to use the Randles-type EEC shown in Fig. 3.13 to represent an electrode/solution interface. In this chapter, CPE was substituted for C according to Eq. 3.2. The values of R_{ct} and C obtained by curve fittings of the impedance spectra are summarized in Table 5.2. The values of R_{ct} are slightly greater than the reported value (R_{ct} = 1.2 MΩ cm^2 [17]) due to the higher film formation potential. The order of R_{ct} among the three grains shows a negative correlation with j_f. The small difference in C means that the thickness of the

oxide film formed on each grain differ less from one another.

Figure 5.10 shows typical MS plots of passive films formed on iron {0 0 1}, {1 0 1}, and {1 1 1} grains. An inverse square of capacitance shows a grain dependency at potentials higher than −0.15 V (SSE). Linear relations between C^{-2} and E in the potential region from −0.15 to 0.20 V (SSE) show positive slopes, indicating that the passive film has an n-type semiconductive property. The values of E_{fb} and N_D are estimated from the slope and the intercept of the relation on a potential axis, respectively, using Eq. 3.3. Since the value of C obtained by EIS was much smaller than that of C_H reported for iron in pH 8.4 borate solution (C_H = 134 μF cm^{-2} [18]), C as measured was regarded as C_{SC} here. Assuming ε = 40 of a passive film on iron [19], the values of E_{fb} and N_D are calculated as summarized in Table 5.2. The values of E_{fb} are almost constant among the three grains, though they are slightly higher than reported values [17,19]. This suggests that the energy levels of the valence and conduction bands of the film are quite similar and that the composition of the passive films is independent of the substrate crystallographic orientation. On the other hand, N_D shows a grain dependency and becomes larger in the order of {1 1 1} > {0 0 1} > {1 0 1} grains, implying that the defect concentration of the passive film becomes greater in the same order as N_D.

Table 5.2. Experimental parameters estimated from EIS and MS analysis. R_{ct}, charge transfer resistance; C, interfacial capacitance; E_{fb}, flat band potential; N_D, donor density calculated by MS equation assuming ε = 40 [19].

Surface	R_{ct} (10^6 Ω cm^2)	C (10^{-6} F cm^{-2})	E_{fb} (V(SSE))	N_D (10^{20} cm^{-3})
{0 0 1}	2.2 ± 0.24	6.2 ± 0.29	−0.17 ± 0.012	1.7 ± 0.10
{1 0 1}	1.8 ± 0.21	5.9 ± 0.14	−0.17 ± 0.013	1.5 ± 0.09
{1 1 1}	1.5 ± 0.054	6.3 ± 0.50	−0.17 ± 0.012	2.1 ± 0.18

5.4. Discussion

Potentiostatic polarization and EIS measurements demonstrated that a highly insulating passive film formed in the order of {0 0 1} > {1 0 1} > {1 1 1} grains. As discussed in Chapters 3 and 4, oxides have defects that allow weak conduction of ions and/or electrons through the film. The defects also serve as a donor state of an oxide semiconductor. MS analysis indicated that the N_D of the film became greater in the order of {1 1 1} > {0 0 1} > {1 0 1} grains. Interestingly, there is no correlation between R_{ct} and N_D even though these values show clear grain dependencies, suggesting that several factors simultaneously affect the property of the passive film and that the grain dependency on R_{ct} and N_D reflects the passivation caused by complex factors. It was reported that the passive film formed in pH 8.4 borate buffer solution had a bi-layered structure with an inner Fe_3O_4 and an outer γ-Fe_2O_3 [10,11] or a spinel structure closely related to Fe_3O_4 and γ-Fe_2O_3 [1,20]. In the following discussion, orientation-dependent

passivation of iron is discussed based on the formation of a passive film with the bi-layered structure.

In Chapters 3 and 4, the grain dependency in oxide formation was explained by the difference of surface energy γ. Thus, it is also thought that γ (summarized in Table 1.2) is one factor affecting grain-dependent passivation in pH 8.4 borate solution. Higher γ values mean greater activity in the oxidation reaction at the substrate iron/oxide interface, even in an aqueous solution environment. This implies that the growth rate of inner Fe_3O_4 is directly affected by γ. The formation of Fe_3O_4 is thermodynamically feasible since ΔG for the formation of Fe_3O_4 from Fe (and γ-Fe_2O_3) in Eq. 3.7 is negative ($\Delta G = -133.0$ kJ mol^{-1}). Therefore, higher γ values can lead to greater formation rates of Fe_3O_4 and make a thickness difference in the order of iron {0 0 1} > {1 1 1} > {1 0 1} grains, which is the same as the order of γ in vacuum. The correlation between γ and the thickness of an inner Fe_3O_4 layer was obtained for thermally grown oxides in Chapter 4. However, it was difficult to observe the same relation in the thickness of oxide films by 2D ellipsometry measurements during polarization in neutral solution. The small grain dependency in the 2D ellipsometric images (Fig. 5.4) suggests that the difference in thickness among substrate grain is significantly small and/or that the thickness resolution of the ellipsometer is insufficient to optimize grain dependency. Since the dissolution of oxide film and/or substrate through the oxide during anodic polarization is negligible in neutral aqueous solution, it is thought that greater γ values indicate greater activity for the aging of the oxide film, leading to the reduction of defects in the oxide rather than introducing Fe^{2+} ions into the oxide. This means that R_{ct} becomes greater in the order of {0 0 1} > {1 1 1} > {1 0 1} in pH 8.4 borate solution. Although this order is slightly different from that of measured R_{ct} and the difference in R_{ct} is less significant than what has been observed in sulfuric acid, it is thought that γ affected the defect structure of the passive oxide film.

The anisotropic growth of oxides is another factor that develops a grain-dependent passivation. It was reported in Chapter 4 that anisotropic growth affected the defect concentration of oxides due to the compressive stress caused by the lateral component of the growth direction of the oxides. The values of N_D of thermally grown oxides became greater in the same order of the magnitude of the lateral component. The same anisotropic relation between an oxide film and substrate iron as the thermally grown oxide was also observed by Davenport et al. [1] for the passive film formed on iron in pH 8.4 borate solution. They implied that the passive film formed on the iron (0 0 1) face was less defective than the formed on the iron (1 0 1) plane, which is related to the fact that the passive film on the iron {0 0 1} grain shows a higher R_{ct} than on the {1 0 1} grain. However, the implied defect structure does not explain the grain dependency of N_D. When the passive film formation is governed only by the movement of ions through the oxide [22], R_{ct} indicates the resistivity for ionic conduction in the oxide, whereas N_D displays the density of electron trap sites. Inconsistency in the grain dependency of R_{ct} and N_D suggests that ionic and electronic conductions are in competition during the measurements of these parameters and in

passive film formation, in which ionic conduction is a major factor during the passivation and electronic conduction is dominant during the measurement of N_D. It is thought that, here, N_D reflects the density of electron trap sites in the oxide film. The inverse magnitude order of {0 0 1} and {1 0 1} for R_{ct} to N_D suggests that greater γ values reduce the lattice defects that act as electron donors in the oxide film formed on {0 0 1} grains, compared to those formed on {1 0 1} grains. The highest ionic conductivity and the largest N_D on the iron {1 1 1} grain were caused by both oxide formation with high γ, which is 95% of that on the iron {0 0 1} grain, and the anisotropic growth of the oxide in the lateral direction.

Furthermore, the acidity of electrolyte solution could change the ratio of dissolution rate to oxide formation rate, depending on the value of γ. In Chapter 3, the values of R_{ct} of the passive films formed in pH 1.3 sulfuric acid became greater in the order of {1 0 1} > {1 1 1} > {0 0 1} grains. The current density during the potentiostatic polarization in pH 1.3 sulfuric acid is greater than in pH 8.4 borate solution while the slope ($-\mathrm{d}\log j / \mathrm{d}\log t$) in pH 1.3 is gentler than in pH 8.4 solution. This is due to the dissolution of an oxide film and/or substrate iron through the film into acidic media. It was reported in Chapter 3 that the consumption of γ-Fe_2O_3 for the formation of Fe_3O_4 depended on γ. This conversion reaction would compete with the dissolution of γ-Fe_2O_3 into solution; the grain dependency of R_{ct} would become much obvious in cases in which no γ-Fe_2O_3 dissolves. In pH 8.4 borate buffer, where the dissolution reaction is negligibly small, the difference in γ could be the main cause of differences in defect concentrations in the oxide. The magnitude relation of R_{ct} might be affected by differences in the formation rate and/or dissolution rate of oxide, depending on both the γ of the substrate and the acidity of solution.

5.5. Conclusions

Grain-dependent passivation behavior of polycrystalline iron in pH 8.4 borate buffer was investigated by means of *in situ* 2D ellipsometry and electrochemical measurements with the MCC. Ellipsometric parameters changed on the entire sample surface as potentiostatic polarization progressed. However, it was difficult to observe the clear heterogeneity of parameters, depending on the metallographic texture of the substrate, even after polarization for 24 h. The heterogeneity of a passive film thickness was too small to observe with the 2D ellipsometer employed. *Ex situ* Raman spectroscopy and XPS analysis suggested that the composition of the passive film was independent of the substrate crystallographic orientation. On the other hand, micro-electrochemical measurements with the MCC demonstrated the grain dependency in the charge transfer resistance R_{ct} and the donor density N_D of the passive film. Little correlation between R_{ct} and N_D for the three iron grains indicated that the γ and anisotropic oxide growth affect grain dependency during passivation. It was also suggested that the acidity of solution during polarization affects anisotropic passive film formation, due to an increase in the dissolution rate of the outer oxide layer.

References

[1] A. J. Davenport, L. J. Oblonsky, M. P. Ryan, and M. F. Toney, *J. Electrochem. Soc.*, **147**, 2162 (2000).

[2] K. Fushimi, K. Azumi, and M. Seo, *ISIJ Int.*, **39**, 346 (1999).

[3] E. Desimoni, G. I. Casella, A. M. Salvi, T. R. I. Cataldi, and A. Morone, *Carbon*, **30**, 527 (1992).

[4] G. T. Burstein and A. J. Davenport, *J. Electrochem. Soc.*, **136**, 936 (1989).

[5] N. Sato, K. Kudo, and R. Nishimura, *J. Electrochem. Soc.*, **123**, 1419 (1976).

[6] J. H. Weaver and H. P. R. Frederikse, in *CRC Handbook of Chemistry and Physics*, W. H. Haynes and D. R. Lide, Editors, p. 12–126, CRC Press, New York (2011).

[7] N. Sato and K. Kudo, *Electrochim. Acta*, **16**, 447 (1971).

[8] T. Ohtsuka, K. Kubo, and N. Sato, *Corrosion*, **42**, 476 (1986).

[9] T. Ohtsuka, *Mater. Trans.*, **37**, 67 (1996).

[10] M. Nagayama and M. Cohen, *J. Electrochem. Soc.*, **109**, 781 (1962).

[11] M. P. Ryan, R. C. Newman, and G. E. Thompson, *J. Electrochem. Soc.*, **142**, L177 (1995).

[12] P. Keller and H.-H. Strehblow, *Corros. Sci.*, **46**, 1939 (2004).

[13] T. Nagatomi, S. Tanuma, and K. Goto, *Surf. Interface Anal.*, **42**, 1537 (2010).

[14] M. Seo and M. Chiba, *Electrochim. Acta*, **47**, 319 (2001).

[15] M. Chiba and M. Seo, *J. Electorchemical Soc.*, **150**, B525 (2003).

[16] A. Schreiber, J. W. Schultze, M. M. Lohrengel, F. Kármán, and E. Kálmán, *Electrochim. Acta*, **51**, 2625 (2006).

[17] T. Yamamoto, K. Fushimi, S. Miura, and H. Konno, *J. Electrochem. Soc.*, **157**, C231 (2010).

[18] S. P. Harrington, F. Wang, and T. M. Devine, *Electrochim. Acta*, **55**, 4092 (2010).

[19] K. Azumi, T. Ohtsuka, and N. Sato, *J. Electrochem. Soc.*, **134**, 1352 (1987).

[20] K. Kuroda, B. D. Cahan, G. Nazri, E. Yeager, and T. E. Mitchell, *J. Electrochem. Soc.*, **129**, 2163 (1982).

[21] W. E. Boggs, R. H. Kachik, and G. E. Pellissier, *J. Electrochem. Soc.*, **112**, 32 (1967).

[22] N. Sato, in *Passivity of metals*, R. P. Frankental and J. Kruger, Editors, p. 29, The Electrochemical Society Inc., Princeton, NJ (1978).

[23] K. Iwauchi, *Jpn. J. Appl. Phys.*, **10**, 1520 (1971).

[24] K. S. Rane, A. K. Nikumbh, and A. J. Mukhedkar, *J. Mater. Sci.*, **16**, 2387 (1981).

[25] V. A. Hiremath and A. Venkataraman, *Bull. Mater. Sci.*, **26**, 391 (2003).

[26] G. V. Samsonov, *The Oxide Handbook*, p. 272, IFI/Plenum, New York (1973).

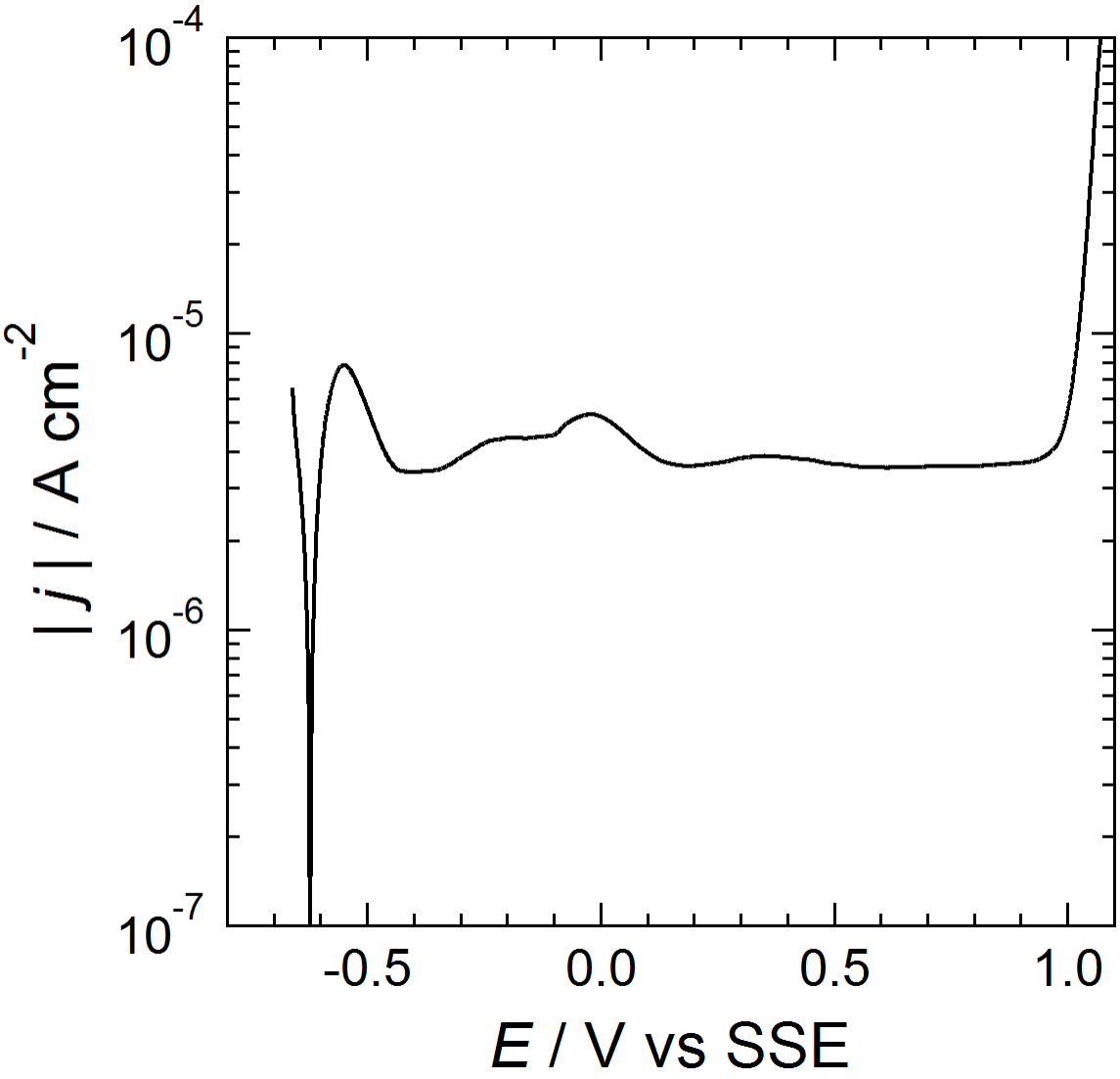

Figure 5.1. Anodic polarization curve of a polycrystalline iron specimen in pH 8.4 borate buffer solution; the potential was swept at 1 mV s^{-1}.

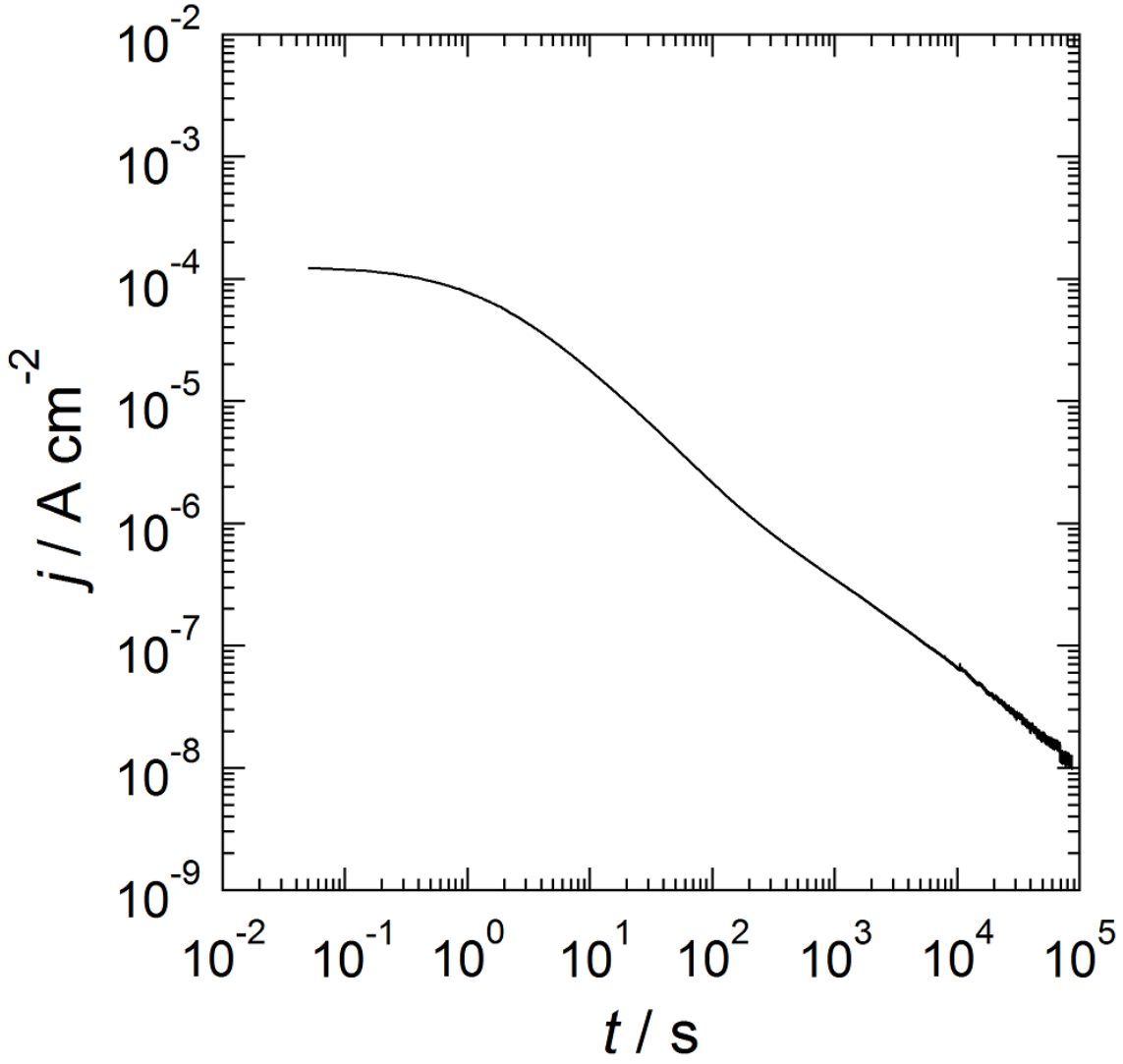

Figure 5.2. Double logarithmic plot of current-time transient of polycrystalline iron specimen under potentiostatic polarization at 0.9 V (SSE) in pH 8.4 borate buffer solution.

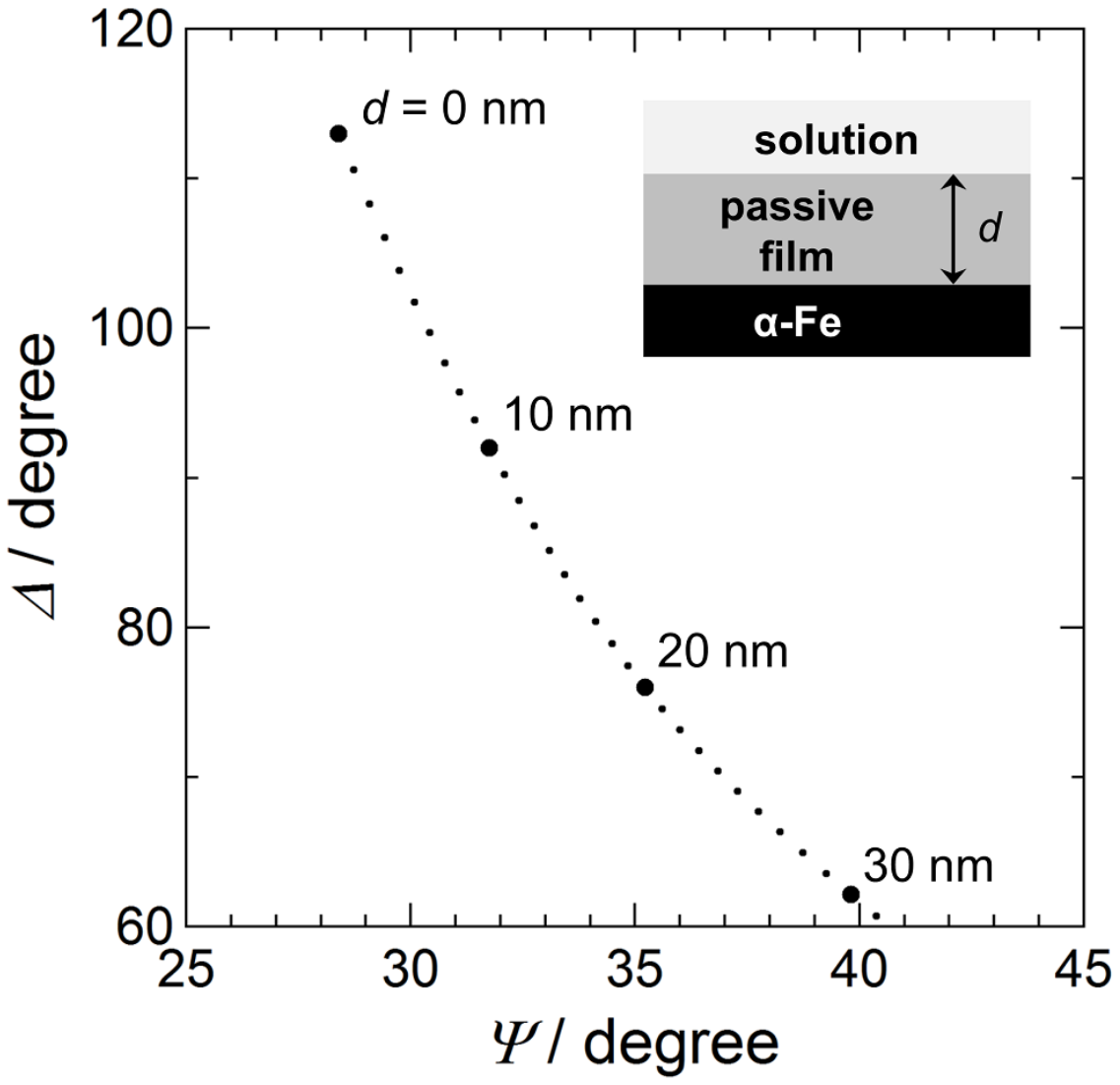

Figure 5.3. Ideal curve of Δ vs Ψ calculated with an optical model for a passive film formed on iron substrate (inset); the dots in the curve are plotted at 1-nm intervals when the thickness *d* of the film changes.

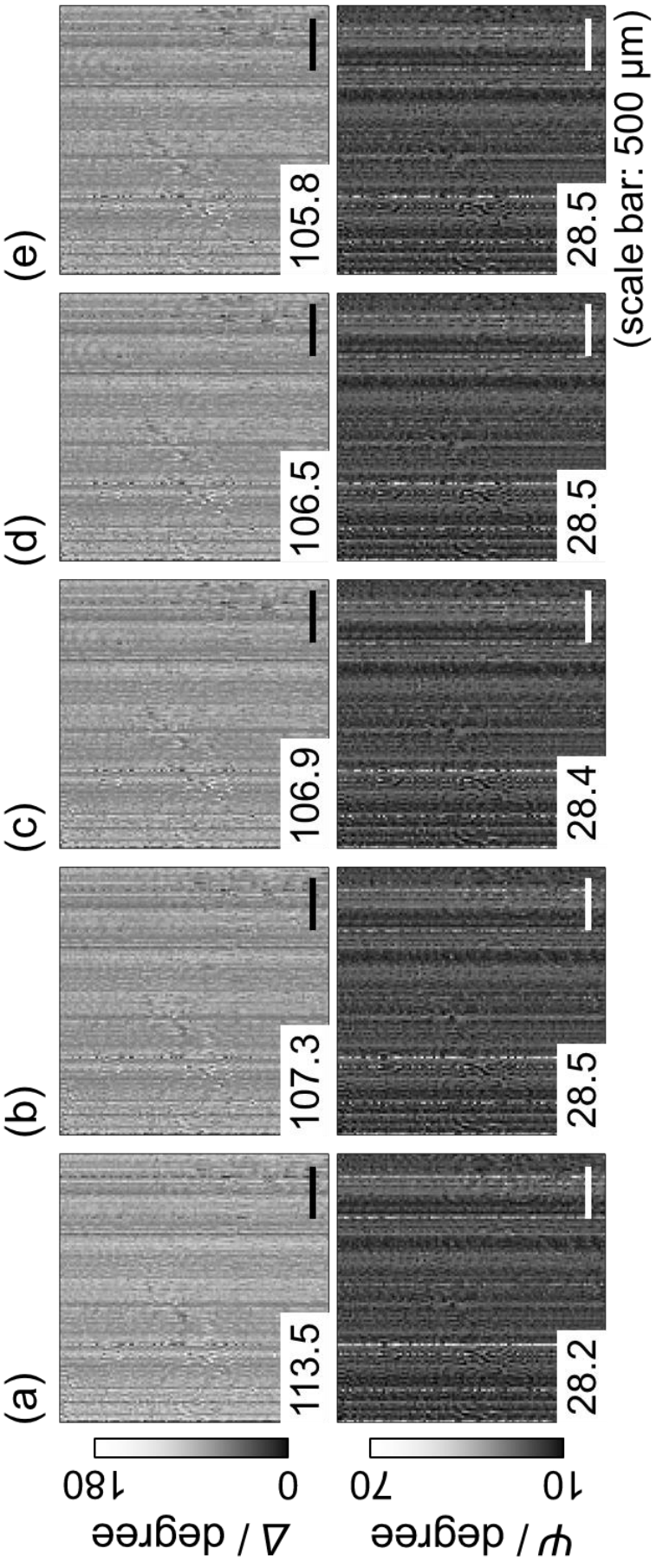

Figure 5.4. 2D images of Δ and Ψ measured on the iron specimen surface by the 2D ellipsometer in pH 8.4 borate buffer solution; *in situ* 2D ellipsometry was conducted during potentiostatic polarization at 0.9 V (SSE) at polarization periods of (a) 0, (b) 1, (c) 6, (d) 12, and (e) 24 h, with the value in the bottom left of each image displaying an average of the entire image.

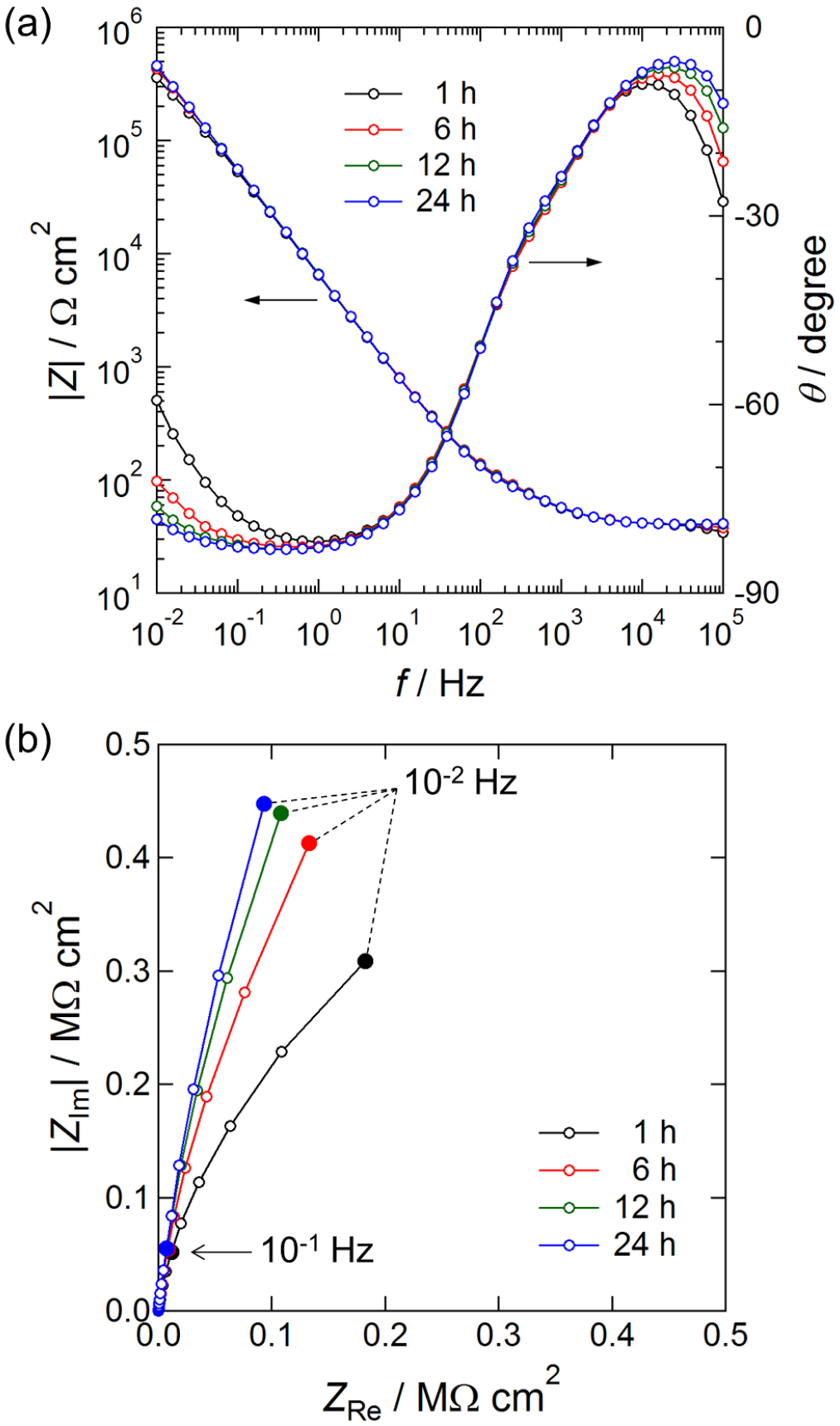

Figure 5.5. (a) Bode plot and (b) Nyquist plot of polycrystalline iron polarized at 0.9 V (SSE) for 1, 6, 12, and 24 h in pH 8.4 borate solution.

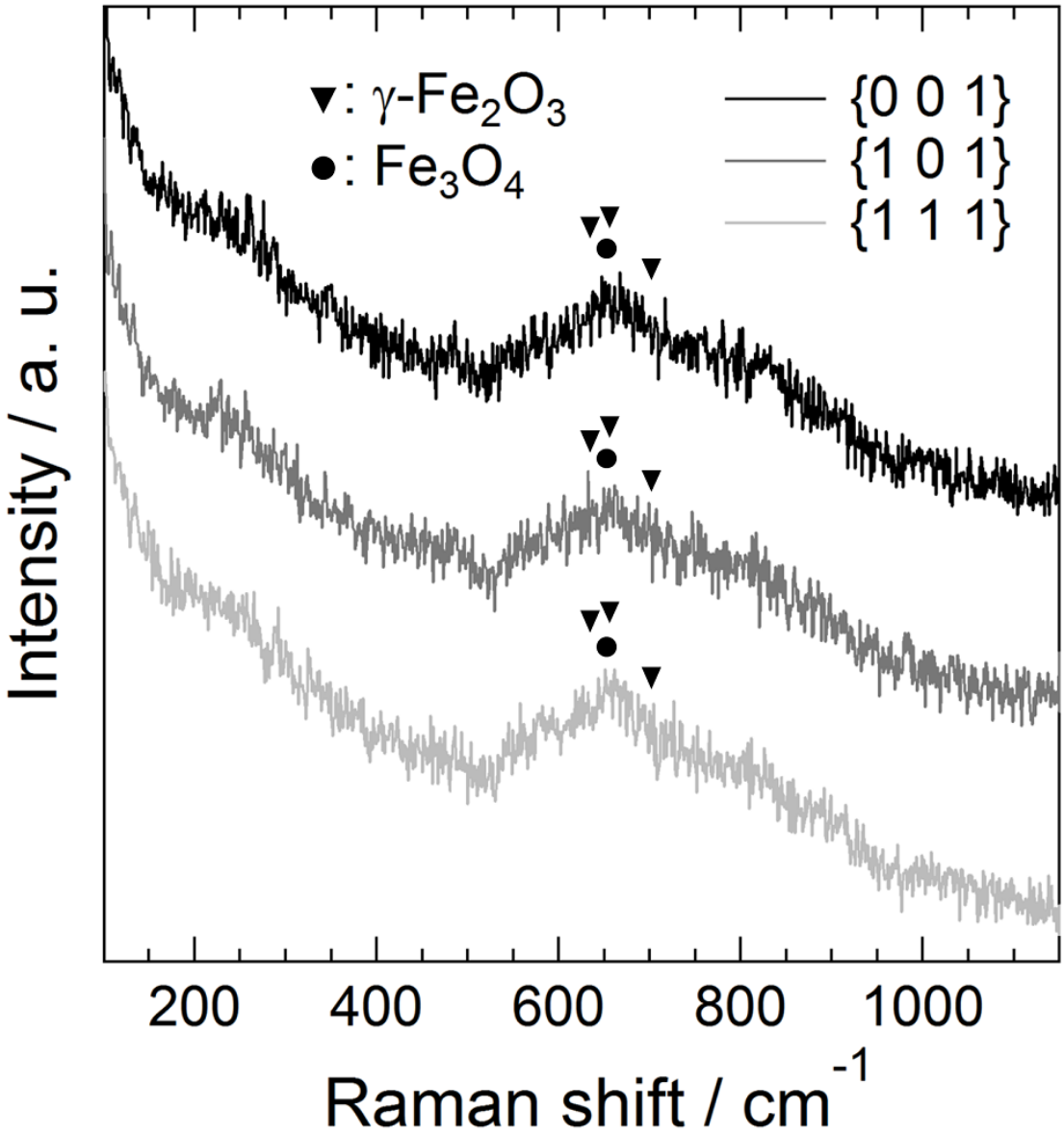

Figure 5.6. Raman spectra measured on iron {0 0 1}, {1 0 1}, and {1 1 1} grains after potentiostatic polarization at 0.9 V (SSE) for 1 h in pH 8.4 borate buffer solution. The strong Raman shifts of γ-Fe_2O_3 and Fe_3O_4 are marked as inverse triangles and solid circles respectively.

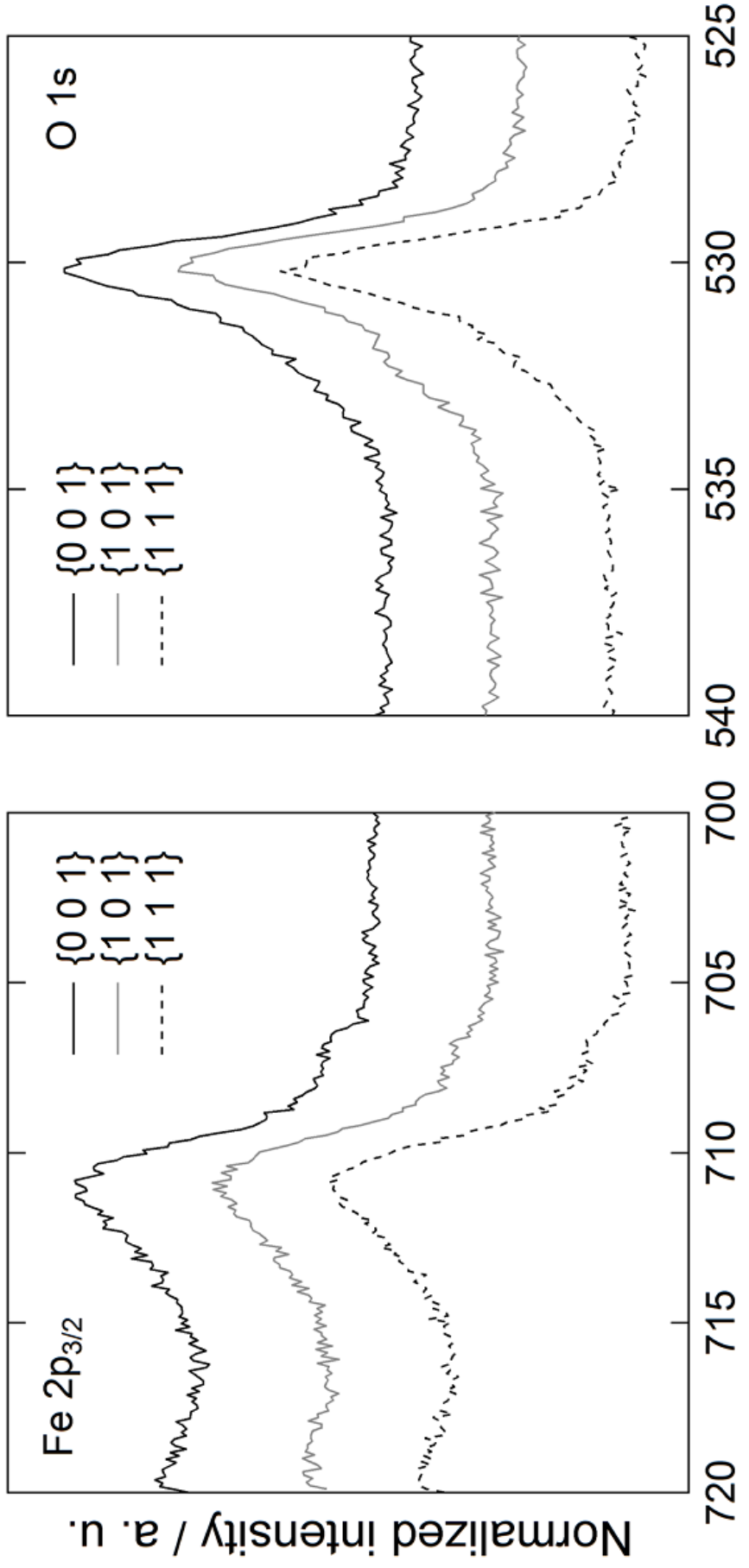

Figure 5.7. (a) Fe $2p_{3/2}$ and (b) O 1s photoelectron spectra measured on iron {0 0 1}, {1 0 1}, and {1 1 1} grains after potentiostatic polarization at 0.9 V (SSE) for 1 h in pH 8.4 borate buffer solution.

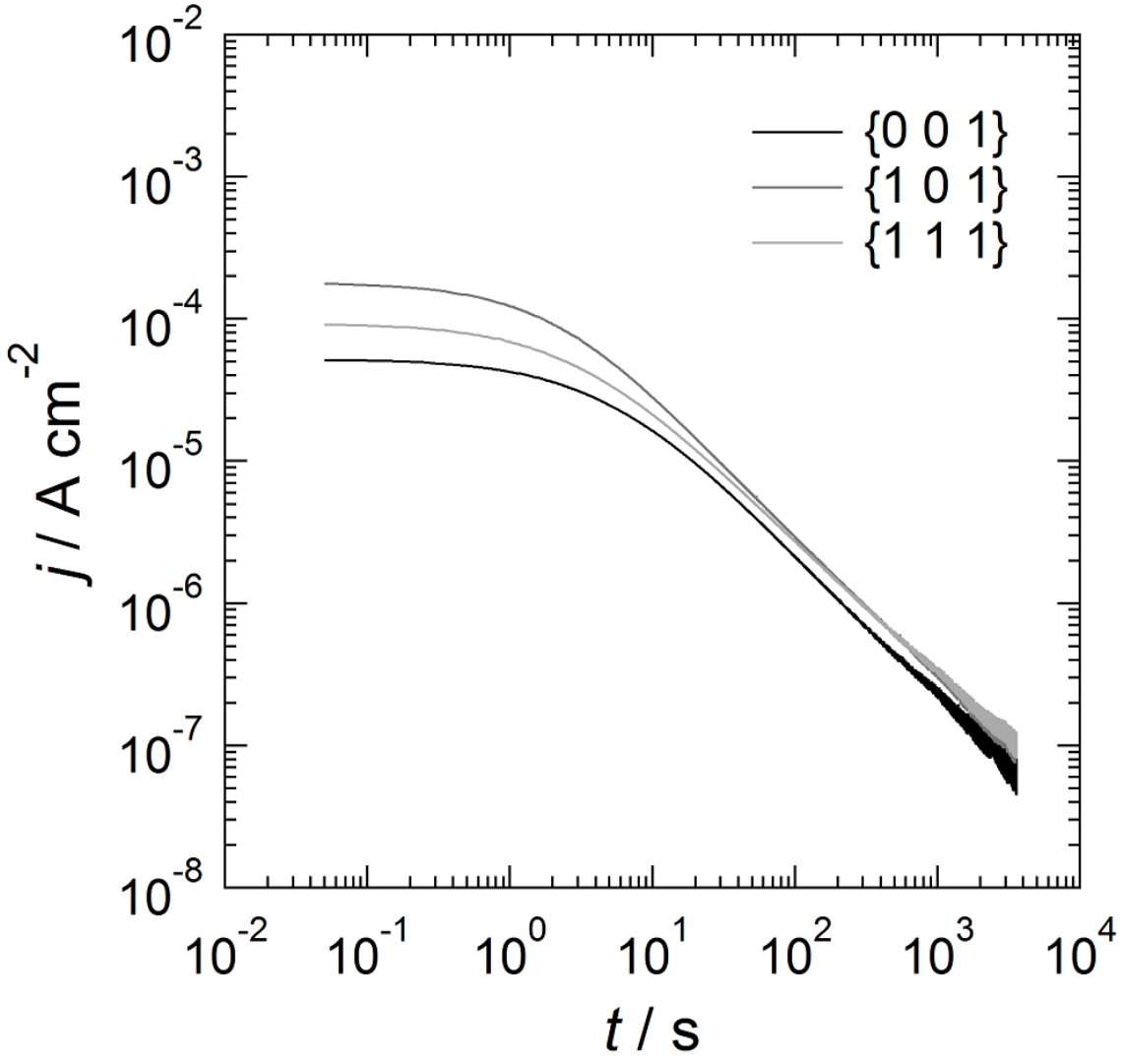

Figure 5.8. Double logarithmic plot of current-time transients of iron {0 0 1}, {1 0 1}, and {1 1 1} grains measured with the MCC during potentiostatic polarization at 0.9 V (SSE) for 1 h in pH 8.4 borate buffer solution.

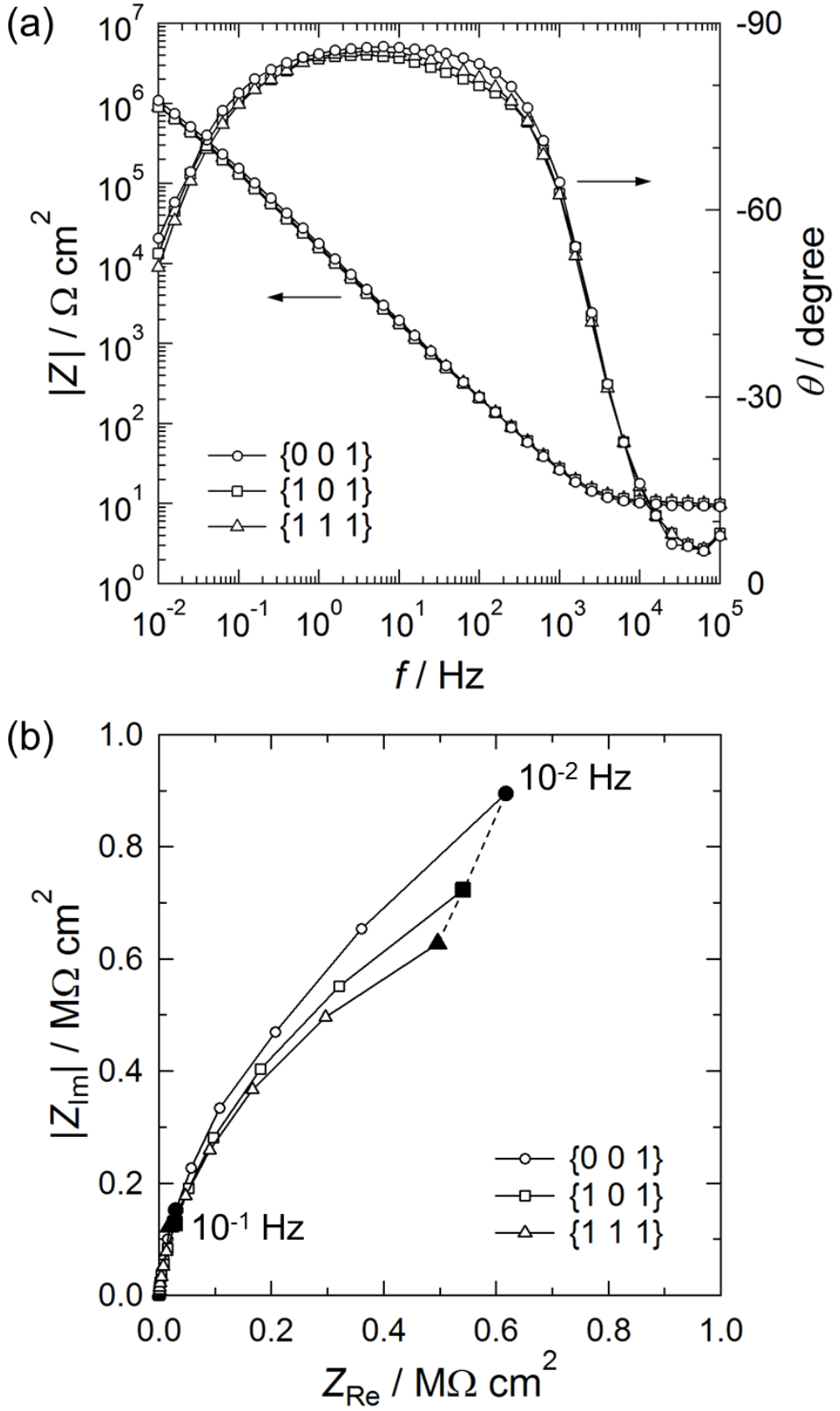

Figure 5.9. Impedance (a) Bode plot and (b) Nyquist plot of iron {0 0 1}, {1 0 1}, and {1 1 1} grains polarized at 0.9 V (SSE) for 1 h in pH 8.4 borate buffer solution.

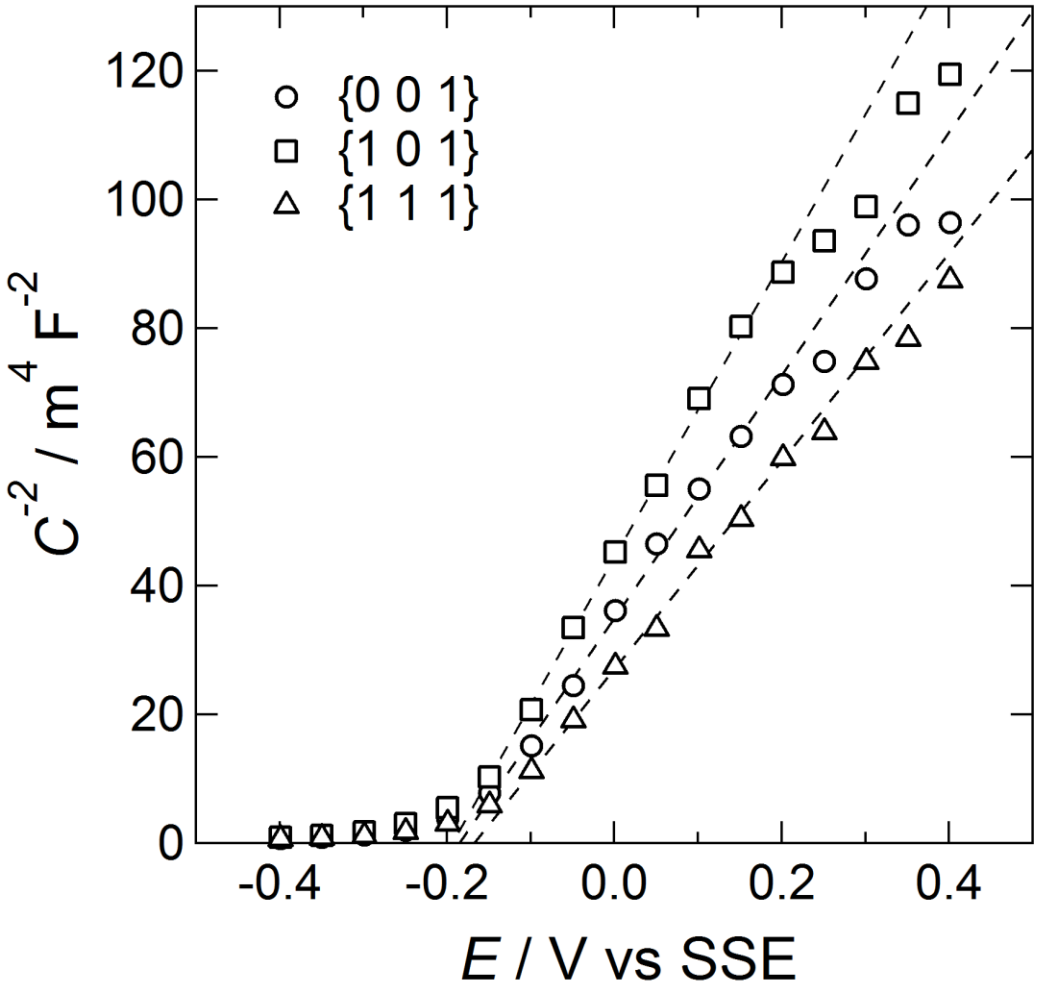

Figure 5.10. Mott-Schottky plot for iron {0 0 1}, {1 0 1}, and {1 1 1} grains polarized at 0.9 V (SSE) for 1 h in pH 8.4 borate buffer solution; each plot was measured at 10 Hz and the potential was changed stepwise in a negative direction.

Chapter 6
Summary

An oxide film formed on metallic materials plays an important role in preventing the corrosion of metallic materials. The formation mechanism and characteristics of this oxide film have been intensively studied since they directly affect the reliability and service time predictions of metallic materials. Most metals and alloys used across a wide range of industries are polycrystalline, and it has been pointed out that the formation rate, thickness, and characteristics of the oxide film at the micro-region on a substrate depend on the metallographic structure, such as the surface crystallographic orientation and grain boundaries. The detailed investigation of the orientation-dependent oxidation behavior of polycrystalline metals and alloys was expected to explain a detailed oxidation mechanism and the kinetics of practical metallic materials. Among such materials, iron is the most commonly used metal in many industries as a base element of steels; it is necessary for daily life. A clear understanding of the heterogeneity of the oxide film formed on polycrystalline iron should lead to predicting the progress of corrosion on steels accurately and to improving the reliability of service time estimations of steel-based structures. Eventually, it could contribute to the realization of a genuinely sustainable society. On the other hand, the technological advancements in the identification technique of surface crystallographic orientations and in micro-electrochemical measurement methods have enabled precise analysis of the oxidation behavior and the physicochemical property of an oxide film formed on a single grain of a polycrystalline substrate. Grain-dependent oxidation behavior and the surface oxide property of the single grain have been reported by several researchers, and the rough trends of the grain-dependent oxidation are now becoming clear. However, the findings in previous reports gave only fragmentary information on the way to the construction of a theory and the development of an analytical technique to explain the relationship between oxide film formation and corrosion resistance of metallic materials from the viewpoint of metallographic structure.

In this dissertation, an improved MCC method and *in situ* 2D ellipsometry were developed as measurement techniques to investigate the heterogeneity of an oxide film formed on polycrystalline iron. The passivation behavior of single grains and oxide film thickness and degradation behavior of the entire polycrystalline surface were investigated using the developed electrochemical measurement techniques.

In Chapter 1, the significance of studying corrosion and the grain-dependent corrosion of polycrystalline metals were introduced. The motivation for investigating polycrystalline iron for

this study and previous work on investigating corrosion behavior were both described. Finally, the precise purpose of this dissertation was presented.

In Chapter 2, sample preparation, experimental setups, and procedures of the MCC and *in situ* 2D ellipsometry were described.

In Chapter 3, passive films formed on single grains of a polycrystalline iron substrate were investigated by the MCC in sulfuric acid. The current-time transients under potentiostatic polarization depended heavily on the crystallographic orientation of the substrate surface. Electrochemical impedance spectroscopy, XPS, and galvanostatic reduction revealed the grain dependency in the charge transfer resistance R_{ct}, composition, and the thickness of outer γ-Fe_2O_3 of the passive film. It was concluded that the grain dependency in the surface energy γ and epitaxial relation between the oxide and substrate affected the defect structure of the passive film, resulting in an inverse correlation between R_{ct} and the thickness of γ-Fe_2O_3.

In Chapter 4, the heterogeneity of the thermally oxidized surface of a polycrystalline iron substrate was investigated by means of 2D ellipsometry and the MCC. A bi-layered structure—an inner Fe_3O_4 layer/an outer α-Fe_2O_3 layer—of the thermally grown oxide was confirmed by Raman spectroscopy, SEM observation, and XPS. The oxide thickness evaluated by *ex situ* 2D ellipsometry was summarized on an IPF of bcc iron as a contour map and the relationship between the oxide thickness and surface crystallographic orientations was clarified. Heterogeneous degradation behavior of the thermally oxidized surface was observed by *in situ* 2D ellipsometry under galvanostatic polarization. The transients of ellipsometric parameters followed different trajectories depending on the substrate orientation, indicating that an oxide film with thicker inner Fe_3O_4 was more susceptible to the alteration of oxide properties caused by cathodic currents. The donor density N_D demonstrated by EIS measurements with the MCC showed a positive correlation with d_{IL} of the thickness of the inner Fe_3O_4 and γ of the iron substrate. It was concluded that the anisotropic growth of two oxide layers affected d_{IL} and the defect structure of the outer α-Fe_2O_3 layer.

In Chapter 5, the passivation behavior of polycrystalline iron in pH 8.4 borate buffer solution was investigated from the viewpoint of both a single grain and a whole polycrystalline substrate. The growth of the passive film on a whole substrate was observed by *in situ* 2D ellipsometry under potentiostatic polarization for 24 h. Ellipsometric images showed little grain dependency in the passivation behavior, suggesting that the difference in thickness among substrate grains was small and/or that the thickness resolution of the ellipsometer is insufficient to optimize grain dependency. MCC measurements revealed the grain dependency in R_{ct} and N_D of the passive film, but a clear correlation between these parameters was not observed. It was

suggested that several factors, such as γ and the anisotropic growth of oxides, simultaneously affected passivation.

Chapter 6 summarizes the findings of Chapters 3–5 regarding grain-dependent oxidation behavior and the oxide film property of polycrystalline iron caused by anodic oxidation in acid and neutral aqueous solutions and by high temperature atmosphere. It was revealed that the formation and degradation of a surface oxide film progressed heterogeneously, depending on the surface crystallographic orientation of the polycrystalline substrate. The obtained grain-dependent parameters are summarized in Table 6.1. The order of magnitude of each parameter among the three iron grains depends on the surrounding environment; there is no clear correlation with the surroundings. This indicates that the surrounding environment greatly affects the grain-dependent oxidation behavior. For example, the difference in the dissolution rate of the oxide and/or substrate iron due to the acidity of electrolyte solution led to different defect structures in the oxide layer film. Under high temperature air, the surface coverage rate of the outer α-Fe_2O_3 layer determined the oxide thickness. Thus, different oxide growth mechanisms led to different grain dependencies; it is demonstrated by the parameters in Table 6.1. This indicates that grain-dependent oxidation behavior is based on the growth mechanism of iron in a certain environment and is affected by orientation-dependent parameters such as γ and the epitaxial relation between the oxide and substrate. Although one may take this conclusion for granted, the investigation of grain-dependent oxidation also provides a detailed elucidation of the oxidation mechanism by providing information that is a key factor in oxide growth.

The MCC and 2D ellipsometry successfully demonstrated the heterogeneity of an oxide film that formed on polycrystalline iron from the viewpoint of single grains and a whole polycrystalline substrate. The findings in this study offer essential information that is necessary for developing a conventional theory of corrosion science based on homogeneous oxide film formation and constructing a new corrosion theory based on heterogeneous oxidation behavior. The new theory will enable advanced corrosion prevention strategies to be implemented and appropriate conservation measures to be applied to practical metallic materials; it also enables the safer operation and longer service time of products that are widespread in our lives. Design guidance for a high corrosion-resistance material that forms a homogeneous surface oxide is also enabled by the new theory. These new approaches are expected to lead the reduction of the enormous corrosion costs of ca. 10 trillion JPY per year. Furthermore, the measurement techniques and the findings in this study are applicable to the elucidation of grain-dependent oxidation of all other metals and alloys; the precise control of corrosion on metallic materials has moved one step closer to realization by continued study of grain-dependent corrosion.

Table 6.1. Grain-dependent parameters for oxide films measured in this study; q_t, total charge density consumed for 1-h potentiostatic polarization; j_f, current density at 1 h; R_{ct}, charge transfer resistance for oxide growth; C, interfacial capacitance; E_{fb}, flat band potential; N_D, donor density.

Parameter	Surrounding	Formation condition	Surface		
			{0 0 1}	{1 1 1}	{1 0 1}
q_t (C cm^{-2})	Sulfuric acid (pH 1.3)	at 1.2 V (RHE) for 1 h	0.54	1.2	0.85
	Borate buffer (pH 8.4)	at 0.9 V (SSE) for 1 h	1.7×10^{-3}	2.1×10^{-3}	2.5×10^{-3}
j_f (A cm^{-2})	Sulfuric acid (pH 1.3)	at 1.2 V (RHE) for 1 h	2.9×10^{-6}	1.9×10^{-6}	1.3×10^{-6}
	Borate buffer (pH 8.4)	at 0.9 V (SSE) for 1 h	6.4×10^{-8}	1.0×10^{-7}	9.7×10^{-8}
R_{ct} (Ω cm^2)	Sulfuric acid (pH 1.3)	at 1.2 V (RHE) for 1 h	4.3×10^{4}	6.9×10^{4}	1.1×10^{5}
	Borate buffer (pH 8.4)	at 0.9 V (SSE) for 1 h	2.2×10^{6}	1.5×10^{6}	1.8×10^{6}
C (F cm^{-2})	Sulfuric acid (pH 1.3)	at 1.2 V (RHE) for 1 h	12×10^{-6}	11×10^{-6}	11×10^{-6}
	Borate buffer (pH 8.4)	at 0.9 V (SSE) for 1 h	6.2×10^{-6}	6.3×10^{-6}	5.9×10^{-6}
E_{fb} (V(RHE))	Sulfuric acid (pH 1.3)	at 1.2 V (RHE) for 1 h	0.46	0.49	0.48
	Borate buffer (pH 8.4)	at 0.9 V (SSE) for 1 h	0.53	0.53	0.53
	In air	573 K for 1 h	0.48	0.52	0.51
N_D (cm^{-3})	Sulfuric acid (pH 1.3)	at 1.2 V (RHE) for 1 h	5.3×10^{20}	4.7×10^{20}	5.1×10^{20}
	Borate buffer (pH 8.4)	at 0.9 V (SSE) for 1 h	1.7×10^{20}	2.1×10^{20}	1.5×10^{20}
	In air	573 K for 1 h	13×10^{20}	1.8×10^{20}	0.89×10^{20}

Appendix

Symbols used in this dissertation

a	[-]	symmetry factor
a_{111}	[-]	relative area of {1 1 1} grain
a_ι	[-]	activity of species ι
A_{111}	[cm^2]	electrode area of {1 1 1} grain part
A_{MCC}	[cm^2]	electrode area achieved by an MCC
B	[mV $decade^{-1}$]	Tafel slope
b_a	[mV $decade^{-1}$]	Tafel slope of iron dissolution reaction
C	[F cm^{-2}]	interfacial capacitance
C_H	[F cm^{-2}]	Helmholtz layer capacitance
$C\iota$	[cm^{-3}]	concentration of species ι
C_{SC}	[F cm^{-2}]	space charge layer capacitance
c	[m s^{-1}]	speed of light in vacuum (c = 2.99792458 × 10^8 m s^{-1} [1])
$D^*\iota$	[cm s^{-1}]	electrochemical diffusivity of species ι
d	[nm]	thickness
d_p	[nm]	maximum possible depth
d_{SC}	[nm]	space charge layer thickness
E	[V]	electrode potential
E_{app}	[V]	applied potential
E_b	[eV]	binding energy
E_{corr}	[V]	corrosion potential
E_{eq}	[V]	equilibrium potential
E_{ext}	[V]	external potential
E_{fb}	[V]	flat band potential
E_{ip}, E_{is}	[-]	complex amplitude of the components of the electric vectors of the incident wave for p- and s-polarizations
E_k	[eV]	kinetic energy of photoelectron
E_{rp}, E_{rs}	[-]	complex amplitude of the components of the electric vectors of the reflected wave for p- and s-polarizations
E_{tp}, E_{ts}	[-]	complex amplitude of the components of the electric vectors of the transmitted wave for p- and s-polarizations
e	[C]	electron charge (e = 1.602176 × 10^{-19} C [1])
F	[C mol^{-1}]	Faraday constant (F = 9.64853 × 10^{-19} C mol^{-1} [1])
f	[Hz]	frequency
f_0	[Hz]	reference frequency
ΔG	[kJ mol^{-1}]	Gibbs free energy change in a chemical process

ΔG^{o}	[kJ mol^{-1}]	standard Gibbs free energy change in a chemical process
$\Delta G_S{}^{o}$	[kJ mol^{-1}]	standard Gibbs free energy change for the Schottky-pair reaction
h	[eV]	Planck constant (h = 6.62607 10^{-34} J s [1])
i	[-]	imaginary number ($i^2 = -1$)
J_e	[A cm^{-2}]	electronic current
J_i	[A cm^{-2}]	ionic current
$J_{V_O^{\cdot\cdot}}$	[mol cm^{-2} s^{-1}]	flux of oxygen vacancy
j	[A cm^{-2}]	current density
j_0	[A cm^{-2}]	exchange current density
j_a	[A cm^{-2}]	anodic current density
j_c	[A cm^{-2}]	cathodic current density
j_{corr}	[A cm^{-2}]	corrosion current density
j_f	[A cm^{-2}]	final current density at potentiostatic polarization
K	[cm^{-1}]	wave number
k	[-]	extinction coefficient
k_B	[J K^{-1}]	Boltzmann constant (k_B = 1.38065 × 10^{-23} J K^{-1} [1])
L_{GB}	[µm]	length of grain boundary in the electrode
l_{XY}	[nm]	distance between points X and Y
M	[g mol^{-1}]	molecular weight
N	[-]	complex refractive index
N_A	[mol^{-1}]	Avogadro constant (N_A = 6.02214 × 10^{23} mol^{-1} [1])
N_D	[cm^{-3}]	donor density
N_x	[-]	complex refractive index of a medium x
n	[-]	refractive index
p	[-]	CPE coefficient
Q	[Ω^{-1} s^{p}]	CPE constant
q	[C cm^{-2}]	electric charge density
q_a	[C cm^{-2}]	electric charge density consumed in an active state
q_c	[C cm^{-2}]	cathodic charge density
q_p	[C cm^{-2}]	electric charge density consumed in a passive state
q_t	[C cm^{-2}]	total electric charge density consumed for 1-h potentiostatic polarization
R	[J K^{-1} mol^{-1}]	gas constant (R = 8.31447 J K^{-1} mol^{-1} [1])
R_{ct}	[Ω cm^2]	charge transfer resistance
R_{el}	[Ω cm^2]	electrolyte resistance
R_{OX}	[Ω cm^2]	ohmic resistance of oxide
r_p, r_s	[-]	Fresnel complex-amplitude reflection coefficients for p- and s-polarizations

s	[m s^{-1}]	speed of light in a medium
t	[s]	time
t_p, t_s	[-]	Fresnel complex-amplitude transmission coefficients for p- and s-polarizations
t_{pa}	[s]	passivating time
u	[cm s^{-1}]	velocity of drift of ions in an oxide film
T	[K]	absolute temperature
V	[V]	voltage drop across thin oxide film
X	[cm]	oxide film thickness at t
X_1	[cm]	characteristic distance depending on the interfacial potential difference and temperature
X_L	[cm]	limiting film thickness
$\|Z\|$	[Ω cm^2]	impedance magnitude
Z_{Im}	[Ω cm^2]	imaginary part of impedance
Z_{Re}	[Ω cm^2]	real part of impedance
z	[-]	valence
α	[-]	coefficient for the potential dependence of $\Delta\phi_{f/s}$
α_a	[cm^{-1}]	absorption coefficient
α_p	[-]	phase change
β	[-]	coefficient for the pH dependence of $\Delta\phi_{f/s}$
β_p	[-]	film phase thickness ($\beta_p = \alpha_p/2$)
γ	[J m^{-1}]	surface energy
Δ	[degrees]	differential change in phase between vibrations of p- and s-polarizations
δ_{rp}, δ_{rs}	[degrees]	arguments of r_p and r_s
ε	[-]	dielectric constant
ε_0	[J^{-1} C^2 m^{-1}]	permittivity in vacuum ($\varepsilon_0 = 8.85419 \times 10^{-12}$ J^{-1} C^2 m^{-1} [1])
ε_F	[V cm^{-1}]	field strength
η	[V]	overpotential
θ	[degrees]	phase shift
θ_0	[degrees]	incident angle
θ_1	[degrees]	refraction angle
λ	[nm]	wavelength of light
μ_ι	[kJ mol^{-1}]	chemical potential of species ι
ν	[s^{-1}]	frequency of electromagnetic wave
P	[-]	ratio of the complex Fresnel reflection coefficients for p- and s-polarizations
ρ	[Ω m]	electrical resistivity

ρ_{ox}	[g cm^{-3}]	density of oxide
ρ_{surf}	[cm^{-2}]	surface atom density
σ	[Ω^{-1} m^{-1}]	electrical conductivity
Φ	[degrees]	Euler angle between the *Z* axis and the *z* axis
Φ_w	[eV]	work function
φ_1	[degrees]	Euler angle between the *X* axis and the N_{SC} axis
φ_2	[degrees]	Euler angle between the N_{SC} axis and the *x* axis
$\Delta\phi_f$	[V]	potential drop across the oxide film on a metal
$\Delta\phi_R$	[V]	potential drop at a solution/reference electrode interface
$\Delta\phi_{f/s}$	[V]	potential drop at a film/solution interface
$\Delta\phi_{m/f}$	[V]	potential drop at a metal/film interface
Ψ	[degrees]	differential change in amplitude between vibrations of p- and s-polarizations
ω''_m	[Hz]	frequency at which the $\lvert Z_{Im}\rvert$ shows a maximum value
Ω	[cm^3 mol^{-1}]	molecular volume

[1] P. W. Atkins and J. De Paula, *Atkins' Physical Chemistry*, 10 th Ed., Oxford University Press, Oxford (2014).

Abbreviations

AES	Auger electron spectroscopy
bcc	body-centered cubic
BE	backscattered electron
CP	cross section polisher
CPE	constant phase element
DFT	density functional theory
EBSD	electron backscatter diffraction
EES	equivalent electronic circuit
EIS	electrochemical impedance spectroscopy
ESCA	electron spectroscopy for chemical analysis
FIB	focused ion beam
GNP	gross national product
IDR	iron dissolution reaction
IPF	inverse pole figure
MCC	micro-capillary cell
MS	Mott-Schottky
ND	normal direction

OCP	open circuit potential
PCA	photonic crystal array
RD	rolling direction
rds	rate-determining step
RHE	reversible hydrogen electrode
TD	transverse direction
SE	secondary electron
SECM	scanning electrochemical microscopy
SEM	scanning electron microscope
SERS	surface-enhanced Raman spectroscopy
SIMS	secondary ion mass spectroscopy
SHE	standard hydrogen electrode
SSE	silver-silver chloride electrode
STM	scanning tunneling microscopy
TEM	transmission electron microscopy
XANES	X-ray absorption near edge structure
XPS	X-ray photoelectron spectroscopy
XRD	X-ray diffraction

List of publications

[1] Yu Takabatake, Koji Fushimi, Takayuki Nakanishi, and Yasuchika Hasegawa, "Grain-Dependent Passivation of Iron in Sulfuric Acid Solution", *Journal of The Electrochemical Society*, Vol. 161, Issue 14, pp. C594–C600 (2014).

[2] Yu Takabatake, Yuichi Kitagawa, Takayuki Nakanishi, Yasuchika Hasegawa, and Koji Fushimi, "Heterogeneity of a Thermal Oxide Film Formed on Polycrystalline Iron Observed by Two-Dimensional Ellipsometry", *Journal of The Electrochemical Society*, Vol. 163, Issue 14, pp. C815–C822 (2016).

Other publications

[1] Koji Fushimi, Yu Takabatake, Takayuki Nakanishi, and Yasuchika Hasegawa, "Microelectrode techniques for corrosion research of iron", *Electrochimica Acta*, Vol. 113, pp. 741–747 (2013).

[2] Hisataka Kataoka, Takayuki Nakanishi, Shun Omagari, Yu Takabatake, Yuichi Kitagawa, and Yasuchika Hasegawa, "Drastically Improved Durability and Efficiency of Silicon Solar Cells Using Hyper-Stable Lanthanide Coordination Polymer Beads", *Bulletin of the Chemical Society of Japan*, Vol. 89, Issue 1, pp. 103–109 (2016).

Acknowledgements

I would like to express my deepest gratitude to my supervisor Associate professor Koji Fushimi for the continuous support and encouragement throughout my Ph. D. program, for his kind guidance and immense knowledge.

I would like to show my sincere appreciation to Professor Kazuhisa Azumi, Kei Murakoshi, Hiroki Habazaki, and Yasuchika Hasegawa for being my advisors and giving insightful comments and suggestions to develop my research.

I also would like to thank Associate professor Masatoshi Sakairi, Assistant professor Takayuki Nakanishi and Yuichi Kitagawa for their helpful advice and warm encouragement.

My sincere thanks also go to colleagues in the laboratory of Advanced Materials Chemistry (AMC), Graduate School of Chemical Sciences and Engineering, Hokkaido University, Japan, who had helped my daily work.

Finally, I gratefully acknowledge the financial support from the Japan Society for the Promotion of Science (JSPS) for Young Scientists by a Grant-in-Aid for JSPS Fellows (No. 26000231).

Yu Takabatake
Sapporo, Japan

March 2017